



CHARACTERISATION AND  
DEVELOPMENT OF THE INCREMENTAL  
SHEAR FORMING PROCESS FOR  
NICKEL-BASED AEROSPACE  
STRUCTURES

MARINE GUILLOT

SUBMITTED IN FULFILMENT OF THE REQUIREMENTS FOR THE DEGREE OF  
*Doctor of Engineering*

DESIGN, MANUFACTURE AND ENGINEERING  
MANAGEMENT

UNIVERSITY OF STRATHCLYDE

SEPTEMBER 2018

© Marine Guillot

## Abstract

The increasing interest from the engineering community to manufacture near-net-shape components in order to improve the material utilisation and cost competitiveness at a product level as well as the product characteristics drives research towards a deeper understanding of cold forming technologies. The herein research investigated the shear forming process applied to 304L stainless steel and Inconel 718 and intended to facilitate an improved exploitation route of the technology into component applications by characterising it geometrically and metallurgically.

First, the identification and impact of the key processing variables (KPVs) on the geometry and surface roughness of the component when applied to 304L stainless steel and Inconel 718 were studied through experimental work using a systematic approach and then compared to the literature (triangulation). A design of experiments approach was undertaken on an industrial scale machine and predictive numerical models were established by statistical analysis to allow optimisation of the process capabilities within component tolerances. The feeds and speeds were revealed to have a significant impact across the different thicknesses and geometries.

Secondly, the microstructure and texture of 304L stainless steel and Inconel 718 post shear forming were studied using scanning electron microscopy coupled with electron back-scattered diffraction. Elongated grains following the roller path were observed as well as shear bands, which are characteristic of high local deformation. The grain size was found to be dependent on the cone angle and an increased hardness was noted. The primary mechanism of deformation was identified as simple shear. The statistical analysis of the texture of the Inconel 718 parts after a two-step aging treatment revealed a significant link between the torsion component B and the cone angle, initial thickness, and their interaction. The research and findings were considered in light of the current literature and recommendations and areas for future research were given.



# Acknowledgements

I would like to thank everyone who has contributed and supported me through this thesis. I am grateful to my academic and industrial supervisors for their help and guidance: Dr Paul Blackwell (main academic supervisor), Mr Thomas McCormack (main industrial supervisor), Dr Andrzej Rosochowski (second academic supervisor), and Dr Martin Tuffs (second industrial supervisor). To Elizabeth Moore who was my industrial supervisor for the first two years of this EngD, thank you for your continuous support and the inspiration you provided me with.

I would like to thank the staff at the Advanced Forming Research Centre (AFRC) and particularly Dr Dorothy Evans for convincing me to start this unexpected journey. I am extremely thankful to Dr Steven Halliday in his role of coordinator Rolls-Royce/AFRC. Dorothy and Steven have constantly been looking out for me, much more than I would have ever expected, and I cannot express how much I appreciate this. For their financial support, I thank Rolls-Royce.

I would like to thank my friends with a special mention to Géraldine and Léa as well as Jill, Liza, Julie, Lucie, and Sébastien for being there for me and keeping me sane. The biggest thank you goes to my family, especially Mum, Dad, Maxou, Ben, Grandma Huguette, and Grandma Monique who have always believed in me and gave me love and support in everything I have done. And finally, I would like to thank my partner and best friend, Stephen, for his love, support, and belief even through the tough times.

*To my Grandpa Jean.*

“La clef de toutes sciences est sans contredit le point d’interrogation; nous devons la plupart des grandes découvertes au Comment? et la sagesse dans la vie consiste peut-être à se demander, à tout propos, Pourquoi?” – Honoré de Balzac

“The key to all science is undoubtedly the question mark. To the word How? we owe most of our greatest discoveries. Wisdom in life may perhaps consist in asking ourselves on all occasions: Why?” – Honoré de Balzac

# **Declaration of Authenticity and Author's Rights**

This thesis is the result of the author's original research. It has been composed by the author and has not been previously submitted for examination which has led to the award of a degree.

The copyright of this thesis belongs to the author under the terms of the United Kingdom Copyright Acts as qualified by University of Strathclyde Regulation 3.50. Due acknowledgement must always be made of the use of any material contained in, or derived from, this thesis.

© Marine Guillot 2018

Signed:

Date:

## Previously published work

The following papers were published by the candidate in support of the application for the degree of Doctor of Engineering.

**Appendix A – Paper A** M. Guillot, A. Rosochowski, P. Blackwell, E. Moore, and S. Halliday. Characterisation and development of the incremental shear forming process for advanced structures. In *Proceedings of the 13th International Cold Forming Congress*, pages 208–215, 2015.

**Appendix B – Paper B** M. Guillot, T. McCormack, M. Tuffs, A. Rosochowski, S. Halliday, and P. Blackwell. Shear forming of 304L stainless steel microstructural aspects. *Procedia Engineering*, 2017.

The work reported in each paper was conducted by the author of this thesis as an individual EngD student. In each case, co-authors provided the same level of general and editorial guidance as they provided for the EngD thesis as a whole.

Signed:

Date:

# List of acronyms and abbreviations

---

	<b>Acronym Abbreviation</b>	<b>Meaning</b>
<b>A</b>	AC	Air Cooling
	AFRC	Advanced Forming Research Centre
	ANOVA	Analysis of Variance
	ATI-SF	Aerospace Technology Institute–Shear Forming
<b>B</b>	BCC	Body-Centred Cubic
	BS	BackScatter
	CMM	Coordinate Measuring Machine
	CNC	Computer Numerical Control
	Comp	Complementary
	<b>D</b>	DB
DoE		Design of Experiments
<b>E</b>	EBSD	Electron BackScatter Diffraction
	EngD	Engineering Doctorate
<b>F</b>	FC	Furnace Cooling
	FCC	Face-Centred Cubic
<b>G</b>	Gauge R&R	Gauge Repeatability & Reproducibility
	GNB	Geometrically Necessary Boundary
<b>H</b>	HT	Heat Treatment

---

<b>Acronym Abbreviation</b>	<b>Meaning</b>
<b>K</b> KPV	Key Processing Variable
<b>M</b> M	Metal atom
<b>N</b> NA	Not applicable
ND	Normal Direction
<b>O</b> ODF	Orientation Distribution Function
<b>P</b> PhD	Doctor of Philosophy
PF	Pole Figure
<b>R</b> R&D	Research & Development
RD	Rolling Direction
<b>S</b> SE	Secondary Electron
SEM	Scanning Electron Microscope
SRX	Static Recrystallisation
<b>T</b> TB	Transition Band
TCP	Topologically close-packed
TD	Transverse direction
TEM	Transmission Electron Microscopy
<b>U</b> UK	United-Kingdom
UTS	Ultimate tensile strength or tensile strength, also denoted TS or R or $R_m$ , in MPa
<b>W</b> WF	WF Maschinenbau und Blechformtechnik

---

# List of symbols

Symbol	Description
$\alpha$	Angle of shear, in $^{\circ}$
$\beta$	Angle of shear of the preform, $^{\circ}$
$\delta$	Angle of approach
$\Delta R$	Variation of outer blank radius, in mm
$\theta_1$	Roller angle
$\lambda c$	Roughness cut-off wavelength
$\lambda f$	Waviness cut-off wavelength
$\lambda s$	Short wavelength filter
$\rho_R$	Roller nose radius, in mm
$\sigma_{\theta}$	Circumferential compressive stress
$\sigma_r$	Radial tensile stress
$\tau_{\theta}$	Circumferential shear stress
$\chi$	Deviation ratio, in %
<b>A</b> $A$	Elongation after fracture, also denoted E, in %
$a_{\gamma}$	Lattice parameter of the $\gamma$ -matrix
$a_{\gamma'}$	Lattice parameter of the $\gamma'$ -phase
$a_{\gamma''}$	Lattice parameter of the $\gamma''$ -phase
$a_{\delta}$	Lattice parameter of the $\delta$ -phase
<b>B</b> $b_{\delta}$	Second lattice parameter of the $\delta$ -phase

	<b>Symbol</b>	<b>Description</b>
<b>C</b>	$C$	Coolant, in L/min
	$c_{\gamma''}$	Second lattice parameter of the $\gamma''$ -phase
	$c_{\delta}$	Third lattice parameter of the $\delta$ -phase
	$C_D$	Compressive deformation, in %
	$Cr_{eq}$	Chromium equivalent, part of Schoefer's relationship
<b>D</b>	$d$	Inside diameter of starting workpiece
	$D_0$	Diameter of starting workpiece
	$D_1$	Diameter of final part
	$D_M$	Outer diameter of the mandrel
	$D_R$	Outer diameter of the roller
<b>F</b>	$F$	Feed rate, in mm/rev
	$F_m$	Feed rate, in m/min
<b>G</b>	$G_{r/m}$	Gap (or clearance) between roller and mandrel, in mm
<b>L</b>	$L$	Lubricant
	$L_m$	Measuring length, in mm
	$l_n$	Evaluation length, in mm
	$l_r$	Sampling length, in mm
<b>M</b>	$M_{d30}$	Temperature at which 50% of martensite is created for a true strain of 30%
	$MPE_E$	Maximum Permissible Error of length, in $\mu\text{m}$
<b>N</b>	$Ni_{eq}$	Nickel equivalent, part of Schoefer's relationship
<b>R</b>	$R^2$	Coefficient of determination, in %
	$R_{adj}^2$	Adjusted coefficient of determination, in %
	$R_a$	Arithmetical mean deviation of the profile, in $\mu\text{m}$
	$R_i$	Inner surface roughness, in $\mu\text{m}$
	$R_o$	Outer surface roughness, in $\mu\text{m}$



---

<b>Symbol</b>	<b>Description</b>
$R_O$	Initial outer blank radius, in mm
$R_{p0.2}$	Yield strength at 0.2%, also denoted YS, in MPa
$r_{tip}$	Stylus tip radius, in $\mu\text{m}$
$Rq$	Root-mean-square deviation of the profile, in $\mu\text{m}$
$RSm$	Mean width of the profile elements, in mm
$Rz$	Ten point height of irregularities, in $\mu\text{m}$
<b>S</b>	
$S$	Actual final thickness, in mm
$S_0$	Starting blank thickness, in mm
$S'_0$	Starting preform thickness, in mm
$S_1$	Final shear formed thickness according to the sine rule (from a blank), in mm
$S'_1$	Final shear formed thickness according to the sine rule (from a preform), in mm
$s_\varepsilon$	Standard error of estimate
$Sp$	Spindle speed, in RPM
$SSE$	Sum of squares for error
$Su$	Surface speed, also called cutting speed, in m/min
<b>T</b>	
$Ts$	Solution temperature, in K or $^\circ\text{C}$
<b>W</b>	
$W$	Flange width
<b>X</b>	
$Xs$	Length of the X-axis segment intersecting with the profile element (surface texture)

---

# Table of contents

<i>Abstract</i>	<i>i</i>
<i>Acknowledgements</i>	<i>ii</i>
<i>Dedication</i>	<i>iii</i>
<i>Author's declaration</i>	<i>iv</i>
<i>Published work</i>	<i>v</i>
<i>List of acronyms and abbreviations</i>	<i>vi</i>
<i>List of symbols</i>	<i>viii</i>
<i>Table of contents</i>	<i>xi</i>
<i>List of figures</i>	<i>xv</i>
<i>List of tables</i>	<i>xviii</i>
<b>1 Introduction</b>	<b>1</b>
1.1 The motivations behind shear forming . . . . .	1
1.1.1 What is shear forming? . . . . .	1
1.1.2 Why use shear forming? . . . . .	2
1.2 The role of nickel-based alloys in aerospace . . . . .	3
1.3 Project aims and objectives . . . . .	5
1.3.1 Aims . . . . .	5
1.3.2 Research questions and objectives . . . . .	6
1.4 Outline of the thesis . . . . .	7
1.5 Research design adopted . . . . .	7

<b>2</b>	<b>Shear forming, an incremental cold forming process</b>	<b>9</b>
2.1	Adopted methodology . . . . .	9
2.2	History and origin . . . . .	11
2.3	Spinning methods . . . . .	12
2.3.1	Classification and terminology . . . . .	12
2.3.2	Machinery development . . . . .	14
2.4	Research on shear forming . . . . .	14
2.4.1	Overview . . . . .	14
2.4.2	Sine rule deviations . . . . .	18
2.4.3	Angle variations . . . . .	20
2.4.4	Tooling considerations . . . . .	20
2.4.5	Surface roughness . . . . .	22
2.4.6	Final geometry . . . . .	24
2.4.7	Forces required . . . . .	26
2.5	Summary . . . . .	27
<b>3</b>	<b>Materials</b>	<b>29</b>
3.1	Adopted methodology . . . . .	29
3.2	Inconel 718, a nickel-based superalloy . . . . .	30
3.2.1	Chemical composition . . . . .	31
3.2.2	Microstructure . . . . .	32
3.2.2.1	$\gamma$ -matrix . . . . .	32
3.2.2.2	$\gamma'$ -phase . . . . .	32
3.2.2.3	$\gamma''$ -phase . . . . .	33
3.2.2.4	$\delta$ -phase . . . . .	34
3.2.2.5	Other phases . . . . .	35
3.2.3	Mechanical properties . . . . .	37
3.3	304L, an austenitic stainless steel . . . . .	38
3.3.1	Chemical composition . . . . .	38
3.3.2	Microstructure . . . . .	40
3.3.2.1	$\gamma$ -matrix and $\delta$ -ferrite . . . . .	40
3.3.2.2	Martensite . . . . .	40
3.3.2.3	Other phases . . . . .	41
3.3.3	Mechanical properties . . . . .	42
3.4	Microstructure evolution . . . . .	42

3.4.1	Recovery . . . . .	44
3.4.2	Recrystallisation . . . . .	44
3.4.2.1	General overview . . . . .	44
3.4.2.2	Static recrystallisation . . . . .	45
3.5	Heat treatments . . . . .	46
3.6	Microstructural considerations when shear forming . . . . .	48
3.7	Summary . . . . .	50
<b>4</b>	<b>Experimental protocol</b>	<b>52</b>
4.1	Shear forming configuration . . . . .	52
4.2	Metallurgical analysis . . . . .	53
4.2.1	Metallurgical sample preparation . . . . .	53
4.2.2	Hardness analysis . . . . .	53
4.2.3	Microstructure observation . . . . .	54
4.2.4	Grain size measurement . . . . .	55
4.2.5	Texture observation . . . . .	56
4.2.5.1	Pole Figures . . . . .	56
4.2.5.2	Orientation distribution functions . . . . .	56
4.3	Surface roughness analysis . . . . .	58
4.4	Geometrical analysis . . . . .	59
4.5	Design of Experiments and statistical analysis . . . . .	61
<b>5</b>	<b>Primary work on 304L stainless steel</b>	<b>63</b>
5.1	Experiments . . . . .	64
5.1.1	Set-up . . . . .	64
5.1.2	Choice of KPVs for the DoE . . . . .	64
5.2	Geometrical and roughness analyses . . . . .	66
5.2.1	Repeatability . . . . .	68
5.2.2	DoE . . . . .	69
5.2.3	Statistical analysis . . . . .	69
5.3	Metallurgical work . . . . .	74
5.3.1	As-received material . . . . .	75
5.3.2	Shear formed material . . . . .	76
5.4	Conclusions . . . . .	83
<b>6</b>	<b>Shear forming of Inconel 718</b>	<b>85</b>

6.1	Experimental work . . . . .	85
6.2	As-received material . . . . .	86
6.2.1	Before heat treatment . . . . .	86
6.2.2	After heat treatment . . . . .	91
6.3	Shear formed material . . . . .	92
6.3.1	Selection of parts . . . . .	93
6.3.2	Before heat treatment . . . . .	93
6.3.3	After heat treatment . . . . .	98
6.4	Conclusions . . . . .	99
<b>7</b>	<b>Shear forming of thicker 304L stainless steel</b>	<b>102</b>
7.1	Preparation prior to forming . . . . .	102
7.2	Experiments . . . . .	106
7.2.1	Set-up . . . . .	106
7.2.2	Choice of KPVs . . . . .	108
7.2.3	Forming loads . . . . .	110
7.3	Geometrical and roughness analyses . . . . .	114
7.4	Metallurgical work . . . . .	120
7.4.1	As-received material . . . . .	121
7.4.2	Shear formed material . . . . .	122
7.5	Summary . . . . .	123
<b>8</b>	<b>Summary, conclusions, and future work</b>	<b>129</b>
8.1	Summary and discussion . . . . .	129
8.2	Contributions to knowledge . . . . .	132
8.3	Limitations and future work . . . . .	133
<b>Appendices</b>		
	Appendix A: Paper A . . . . .	134
	Appendix B: Paper B . . . . .	143
	Appendix C: Equipment . . . . .	150
	Appendix D: Data sheet . . . . .	195
	Appendix E: Geometries completed in the ATI SF . . . . .	198
	Appendix F: New designs . . . . .	205
	<b>References</b>	<b>225</b>

## List of figures

1.1	Sketch explaining the shear forming process. . . . .	2
1.2	The Trent XWB, a Rolls-Royce engine. . . . .	4
1.3	The WF 3-Roller-Flow Forming and Spinning Machine, AFRC, 2013. . . . .	5
2.1	Flowchart employed in the search and selection of publications. . . . .	10
2.2	Worldwide repartition of the selected publications on shear forming. . . . .	11
2.3	Shear forming from (a) a blank and (b) a preform. . . . .	15
2.4	Tool path inclination. . . . .	16
2.5	Examples of shear formed geometries. . . . .	16
2.6	Spinnability test. . . . .	17
2.7	Stress involved during shear forming. . . . .	19
2.8	Sine rule deviations. . . . .	19
2.9	Roller shapes and their application for shear forming. . . . .	21
2.10	Die-less shear forming concept. . . . .	21
2.11	Effects of (a) blank thickness and (b) roller nose radius at multiple feed rates on the inner and outer surface roughnesses. . . . .	23
2.12	Shear forming of conical parts with transverse inner rib. . . . .	26
2.13	Effects of the spindle speed and feed rate on the tangential force for a 4.11 mm 1100-O Aluminium blank formed with a roller nose radius of 4.8 mm. . . . .	27
3.1	FCC crystal structure of the $\gamma$ -matrix. . . . .	32
3.2	$\gamma'$ -phase: (a) crystal structure and (b) Inconel 792 micrograph. . . . .	33
3.3	$\gamma''$ -phase: (a) unit cell of $\text{Ni}_3\text{Nb}$ and (b) Inconel 718 micrograph. . . . .	34
3.4	Inconel 718 micrograph showing $\delta$ -phase at $\gamma$ -grain boundaries and intragranularly. . . . .	35
3.5	Ta-rich MC carbide observed in single crystal Ni-based superalloy exhibiting (a) blocky, (b) script, and (c) nodular morphologies. . . . .	36

3.6	Micrograph of extracted TCPs observed in single crystal RR2072 superalloy. . . . .	37
3.7	Schematic of the restoration processes. . . . .	43
3.8	Typical heat treatment for superalloys. . . . .	47
3.9	Microstructure of a 30° shear formed part under a null deviation ratio. . . . .	50
4.1	Positions of micro-assessment evaluation of (a) a part with external flange and (b) a part without external flange. . . . .	53
4.2	Location of the hardness measurements – Part without an outer flange. . . . .	54
4.3	Set-up of the Surftest SJ-210 and its fixture to measure the surface roughness of a shear formed part. . . . .	59
4.4	Scanning with a rotating table and a frame using ATOS III Triple Scan. . . . .	60
4.5	Set-up of a shear formed part on the fixture for CMM measurement. . . . .	61
5.1	Drawing: Shear formed part – 31.5°, 5.90 mm thick, EngD. . . . .	65
5.2	Surface plot of the predictive numerical model for the first diameter (a) with coolant and (b) with lubricant. . . . .	72
5.3	Surface plot of the predictive numerical model for the cone angle (a) with coolant and (b) with lubricant. . . . .	73
5.4	3D visualisation of the variation of the thickness along the part. . . . .	73
5.5	Plot of the predictive numerical model for the final thickness. . . . .	73
5.6	Plot of the predictive numerical model for the outer surface roughness. . . . .	74
5.7	BS micrographs of the as-received material – area M1 of part P <sub>2</sub> 7. . . . .	75
5.8	Texture of the as-received material along the slip planes for the two phases – area M1 of part P <sub>2</sub> 7 (top: PFs, bottom: ODFs). . . . .	76
5.9	BS micrographs of the shear formed material – areas M3 (left) and M5 (right) for parts (a) P <sub>2</sub> 1, (b) P <sub>2</sub> 3, (c) P <sub>2</sub> 7, and (d) P <sub>2</sub> 9. . . . .	77
5.10	BS micrographs of the shear formed material – areas M3 (left) and M5 (right) for parts (a) P <sub>2</sub> 19, (b) P <sub>2</sub> 21, (c) P <sub>2</sub> 25, and (d) P <sub>2</sub> 27. . . . .	78
5.11	Simple shear: (a) illustration of the principle and (b) plot of the shear as a function of the cone angle. . . . .	79
5.12	Texture representations for part P <sub>2</sub> 7 in the middle of the thickness of area M4 (top: PFs, bottom: ODFs). . . . .	81
5.13	Main torsion texture components: (a) Miller indices and (b) representation on ODFs. . . . .	81

5.14	Texture representations for part P <sub>27</sub> at the surfaces of area M4: (a) mandrel surface and (b) roller surface (top: PFs, bottom: ODFs). . . .	82
6.1	Optical micrographs of the 6 mm thick as-received material along the rolling direction. . . . .	88
6.2	Optical micrographs of the 12 mm thick as-received material along the rolling direction. . . . .	89
6.3	Texture of the 6 mm thick as-received material before heat treatment. .	90
6.4	Texture of the 12 mm thick as-received material before heat treatment.	90
6.5	Optical micrographs of the 6 mm thick as-received material after heat treatment along the rolling direction. . . . .	91
6.6	Texture of the 6 mm thick as-received material after heat treatment. . .	92
6.7	Texture of the 12 mm thick as-received material after heat treatment. .	92
6.8	Optical micrographs of part P <sub>Inco3</sub> before heat treatment in areas M2–M5.	95
6.9	Texture of part P <sub>Inco3</sub> before heat treatment in areas M2–M5. . . . .	97
6.10	Backscattered micrograph of part P <sub>Inco3</sub> after heat treatment. . . . .	98
6.11	Texture of part P <sub>Inco3</sub> after heat treatment in areas M2–M5. . . . .	100
7.1	Drawing: Blank – 43°, 15 mm thick, EngD. . . . .	103
7.2	Drawing: Shear formed part – 43°, 15 mm thick, EngD. . . . .	104
7.3	Assembly drawing – 43° geometry. . . . .	105
7.4	Drawing: 6 mm nose radius roller – ATI–SF. . . . .	111
7.5	Drawing: 6 mm nose radius roller – ATI–SF. . . . .	112
7.6	Plot of the roller loads compared with the roller position. . . . .	113
7.7	Surface plot of three predictive models. . . . .	119
7.8	BS micrographs of the 15 mm thick as-received material. . . . .	121
7.9	Texture of the 15 mm thick as-received material (top: PFs, bottom: ODFs). . . . .	122
7.10	BS micrographs of the shear formed material in area M3 for parts P3–P6.	123
7.11	Texture of parts P3 and P4 in the middle of area M3. . . . .	124
7.12	Texture of parts P5 and P6 in the middle of area M3. . . . .	125
7.13	Texture of parts P3 on the mandrel and roller sides of area M3. . . . .	126



## List of tables

2.1	Classification of the spinning methods. . . . .	12
2.2	Spinning terminology. . . . .	13
2.3	Tolerances achievable with shear forming when applied to copper. . .	25
3.1	Typical chemical composition of Inconel 718. . . . .	31
3.2	Mechanical properties of hot-rolled sheets or final products made of Inconel 718. . . . .	37
3.3	Typical chemical composition of 304L stainless steel. . . . .	39
3.4	Mechanical properties of plates, sheets, or strips in the annealed condition made of 304L stainless steel and forgings. . . . .	43
3.5	Multiple heat treatments for Inconel 718. . . . .	48
4.1	Settings employed to generate the PFs. . . . .	57
4.2	Settings employed to generate the ODFs. . . . .	57
5.1	DoE employed for the forming of 304L stainless steel blanks on the 31.5° geometry using one roller. . . . .	67
5.2	Geometrical and roughness measurements: Repeatability, 31.5° geometry, 2 rollers, 304L stainless steel. . . . .	68
5.3	Minimum, maximum, average, and standard deviation of the geometrical and roughness measurements of the parts included in the factorial DoE. . . . .	69
5.4	Geometrical and surface roughness outputs of the DoE given in Table 5.1.	70
5.5	Assessment of the predictive models and statistical significance of the factors and/or their interaction. . . . .	71
5.6	Chemical composition of the 304L stainless steel as-received sheet. . .	74
5.7	Mechanical properties of the 304L stainless steel as-received sheet. . .	75
6.1	Inconel 718: Chemical composition of the different sheets. . . . .	86

---

6.2	Inconel 718: Mechanical properties of the different sheets. . . . .	87
6.3	DoE employed for the microstructural analysis of the Inconel 718 shear formed parts. . . . .	94
6.4	Assessment of the predictive models and statistical significance of the factors and their interactions for the grain size and torsion component B. . . . .	96
7.1	Set-up of parts S1–S3. . . . .	108
7.2	Set-up of parts S3–S6. . . . .	108
7.3	KPVs employed for parts P1–P15b. . . . .	109
7.4	Geometrical and roughness measurements – Parts P1–P14 excluding P10a. . . . .	115
7.5	Assessment of the predictive models for the final part geometry and statistical significance of the factors and/or their interactions. . . . .	117
7.6	Chemical composition of the 15 mm thick 304L stainless steel as-received sheet. . . . .	120
7.7	Mechanical properties of the 15 mm thick 304L stainless steel as-received sheet. . . . .	121

# Chapter 1

## Introduction

This Engineering Doctorate (EngD) project was a three-party contract between the student, the University of Strathclyde, and Rolls-Royce. This research project took place at the Advanced Forming Research Centre (AFRC), which is part of the Design, Manufacture & Engineering Management — department of the University of Strathclyde.

Chapter 1 presents the context of this project. First, the interest of the shear forming process and the importance of nickel-based alloys for aerospace are given. Secondly, the aims and objectives are stated. Then, the outlines of the thesis are established. Lastly, the research planning is presented.

### 1.1 The motivations behind shear forming

#### 1.1.1 What is shear forming?

Shear forming is an incremental cold rotary forming process typically used to manufacture conical parts. It involves four main elements as shown in Figure 1.1:

- The blank is the material that will be shear formed. Its initial thickness is denoted  $S_0$ .
- The mandrel is instrumental in defining the final geometry of the part. This conical component is characterised by the angle of shear, denoted  $\alpha$ . The mandrel rotates during the shear forming operation at a given spindle speed.

- The tailstock clamps the blank into position. As a result, during the forming operation, the blank rotates with the mandrel.
- One or more rollers are used to push the blank onto the mandrel during the shear forming operation. The tool path is given and it controls the axial and transverse movements of the rollers. The feed rate is their displacement speed. The rollers are not driven but their rotation is induced by the spin of the blank.

The action of the roller(s) onto the blank results in a reduction of the starting thickness. The new thickness is denoted  $S_1$ . This phenomenon is controlled by the sine rule, which is derived from the law of equal volume. The sine rule geometrically expresses the deformation as given in Equation 1.1.

$$S_1 = S_0 \cdot \sin(\alpha) \quad (1.1)$$

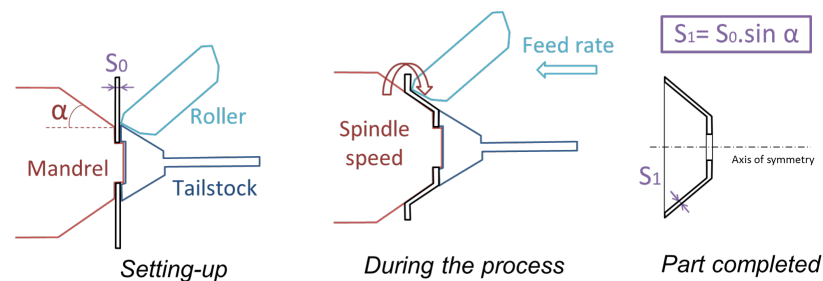


Figure 1.1: Sketch explaining the shear forming process.

### 1.1.2 Why use shear forming?

Historically, cold forming was an experience based technology. During the past 50 years, scientifically structured approaches to its development have been promoted through focused R&D activity. The shear forming process has been principally studied for applications using aluminium alloys or steels. Shear forming currently has a limited use within the aerospace sector due to the lack of design rules, the limited supply chain, and the difficulty to source the appropriate raw material state. It is mainly employed on exhaust cones such as the 18-8 stainless steel exhaust cone manufactured for the RB211 by Rolls-Royce. Such a process could however offer potential applications ranging from conical structures used in gas turbine engines, such as seals to casings and support structures. In addition, shear forming could present numerous benefits for Rolls-Royce, the main ones being:

- Compared with the current forged and machined manufacturing routes, shear forming could:
  - Improve the buy-to-fly ratio at a product level
  - Reduce the machining, essentially eliminating some secondary machining operations, such as the machining of heavy wall forgings
  - Reduce the manufacturing timesAccordingly, the material, production, and energy costs could be reduced. When optimised, the shear forming process is estimated to halve the overall cost of a component (Sweeney and Atkinson, 2012).
- Better product characteristics:
  - Smoother surface finish
  - Improved geometric control
  - Enhanced strength
- Compared with over forming processes that are applied to entire components, shear forming allows:
  - Reduction and simplification of the forming loads and friction
  - Lower cost tooling
  - Easy integration of additional manufacturing operations
  - Forming of hard formable material
  - Opportunities in terms of design flexibility leading to performance improvements

## **1.2 The role of nickel-based alloys in aerospace**

As shown in Figure 1.2, a Rolls-Royce Trent engine is composed of four main sections. Different materials are used in its manufacture depending on the function of the part and environmental requirements for each section. Titanium alloys are generally employed for the fan blades, fan discs, and initial stages of the low pressure compressor due to their adequate fracture toughness, high strength, good fatigue performance, light weight, and good impact resistance. Nevertheless, when reaching temperatures greater than 570°C in the compressor, nickel alloys are utilised due to their high strength and corrosion resistance at high temperatures. The most common nickel-based alloys used in engines are Inconel 718, Udimet 720, and RR1000.

The combustor experiences temperatures of up to 2100°C. Consequently, the

inside of the combustion chamber is often lined with ceramics. Alloys such as Nimonic C263 (nickel-chromium-cobalt alloy) and Haynes 230 (nickel-chromium alloy) are utilised respectively in welded structures and in combustor casings. The temperature in the gas stream of the turbine goes up to 1700°C. The requirements in terms of material are a good creep resistance, a thermal shock resistance, and an operating temperature range of up to 1100°C. The temperature reached by the material is reduced by the combination of thermal barrier coatings (generally advanced ceramic material) and interpass cooling to allow the use of highly creep resistant nickel superalloys, such as CMSX-4 and TMS138A for high and intermediate pressure turbine blades respectively.

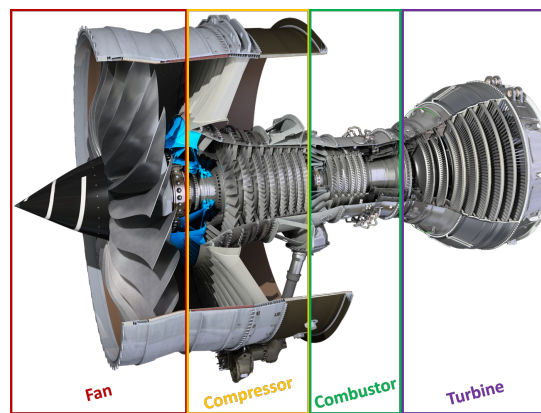


Figure 1.2: The Trent XWB, a Rolls-Royce engine ©Rolls-Royce plc.

Throughout the engine, nickel-based superalloys, due to their mechanical properties and temperature capability, are heavily utilised in the compressor, combustor, and turbine. Thence, these materials have a major role in the aerospace sector. If a sheet forming process such as shear forming could be applied further to these superalloys, it could become an asset for this sector. Indeed the use of shear forming is currently limited to obvious simple parts of the engines and exploiting it more broadly could reduce costs at a product level and offer opportunities for design flexibility leading to performance improvements.

## 1.3 Project aims and objectives

### 1.3.1 Aims

This EngD project sought to address a known gap in knowledge, theory, and capability associated with shear forming of aerospace grade alloy materials; the specific alloy of research being Inconel 718. Considering its widespread availability and formability as well as lower cost compared with nickel-based superalloys, 304L stainless steel was used as a cost effective trial material in the early development of parameters for this research. The research aim was to characterise metallurgically and geometrically the shear forming process.

The AFRC as well as its clients and partners are interested in forging and forming processes. A study of the shear forming process was a way to contribute to the global development of knowledge in cold forming processes and this fed into the AFRC's research topic 'Process characterisation and material characterisation'. Furthermore, the full scale 3-Roller-Flow Forming and Spinning Machine from WF Maschinenbau und Blechformtechnik GmbH (WF) has the capability of shear forming along with cylindrical flow forming and spinning (processes described in Chapter 2). This machine (Figure 1.3), thereafter called the flow former, is available at the AFRC and had only been used for cylindrical flow forming prior to the launch of this EngD project. Hence, studying shear forming also expanded the AFRC's capabilities, which could bring in more clients and/or projects, and potentially answer the industry need for cheaper manufacturing routes.

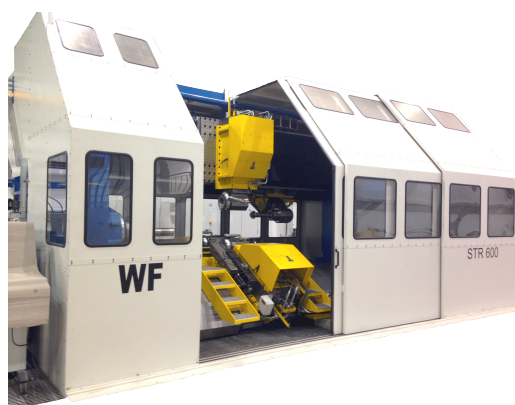


*Figure 1.3: The WF 3-Roller-Flow forming and Spinning Machine (type STR 600 3/6), AFRC, 2013.*

For Rolls-Royce, the project was intended to support its wider strategy on development and exploitation of near-net-shape material forming technologies. Rolls-Royce had determined, through business case development, the cost, quality, and delivery benefits associated with the shear forming process. The research project was expected to underpin many elements of that strategy and business case development, enabling the company to maximise the exploitation of the process across its intended part range and be a more intelligent customer.

### **1.3.2 Research questions and objectives**

This EngD project should enable a baseline understanding of the shear forming process through scientific research, theoretical development, and validation. To express what this project intended to address, four research questions were raised:

- Q1 – What and how are the key process variables influencing the final geometry and surface roughness of a shear formed part?
- Q2 – How to optimise the final geometry and surface roughness of a shear formed component?
- Q3 – How does the microstructure and texture of 304L stainless steel and Inconel 718 behave when shear formed?
- Q4 – What is the material deformation mechanism involved in the shear forming process?

From these research questions, the objectives were derived:

- O1 – Describe the state of the art for the shear forming of 304L stainless steel and Inconel 718
- O2 – Identify and study the effect of the key processing variables on the geometry and surface roughness of the component when applied to 304L stainless steel and Inconel 718 through experimental work using a systematic approach
- O3 – Study the microstructure and texture of 304L stainless steel and Inconel 718 post shear forming in order to identify the material deformation mechanism

The completion of these objectives aimed to the acquisition of manufacturing process level data, understanding, and knowledge under shear forming conditions. Consequently, a design and manufacturing envelope for shear forming applied to conical aerospace structures could be better defined.



## 1.4 Outline of the thesis

Chapters 2 and 3 give the state of the art for the shear forming process and for both 304L stainless steel and Inconel 718. Chapter 4 presents the experimental protocol. The equipment used is introduced as well as the methods employed. Where relevant, specifications, standards, and calibration procedures are given.

The main focus of the next three chapters is on the geometry, roughness, microstructure, texture, and mechanical properties of the material when shear forming at different cone angles using materials with a starting thickness of up to 15 mm. The content of each chapter is outlined below.

Chapter 5 consider the case of shear forming of 304L stainless steel. This was used as a cheaper model material, rather than Inconel 718, for early trial work. This was formed onto a 31.5° mandrel with a starting thickness of 6 mm. A Design of Experiments (DoE) approach was used and was analysed by statistical analysis.

Chapter 6 is built on the outcomes of the work already carried out in Chapter 5. It examines the shear forming of Inconel 718 over three different geometries and for starting thicknesses of up to 12.7 mm. Once more, statistical analysis was adopted and more advanced metallurgical work is presented.

Chapter 7 focuses on the shear forming of 304L stainless steel with a starting thickness of 15 mm onto a 43° mandrel. It presents the primary work undertaken in order to get a general understanding of the impact of such a thick blank.

Finally, Chapter 8 gives an overall review. A discussion of the work as a whole and recommendations for future work are provided.

## 1.5 Research design adopted

The research questions were raised in Subsection 1.3.2. Literature reviews of the shear forming process and of both 304L stainless steel and Inconel 718 were completed. A triangulation technique was employed as it helped ensure “that the data is telling you what you think they are telling you” (Saunders et al., 2012). Therefore, secondary data were collected through different publications. A mixed method was used as these data were qualitative and quantitative to a certain extent.

An experimental strategy was carried out to examine the effect of changing a control variable on a dependent (output) variable. DoE techniques were undertaken to generate the primary data. Measurement and observation methods were employed to collect these data. On one hand, quantitative data was examined through statistical analysis to describe the outcomes, explore the relationships and present the trends. On the other hand, data sampling was used for the qualitative data generated by the metallurgical analysis. This inductive approach was then combined with a deductive approach. The acquired knowledge was utilised to predict the impacts of shear forming in a slightly different context (different material and geometry). This enabled the theory to be tested.

To enhance the credibility of the work, another triangulation of the data was undertaken by comparing primary data to secondary data. Furthermore, the findings were disseminated through formal presentations and/or publications as given in 'Previously published work' (p. v).

## **Chapter 2**

# **Shear forming, an incremental cold forming process**

Chapter 2 introduces the shear forming process. An overview of the relevant literature covering its fundamentals and principles as well as its major advantages and capabilities is given. First, the methodology adopted to complete this review is detailed. Secondly, the origin and history of this process are provided. Then, the classification and terminology associated with spinning processes are presented along with the machinery development. The different aspects of research undertaken so far on the shear forming process are discussed. Finally, conclusions are drawn on the overall state-of-art of this process and its relevance for the EngD project.

### **2.1 Adopted methodology**

The aim of this review was to get a broad understanding of the shear forming process using both academic and industrial perspectives. Several scientific databases were interrogated and a couple of hundred documents were identified. Figure 2.1 shows the process employed for this systematic review. To be considered in this literature review, the entry had to meet one of the four following inclusion criteria:

- Report on the principles of shear forming or compares it with other metal spinning methods.
- Explain the advantages and capabilities of the shear forming process.

- Study the effects of process parameters and/or tooling for the shear forming process.
- Provide information on a new technique applied to shear forming.

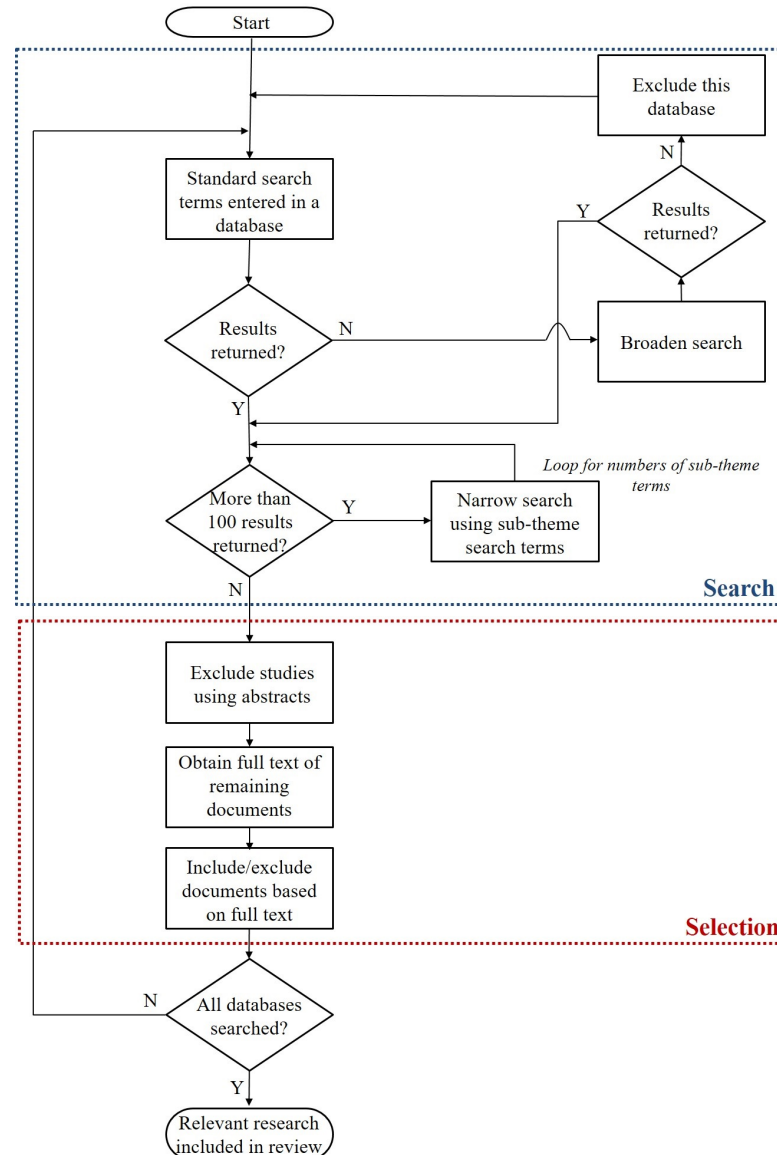


Figure 2.1: Flowchart employed in the search and selection of publications – adapted from Higgins and Green (2011).

As a starting point, documents were excluded if they were written in a language other than English or French, document did not refer to shear forming or spinning methods. Some documents were discounted for redundancy. As shown by the

worldwide classification of the selected publications in Figure 2.2, shear forming had principally been studied in the UK, China and Japan.

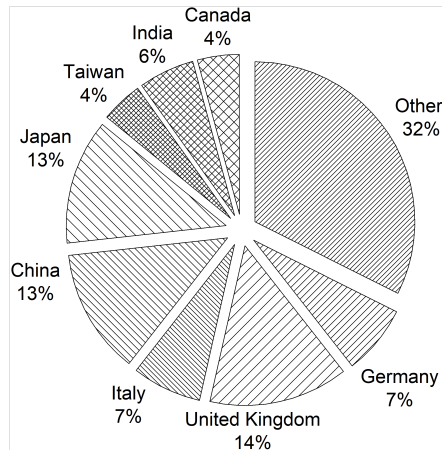


Figure 2.2: Worldwide repartition of the selected publications on shear forming.

## 2.2 History and origin

Kalpakjian (1984) categories shear forming as a sheet metal forming process along with conventional spinning, bending, stretching, and deep drawing. Shear forming is also classified as a spinning method and thus is a chipless turning process, which produces rotationally symmetrical hollow shapes and involves the rotation of the workpiece and tools. Metal spinning methods were born with the art of potting clay in ancient Egypt before spreading to China in the 10<sup>th</sup> century and across the United States of America nine centuries later. At the beginning of the 20<sup>th</sup> century, due to the tacit knowledge required when using these methods, they were still described as ‘art’ instead of ‘science’ and were essentially employed for non-critical components, such as domestic products. The growth of near-net-shape manufacturing mostly through the development of European and American aerospace industries led to the expansion of spinning especially during the past 60 years (Music et al., 2010, Wong et al., 2003).

## 2.3 Spinning methods

### 2.3.1 Classification and terminology

As defined in Table 2.1, according to the German standard DIN 8582, spinning methods are divided into the two following categories:

- Flow forming: A group of two processes (cylindrical flow forming and shear forming), both involving only compression forces and reducing the initial material thickness.
- Conventional spinning: A process obtained by a combination of tension and compression in the material, during which the thickness remains.

Cylindrical flow forming is commonly called flow forming but in this review ‘flow forming’ refers only to the generic term for cylindrical flow forming and shear forming to avoid any ambiguities. Before describing these processes, the spinning terminology which includes numerous alternative terms is given in Table 2.2.

Table 2.1: Classification of the spinning methods – adapted from Runge (1993).

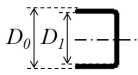
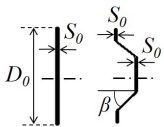
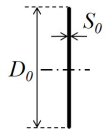
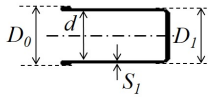
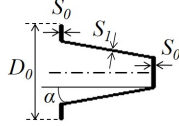
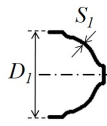
Spinning methods		
Flow forming processes		Conventional spinning
Cylindrical flow forming	Shear forming	
 <p>Cup</p>	 <p>Disc blank or preform</p>	 <p>Disc blank <math>D_0 &gt; D_1</math></p>
 <p>Wall thickness <math>S_1 = \frac{1}{2} (D_1 - d)</math></p>	 <p>Wall thickness <math>S_1 = S_0 \cdot \frac{\sin \alpha}{\sin \beta}</math></p>	 <p>Wall thickness <math>S_0 \approx S_1</math></p>
<p><math>D_0</math> Diameter of starting workpiece <math>D_1</math> Diameter of final part <math>d</math> Inside diameter</p>	<p><math>S_0</math> Starting wall thickness <math>S_1</math> Final wall thickness</p>	<p><math>\alpha</math> Cone angle <math>\beta</math> Inclined angle of the preform</p>

Table 2.2: Spinning terminology – updated and partially reproduced from Music et al. (2010) with permission from Elsevier.

Terminology	Alternatives	Description
Conventional spinning	Multi-pass/deep-drawing/simple spinning, spinning	“Spinning process where a sheet blank is formed into a desired axisymmetric shape without a change in the wall thickness and with a deliberate reduction in diameter either over the whole length or in specific areas.”
Cylindrical flow forming	Hydrodynamic/tube spinning, flow turning, flow forming	Spinning process classified under the generic term flow forming. Process where a tube or cup is “formed by rollers into an axisymmetric part with a desired shape and thickness distribution” in one or more passes. “The thickness is deliberately reduced to obtain a desired distribution.”
Shear forming	Shear/power spinning, spin forging, conical/concave/convex flow forming, flow forming, shear turning	Spinning process classified under the generic term flow forming. Process where a disc blank or preform is “formed by roller(s) into an axisymmetric part with a desired shape and thickness distribution” in one or more passes. “The thickness is deliberately reduced to obtain a desired distribution.”
Cone angle	Half included/wall/semi-cone angle, angle of shear	“Angle between the rotational axis and the wall of the part being formed.”
Feed rate	Roller/linear feed rate	Displacement feed of the roller(s), generally given in mm/min.
Feed ratio	Feed per rotation, revolutional feed rate	“Ratio of roller feed rate to mandrel rotational speed in mm/ revolution.”
Mandrel	Chuck	“Rigid axisymmetric tool with the profile of the final component” (for shear forming). “Supports the sheet during deformation.”
Mandrel speed	Rotational/spindle speed	“Rotational speed of the mandrel in RPM.”
Over-spinning	Over-reduction	Shear forming “to a thickness less than predicted by the sine rule.”
Roller	/	Rigid roller that pushes the sheet/blank/tube/cup onto the mandrel.
Roller nose radius	Corner/edge radius	“Blending radius between the two flat surfaces on the outer surface of the roller.”
Spinnability	Deformation limit	“Maximum percent reduction in thickness a material can undergo before fracture.”
Spinning ratio	Forming ratio	“Ratio of the initial to final blank diameter in conventional spinning.”
Tailstock	/	Circular piece that clamps the sheet/blank/tube/cup into position, against the mandrel. “May be flat or curved to fit over the mandrel and further support the part during deformation.”
Tangential, axial and radial forces	/	“Three mutually perpendicular components of the roller force.”
Under-spinning	Under-reduction	Shear forming “to a thickness greater than predicted by the sine rule.”

### 2.3.2 Machinery development

In the Middle Ages, the manual flywheel of wooden spinning lathes was supplying the required force to form the metal piece. In the 1930s, these lathes evolved to electrical spinning machines utilising at first a forming bar to help the movement before the installation of roller-forming levers. As parts got bigger and manual spinning became impossible, tool slides were created. The first hydraulic lathes emerged in 1945 allowing complex parts to be formed with thicker or higher strength materials. To prevent the risks of tooling damage and enhance the machine repeatability, templates and copying tracers were introduced leading to the birth of automatic spinning methods.

At the beginning of the 1970s, Computer Numerical Control (CNC) spinning machines were introduced and performance data computers, also called playback controls, emerged a decade later (Wong et al., 2003). The latter development eased the communication between human and machine as programming skills were no longer required and the forming path had to be described only once.

Today's spinning and flow forming machines are predominantly controlled numerically and programming is typically performed offline to save time on the machine. Two or three-rollers flow formers are commonplace and provide a roller path resolution in the micrometre range (Runge, 1993). Flow formers are typically horizontal but a vertical configuration exists too. The machinery development in terms of sizes allows the forming of blanks with an outside diameter of up to 6,860 mm and 1,200 mm for conventional spinning and flow forming respectively (MJC Engineering & Technology, c. 2017a,c). As shear forming can be carried out on spinning machines, shear formed parts with an outside diameter of up to 6,860 mm are potentially achievable.

## 2.4 Research on shear forming

### 2.4.1 Overview

As described in Chapter 1 (p. 1), shear forming's three operational steps are:

- A flat circular blank or preform is clamped against a mandrel by a tailstock.



- The mandrel is rotated.
- One or more rollers then force the blank to incrementally take the shape of the mandrel by following a programmed path using a controlled feed rate.

Only a single pass is generally required to produce the final shape but multiple passes are sometimes undertaken to enhance dimensional control.

As previously emphasised, shear forming differs from conventional spinning as thickness reduction is promoted. Both processes are sometimes combined when thickness reduction is only required on a specific area of the final component. Shear forming follows the sine rule, which links the final thickness ( $S_1$  for a blank,  $S'_1$  for a preform) to the starting thickness ( $S_0$  for a blank,  $S'_0$  for a preform), the cone angle ( $\alpha$ ), and the preform inclined angle ( $\beta$ ) as illustrated in Figure 2.3. Equation 2.1 gives this relationship for a blank and a preform and shows that the cone angle determines the amount of material reduction. A smaller cone angle produces a smaller thickness in the shear formed areas whereas the thickness remains the same in the unformed areas.

$$\text{Blank: } S_1 = S_0 \cdot \sin \alpha \quad \text{Preform: } S'_1 = S'_0 \cdot \frac{\sin \alpha}{\sin \beta} \quad (2.1)$$

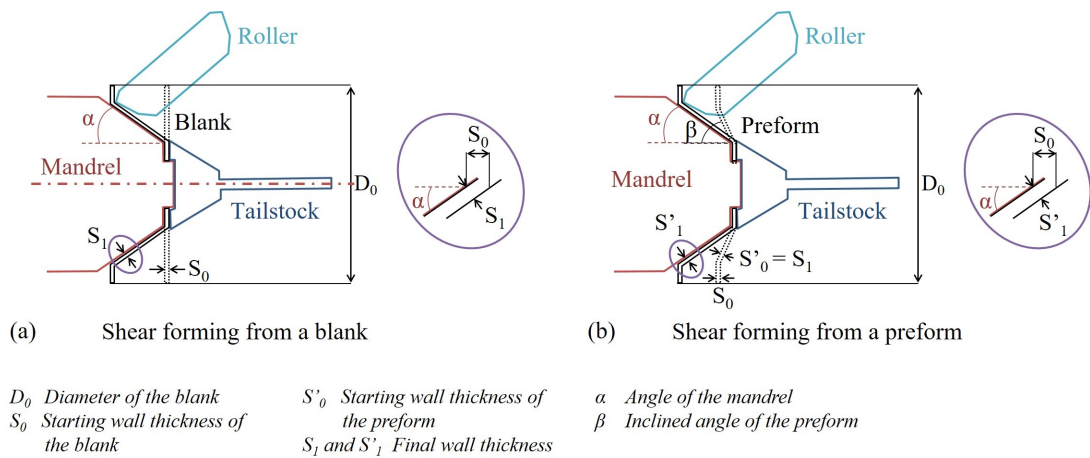


Figure 2.3: Shear forming from (a) a blank and (b) a preform.

The gap between roller and mandrel ( $G_{r/m}$ ), also called clearance, is controlled to achieve the required thickness from which the compressive deformation ( $C_D$ ) and deviation ratio ( $\chi$ ) are defined as shown in Equations 2.2 and 2.3. During forming, the material springs back generally towards its largest diameter. To compensate for this phenomenon, the tool path is sometimes inclined as shown in Figure 2.4.

$$C_D (\%) = \frac{(S_0 - G_{r/m}) \cdot 100}{S_0} \quad (2.2)$$

$$\chi (\%) = \frac{(G_{r/m} - S_1) \cdot 100}{S_1} \quad (2.3)$$



Figure 2.4: Tool path inclination – adapted from Kunert et al. (2005).

During shear forming, the material is displaced in the axial direction. The final part is conical, concave, convex or a combination of these. Figure 2.5 gives some examples of shear formed geometries. For the last two shapes presenting no flat central areas, the use of a tailstock is made impossible. To address this issue, in 1966, Bosch developed a new clamping system supporting the blank around the edges and moving with the roller(s) (Music et al., 2010).

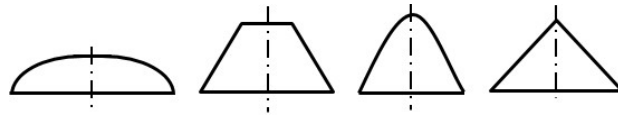


Figure 2.5: Examples of shear formed geometries – adapted from Music et al. (2010).

To establish the maximum thickness reduction a material can achieve before failing, a spinnability test is performed. This consists of the shear forming of a blank over an ellipsoidal mandrel as sketched in Figure 2.6. The initial blank thickness is reduced according to the sine rule until the metal fails at a specific thickness. The maximum thickness reduction for a cone made of Waspaloy or René 41, nickel alloys, is estimated at 40 % whereas 75 % is achievable with 321 or 347, 300 series stainless steels (Bewlay and Furrer, 2006). Furthermore, Kalpakcioglu (1961) explains that variations from the sine rule will impact significantly the spinnability of a material and should therefore be considered.

Common materials currently industrially shear formed are 300/400 series and precipitation hardening stainless steels, iron-nickel, nickel-base and cobalt-base

superalloys, and other non-ferrous alloys like aluminium, brass, copper, and platinum. A much wider range of materials has also been successfully shear formed in laboratory trials (Runge, 1993). Process parameters, such as feed and speed, have less effect on the spinnability compared with an increased temperature. Annealing or heating up the material can enhance formability and spinnability as the flow stress<sup>1</sup> is decreased, which improves the component ductility. This is particularly useful when the alloy ductility is too low, the material readily work hardens.

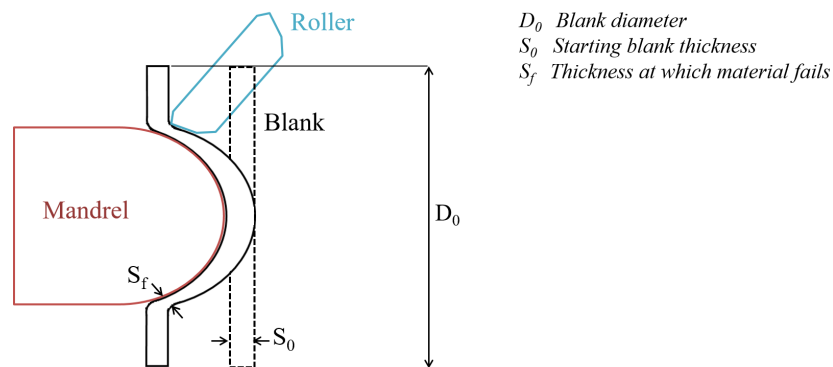


Figure 2.6: Spinnability test – adapted from Hagan and Jeswiet (2003).

The coolant commonly employed is a generic metal working coolant employed for machining. This is utilised to dissipate the heat and lower the component final surface roughness. Shear forming is performed either at constant spindle speed ( $Sp$ , in RPM) or constant surface speed ( $Su$ , in m/min), also called cutting speed. According to Equation 2.4, if the surface speed remains constant then the spindle speed decreases during the process as the shear formed diameter increases. For most flow formers, the feed rate ( $F$ , in mm/rev), also called working speed, is automatically adjusted with the diameter being formed and the constant surface speed implemented. The equivalent feed rate ( $F_m$ , in m/min) is obtained using Equation 2.5.

$$Sp = \frac{Su}{\pi \cdot Diameter} \quad (2.4)$$

$$F_m = \frac{F}{1000} \cdot Sp \quad (2.5)$$

<sup>1</sup>Flow stress: Stress that must be applied to cause a material to deform at a constant strain rate in its plastic range.

Best quality components are commonly shear formed at high speeds with a surface speed in the range of 300–600 m/min and a minimum of about 120 m/min is employed for small-diameter components. Feed rates are typically constant during the process and of 0.25–2 mm/rev (Bewlay and Furrer, 2006).

For a more in depth analysis, process modelling is implemented to further the outcomes of experimental and analytical studies. The first attempt to model such processes was undertaken by Alberti et al. (1989) who assumed axisymmetric deformation for their spinning model. In 2002 Quigley and Monaghan (2002) developed the first 3D model of the spinning process but were unable to predict the true 3D stress state as a fine mesh was required. Klocke and Wehrmeister (2004) established an implicit model for the laser-assisted hot spinning of stainless steel with both thermal and mechanical models analysed separately in which the heat generated due to plastic deformation was omitted. Later, Mohebbi and Akbarzadeh (2010) established a numerical model for the cylindrical flow forming of AA 6063 alloy with a single roller; however as for the works of Quigley and Monaghan (2002) the validation of forming loads with experimental data was not made. As can be seen several publications on the modelling of rotary forming processes are available in the literature but the incremental nature of the process requires fine element meshes and a large number of time steps leading to large computational resources. This explains why most models developed so far use simplified assumptions such as isothermal models and flow stress representations established by quasi-static testing (Roy and Maijer, 2015).

#### 2.4.2 Sine rule deviations

Although the thickness reduction during the shear forming operation is supposedly following the sine rule (Equation 2.1, p. 15), deviations are sometimes observed leading to failure or defects in the part. These deficiencies are due to induced radial stress throughout the component when not truly shear formed, which Figure 2.7 outlines.

Figure 2.8 shows that the flange (remainder of the initial blank) is a stress-free zone and thus stays perpendicular to the rotational axis when true shear forming occurs whereas in the case of under-spinning or over-spinning, the stress is extended into the flange, which is pushed inwards or outwards respectively. When severe under-

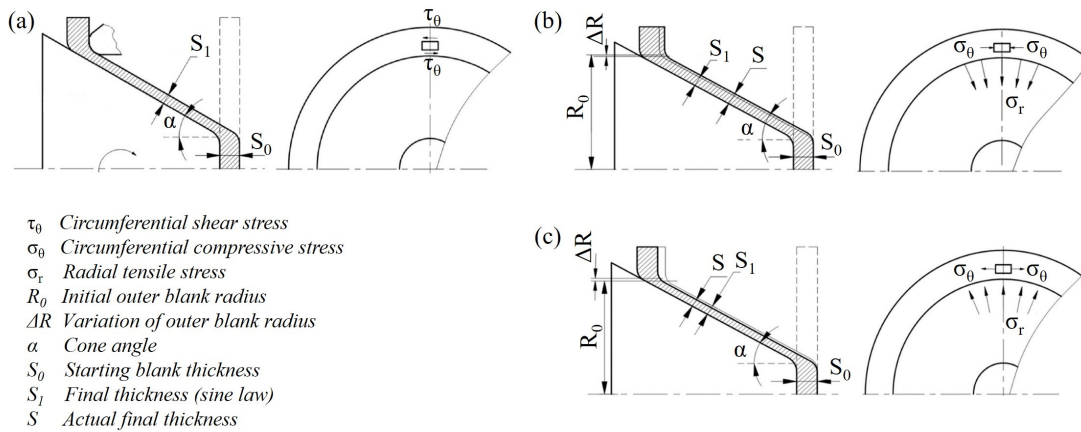


Figure 2.7: Stress involved during (a) true shear forming, (b) under-spinning, and (c) over-spinning (Zhan et al., 2016) – reproduced with permission from Elsevier.

spinning is observed, defects like wrinkles might appear and a slight reduction of the outer diameter is observed. Hayama et al. (1966) studied the wrinkling of the flange by the means of strain gauges and concluded that the feed rate, roller diameter and blank thickness also play a major role. Over-spinning, which is promoted when forming thick materials or when the gap between roller and mandrel is too small, originates from material build-up in front of the roller. In this case, the thickness under the roller is greater than the initial one and the blank outer diameter might be increased when forming. Using two rollers instead of one and introducing an offset between them or shear forming in more than one step as described in Subsection 2.4.3 help prevent this phenomenon (Wong et al., 2003).

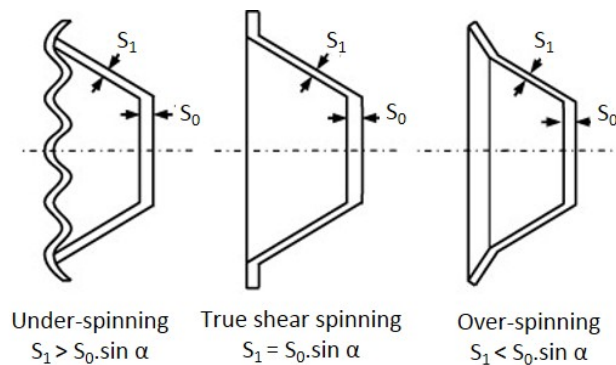


Figure 2.8: Sine rule deviations (Music et al., 2010) – reproduced with permission from Elsevier.

### 2.4.3 Angle variations

According to Runge (1993) and Kunert et al. (2005), the maximum cone angle achievable by shear forming is in the range 80–85° because higher cone angles only involve small reductions without plastic deformation, which leads to significant springback. Conversely, the minimum cone angle is about 10–18°, dependent on the material being formed; smaller angles as low as 3–4° can be produced using a stepwise approach. With this method, multiple passes at different angles for each pass are performed with each successive pass being applied to a smaller cone angle than the previous one until reaching the required geometry. Determining the intermediate angle(s) to employ such a technique is difficult and essentially based on experience and spinnability test results.

In a more recent publication, Bewlay and Furrer (2006) stated that this approach is now generalised to components with a cone angle of 35° or less or if high thickness reduction is to be achieved. Annealing or stress relief treatments between passes are carried out to help maintain the material spinnability. As this technique requires multiple tooling, which incurs extra costs, preforms are sometimes directly obtained by cold forming in a die, hot forging, machining, or a combination of the last two.

### 2.4.4 Tooling considerations

Shear forming with one roller is possible, but two rollers in the diametrically opposite positions with respect to the blank are commonly employed to balance the radial loads and prevent pushing the mandrel off its position. For high-volume production (250–750 components), the mandrel and rollers are generally made of tool steels like D2 and D4, hardened to 60–65 HRC to provide wear resistance and their maximum recommended roughness ( $Ra$ ) is of 1.5  $\mu\text{m}$  and 0.25  $\mu\text{m}$  respectively (Bewlay and Furrer, 2006). The roller shape varies depending on the application as shown in Figure 2.9. The roller design, especially the roller angle ( $\theta_1$ ), is adjusted to ensure clearance so the workpiece does not contact the roller faces during forming and is therefore mainly dependent on the cone angle. As a general rule, the roller nose radius ( $\rho_R$ ) should not be less than the component final thickness (Bewlay and Furrer, 2006).

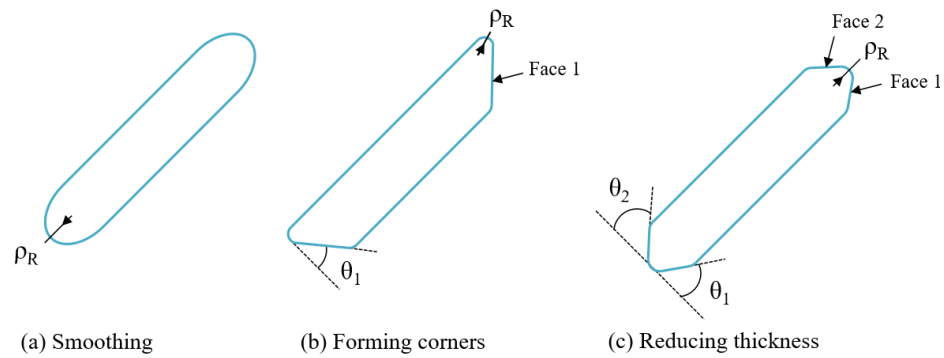


Figure 2.9: Roller shapes and their application for shear forming.

New shear forming methods emerged with the development of both the process and machine capabilities. In the research conducted by Kawai et al. (2007), die-less shear forming was employed where instead of a mandrel corresponding to the component final shape, a cylindrical mandrel was utilised to support the blank at its end and to drag it in rotation as can be seen in Figure 2.10. Even though higher springback was generated, this work on aluminium sheets emphasised that the tool path could reduce this effect. Employing this die-less method reduces the tooling costs as the same mandrel is utilised for multiple cone angles, but with feed rates being lower than usual, the manufacturing time increases. This concept is mostly applicable and relevant to components which do not require high accuracy.

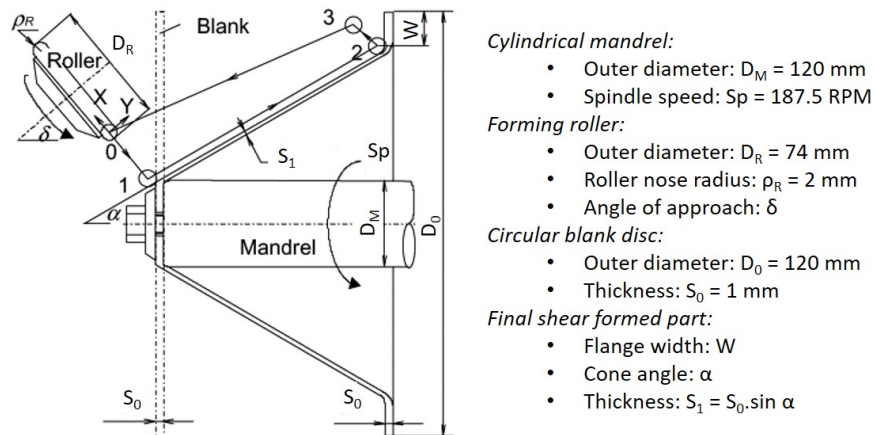


Figure 2.10: Die-less shear forming concept (Kawai et al., 2007) – reproduced with permission from Elsevier.

### 2.4.5 Surface roughness

Depending on the final application of the shear formed component, the surface roughness might be critical as mechanical properties are likely to be impacted. When shear forming, the action of the roller(s) onto the part creates grooves, also called rills, in the external surface. Process parameters, such as feed, speed, and roller shape, impact the size and depth of these grooves, which look like indentations. The inner surface roughness is typically a function of the mandrel surface roughness as a result of the roller(s) load. However, dimpled skin is sometimes noted due to slip-bands remaining at the surface when the blank does not properly contact the mandrel (Kunert et al., 2005). According to Runge (1993), for the conventional spinning of thin sheets, internal grooves might be observed as mirrors of the external ones. Being due to the compressive forces, this phenomenon is also observed in shear forming. For conventional spinning, a smoother surface finish is noted for reduced feeds, higher speeds, or when a smoothing roller is employed.

Studies of the effect of Key Processing Variables (KPVs) on the surface roughness were undertaken by Chen et al. (2001) using a portable roughness tester. In their research, experiments were completed with 173.84 mm aluminium 1100-O square blanks on a 25° mandrel cone using a constant spindle speed. Multiple combinations of four KPVs at five different levels were tested, which included the initial thickness  $S_0$  (1.5–7.0 mm), the roller nose radius  $\rho_R$  (2.5–7.1 mm), the spindle speed  $Sp$  (20–90 RPM), and the feed rate  $F$  (0.1–0.2 mm/rev). For the 36 selected combinations, the roller nose radius was always larger than the final component thickness as suggested in Subsection 2.4.4. The feeds and mainly the speeds appeared to be lower than the common values indicated in Subsection 2.4.1. By the means of statistical analysis, Equations 2.6 and 2.7 were established linking the inner ( $R_i$ ) and outer ( $R_o$ ) surface roughnesses to these KPVs with a 95 % confidence level.

$$R_i = 4.01 + 0.83S_0 - 53.47F + 0.20S_0^2 - 0.45S_0 \cdot \rho_R + 10.15\rho_R \cdot F \quad (2.6)$$

$$R_o = -1.15 + 0.70S_0 - 0.09\rho_R - 0.004Sp + 22.55F - 0.006S_0 \cdot \rho_R \\ + 0.001\rho_R \cdot Sp - 0.83\rho_R \cdot F - 0.08Sp \cdot F \quad (2.7)$$

The inner surface roughness was found independent of the spindle speed whereas the outer surface roughness was impacted by all KPVs. The interaction between feed rate and nose radius showed that a rise of the feed rate increased the inner surface roughness for a nose radius greater than 5.27 mm and decreased it



otherwise. Figure 2.11-(a) illustrates the latter case and also shows that an optimum inner roughness was observed at a specific initial thickness for a fixed roller nose radius. According to Equation 2.7, decreasing the feed rate, increasing the spindle speed and/or the roller nose radius reduced the outer surface roughness independently of the other KPVs. In a more recent study, Chen et al. (2005) also looked at the effect of the gap between roller and mandrel (0.3–0.7 mm) in addition to the other KPVs already studied in the same configuration in their previous work. They confirmed that a larger nose radius leads to a lower outer roughness, which is due to the larger contact area allowing a smoother deformation. An example of the impact on the outer roughness for a fixed spindle speed can be seen in Figure 2.11-(b).

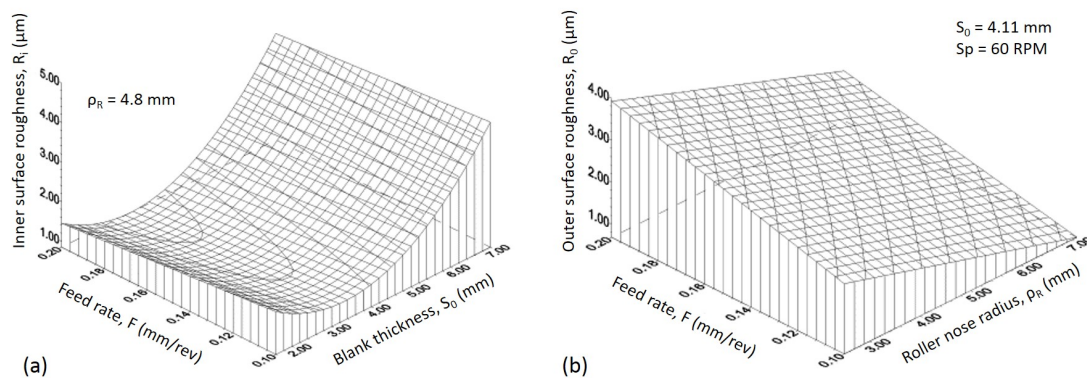


Figure 2.11: Effects of (a) blank thickness and (b) roller nose radius at multiple feed rates on the inner and outer surface roughnesses (Chen et al., 2001) – reproduced with permission from Elsevier.

Completing a mixed DoE approach, Kunert et al. (2005) also studied the effect of the KPVs on the surface roughness by employing qualitative scales instead of direct surface roughness measurements. Aluminium AA-1050A disc blanks with an outer diameter of 260 mm and a thickness of 2 mm were shear formed onto a 42° mandrel. The novelty of this research was to take into account the gap between roller and mandrel (1.138–1.538 mm) and tool path inclination (-0.1–0.1 mm) in addition to the roller nose radius (10–20 mm), feed rate (400–800 mm/min), and spindle speed (800–1200 RPM). A decrease of the outer and inner surface roughnesses was noted when either the spindle speed, gap between roller and mandrel or roller nose radius were increased or when the feed rate was reduced. Conversely, in the work of Chen et al. (2005), a smoother surface roughness was noted when decreasing the clearance and an optimum value of the gap, about mid-range, was

found to lower the outer roughness when considering a fixed initial thickness. The inner roughness was substantially smoother when employing a lower feed rate and/or a smaller gap because the deformation rate was slowed down and a stronger contact between mandrel and blank took place. These differences might be explained by the interaction observed by Kunert et al. (2005) between the roller nose radius and the gap between roller and mandrel for both inner and outer roughnesses. They stated that the indentation of a larger nose radius varies less and is thus less noticeable when using a greater gap between roller and mandrel as the load applied is reduced, leading to a quasi-constant surface roughness. For the inner surface roughness, an additional interaction was identified between feed rate and tool path inclination.

The drawback of both studies was not to mention the starting roughness of the blanks whereas this potentially impacts the final outcomes. These works showed that the effects of the spindle speed and feed rate on the outer roughness correlate with those of conventional spinning.

After shear forming, the obtained surface roughness is generally considered good enough so no additional machining is required. This can be reduced further by the use of a low viscosity lubricant (Music et al., 2010). Although Bewlay and Furrer (2006) indicated roughness values being typically recorded about 1.5  $\mu\text{m}$  with achievable decrease down to 0.5  $\mu\text{m}$  when using appropriate tooling, Chen et al. (2001) registered rougher values, which was potentially explained by the use of the low speeds.

### 2.4.6 Final geometry

Shear forming allows the production of conical parts up to 3 m in diameter with tolerances smaller than  $\pm 0.5$  mm (Bewlay and Furrer, 2006). Table 2.3 gives an example of the tolerances achievable by the process when applied to copper. Although Runge (1993) stated that tighter tolerances are attainable depending on the thickness, flatness, and hardness of the blank, no reference values were given. The machine capabilities have evolved since the publication of this book in 1993. As a result, Table 2.3 must be considered for guidance only and should ideally be updated to encompass further materials when the available data in the literature becomes sufficient.

Table 2.3: Tolerances achievable with shear forming when applied to copper – adapted from Runge (1993).

Workpiece reference dimensions		Tolerances	
Cone height	50–300 mm	Wall thickness, longitudinal direction	$\pm 0.03$ mm
Diameter at open end	40–300 mm	Wall thickness, circumferential	$\pm 0.2$ mm*
Inclined angle	25–50°	Ovality – disc blank	$\leq 0.04$ mm*
Wall thickness	2–10 mm	Ovality – square blank	$< 0.08$ mm
Starting thickness	5–13 mm	Angle	$\pm 0.5^\circ$
Material	Cu 99.9	Average surface roughness	$\leq 0.4$ $\mu\text{m}$

\* Lower values achievable depending on the blank thickness, flatness, and hardness

As for the surface roughness, KPVs play a role in the final geometry. Kunert et al. (2005) looked at their effects on the final component cone angle, flange angle, and average thickness. The tool path inclination alone significantly affected the overall component final geometry as previously outlined by Kawai and Hayama (1987). A higher roller nose radius, gap between roller and mandrel or tool path inclination increased both cone angle and average thickness. Interactions between roller nose radius and tool path inclination, and feed rate and gap between roller and mandrel were also identified to have an effect on the cone angle whereas the flange angle was impacted by the interaction between roller nose radius and gap between roller and mandrel. In addition, Chen et al. (2005) noted an enhanced thickness consistency when reducing the clearance whereas in the survey completed by Music et al. (2010) it was the use of high feed ratio that led to a uniform thickness even though this lowered geometrical accuracy. The drawback of these studies was the lack of clarity in respect to the geometrical measurement method (manual measurements, 3D scans or automatic method) as this would have helped estimate the range of errors, which was not provided.

With the development of the shear forming process more complex shapes are achievable, which includes the forming of internal features as demonstrated in the works of Ma et al. (2010). Even though the complexity of the internal features of the component completed in this study was relatively low as illustrated in Figure 2.12, this research expanded the future applications of the shear forming process. Furthermore,

due to the shape of the final shear formed workpiece, a modular mandrel was utilised to ease its removal, an approach that could be utilised in the future to use the same mandrel in order to achieve multiple part geometries.

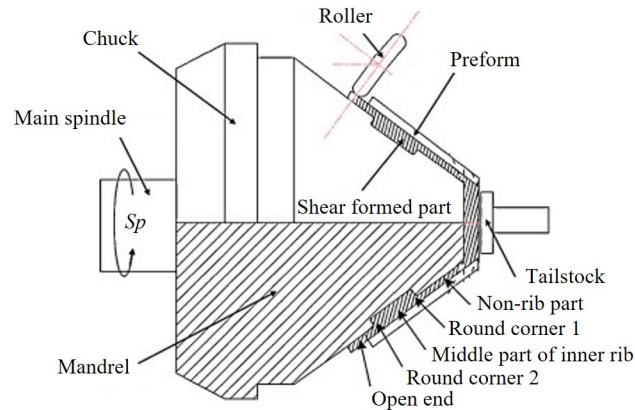


Figure 2.12: Shear forming of conical parts with transverse inner rib (Ma et al., 2010) – reproduced with permission from Elsevier.

### 2.4.7 Forces required

The forces involved between blank and roller(s) in shear forming are typically recorded by load sensors located in the roller boxes using either an external system or the flow former itself. Even though thanks to local deformation these forces are generally lower compared with conventional forming techniques, they can reach up to 3.5 MN (Bewlay and Furrer, 2006). Tangential, axial, and radial forces are generated, out of which the tangential force is usually found to be the smallest (Chen et al., 2001, 2005, Wong et al., 2003). Multiple researchers have attempted to calculate the latter by considering shear deformation or its combination with bending strain. Indeed Avitzur and Yang (1960) discovered experimentally that the mechanism of deformation involved in shear forming is close to pure bending for large angles of shear whereas pure shear seems more appropriate to be considered for smaller cone angles. Chen et al. (2001) established equations linking forces to KPVs. As revealed in Figure 2.13, for a fixed roller nose radius and initial thickness, an optimum link between feed rate and spindle speed was found in order to lower the tangential force, which as reported by Wong et al. (2003) was also identified by Slater (1979) using 2 mm thick 70/30 brass blanks. Although both studies aligned with this last point using different materials, only Chen et al. (2001) noted interactions between these

two KPVs, which might have been down to their DoE approach. In the work undertaken by Kim et al. (2006), the speed was not studied and increasing the feed rate was observed to increase gradually the forces. Little effect of the nose radius was recorded and due to the higher amount of deformation, a smaller cone angle led to higher forces with the exception of the radial load. As expected, for fixed parameters the shear forming of a thicker blank implies higher forces as outlined by Chen et al. (2001) and Kim et al. (2003, 2006). In their more recent study, Chen et al. (2005) also noted a clear impact of the gap between roller and mandrel on the forces.

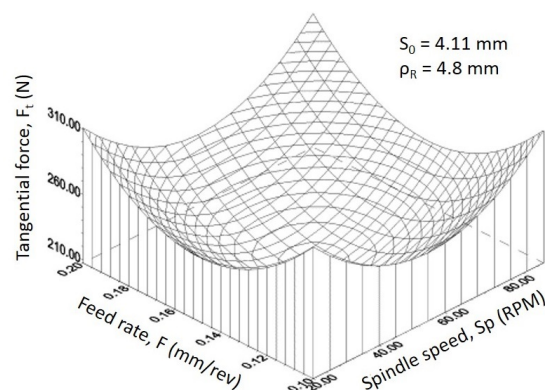


Figure 2.13: Effects of the spindle speed and feed rate on the tangential forces for a 4.11 mm 1100-O Aluminium blank formed with a roller nose radius of 4.8 mm (Chen et al., 2001) – reproduced with permission from Elsevier.

Although the simulation of the shear forming process is complicated due to its incremental nature, Liu et al. (2002), Mori and Nonaka (2005), and Zhan et al. (2007) were able to predict the strain, stress, failure and build-up in shear forming. Kim et al. (2003) first obtained convergence of experimental and theoretical tangential forces by considering a pure shear model. Understanding the forces required to shear form a blank is essential to define the capabilities of such a process and this involves comprehension of the effect of process parameters as well as the material behaviour.

## 2.5 Summary

The main difficulty of carrying out this literature review on shear forming was the confusing terminology due to the multiple alternative terms; hence the necessity to list and define them. The research on spinning methods had been principally focused on

cylindrical flow forming and conventional spinning rather than shear forming until the past few decades.

According to the literature, parts with a cone angle between  $3^\circ$  and  $85^\circ$  can be shear formed, which opens up the range of achievable geometries. The effects of the KPVs on the surface roughness, component final geometry, and forces have previously been studied to understand and enhance process control. All the works mentioned in this review were completed on relatively soft materials, especially aluminium alloys, and using a range of parameters sometimes quite narrow. The roller nose radius and the gap between roller and mandrel were found to impact both component surface roughness and geometry whereas feeds and speeds predominantly had an effect on the surface roughness. A rise of the forces generated during forming was observed when increasing the initial blank thickness. Furthermore, employing solely specific mathematical predictive models instead of more generic finite element approaches to incremental forming is recommended due to the complexity and computational resource required of the latter.

This critical survey showed the importance of providing detail of the methods employed along with the associated errors to enforce the reliability of the results. Interactions between KPVs are also to be considered. The EngD project defines the effect of some KPVs using 304L stainless steel and Inconel 718 on the surface roughness and component final geometry using a systematic approach. The articles discussed above are used as database for comparison to develop further the process understanding.

# Chapter 3

## Materials

Chapter 3 is a systematic literature review related to Inconel 718 and 304L stainless steel, the two materials used in this study, and the microstructure involved in shear forming. The first two sections of this chapter detail the characteristics of Inconel 718 and 304L stainless steel, such as their chemical composition, microstructure, and mechanical properties. Additionally, the factors affecting microstructural development including the potential heat treatments (HT) for Inconel 718 are presented as different microstructural outputs can be obtained. Finally, before summarizing the outcomes of this review, the knowledge available from the effect of shear forming on the material microstructure is reported.

### 3.1 Adopted methodology

The aim of this review was to get a basic understanding of Inconel 718 and 304L stainless steel along with the effect of shear forming on the material microstructure. As for the shear forming process, the flow diagram given in Figure 2.1 (p. 10) was utilised for this systematic search. To be considered in this literature review, the entry had to meet one of the four inclusion criteria:

- Reports on the chemical, microstructural, or mechanical characteristics of Inconel 718 or 304L stainless steel
- Provides information on the various stages involved in the production of hot rolled sheets.
- Explains the fundamentals of restoration processes.

- Studies the effects of shear forming on the microstructure/texture of Inconel 718, 304L stainless steel, or another material.

Documents were excluded if they were published before 1983 (out with the last three decades considering the starting year of the EngD project), were written in a language other than English or French, or did not refer to Inconel 718, 304L stainless steel or material considerations after shear forming. Some documents were discounted for redundancy.

## **3.2 Inconel 718, a nickel-based superalloy**

Superalloys have complex chemistries often featuring nickel and chromium at substantial levels. They are mostly employed for their properties at high temperatures as they are mechanically and chemically resistant up to temperatures close to their melting point. For instance, above 540°C, the mechanical properties of steels and titanium alloys are reduced and these alloys are subject to oxidation. Superalloys exhibit high strength, creep resistance, toughness, are metallurgically stable, and have excellent surface stability resulting in resistance to environmental attack at temperatures up to almost 1500°C (Lours, 2011). Superalloys emerged in the 1950s principally to respond to the needs of the aerospace sector and their development is still ongoing.

Inconel 718 is a Ni-based precipitation hardening superalloy created by Eiselstein for the company Huntington Alloys Corporation in the 1950s (Eiselstein and Tillack, 1991, Kuo et al., 2009). Compared with other superalloys, for example Cr-based, the main advantage of Ni-based superalloys is their better high-temperature strength thanks to their crystallographic arrangement. According to Deleume (2007), in 2007, Inconel 718 was the superalloy most utilised worldwide. Indeed, due to the multiple microstructures this material offers depending on the treatments it receives, it can be utilised in diverse fields, such as aeronautics, power plant, marine, cryogenics, and petrochemistry.



### 3.2.1 Chemical composition

The nominal chemical composition of Inconel 718 is given in Table 3.1. The main element, nickel, improves the yield strength and the stress rupture whereas chromium provides good oxidation resistance by the creation of the oxide layer  $\text{Cr}_2\text{O}_3$  on the material surface. Iron balances the chemical composition and reduces the material cost but its content is moderate in order to preserve the oxidation resistance property. Niobium has a major role as it forms hardening precipitates with nickel and also different carbides. Cobalt modifies the precipitation by reducing the solubility of titanium and aluminium, present in one of the strengthening phases of this alloy, which thus ensures good mechanical properties at high temperatures. Conversely, the solubility of carbon, found in carbides, is increased by cobalt reducing the number of carbides and thus saving niobium for the creation of hardening precipitates. Other elements are sometimes noted in small amounts, such as cobalt, manganese, molybdenum, and tantalum.

*Table 3.1: Typical chemical composition of Inconel 718 (ASTM International, 2016b).*

	Composition (weight, %)			Composition (weight, %)	
	<i>Minimum</i>	<i>Maximum</i>		<i>Minimum</i>	<i>Maximum</i>
Nickel	50.0	55.0	Manganese	-	0.35
Chromium	17.0	21.0	Silicon	-	0.35
Iron	Balance	Balance	Copper	-	0.30
Niobium + Tantalum	4.75	5.50	Carbon	-	0.08
Molybdenum	2.80	3.30	Phosphorus	-	0.015
Titanium	0.65	1.15	Sulphur	-	0.015
Aluminium	0.20	0.80	Boron	-	0.006
Cobalt	-	1.0			

## 3.2.2 Microstructure

### 3.2.2.1 $\gamma$ -matrix

As for all Ni-based superalloys, Inconel 718 is founded on a non-ferromagnetic and austenitic  $\gamma$ -matrix. As shown in Figure 3.1, this phase has a Face-Centred Cubic (FCC) crystal structure. This matrix has a high tolerance for solute with a large solubility and its strengthening is provided with the reduced dislocation movement resulting from internal strains generated during the insertion of solute atoms (Stoloff, 1990).

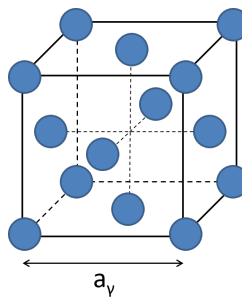


Figure 3.1: FCC crystal structure of the  $\gamma$ -matrix.

### 3.2.2.2 $\gamma'$ -phase

The component  $\text{Ni}_3(\text{Al}, \text{Ta}, \text{Ti})$  is an intermetallic phase called  $\gamma'$ -phase, which was discovered in the 1940s (Chapman, 2004). As illustrated in Figure 3.2-(a), it has a primitive cubic crystal structure  $\text{L1}_2$  with a lattice parameter,  $a_{\gamma'}$ , measuring 0.3570–0.3603 nm at room temperature (Deleume, 2007, Reed, 2008). A small lattice misfit exists between the  $\gamma$  and  $\gamma'$ -phases as the lattice parameter of pure Ni is 0.3517 nm (Reed, 2008). Thus, between 600°C and 900°C, the  $\gamma'$ -phase precipitates evenly through the  $\gamma$ -matrix and is coherent with it (Chapman, 2004). For a mismatch under 0.2 %,  $\gamma'$ -precipitates are generally spherical whereas for a mismatch between 0.5 and 1 % or greater than 1.25 % they adopt a cuboidal or platelike shape respectively (Lours, 2011, Stoloff, 1990). An example of the cuboidal morphology is shown in Figure 3.2-(b). This stable phase takes part in the superalloy precipitation hardening as it obstructs dislocation movements in the matrix. It also provides high-temperature strength and creep resistance (Stoloff, 1990).

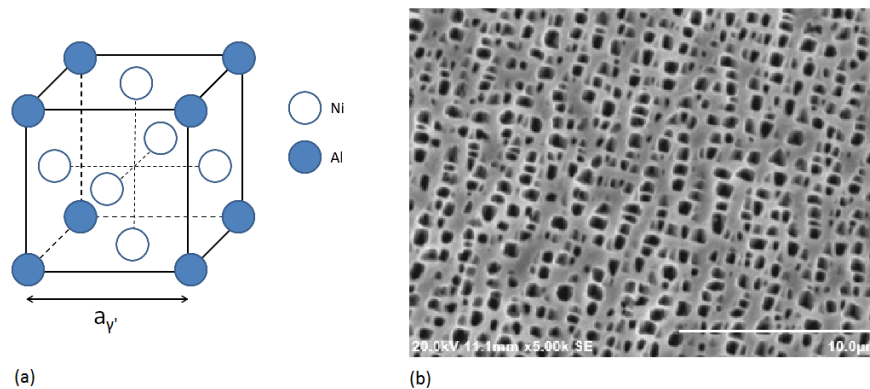


Figure 3.2:  $\gamma'$ -phase: (a) crystal structure and (b) Inconel 792 micrograph by Yang et al. (2011) – reproduced with permission from Elsevier.

### 3.2.2.3 $\gamma''$ -phase

In Ni-based superalloys with a high composition of niobium like Inconel 718, a  $\gamma''$ -phase is observed. This metastable phase with a formula of  $\text{Ni}_3\text{Nb}$  is body-centred tetragonal and has a  $\text{D0}_{22}$  crystal structure as shown in Figure 3.3-(a). Its lattice parameters,  $a_{\gamma''}$  and  $c_{\gamma''}$ , measure 0.362–0.3626 nm and 0.740–0.7416 nm respectively (Deleume, 2007, Reed, 2008). As they are greater than the lattice parameter of the matrix ( $a_{\gamma_{718}}$ , in the order of 0.3598 nm (Deleume, 2007)), high coherency strains are noted, which contribute significantly to hardening. Due to the latter, the  $\gamma''$ -precipitation kinetics is slow but the  $\gamma''$ -precipitates distribution is typically uniform. As captured in Figure 3.3-(b), the  $\gamma''$ -phase generally precipitates between 600°C and 900°C with a disc-shaped morphology inside the grains of the matrix with which it is coherent. In Inconel 718, the volume fraction of  $\gamma''$ -precipitates is four times more than that of  $\gamma'$ -precipitates, making the  $\gamma''$ -phase the primary precipitation phase (Azadian et al., 2004, Devaux et al., 2008). The  $\gamma''$ -phase also provides high strength at low to medium temperatures (Stoloff, 1990). In the literature, the  $\gamma'$ -solvus temperature is estimated at 900–925°C and found to be dependent on the chemical composition (Lours, 2011, Mosser et al., 1989). According to Acharya et al. (2015), the  $\gamma'$  and  $\gamma''$ -solvus temperatures are identical. This temperature could actually be considered more as an equilibrium between the  $\gamma'$  and  $\gamma''$ -phases.

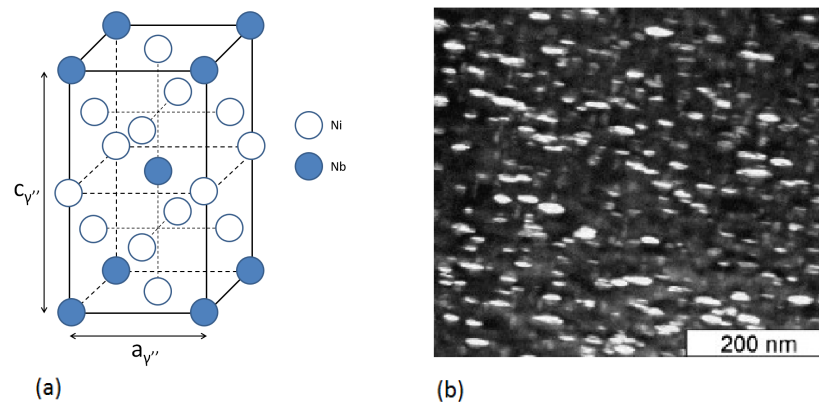


Figure 3.3:  $\gamma''$ -phase: (a) unit cell of  $Ni_3Nb$  and (b) Inconel 718 micrograph by Devaux et al. (2008) – reproduced with permission from Elsevier.

#### 3.2.2.4 $\delta$ -phase

For the Ni-based superalloys which strengthen by the creation of  $\gamma''$ -phase, some  $\delta$ -phase can be observed. This stable phase is orthorhombic and its formula is  $Ni_3Nb$ . The  $\delta$ -phase is incoherent with the matrix and thus gives little strengthening to the superalloy (Stoloff, 1990). For Inconel 718, its lattice parameters,  $a_\delta$ ,  $b_\delta$ , and  $c_\delta$ , measure 0.5106–0.511 nm, 0.4210–0.4251 nm, and 0.4520–0.4556 nm respectively (Donachie and Donachie, 2002, Li et al., 2002). The  $\delta$ -phase precipitates between 700°C and its solvus temperature when the ageing time is under 100 hours. The  $\delta$ -solvus temperature increases with the amount of niobium and typically fluctuates between 990°C and 1020°C (Azadian et al., 2004, Mosser et al., 1989).

In the case of precipitation by nucleation,  $\delta$ -precipitates form either at  $\gamma$ -grain boundaries and then grow into thin plates that can extend into the grains as illustrated in Figure 3.4; or appear intragranularly with an acicular shape when  $\gamma''$ -plates are already present, which facilitates crack propagation. The fragmentation of the thin plates can lead to the formation of equiaxed or slightly elongated globular  $\delta$ -precipitates, which are good for creep resistance and grain size control (Azadian et al., 2004). Although Camus (1986) and Desvallées et al. (1994) disagreed on the range of temperatures within which the different morphologies are noticed, they concluded that the temperature impacts the  $\delta$ -phase shape. Huang and Langdon (2007) also showed a dependency on the level of deformation; from blocky or globular to needle or platelike for low and high deformations.

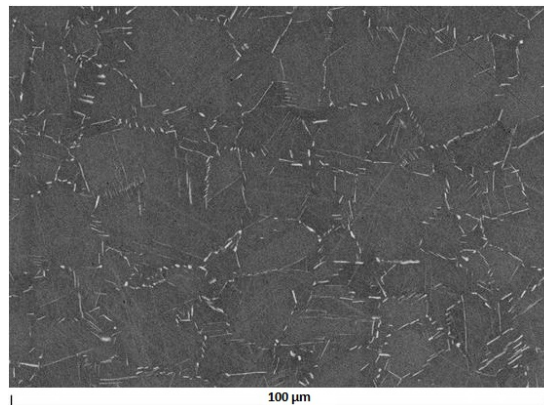


Figure 3.4: Inconel 718 micrograph showing  $\delta$ -phase at  $\gamma$ -grain boundaries and intragranularly (Dehmas et al., 2011) – reproduced with permission from Hindawi Publishing Corporation.

The  $\delta$ -precipitation kinetics is slow and so even if the  $\delta$ -phase is thermodynamically more stable than the  $\gamma''$ -phase, its precipitation up to about 900°C always comes after the formation of  $\gamma''$ -phase. In situations where cold working has taken place, the  $\delta$ -precipitation time is reduced as cold working promotes the segregation of niobium at the deformation bands contributing to the formation of  $\delta$ -precipitates (Liu et al., 1997, Mosser et al., 1989).  $\delta$ -precipitates help control and refine the grain size by reducing the grain boundary movement due to grain boundary pinning. Tensile and fatigue properties as well as grain boundary fracture resistance are then improved, and static recrystallisation and grain growth – restoration processes detailed in Section 3.4 (pp. 45–46) – are slowed down. As both  $\delta$  and  $\gamma''$ -phases are rich in niobium, precipitating the  $\delta$ -phase reduces the amount of  $\gamma''$ -precipitates, which thus deteriorates the hardening of Inconel 718 and therefore explains why the amount of  $\delta$ -precipitates has to be controlled.

### 3.2.2.5 Other phases

Carbides are generally created by the combination of carbon with a metal atom, denoted M. Common carbides include MC,  $M_6C$ ,  $M_{23}C_6$ ,  $M_7C_3$ , and  $M_3C_2$ . They are typically located at grain boundaries or at interdendritic regions and as illustrated in Figure 3.5, they have a blocky, globular, script, platelet, lamellae, cell, or nodular shape. MC carbides are very stable but are difficult to dissolve even at high temperatures. Borides are components made of boron and chromium or molybdenum,

which tend to reside at  $\gamma$ -grain boundaries under blocky and half-moon morphologies (Stoloff, 1990). Carbides and borides improve creep properties at high temperatures. When locating at grain boundaries, they prevent or retard the grain boundary sliding by reinforcing the rupture strength and allowing stress relaxation (Davis et al., 1997, Stoloff, 1990). In Inconel 718, in absence of  $\delta$ -phase, carbides help control the grain growth but depending on their size and shape they make the material more brittle and lower fatigue and creep resistances (Donachie and Donachie, 2002). Discrete and blocky carbides at grain boundaries are ideal. However, as for  $\delta$ -precipitates, their volume fraction has to be controlled because they consume niobium and titanium which play a major role in the formation of hardening precipitates (Davis et al., 1997).

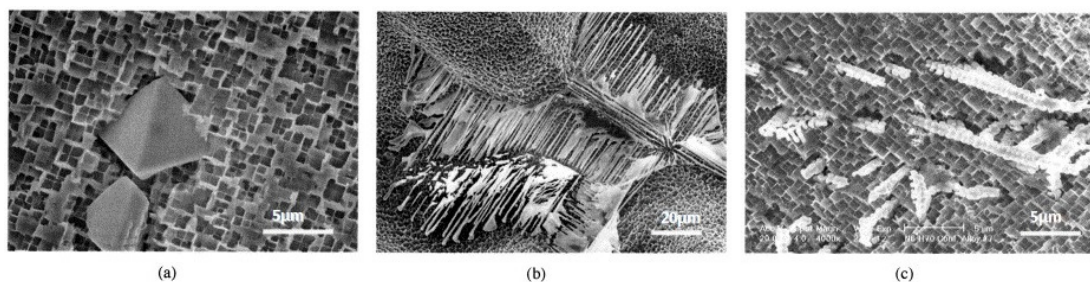


Figure 3.5: Ta-rich MC carbide observed in single crystal Ni-based superalloy exhibiting (a) blocky, (b) script, and (c) nodular morphologies (Tin and Pollock, 2003) – reproduced with permission from Elsevier.

The topologically close-packed (TCP) phases, such as  $\mu$ ,  $\sigma$ , and Laves are observed in Ni-based superalloys in the aged condition. As these phases embrittle the alloy by lowering rupture strength and ductility, the superalloy chemical composition is chosen in order to avoid their creation (Reed, 2008, Stoloff, 1990). In general, the TCP phases have a formulae  $A_xB_y$  with A and B being transition metals. These are some examples:

- $\mu$ -phase: Rhombohedral cell, for example  $Mo_6Co_7$
- $\sigma$ -phase: Tetragonal cell observed in Figure 3.6, such as FeCr
- P-phase: Primitive orthorhombic cell observed in Figure 3.6, for instance  $Cr_{18}Mo_{42}Ni_{40}$
- R-phase: Rhombohedral cell, such as  $Fe_{52}Mn_{16}Mo_{32}$

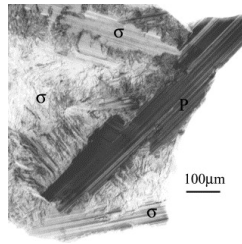


Figure 3.6: Micrograph of extracted TCPs observed in single crystal RR2072 superalloy (Rae and Reed, 2001) – reproduced with permission from Elsevier.

### 3.2.3 Mechanical properties

The mechanical properties of an Inconel 718 component depend on its final geometry and microstructure, thus the forming process and heat treatment temperatures play a major role. The blanks that were shear formed in this EngD project were hot rolled and annealed. Final heat treatment was only performed after shear forming. Table 3.2 gives the main mechanical properties of Inconel 718 for hot-rolled sheets or finished products manufactured from these after final annealing and aging treatments; minimum conditions to be reached after shear forming and final heat treatment.

Table 3.2: Mechanical properties of hot-rolled sheets or final products made of Inconel 718 (Rolls-Royce plc, 2006, *Special Metals*, c. 2015).

Property *	20°C	650°C
Yield strength at 0.2 %, $R_{p0.2}$	≥ 1030 MPa	≥ 830 MPa
Ultimate tensile strength, $UTS$	≥ 1240 MPa	≥ 1000 MPa
Elongation after fracture, $A$	≥ 12 %	≥ 5 %
Stress	/	695 MPa
Stress rupture Life	/	23h
A	/	4 %
Hardness	362–486 HV	/

\* For thickness ≥ 0.65 mm when one of the following heat treatments has been performed:

- 950-990°C/Rapid cooling +  $\left\{ \begin{array}{l} 720^\circ\text{C}/8\text{h}/\text{Furnace Cooling to } 620^\circ\text{C}/8\text{h}/\text{Air cooling} \\ 750^\circ\text{C}/4\text{h}/\text{Furnace Cooling to } 650^\circ\text{C}/4\text{h}/\text{Air Cooling} \end{array} \right.$
- 925-1010°C/Rapid cooling + 720°C/8h/Furnace Cooling to 620°C/Until total aging time reaches 18h/Air Cooling

### 3.3 304L, an austenitic stainless steel

Stainless steels are Fe-Cr alloys with a minimum chromium content of 10.5–12 % providing corrosion resistance in aqueous environment or service at elevated temperatures (Blair, 1990, Hummel, 2004). The first discoveries and developments on stainless steel technology started in England, France, and Germany in 1900–1910 (Delagnes and Lours, 2011). Since the middle of the 20<sup>th</sup> century, their worldwide consumption increased by 6 % per annum (Outokumpu Stainless AB, 2013). Stainless steels are used for consumer items and industrial equipment in diverse domains, such as the oil and gas, nuclear, aerospace, transportation, chemical industry, and food and beverage sectors. The most common group of stainless steels is the austenitic grades, which have excellent mechanical properties, such as good high-temperature strength, toughness, ductility, formability, weldability, and predictable corrosion resistance (McGuire, 2008, Washkot and Aggen, 1990). Out of all stainless steels, 302, 304, and 316 are the most popular austenitic wrought grades (Vander Voort et al., 2004). 304 stainless steel and its variant 304L stainless steel represent 50 % of the global production of stainless steels and thus are the most employed (Outokumpu Stainless AB, 2013). The mechanical properties of 304L stainless steel along with its abundance and reduced cost compared with Inconel 718 made it the ideal base material for this study.

#### 3.3.1 Chemical composition

304L stainless steel is an austenitic stainless steel included in the Cr-Ni grades. Its chemical composition is given in Table 3.3 for pressure vessels and general applications when in plate, sheet, and strip form, which is applicable for this EngD project. Its lower carbon content compared with 304 stainless steel (0.030 % instead of 0.070 %) is denoted ‘L’ and enables sensitisation reduction when welding (Vander Voort et al., 2004, Washkot and Aggen, 1990). Carbon provides strength in high-temperature applications but is also detrimental to corrosion resistance because of its interaction with chromium (Sourmail, 2002, Washkot and Aggen, 1990). As previously mentioned, chromium gives the material corrosion resistance by the creation of an oxide layer on its surface and improves oxidation resistance at high temperatures (McGuire, 2008, Outokumpu Stainless AB, 2013). Manganese enhances



hot ductility, raises the nitrogen solubility, and is sometimes employed to partially substitute nickel for economical reasons whereas silicon improves oxidation resistance (Outokumpu Stainless AB, 2013, Sourmail, 2002). Other elements are seen in smaller quantities, such as nitrogen which improves strength and corrosion resistance and the element sulphur which enhances machinability (McGuire, 2008).

*Table 3.3: Typical chemical composition of 304L stainless steel (ASTM International, 2016a).*

	Composition (weight, %)	
	Minimum	Maximum
Chromium	17.5	19.5
Nickel	8.0	12.0
Iron	Balance	Balance
Manganese	-	2.00
Silicon	-	0.75
Nitrogen	-	0.10
Phosphorus	-	0.045
Carbon	-	0.030
Sulphur	-	0.030

Chromium is a ferrite stabiliser and thus leads to a ferritic structure if austenite stabilisers are not present in sufficient quantity (Sourmail, 2002, Vander Voort et al., 2004). Nickel improves toughness, ductility, corrosion resistance in mineral acids, promotes repassivation, and stabilises the austenitic structure (McGuire, 2008, Outokumpu Stainless AB, 2013). Other alloying elements are classified either as austenite or ferrite stabilisers and the notion of Cr and Ni-equivalent is often used in the literature. The most common examples of this concept are Schoefer's relationships given in Equations 3.1 and 3.2 (Blair, 1990). When applying these to the composition of 304L stainless steel given in Table 3.3 for the minimum amounts of chromium and nickel,  $Cr_{eq}$  and  $Ni_{eq}$  are found at 13.6 % and 14.8 % respectively.

$$Cr_{eq} = Cr + 1.5Si + 1.4Mo + Nb - 4.99 \text{ weight } \% \quad (3.1)$$

$$Ni_{eq} = Ni + 30C + 0.5Mn + 26(N - 0.02) + 2.77 \text{ weight } \% \quad (3.2)$$

### 3.3.2 Microstructure

#### 3.3.2.1 $\gamma$ -matrix and $\delta$ -ferrite

Austenitic stainless steels Fe-Cr-Ni are called austenitic due to their austenitic structure at room temperature. 304L stainless steel is founded on a  $\gamma$ -matrix, which is metastable, austenitic, and has a FCC crystal structure as illustrated in Figure 3.1 (p. 32) (Biehler et al., 2017, Cakmak et al., 2014, Das et al., 2008, Hummel, 2004). This  $\gamma$ -matrix is non-ferromagnetic in the annealed condition and has a lattice parameter,  $a_{\gamma 304L}$ , estimated at 0.360 nm (Marshall, 1984, Washkot and Aggen, 1990). The microstructure of 304L stainless steel often features retained  $\delta$ -ferrite as the low-carbon content increases the likelihood towards  $\delta$ -ferrite stabilisation even if its amount is limited (Blair, 1990, Vander Voort et al., 2004). For instance, in cast austenitic alloys, 5–20 % of ferrite is discontinuously distributed throughout the matrix depending on the contents of chromium, nickel, and carbon. In 304L stainless steel,  $\delta$ -ferrite is beneficial and intentional to enhance weldability and maximise corrosion resistance but becomes detrimental at high temperatures (Blair, 1990).

Austenitic stainless steels cannot be hardened by undertaking heat treatment as martensite is not created when quenching from an elevated temperature, which results from an insufficient quantity of carbon and/or other alloying elements. Cold working is utilised instead. In the case of austenitic stainless steels, applying more plastic strain requires higher stress to deform further. This phenomenon is called work (or strain) hardening and is caused by an increase of the dislocation density reducing the dislocation movement (Milad et al., 2008). If significant, work hardening leads to martensite formation.

#### 3.3.2.2 Martensite

Martensite is very hard and brittle, its formation results in an increase in alloy hardness and reduction in ductility (Hummel, 2004). This phase is formed by either cooling the workpiece to temperatures under the martensite start temperature, which is generally below room temperature, or by application of considerable plastic deformation through cold working (Biehler et al., 2017, Cakmak et al., 2014). In this study, only the latter case is of interest and for this reason is the only one detailed here. Two types of martensite have been recorded:

- $\varepsilon$ -martensite, which has a hexagonal close-packed structure and is non-ferromagnetic
- $\alpha'$ -martensite, which presents a Body-Centred Cubic (BCC) structure, is ferromagnetic, and thermodynamically more stable than the  $\varepsilon$ -martensite

The martensite transformation following plastic deformation is thoroughly discussed in the literature and its mechanism is described as  $\gamma \rightarrow \varepsilon \rightarrow \alpha'$ , where the amount of  $\varepsilon$ -martensite is reduced when high deformation is registered as  $\alpha'$ -martensite grows at its expense (Llewellyn, 1997, Milad et al., 2008, Tavares et al., 2003). Austenitic stainless steels thus become ferromagnetic after high deformation. Martensite transformations are sometimes characterised by  $M_{d30}$ , temperature at which 50 % of martensite is created for a true strain of 30 % and which is dependent on the chemical composition as shown in Equation 3.3 (Sourmail, 2002). When martensite transformation occurs due to plastic deformation above  $M_{d30}$ , the transformation becomes dependent on the temperature of deformation, strain rate, stress, and chemical composition (Das et al., 2008). This temperature is estimated at 14.1°C maximum when using Equation 3.3 for the composition of 304L stainless steel given in Table 3.3.

$$M_{d30} (^{\circ}C) = 497 - 462(C + N) - 9.2Si - 8.1Mn - 20Ni - 13.7Cr - 18.5Mo \text{ weight}\% \quad (3.3)$$

In the literature, contradictions on the amount of martensite introduced by cold working are noted, but it is agreed that cold working promotes martensite formation which thus increases hardness (Amitava et al., 2004, Kain et al., 2004, Peguet et al., 2007). Milad et al. (2008) found that the Vickers hardness for 304 stainless steel doubles during the initial stages of cold rolling for deformations up to 25 % whereas for subsequent deformations up to 50 %, the hardness increases by 7 % only. Biehler et al. (2017) confirmed that cold working improves surface hardness in 304L stainless steel.

### 3.3.2.3 Other phases

The main carbide observed in 304L stainless steel is  $(Fe,Cr)_{23}C_6$ , which is metastable, and has a FCC structure with a lattice parameter of 1.057–1.068 nm (Marshall, 1984). Between 500°C and 950°C, the  $M_{23}C_6$  carbide appears in sheetlike, globular, or lamellar form at grain boundaries, twin boundaries, and intragranular

sites (Delagnes and Lours, 2011). It degrades intergranular corrosion resistance, tensile properties, and mainly ductility and toughness (Marshall, 1984). As the carbon content in 304L stainless steel is low, the number of carbides is reduced, but if they are observed they can be completely dissolved by solution heat treating (Vander Voort et al., 2004).

Intermetallic phases and diverse sulphides are noticed in stainless steels with MnS and  $\sigma$  being the most common of each type (Vander Voort et al., 2004, Washkot and Aggen, 1990). The  $\sigma$ -phase has a tetragonal unit cell with lattice parameters of 0.87–0.92 nm and 0.4540–0.48 nm (Marshall, 1984, Sourmail, 2002). With long-time exposure at 650–900°C, this TCP phase is found in 304L stainless steel as FeCr. This phase is a strong embrittler for temperatures lower than 595°C and is promoted by silicon and cold working (Vander Voort et al., 2004).

### 3.3.3 Mechanical properties

The mechanical properties for plates, sheets, or strips of 304L stainless steel in the annealed condition as well as forgings are given in Table 3.4. The reduced carbon level leads to slightly lower variations in material properties compared with 304 stainless steel. Its combination of low yield strength and high elongation provides 304L stainless steel with an excellent formability in terms of deep drawing and roll forming, and good formability for spinning compared with other austenitic stainless steels (Washkot and Aggen, 1990). 304L stainless steel thus allows the forming of complex shapes but work hardens efficiently so solution heat treating is generally required. When solution heat treating is properly undertaken, the end-microstructure shows equiaxed grains with twins and a single grain size distribution (Vander Voort et al., 2004). The blanks that were shear formed in this EngD project were hot rolled and annealed.

## 3.4 Microstructure evolution

Both the Inconel 718 and 304L stainless steel used in this project were annealed hot-rolled sheets. Zhou and Baker (1995) explained that hot rolling modifies the microstructure and facilitates dynamic and metadynamic recrystallisation as well as grain growth. These mechanisms are detailed in this section.

Table 3.4: Mechanical properties of plates, sheets, or strips in the annealed condition made of 304L stainless steel and forgings (ASTM International, 2016a, Washkot and Aggen, 1990, Switzner et al., 2019).

Property	20°C	843°C *
Yield strength at 0.2 %, $R_{p0.2}$	$\geq 170$ MPa	$\geq 580$ MPa
Ultimate tensile strength, UTS	$\geq 480$ – $485$ MPa	$\geq 760$ MPa
Elongation after fracture, A	$\geq 40$ %	$\geq 37$ %
Hardness	$\leq 178$ – $197$ HV	/

\* For forgings at 843°C

When cold working is undertaken, which is the case of the shear forming process, the mechanical energy generated is predominantly dissipated by heat, but some is also stored in the grains, especially in dislocations and point defects, such as vacancies. The material becomes thermodynamically unstable. To recover the original properties of the material and lower the stored energy, restoration processes may take place when thermally activated. For these processes to occur, the amount of cold working required is estimated to be about 30–50 % reduction in thickness or above (Raabe, 2014). Recovery, recrystallisation, and grain growth are the three main restoration processes and are illustrated in Figure 3.7. These processes occur either heterogeneously throughout the material, in this case, the nucleation and growth steps are clearly identified and the processes are discontinuous; or homogeneously for continuous processes (Humphreys, 1997). Recovery and recrystallisation are defined in this section with specific references to Inconel 718 only, as this EngD project does not intend to study the heat treatment of 304L stainless steel and does not involve grain growth.

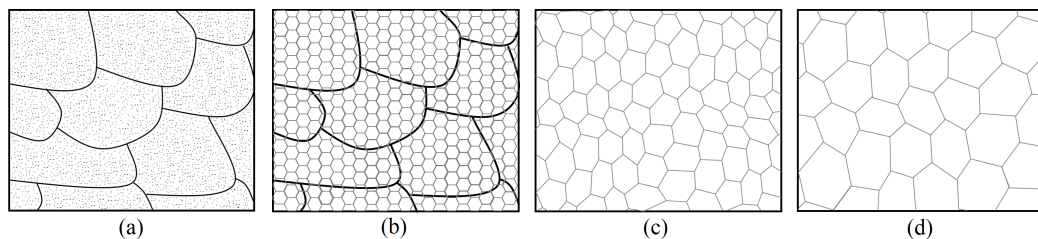


Figure 3.7: Schematic of the restoration processes: (a) deformed, (b) recovered, (c) recrystallised, and (d) grain growth – adapted from Rollett et al. (2004).

### 3.4.1 Recovery

During recovery, the accumulated strain energy is partially relieved by microstructural and submicroscopic rearrangements, such as reduction in density and changes of the dislocation distribution and creation of point defects. To reach this metastable state, annihilation (when two dislocations of opposite sign attract and merge to annihilate their allocated stored energy) and rearrangement of dislocations take place leading to the creation of subgrains with slightly different orientations or to the coarsening of subgrains, phenomena called continuous recovery by subgrain growth and discontinuous recovery respectively. In the latter case, low-angle boundaries migrate and merge or coalescence of adjacent subgrains occurs (Humphreys, 1997, Mittemeijer, 2010, Smallman and Bishop, 1999). Static recovery generally happens after deformation when solution heat treating below half the melting temperature, i.e. for temperatures lower than 630–668°C for Inconel 718. The recovery kinetics increases with time and decreases with temperature, so when higher temperatures are registered, recovery occurs during deformation and is then called dynamic recovery (Bapokutty et al., 2012). The extent of the recovery process is characterised by a slight decrease in hardness (Baker, 2000, Smallman and Bishop, 1999).

As recovery does not produce strain-free grains, recrystallisation might occur, which involves higher temperatures. In some cases, both processes overlap because discontinuous subgrain growth initiated the first step of the recrystallisation, called nucleation (Humphreys, 1997, Mittemeijer, 2010, Raabe, 2014).

### 3.4.2 Recrystallisation

#### 3.4.2.1 General overview

First identified at the beginning of the 20<sup>th</sup> century, recrystallisation is a process where new nuclei are created in the deformed matrix (nucleation); and then grow to become almost equiaxed strain-free grains (growth) (Rollett et al., 2004). This occurs by the formation and migration of high-angle boundaries, which lead to grain orientation changes and release of stored-strain energy by absorption of the point defects and dislocations (Mittemeijer, 2010, Smallman and Bishop, 1999). These

microstructural changes modify the material properties, for instance, material strength and hardness are reduced. Recrystallisation has to be thermally activated and the minimum temperature required for this process to start is called recrystallisation temperature. The higher the degree of cold working, the lower the recrystallisation temperature and the smaller the grain size (Smallman and Bishop, 1999, Wu et al., 2014). The recrystallised volume fraction, sometimes denoted as  $X$ , is generally measured by optical metallography and/or Transmission Electron Microscopy (TEM) (Baker, 2000).

Recrystallisation is either continuous or discontinuous if a few grains grow bigger than the other ones (Humphreys, 1997). Three types of recrystallisation are identified. Dynamic recrystallisation takes place during deformation whereas metadynamic recrystallisation happens at the end of the deformation when the material is still hot. Static recrystallisation occurs only after deformation during solution heat treating. As Duquesnoy (1992) estimated the temperatures implied by flow forming at 250–350°C, it was judged out of scope in this EngD project to look at dynamic and metadynamic recrystallisation as this is observed for Inconel 718 for temperatures greater than 925–950°C (Medeiros et al., 2000, Mosser et al., 1989, Na et al., 2003, Zhou and Baker, 1995).

#### **3.4.2.2 Static recrystallisation**

Static recrystallisation (SRX) follows and competes with recovery. In contrast to dynamic and metadynamic recrystallisation, SRX requires an incubation time and consequently occurs after deformation (Smallman and Bishop, 1999). The higher the temperature is, the more likely recrystallisation is to be promoted. The recrystallisation temperature is typically above the recovery temperature and about 0.5–0.7 times the melting temperature for impure materials, i.e. around 630–935°C for Inconel 718. Cold working, temperature, time, initial grain size, chemical composition, presence of second phases, texture, and amount of recovery influence SRX (Raabe, 2014). The recrystallisation kinetics often follows an Avrami-type equation.

Until 20 years ago, recovery, recrystallisation, and grain growth were clearly distinguished. However, due to the improved techniques employed to study microstructure and to our limited understanding of plastically deformed state, borders between these processes are not as clear as they used to be and their overlap is

possible (Humphreys, 1997, Mittemeijer, 2010). The importance of the restoration processes for the material properties explains why heat treatment after cold working is crucial.

### 3.5 Heat treatments

Heat treatments are performed to optimise the alloy properties and are defined by Donachie and Donachie (2002) as processes during which a temperature is applied for any time in order to either lead to the reduction of stress, the promotion of grain growth or new recrystallised grains, the phase dissolution, the creation of new phases, the redistribution of alloy elements, or the change in surface chemistry. As shown in Figure 3.8, the heat treatment of superalloys generally consists of a solution heat treating and quenching step followed by a two-step aging treatment.

Solution heat treating dissolves secondary phases to either obtain a good corrosion resistance or to prepare for aging. Quenching is then undertaken to retain a portion of the supersaturated solid solution at room temperature. In the case of precipitation-hardened alloys, precipitates might not always entirely dissolve. Overall, solution heat treating homogenises the microstructure to ensure maximum ductility and its effect depends on the solution temperature, denoted  $T_s$ . After cold forming, solution heat treating is typically performed to reduce the stress generated by cold working and to restore ductility.

Aging, also called precipitation hardening, is employed to precipitate hardening phases from the supersaturated matrix after solution heat treating. For superalloys, the long-term aging performed for classical alloys, which may provoke coarsening of precipitates, is commonly replaced by two shorter age treatments at different temperatures. As the temperature influences the type and size of the precipitates, two-step aging helps control the size distribution and volume fraction of the hardening phases along with the carbide morphology at grain boundaries. The selection of the number of aging steps, precipitation time and temperature are dependent on the kind and number of precipitating phases, service temperature, precipitate size, strength, and ductility required (Lours, 2011).



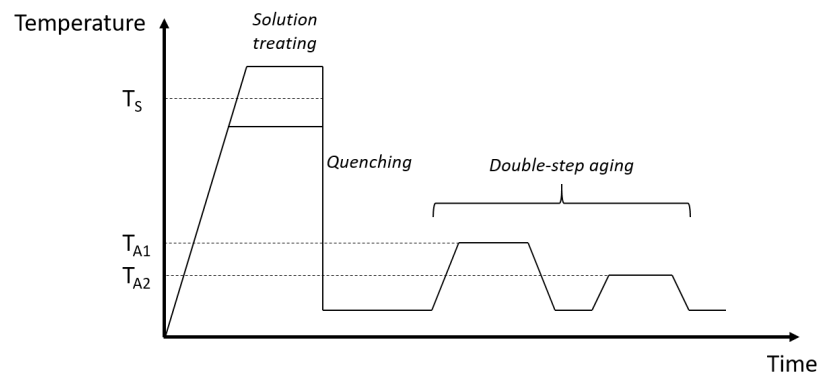


Figure 3.8: Typical heat treatment for superalloys.

**Case of Inconel 718** Prior to machining, forming, or welding, Inconel 718 is generally in an annealed or stress-relieved state and it is only after such an operation that one of the common heat treatments summarized in Table 3.5 is performed (Special Metals, c. 2015). Heat treatments (1), (2), (3), and (6) from the table below use  $T_s$  between the  $\gamma'/\gamma''$  and  $\delta$ -solvus temperatures, which are estimated at 900/925°C and 990/1020°C respectively according to Sub-subsections 3.2.2.3 and 3.2.2.4 (pp. 33–35). If  $T_s$  is chosen lower than 980°C,  $\gamma'$  and  $\gamma''$ -precipitates are partially dissolved, some  $\delta$ -phase is created, and the small grain size remains enhancing fatigue and tensile properties (Mosser et al., 1989, Lours, 2011). In contrast, if  $T_s$  is higher but still lower than the  $\delta$ -solvus temperature, the hardening phases are totally dissolved, some  $\delta$ -phase is created, and grain growth occurs depending on the initial microstructure, amount of  $\delta$ -precipitates, and cold working, which improves creep resistance (Lours, 2011, Mosser et al., 1989). For heat treatment (4),  $T_s$  is above the  $\delta$ -solvus temperature and thus this phase is dissolved. Grain growth and more extensive dissolution of carbides occur, which is found useful especially in the nuclear field (Deleume, 2007). Nevertheless, if the application requires  $\delta$ -precipitates, another solution heat treating step is performed to generate it as shown in heat treatment (5). For all heat treatments,  $\gamma'$  and  $\gamma''$ -precipitates are created upon cooling from  $T_s$ .

All the heat treatments given in Table 3.5 have a double-step aging with similar temperatures included in the precipitation range of the  $\gamma'$  and  $\gamma''$ -phases. Additional  $\gamma'$  and  $\gamma''$ -precipitates are therefore formed and their coarsening takes place. This provides strength to the superalloy mainly through the  $\gamma''$ -phase. Furnace cooling is usually performed in between these two aging steps with a cooling rate of 45–65°C/h.

Table 3.5: Multiple heat treatments for Inconel 718.

	Solution heat treating			Double-step aging		Cooling
	Temp. (°C)	Duration	Cooling	Temp. (°C)	Duration	
(1)	925–1010	NA	AC	720	8 h	AC
				620	8 h	AC
(2)	927–1010	0.5 h	Equivalent AC or faster	718 ± 14	8 h	FC
				621 ± 14	Until total aging time has reached 18 h	AC
(3)	927–1010	NA	Rapid cooling, typically AC	718	8 h	FC
				621	Until total aging time has reached 18 h	AC
(4)	1038–1066	NA	Rapid cooling, typically AC	760	10 h	FC
				649	Until total aging time has reached 20 h	AC
(5)	1095	1 h	AC	720	8 h	FC
	955	1 h	AC	620	8 h	AC
(6)	980	1 h	AC	720	8 h	FC
				620	8 h	AC

NA: Not Applicable, AC: Air Cooling, FC: Furnace Cooling

(1) Lours (2011)

(2) ASTM International (2016b)

(3) and (4) Special Metals (c. 2015)

(5) Donachie and Donachie (2002), Kuo et al. (2009)

(6) Donachie and Donachie (2002)

### 3.6 Microstructural considerations when shear forming

As previously stated in Chapter 2, local deformation of the material occurs during shear forming, which improves material properties thanks to the uninterrupted grain flow. Only a couple of studies were available in the literature. The works presented here focused on Al and Al-Mg alloys, which have a common crystal structure with the materials studied in this EngD project.

Zhan et al. (2016) studied the microstructure and hardness of 6 mm thick blanks with an outer diameter of 290 mm made of 3A21-O aluminium alloy. The workpieces were shear formed on a 30° mandrel at a feed rate and spindle speed of 1 mm/rev and 100 RPM. The influence of the gap between roller and mandrel was analysed using positive, null, and negative deviation ratios ( $\chi$ , definition given in Chapter 2, p. 16). After shear forming, the grains were so elongated that Electron BackScatter Diffraction (EBSD) techniques were utilised to study the grain size variation and a reduction of the average grain diameter by 5.1–5.6 times was noted as a result of the creation of small refined grains. The grains undergoing multiple strains were divided into several areas with different orientations. The increased misorientation between these regions led to the creation of high-angle boundaries especially when under

negative deviation ratio. Deformation bands (DBs) and transition bands (TBs) were then formed as seen in Figure 3.9, which also shows the grain orientations along the FCC slip planes. DBs are subdivisions of the grains into areas with different orientations and originate from heterogeneous stress from neighbouring grains or intrinsic instability of the grain while plastically deformed. The orientation within the same DB is quite homogeneous and TBs, which are typically narrower, are located in-between them (Rollett et al., 2004). Geometrically necessary boundaries (GNBs), also called dense dislocations walls or microbands, are created between areas of different strain patterns and some were identified in Zhan et al.'s work at 35° to the rolling direction (RD) within the grains for the null deviation ratio while crossed GNBs were noted under positive and negative deviation ratios.

Zhan et al. (2016) also observed a reduction of the overall hardness when decreasing the deviation ratios and variations across the thickness were noted. A neutral zone was identified near the component middle thickness where almost no deformations had occurred. From this region the microstructure was symmetrically distributed showing a reduction of the material deformation from the surfaces towards this area. Higher deformation was observed from the outer surface as a result of the action of the rollers against the workpiece. This explained the neutral zone being located slightly more towards the inner surface even though the deformation generated by the friction between mandrel and blank was not negligible. For both positive and null deviation ratios, almost no refined grains were identified in the neutral zone, which correlates with the smaller hardness values obtained in this area. Conversely, when under negative deviation ratio, refined grains were noted because of the higher degree of deformation implying the flow of the material throughout the component thickness. In this case, the local hardness gradually increased from the inner to the outer surface.

Zhan et al. (2016) concluded that DBs were the main mechanism of grain refinement in shear forming. Even though EBSD data was acquired, this article did not give the texture distribution.

Radović et al. (2012) studied the influence of grain size and thickness reduction on microstructure, properties and deformation behaviour for the alloy AlMg6Mn when shear forming. After being hot rolled, 3 mm thick and 130 mm wide square blanks were shear formed. Two rollers with a feed rate of 150 mm/min were utilised to shear form on a 45°, 30°, and 20° mandrel along with a spindle speed set at

400 RPM and 660 RPM for the last two geometries. The as-received microstructure was partially recrystallised after hot rolling and gradually refined when shear forming. The elongated grains were almost parallel to the axis of rotation and stretched along the circumferential direction. These phenomena were more pronounced with a larger thickness reduction. According to Radović et al. (2012), as a result of the tangential force, the direction of the grains was slightly deviated from the axis of rotation. Partially attributed to grain refinement, higher thickness reduction was found to raise the ultimate strength and hardness but decreased the elongation as the material was less able to plastically deform.

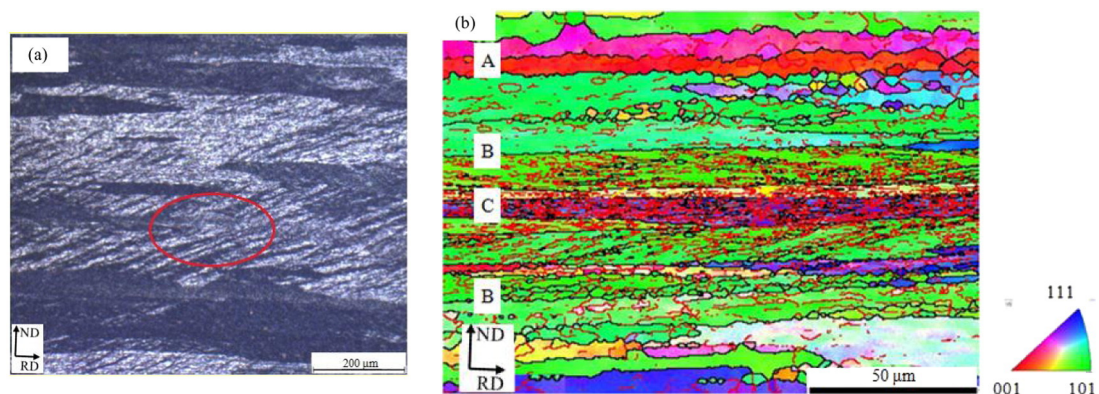


Figure 3.9: Microstructure of a  $30^\circ$  shear formed part under a null deviation ratio: (a) optical microscopy (b) EBSD map in the localised area defined in (a) (Zhan et al., 2016) – reproduced with permission from Elsevier.

### 3.7 Summary

This literature review showed that Inconel 718 and 304L stainless steel are used widely in diverse applications and thus their composition, microstructure, and mechanical properties are well understood, which will help analyse the microstructures of both materials prior to and after shear forming. Although research on both materials is quite broad, nothing has been published so far in correlation with the shear forming process.

The understanding for 304L stainless steel in terms of cold working provides good basics to study the impact of the shear forming process and some articles discussed above will be compared with the results of the current study. Inconel 718 has rarely been studied in such a condition, which, in the context of developing a

sound understanding of the effect of shear forming of Inconel 718 for aerospace applications, demonstrates the requirement for this EngD project.

Although Zhan et al. (2016) and Radović et al. (2012) studied the microstructure and texture of shear formed components made of Al and Al-Mg alloys, the texture was not analysed and the material deformation mechanism was not identified. The EngD project aimed to fill this gap of knowledge.

## **Chapter 4**

# **Experimental protocol**

Chapter 4 deals with the experimental protocol involved in this EngD project. The equipment utilised is presented. The shear forming configuration of the full scale flow former is introduced. Then, the metallurgical analysis is detailed, which includes the material preparation, the microstructure and texture observations and analyses, and the hardness study. The measurement of the surface roughness with non-contact and contact methods is highlighted. Finally, the section dedicated to the geometrical analysis presents the measurement methods followed by the concept of design of experiments and statistical analysis.

### **4.1 Shear forming configuration**

When set up for shear forming, the physical configuration of the flow former remains the same, regardless of the specific tooling geometry. The arrangement of the flow former with the tooling geometry employed for the site acceptance trials and its main elements are presented in Appendix C (pp. 151–154).

The technical capabilities of the flow former, the CNC code which individually controls each of its axes, and the ability to record data during the process, such as the loads, are described in Appendix C (pp. 152–162). This appendix also details the calibration and procedures followed. The range of variables associated with the machine parameters was highly dependent on the geometry, material type, and material thickness being studied. The particular machine parameters will be given in the relevant sections.

## 4.2 Metallurgical analysis

### 4.2.1 Metallurgical sample preparation

The metallurgical sample preparation is crucial to acquire quality pictures of the microstructure and to observe the material texture. For that, each shear formed part of interest was first cut by electrical discharge machining or water jet cut in order to obtain a slice of the part as shown in Figure 4.1. Then, the slice was cut into the five areas denoted M1 to M5 on this figure. Secondly, each sample was mounted, ground, and polished. Etching was sometimes required to reveal the microstructure. The methods followed in this EngD project, for both 304L stainless steel and Inconel 718, are detailed in Appendix C (pp. 162–165).

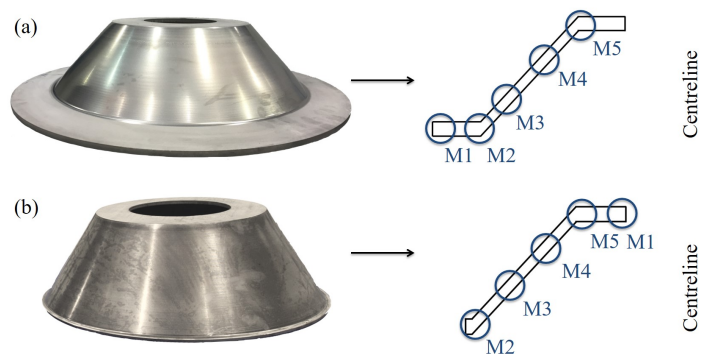


Figure 4.1: Positions of micro-assessment evaluation of (a) a part with external flange and (b) a part without external flange – adapted from Norton (2015).

### 4.2.2 Hardness analysis

The hardness measurements were performed at the AFRC using the micro-hardness tester Zwick-Roell Indentec ZH $\mu$ -AFHD. In this EngD project, the Vickers indenter was utilised at a test force of 1 kgf. This is considered as low-force Vickers hardness test and is denoted HV1. The Vickers hardness is in kgf.mm<sup>-2</sup>. The calculation of the surface area of the indentation requires the average of the two diagonal lengths of the indent. The measurements were manually taken and the Indentec ZH $\mu$ -AFHD's software then calculated automatically the hardness. The ISO standard 6507-1 (British Standard Institution, 2006a) was followed:

- The samples were mounted and polished with a depth under resin big enough to meet Section 6 “Test piece” of this standard.
- The temperature of the room where the tests were performed, the location of the measurements and the lens (here 20x) were chosen to meet Section 7 “Procedure” of this standard. Furthermore, as required by this section, it was stated next to the measurement value if the difference between the lengths of two indentation diagonals was greater than 5 %.

As required by Rolls-Royce plc (2012), the laboratory floor was anti-vibration, but the Indentec ZH $\mu$ -AFHD’s camera did not have any movement compensations.

The measurements were taken as described in Figure 4.2. The hardness values provided in this document are an average of three indents taken across the thickness of the specimen and are given with an uncertainty band of  $\pm 9$  HV1. The specifications, standards, calibration, and repeatability and accuracy study utilised in this project are described in Appendix C (pp. 165–167).

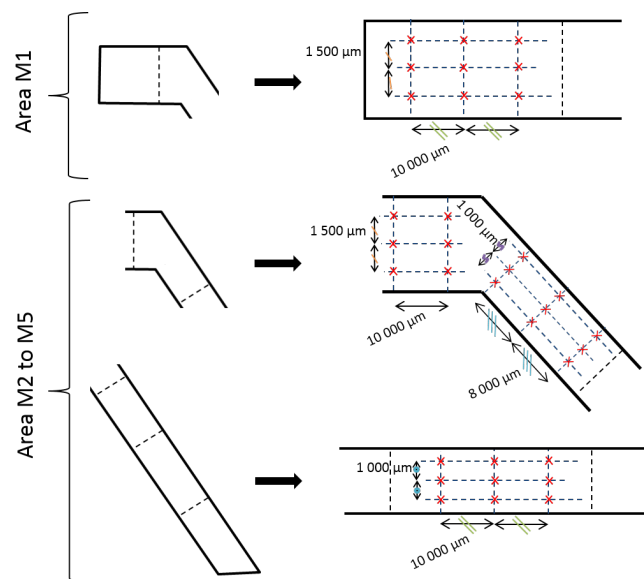


Figure 4.2: Location of the hardness measurements – Part without an outer flange.

### 4.2.3 Microstructure observation

The material microstructure can be observed with different techniques, such as optical, scanning electron, and transmission electron microscopies. In this study, the first two options were selected. More detail about these is given in Appendix C



(pp. 168–169). Although the Scanning Electron Microscope (SEM) Quanta 250 FEG offers an accelerating voltage from 200 V to 30 kV, voltages of 15 kV and 20 kV are commonplace and were used in this EngD project. In high vacuum, the electron beam resolution of the Quanta 250 FEG can reach 1.0 nm at 30 kV and 2.5 nm at 30 kV in backscatter (BS) mode. In this study, the spot size, also called beam size, was varying between 3.5 and 4.5 and high vacuum was employed. Micrographs were taken in BS mode. The coordinate systems adopted for reporting the microstructural data of area M1 were the rolling direction (RD), transverse direction (TD) and normal direction (ND) of the blank sheet whereas the cylindrical coordinates ( $R, \theta, Z$ ) were used for the remaining areas. When not specified, pictures and measurements were taken in the middle of the thickness of the area of interest.

#### 4.2.4 Grain size measurement

In this project, the material texture, phase identification, and grain size were observed with the SEM using EBSD techniques. EBSD maps were acquired with a step size of 1  $\mu\text{m}$  and 0.3  $\mu\text{m}$  for the as-received and shear formed areas respectively. Due to the elongation of the grains after shear forming, the grain size was analysed from the EBSD data with the Module ‘Tango’ of the software Channel5. First, a noise reduction was performed and then the wild spikes, which are “isolated points that have been incorrectly indexed” due to polishing relief and/or scratches, were removed. These false small grains are generally part of larger grains (Oxford Instruments, 2010). Then the zero solutions, which are points that could not be indexed, were “filled in using copies of neighbouring points.” (Oxford Instruments, 2010) In this study, the number of indexed neighbours was set at 4.

The upper critical misorientation is “the main method of defining a grain boundary wherever the local misorientation exceeds the ‘critical misorientation’ angle” whereas the lower critical misorientation helps “detect grains, where there are incomplete boundaries without introducing noise into the result.” (Oxford Instruments, 2010) These were set at  $10^\circ$  and  $3^\circ$  as this is appropriate for most materials. Additionally, twins were disregarded and the diameter of the grains was multiplied by two or four if the grains touched one or two borders respectively. The grains were then detected according to the above parameters and grains smaller than 5 pixels (i.e. 5  $\mu\text{m}$  if step size of 1  $\mu\text{m}$ ) were disregarded to prevent taking into

consideration false grains. This is considered as a common practice according to Bastos et al. (2006). Where the grains were not equiaxed, the average grain area was investigated instead of the average grain circle equivalent diameter to ensure relevance.

### 4.2.5 Texture observation

The texture is defined as “the sum of the crystallographic orientations of the crystallites within a polycrystalline material” (Kubilay, 2014). To study the texture, Pole Figures (PFs) and Orientation Distribution Functions (ODFs) were utilised.

#### 4.2.5.1 Pole Figures

PFs are the most common representation of material texture and show “the projected position of a particular set of crystallographic planes which have been projected onto a sphere and then onto a circle” (Oxford Instruments, 2010). They are typically employed to describe distributions of orientations along with their intensities, which are shown as contour lines (Field, 2004).

The parameters employed for the display of the PFs with the module ‘Mambo’ of Channel5 are given in Table 4.1. “The half width value controls how much the pole (plane normal or crystal direction) is spread out over the surface of the project sphere.” (Oxford Instruments, 2010) The value was set at  $10^\circ$ , which is the usual value according to Oxford Instruments (2010). “Clustering speeds up the calculations. It looks at the data and finds clusters of the same orientation (e.g. from the same grain) and replaces them by a single orientation with an increased weighting.” (Oxford Instruments, 2010) Stereographic projection is typically employed (Field, 2004) as this allows angular relationships in the crystal to be preserved in the projection (Engler and Randle, 2009). The planes selected met the cubic configuration of each phase. Finally, the maximum colour intensity and contour line were set at 6 for a clearer display.

#### 4.2.5.2 Orientation distribution functions

“The ODF is a means of representing preferred orientations for materials. It is a four dimensional object – the four dimensions being the three Euler angles and a

density value corresponding to how strongly a particular orientation appears. This strength is expressed as a ratio to that expected for a completely random distribution of orientations.” (Mohamed Zaky Ahmed, 2009) In the case of ODFs, the texture is given as “a function that provides the probability of finding the orientation of the crystallites relative to the sample coordinate system. ODFs are represented as two dimensional sections of a rectangular Euler space which is represented by three Euler angles.” (Kubilay, 2014)

Using the software Channel5 – Module ‘Salsa’, the ODFs were displayed using the settings given in Table 4.2. A Gaussian estimation was utilised, which is an indirect method, with a half width of 5° as this is the usual value employed according to Oxford Instruments (2010). In this case, the Gaussian half width helps control the spreading out of the EBSD data in the Euler space. Finally the sample symmetry chosen was triclinic, so no preferential symmetries were assumed.

*Table 4.1: Settings employed to generate the PFs.*

Half width	Cluster size	Coordinate system	Contour lines
10°	5°	As-received: RD, TD, ND Shear formed: R, $\theta$ , Z	Step width of 1.5 Max. at 6
Colours	Projection hemisphere	Projection type	Planes
Max. intensity at 6	Upper	Stereographic	{100}, {110}, {111}

*Table 4.2: Settings employed to generate the ODFs.*

Half width	Cluster size	Coordinate system	Contour lines	Colours
Gaussian, 5°	5°	As-received: RD, TD, ND Shear formed: R, $\theta$ , Z	At 2, 4, 6, 8, and 10	Rainbow
Sample symmetry	Resolution	Method	Calculation	
Triclinic	128x32x32	Gaussian estimation	Based on full map	

## 4.3 Surface roughness analysis

In this project, two methods were employed for the surface roughness measurements. In 2013, the only instrument available at the AFRC to study the surface roughness was the Alicona InfiniteFocus G4, which was a non-contact method. With this equipment, due to the size of the shear formed parts, replicas of the surface had to be taken in four areas along the shear formed length.  $Ra$  was given by the software as the mean of the values obtained for a set number of profiles. This allowed the impact of a single non-typical peak or valley to be excluded from consideration. Here, the width was five pixels, which represents five calculated profiles. This method was proved reliable by performing a type 1 gauge study to compare the results between replica and part.

In 2014, a Mitutoyo portable surface roughness tester, the SurfTest SJ-210, was purchased by the AFRC. This contact device was able to measure, in a few seconds, the surface roughness directly on the part. As advised by Leach (2014), the device was switched on at least one hour before measuring to allow time for the instrument to stabilise. The measurements were taken perpendicular to the lay to meet the ISO standard 13565-1 (British Standard Institution, 1997a) and Rolls-Royce standard RRES90036 (Rolls-Royce plc, 2009). As illustrated in Figure 4.3, a fixture system had to be used to ease the measurement of  $Ra$  along the shear formed length. The measurement was more efficient than with the InfiniteFocus as no replicas were required.

As measurements had already been taken with the InfiniteFocus, both instruments were studied and compared using type 1 gauge studies. Even though the InfiniteFocus was more consistent than the SurfTest SJ-210, both instruments were accurate enough for this project. In 2015, for comparison purposes, it was decided to use the SurfTest SJ-210 only, which is normal industry practice. The measurement methods, specifications, standards, calibration, repeatability studies, and accuracy for both instruments are described in more detail in Appendix C (pp. 169–178).



*Figure 4.3: Set-up of the Surfatest SJ-210 and its fixture to measure the surface roughness of a shear formed part.*

## 4.4 Geometrical analysis

Geometrical conformance is of most importance in engineering and is sometimes part of the process optimisation. As for the surface roughness measurements, in this project, contact and non-contact instruments were employed to measure the geometry of the parts. The GOM ATOS III Triple Scan and Mitutoyo Crysta-Apex C 121210 were respectively non-contact and contact instruments available at the AFRC and utilised for geometrical analyses.

The ATOS III Triple Scan gave a 3D visualisation of the part. This was useful especially when looking at the variation of the thickness along the part. This was the first method selected because the training required to use this equipment was more efficient, and could be performed entirely by the author. A rotating table was used to partially automate the scanning operation as well as a frame into which the part was glued in order to increase the stability during the scanning operation as can be seen in Figure 4.4. When using the ATOS III Triple Scan, if the surface of the part was shiny then it could not be scanned properly. To fix this problem, prior to measurement, the part was cleaned and painted with Ardrox 9D1B. Before scanning, reference points were applied to the frame and part. They helped the software ATOS

Professional V7.5 merge the scans. Putting reference points onto the frame decreased the amount required on the actual part. Due to the geometry of the shear formed parts, two series of scans were required on both sides of the part, which were then combined to obtain the final 3D part.



*Figure 4.4: Scanning with a rotating table and a frame using ATOS III Triple Scan.*

This EngD project was not the only shear forming project undertaken at the AFRC. Other projects decided, due to time constraints, to use the contact method. Consequently, in 2015, to have a better consistency in the results and to get a crossover between the different projects, the contact method instrument started to be operated.

First, the shear formed part was loaded onto a fixture with three pins in the middle of the CMM bed (Figure 4.5). To ensure the probe did not collide with the fixture, the pins were not lined up with the X or Y axes of the machine. Furthermore, the dowel hole had to be located at the back of the CMM. Secondly, for the machine to know where the part was, a few points were taken manually on the internal and external flanges of the part as well as inside the dowel hole and internal diameter using the probe. Then, the CNC program was ready to run. The measurements were established in a different way depending on the features as described in Table C.14 (pp. 186–187).

Both instruments were studied and compared using type 1 gauge studies and were found accurate enough for this study according to British Standard Institution (2012). The detailed measurement methods, calibration, repeatability studies, and accuracy for both instruments are described in Appendix C (pp. 179–190). Prior to any measurements, parts were put in the temperature controlled measurement laboratory for a full day.



Figure 4.5: Set-up of a shear formed part on the fixture for CMM measurement.

## 4.5 Design of Experiments and statistical analysis

In this EngD project, the literature review helped identify several possible parameters impacting the process. In this case, Antony (2014) advises to use a Design of Experiments (DoE) approach. DoE involves the planning, design and analysis of the experiments in order to obtain effectively and efficiently valid and objective conclusions (Antony, 2003). In this EngD project, principally factorial DoE was utilised. This design enabled the study of the joint effect of the factors on a response. A full factorial DoE includes all possible combinations of levels for all factors. The total number of runs for studying  $k$  factors at  $y$ -levels is  $y^k$ . To identify a non-linear function, the study of variables at three or more levels is advised. This helps quantify the non-linear or curvature effect of the process parameter on the response function. Rosochowski (2013) introduced the notion of augmentation of the original experiment. This is employed to resolve any ambiguities in the interpretation of the previous experiment. The purpose of this experiment is to evaluate some configurations that have not previously been tried. The added runs are called an augmentation of the original experiment.

Statistical analysis was used to distinguish between significant and insignificant effects in an experiment as the latter is arising from random variation. To perform such an analysis, Minitab software was used. Analyses of the variance (ANOVA) as well as F-tests were carried out on the factorial DoE. This helped build a model for predicting response function. A regression model approach was employed to illustrate the relationship between a response and the process parameters which affect the response. This was used to predict the response for different combinations of process parameters. When using 3-level factors, second order equations can be generated

(Grove and Davis, 1992). The assessments of the models are presented in Appendix C (pp. 189–194) where an example is also given.

This chapter has given an overview of the experimental procedures used in this work. The remainder of the thesis now discusses the outcomes obtained from these experimental procedures.



## Chapter 5

### Primary work on 304L stainless steel

Chapter 5 presents the first experiments undertaken at the AFRC since the commissioning of the flow former, which included a repeatability study as well as a DoE approach. This exploration of the shear forming process focused on the commissioning tooling, a 31.5° cone geometry, using 304L stainless steel. 304L stainless steel is commonly used as a cost effective trial material by Rolls-Royce in early development of parameters for forming processes due to its widespread availability and formability, and its lower cost compared with nickel-based superalloys. The aim was to obtain some baseline understanding about the shear forming process and the flow former to aid future work including the use of Inconel 718.

First, Chapter 5 introduces the set-up and experiments including the choice of KPVs for the DoE. Secondly, the outcomes in terms of final geometry and surface roughness are statistically analysed based on the methodology presented in Paper A, which is in Appendix A. Then, the microstructure, texture and hardness are detailed to enable better understanding of the material behaviour during the shear forming process. This work was published in Paper B, which is in Appendix B. Finally, the results are discussed and compared with the literature.

## 5.1 Experiments

### 5.1.1 Set-up

The commissioning tooling, a  $31.5^\circ$  cone geometry, was utilised for these first experiments. The associated assembly drawing and the design of the two 3 mm nose radius rollers employed here are given in Appendix B (pp. 153–154). The blanks were 6 mm thick stainless steel discs with internal and outside diameters of 150 mm and 430 mm respectively. Figure 5.1 is an updated concept drawing of the final shear formed part. The blanks were water jet cut and inspected prior to forming. This information was reported in a data sheet specific to each part, which was filled in after each forming or inspection operation. A blank version of this data sheet is given in Appendix D (pp. 195–197). This applied for all experiments undertaken within this project.

The repeatability study presented in this chapter was undertaken using the commissioning set-up and CNC program, i.e. with two rollers, a feed rate of 1 mm/rev and a surface speed of 400m/min. For the DoE, it was decided to employ only one roller to allow a direct comparison with the Rolls-Royce supply chain. The CNC program for two rollers is described in Appendix B (pp. 157–159).

### 5.1.2 Choice of KPVs for the DoE

As the necessity to use coolant is not clear in the literature, the coolant flow rate ( $C$ ) was selected to be an additional variable of this DoE. This flow rate was adjusted manually using the taps located inside the flow former, but no real flow meters were installed on the machine preventing an accurate reading. After forming a part without lubricant or coolant, pick-ups on the roller were recorded. As a result, lubricant was painted onto the blanks for the parts to be formed without coolant and grease was applied on the blank and tooling. The lubricant was a protective/lubricating coating called Driform 61A, which was a dispersion of inorganic and polymeric organic solid lubricants in a solution of organic resin in isopropanol. Driform 61A was already employed at the AFRC in rotary forging, another incremental cold forming process.

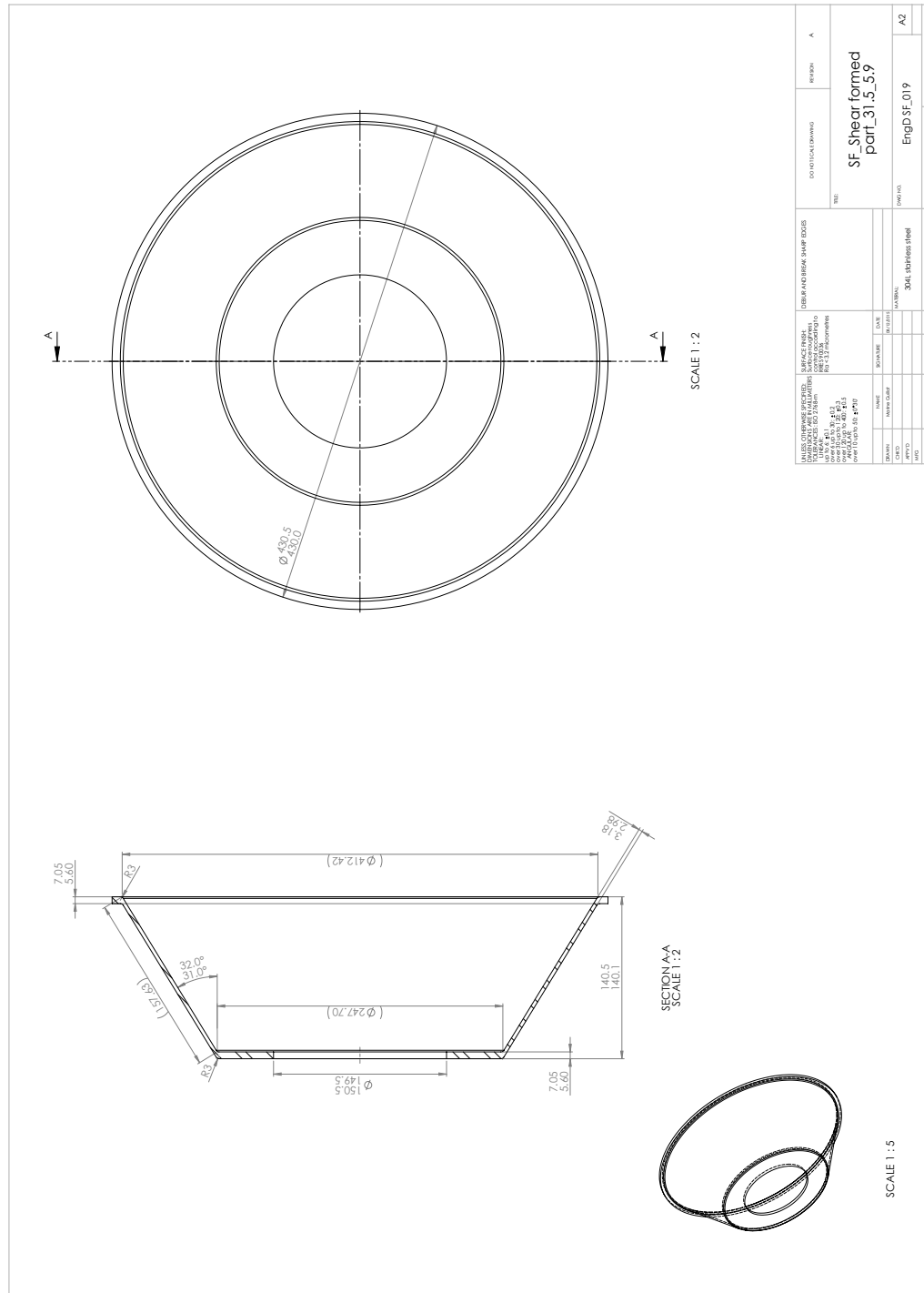


Figure 5.1: Drawing: Shear formed part – 31.5°, 5.90 mm thick – EngD SF\_019, “SF\_Shear formed part\_31.5\_5.9”.

The surface speed (or spindle speed) and feed rate were considered as variables for the DoE. According to the literature, a surface speed less than 300 m/min is not recommended to obtain good quality components. Furthermore, forming without coolant leads to an increased heat and reducing the feed rate while forming with only one roller will generate even more heat. For these reasons, the lowest values of feeds and speeds tested were of 0.6 mm/rev and 300 m/min respectively. According to Equation 2.4 (p. 17), the spindle speed is dependent on the surface speed and if the latter is kept constant the spindle speed is at its maximum at the start of the forming operation. As a result, the maximum surface speed was set at 480 m/min to provide a safety margin relative to the upper limit of the spindle speed. To help select the highest feed rate value, a pre-trial part was run at 1.5 mm/rev. A step at the start of the cone section was noted as if the roller had missed the first contact point and the surface roughness obtained was poor, which indicated that the feed rate was too high. Furthermore, as the effect of using only one roller and lubricant was uncertain, the highest level value of the feed rate was assigned to the initially recommended value of 1 mm/rev.

A full three-level factorial DoE was carried out with the three variable parameters feed rate ( $F$ ), surface speed ( $Su$ ), and coolant flow rate ( $C$ ) designated as factors. This  $3^3$  design generated 27 runs. The lubricant ( $L$ ) was included in the experiment as an additional two-level factor, which did not increase the number of runs as  $L$  was only used when  $C$  was turned off. Table 5.1 gives this factorial DoE, which allowed the prediction of the main effects of each factor as well as their interactions (with the exception of the interaction between  $C$  and  $L$ ). The blank average thickness was not considered as a variable thanks to its consistency.

## 5.2 Geometrical and roughness analyses

The surface roughness and geometrical measurements were completed using InfiniteFocus and ATOS III Triple Scan. The measurement methods are described in Appendix C, Sub-subsection C.3.2.1 (pp. 172–173) and Sub-subsection C.4.1 (pp. 180–183). The average surface roughness and thickness of the blanks were measured at 3.68  $\mu\text{m}$  and 5.93 mm respectively.

Table 5.1: DoE employed for the forming of 304L stainless steel blanks on the 31.5° geometry using one roller.

Part identification*	$F$ (mm/rev)	$Su$ (m/min)	$C$ (L/min)	$L$
P <sub>2</sub> 1	0.6	480	400	0 (=No)
P <sub>2</sub> 2	0.6	400	400	0 (=No)
P <sub>2</sub> 3	0.6	300	400	0 (=No)
P <sub>2</sub> 4	0.8	480	400	0 (=No)
P <sub>2</sub> 5	0.8	400	400	0 (=No)
P <sub>2</sub> 6	0.8	300	400	0 (=No)
P <sub>2</sub> 7	1	480	400	0 (=No)
P <sub>2</sub> 8	1	400	400	0 (=No)
P <sub>2</sub> 9	1	300	400	0 (=No)
P <sub>2</sub> 10	0.6	480	200	0 (=No)
P <sub>2</sub> 11	0.6	400	200	0 (=No)
P <sub>2</sub> 12	0.6	300	200	0 (=No)
P <sub>2</sub> 13	0.8	480	200	0 (=No)
P <sub>2</sub> 14	0.8	400	200	0 (=No)
P <sub>2</sub> 15	0.8	300	200	0 (=No)
P <sub>2</sub> 16	1	480	200	0 (=No)
P <sub>2</sub> 17	1	400	200	0 (=No)
P <sub>2</sub> 18	1	300	200	0 (=No)
P <sub>2</sub> 19	0.6	480	0	1 (=Yes)
P <sub>2</sub> 20	0.6	400	0	1 (=Yes)
P <sub>2</sub> 21	0.6	300	0	1 (=Yes)
P <sub>2</sub> 22	0.8	480	0	1 (=Yes)
P <sub>2</sub> 23	0.8	400	0	1 (=Yes)
P <sub>2</sub> 24	0.8	300	0	1 (=Yes)
P <sub>2</sub> 25	1	480	0	1 (=Yes)
P <sub>2</sub> 26	1	400	0	1 (=Yes)
P <sub>2</sub> 27	1	300	0	1 (=Yes)

\* P<sub>2</sub>: P for Part and 2 for second set of experiments

### 5.2.1 Repeatability

Table 5.2 gives the outcomes for the repeatability parts. The values obtained for the first diameter shear formed were not matching the expected 247.7 mm diameter of the mandrel, which might have been due to the gap between roller and mandrel being too large.

The consistency of the cone angle and thickness were satisfactory as a maximum variation of  $0.07^\circ$  and 0.06 mm were respectively observed. The measured cone angle was larger than expected, which was explained by the springback. The final thickness being linked by the sine rule to the initial thickness and cone angle was therefore slightly greater than the nominal target value.

After forming, the inner and outer surface roughnesses were considerably reduced. The values observed for the inner roughness were less consistent and larger than those of the outer surface roughness. It was assumed that the gap between roller and mandrel was too large leading to a lack of pressure against the mandrel's face because dimpled skin was noted as reported in the literature by Kunert et al. (2005).

The standard deviations showed overall that the measured values of both geometry and surface roughness were close. Due to the difficulties measuring the final diameter and the height, larger deviations were observed for these features.

*Table 5.2: Geometrical and roughness measurements: Repeatability,  $31.5^\circ$  geometry, 2 rollers, 304L stainless steel.*

	Values observed			Standard deviation
	Maximum	Minimum	Average	
Internal diameter, $d$ (mm)	149.91	149.66	149.79	0.08
First diameter (mm)	249.55	249.27	249.34	0.07
Final diameter, $D_1$ (mm)	422.39	420.81	421.57	0.50
Height (mm)	143.06	142.41	142.7	0.22
Cone angle ( $^\circ$ )	32.01	31.94	31.98	0.02
Final thickness, $S$ (mm)	3.27	3.21	3.24	0.02
Inner surface roughness, $R_i$ ( $\mu\text{m}$ )	2.09	1.49	1.80	0.23
Outer surface roughness, $R_o$ ( $\mu\text{m}$ )	1.44	1.16	1.30	0.09

### 5.2.2 DoE

According to Table 5.3, the average final thickness was consistent across the parts whereas the final diameter and height varied significantly. The height and final diameter were not statistically analysed due to the difficulties to measure them and neither was the internal diameter as this latter was independent of the shear forming operation. Table 5.4 gives the values of the geometrical features and roughness for each of the trials of the DoE.

*Table 5.3: Minimum, maximum, average, and standard deviation of the geometrical and roughness measurements of the parts included in the factorial DoE.*

	Values observed			
	Maximum	Minimum	Average	Standard deviation
Internal diameter, $d$ (mm)	149.88	149.60	149.75	0.08
First diameter (mm)	250.27	248.82	249.59	0.41
Final diameter, $D_1$ (mm)	427.35	416.43	421.53	3.36
Height (mm)	142.90	140.65	141.78	0.55
Cone angle ( $^\circ$ )	32.80	31.88	32.23	0.25
Final thickness, $S$ (mm)	3.37	3.22	3.30	0.04
Inner surface roughness, $R_i$ ( $\mu\text{m}$ )	1.63	0.84	1.06	0.18
Outer surface roughness, $R_o$ ( $\mu\text{m}$ )	2.43	0.77	1.31	0.35

### 5.2.3 Statistical analysis

Regression equations linking the process parameters to the geometry and the surface roughness were obtained by statistical analyses as described in Chapter 4, Section 4.5 (pp. 61–62). Table 5.3 summarises the results. Predictive numerical models were established (Equations 5.1–5.4, p. 72). Their assessment and the statistical significance of the factors are given in Table 5.5. For every response,  $F$  and  $L$  had a significant effect whereas varying  $C$  had no impacts. The optimised values were generated and are given in this table.

Table 5.4: Geometrical and surface roughness outputs of the DoE given in Table 5.1.

Part identification	Internal diameter $d$ (mm)	First diameter (mm)	Final diameter $D_1$ (mm)	Height (mm)	Cone angle ( $^\circ$ )	Final thickness $S$ (mm)	Inner surface roughness, $R_i$ ( $\mu\text{m}$ )	Outer surface roughness, $R_o$ ( $\mu\text{m}$ )
P <sub>2</sub> 1	149.69	249.49	423.41	142.90	31.96	3.26	0.98	0.78
P <sub>2</sub> 2	149.84	249.07	422.46	142.24	32.14	3.33	1.14	0.93
P <sub>2</sub> 3	149.82	248.82	422.49	141.76	32.28	3.29	0.90	0.97
P <sub>2</sub> 4	149.64	249.98	419.75	142.56	31.88	3.29	1.12	1.15
P <sub>2</sub> 5	149.78	249.62	418.82	141.92	32.08	3.32	1.16	1.26
P <sub>2</sub> 6	149.77	249.51	418.29	141.32	32.23	3.31	1.18	1.38
P <sub>2</sub> 7	149.87	250.27	416.43	141.17	32.02	3.34	1.00	1.51
P <sub>2</sub> 8	149.88	250.21	416.53	141.10	32.06	3.35	0.84	1.59
P <sub>2</sub> 9	149.8	249.69	416.61	141.52	32.04	3.36	0.91	1.43
P <sub>2</sub> 10	149.73	249.49	422.36	142.58	32.06	3.27	0.85	1.02
P <sub>2</sub> 11	149.72	249.21	422.37	142.21	32.18	3.29	0.87	0.77
P <sub>2</sub> 12	149.67	249.04	421.61	141.40	32.35	3.27	1.07	0.79
P <sub>2</sub> 13	149.84	250.18	419.19	141.84	32.04	3.32	1.33	1.29
P <sub>2</sub> 14	149.64	249.63	419.50	142.31	31.97	3.29	0.95	1.34
P <sub>2</sub> 15	149.73	249.31	419.38	141.79	32.18	3.34	1.16	1.37
P <sub>2</sub> 16	149.78	250.16	420.35	142.08	31.94	3.36	1.08	1.45
P <sub>2</sub> 17	149.7	250.05	416.93	141.97	31.98	3.35	1.00	1.45
P <sub>2</sub> 18	149.75	249.74	417.44	141.75	32.07	3.37	1.08	1.45
P <sub>2</sub> 19	149.64	249.33	427.09	142.09	32.42	3.25	0.99	1.02
P <sub>2</sub> 20	149.6	249.24	426.28	142.01	32.34	3.23	0.91	1.05
P <sub>2</sub> 21	149.6	248.93	426.61	142.07	32.28	3.22	0.99	1.02
P <sub>2</sub> 22	149.83	249.70	427.35	142.08	32.35	3.24	1.28	1.54
P <sub>2</sub> 23	149.7	249.59	424.61	141.49	32.56	3.22	1.33	1.49
P <sub>2</sub> 24	149.88	249.14	424.51	141.38	32.54	3.29	0.93	1.47
P <sub>2</sub> 25	149.65	250.12	424.97	140.71	32.70	3.26	0.88	1.75
P <sub>2</sub> 26	149.79	249.95	422.83	140.65	32.80	3.28	1.63	1.74
P <sub>2</sub> 27	149.81	249.53	423.13	141.10	32.69	3.26	0.95	2.43



Table 5.5: Assessment of the predictive models and statistical significance of the factors and/or their interaction.

			First diameter	Cone angle	Final thickness	Outer surface roughness
<b>Assessment of the predictive model</b>	<i>SSE</i>		0.31	0.12	0.01	0.22
	$s_\varepsilon$		0.12	0.08	0.02	0.10
	$R_{adj}^2$ (%)		92.43	91.24	81.05	90.25
	F-value of the model		106.84	55.18	36.29	81.21
	Critical F-value	At 95 %	3.03	2.68	3.40	3.03
		At 99 %	4.76	4.04	5.61	4.76
	Confidence interval at 95 % *		± 0.11	± 0.10	± 0.02	± 0.11
Prediction interval at 95 % *		± 0.26	± 0.19	± 0.04	± 0.23	
<b>Statistical significance of the factors and/or their interactions</b>		<i>F</i>	209.74	10.16	39.19	112.45
		<i>Su</i>	102.95	8.49	/	/
	F-value	<i>L</i>	7.83	206.91	74.02	22.55
		<i>FL</i>	/	48.84	/	5.43
		<i>Su.L</i>	/	6.34	/	/
	Critical F-value	At 95 %	4.28	4.32	4.26	4.28
At 99 %		7.88	8.02	7.82	7.88	
<b>Optimisation of the output value</b>	Target value*		247.00	31.50	3.14	Minimum
	Best possible fit*		248.84	31.90	3.22	0.92
		<i>F</i>	0.6	1.0	0.6	0.6
	Optimised values	<i>Su</i>	480	300	/	/
		<i>L</i>	1	0	1	0

\* The values given are in millimetres with the exception of the cone angle and surface roughness, which are in degree and micrometres respectively.

$$\text{First diameter (mm)} = 249.264 - 0.003Su + 1.973F - 0.132L \quad (5.1)$$

$$\begin{aligned} \text{Cone angle (mm)} = 31.919 + 0.001Su - 0.359F - 0.201L - 0.001Su \cdot L \\ + 1.320F \cdot L \end{aligned} \quad (5.2)$$

$$S \text{ (mm)} = 3.203 + 0.144F - 0.069L \quad (5.3)$$

$$R_o \text{ (\mu m)} = 0.012 + 1.508F - 0.143L + 0.469F \cdot L \quad (5.4)$$

As illustrated in Figure 5.2, the results showed that the first diameter increased with  $F$  and/or a decrease of  $Su$  and/or  $L$ . Using a low feed rate at the first contact point was necessary in order to obtain the appropriate diameter.

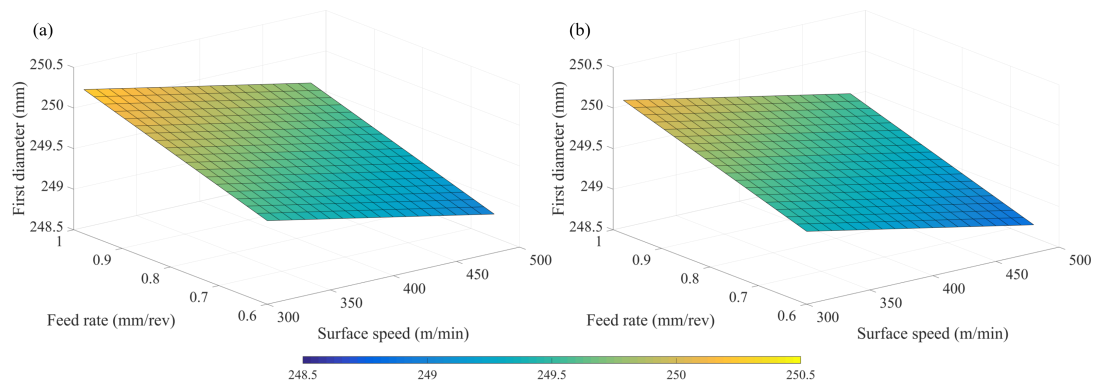


Figure 5.2: Surface plot of the predictive numerical model for the first diameter (a) with coolant and (b) with lubricant.

The different behaviours of the cone angle are given in Figure 5.3. When  $L$  was set at 0, the cone angle rose for an increase of  $Su$  and/or a decrease of  $F$  whereas when  $L$  was set at 1, the cone angle was insensitive to  $Su$  and increased with increasing  $F$ . By opposition to the optimisation of the first diameter, a high feed rate was required for optimising the cone angle.

As illustrated in Figure 5.4, at approximately a third of the cone length, the thickness was consistently noted to be a few tenths of a millimetre lower than average independently of the KPVs. The thickness typically reached its maximum at the end of the process and its average was generally greater than the thickness expected when using the sine rule. Increasing  $F$  led to a higher average thickness and a variation of about 0.07 mm was observed depending on the presence of lubricant as seen in Figure 5.5.

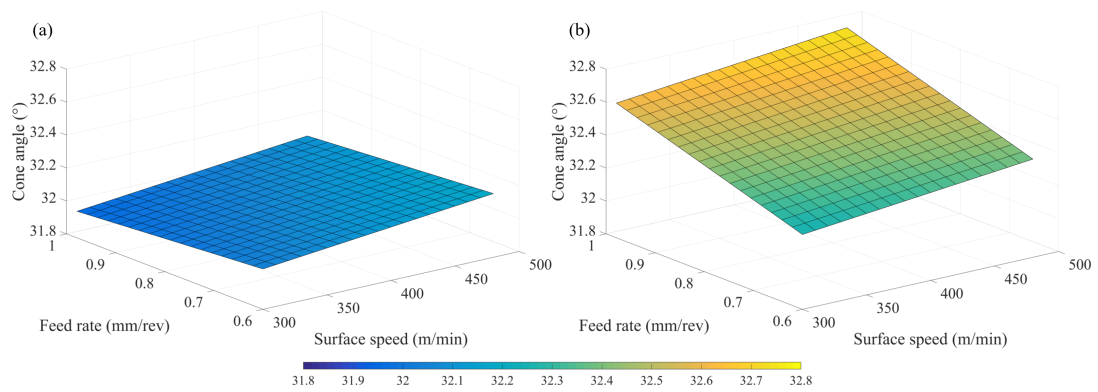


Figure 5.3: Surface plot of the predictive numerical model for the cone angle (a) with coolant and (b) with lubricant.

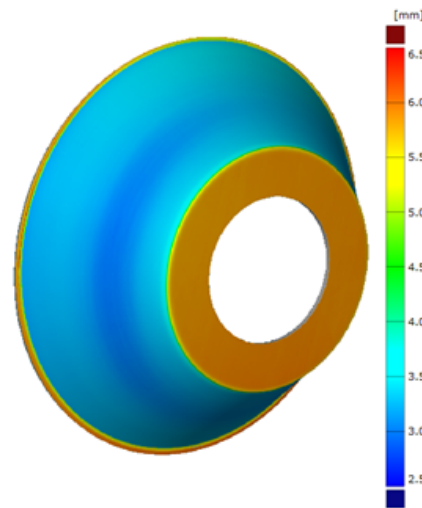


Figure 5.4: 3D visualisation of the variation of the thickness along the part using ATOS III Triple Scan.

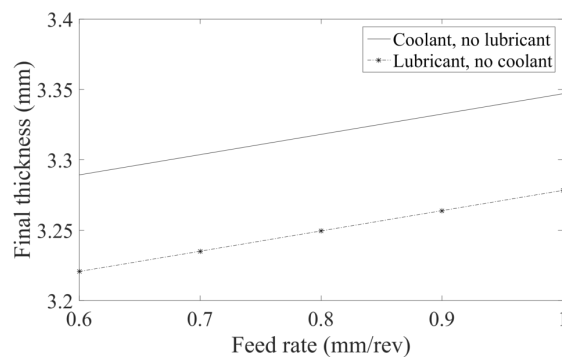


Figure 5.5: Plot of the predictive numerical model for the final thickness.

The roughness measurements were less than  $3.2\ \mu\text{m}$  and hence met Rolls-Royce's requirement. According to Appendix C, Subsection C.4.1 (p. 175), an uncertainty band of  $\pm 0.1\ \mu\text{m}$  was judged appropriate for the measurements of the roughness. As the confidence interval of the predictive model was almost equal to this uncertainty band, it was advised to use the model cautiously. As illustrated in Figure 5.6, the outer surface roughness was consistently reduced when shear forming with coolant and/or with a lower feed rate. Conversely, no significant effects of the KPVs were noted for the inner surface roughness.

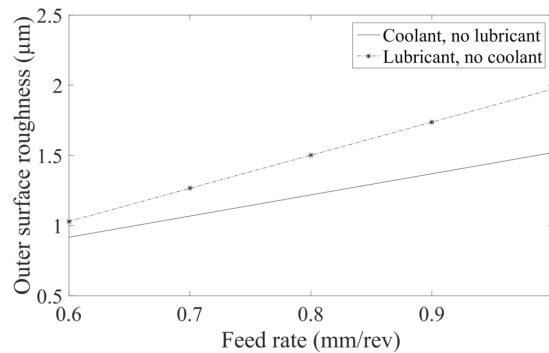


Figure 5.6: Plot of the predictive numerical model for the outer surface roughness.

## 5.3 Metallurgical work

To enable better understanding of the material behaviour during the shear forming process, the microstructure and texture were observed in the areas of interest described in Figure 4.1 (p. 53). The samples were prepared for observation as described in Appendix C (pp. 162–165). SEM using EBSD techniques was utilised. The hardness measurements were taken as described in Chapter 4 (pp. 53–54). The chemical composition and mechanical properties of the as-received sheet are given in Tables 5.6 and 5.7.

Table 5.6: Chemical composition (% by mass) of the 304L as-received sheet.

Material	Heat number	Chemical composition (%)							
		C	Cr	Mn	N	Ni	P	S	Si
304L	C4AW	0.018	18.050	1.773	0.067	8.035	0.031	0.002	0.449

Table 5.7: Mechanical properties of the 304L stainless steel as-received sheet.

Ultimate tensile strength	Yield strength at		Elongation after fracture		Vickers hardness
	0.2 %	1 %	A50	A5	
635 MPa	348 MPa	391 MPa	52 %	53 %	186 HV1

### 5.3.1 As-received material

From EBSD analysis it was estimated that the as-received material, represented by area M1, had approximately equiaxed grains with an average grain size of 11.3  $\mu\text{m}$  with 70 % of the grains being greater or equal to 10.0  $\mu\text{m}$ . The initial material was heterogeneous and its microstructure is given in Figure 5.7.

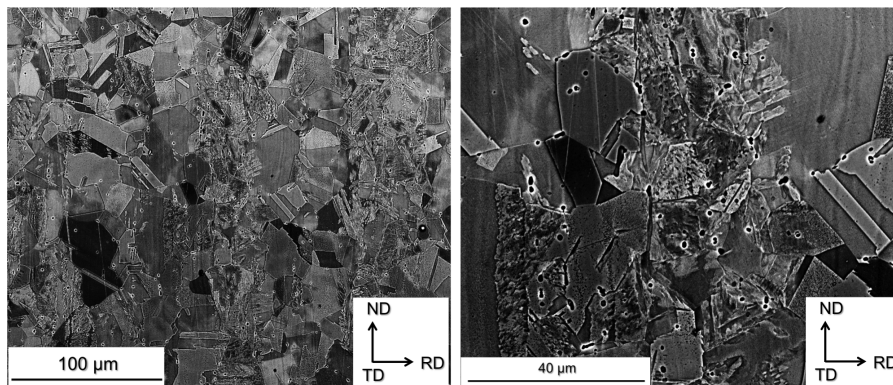


Figure 5.7: BS micrographs of the as-received material – area M1 of part P27.

According to Kumar et al. (2004), the PFs  $\{111\}_{\text{FCC}}$  and  $\{110\}_{\text{BCC}}$  of rolled 304 stainless steel should both have two elements at each side of the centre (right and left for the orientation shown in Figure 5.8) and a third one in the centre for the martensite, which was only partially apparent in this study. Furthermore, the ODFs did not reveal any strong components for  $\Phi_2 = 0^\circ$  and  $\Phi_2 = 45^\circ$  as should have been expected. The as-received material had a relatively weak rolling texture, which was not surprising as hot rolling was performed followed by solution treating.

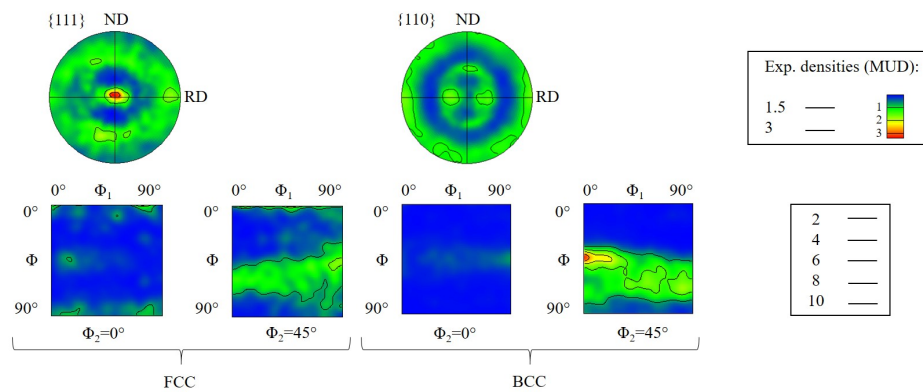


Figure 5.8: Texture of the as-received material along the slip planes for the two phases – area M1 of part P<sub>27</sub> (top: PFs, bottom: ODFs).

### 5.3.2 Shear formed material

Parts P<sub>21</sub>, P<sub>23</sub>, P<sub>27</sub>, P<sub>29</sub>, P<sub>219</sub>, P<sub>221</sub>, P<sub>225</sub>, and P<sub>227</sub> were selected to create a small factorial DoE composed of the lowest and highest levels of process parameters employed (see Table 5.1). The shear formed areas M2–M5 presented elongated grains and only slight microstructural differences were noticed within the same part. As a result, only the micrographs obtained for these parts in areas M3 (shear formed area) and M5 (transition area) are given in Figures 5.9 and 5.10 where the images are taken perpendicular to the rolling direction. Shear bands representative of high local deformation during plastic deformation were observed. They presented primary orientations along the  $\theta$  axis of the cylindrical coordinates and slightly tilted from the shear forming direction. These aligned shear bands were ascertained with a principal spacing around 1  $\mu\text{m}$ . A change of the microstructure between parts was noted. For instance, P<sub>23</sub> presented shear bands in the two orientations mentioned above whereas P<sub>225</sub> only had shear bands slightly tilted from the shear forming direction with the exception of area M3 where a few along the  $\theta$  axis were observed. The effect of KPVs could not be identified clearly for these eight parts just by using pictures. Further work, such as the acquisition of EBSD maps, would be required to be certain, which is the work presented in Chapters 6 and 7.

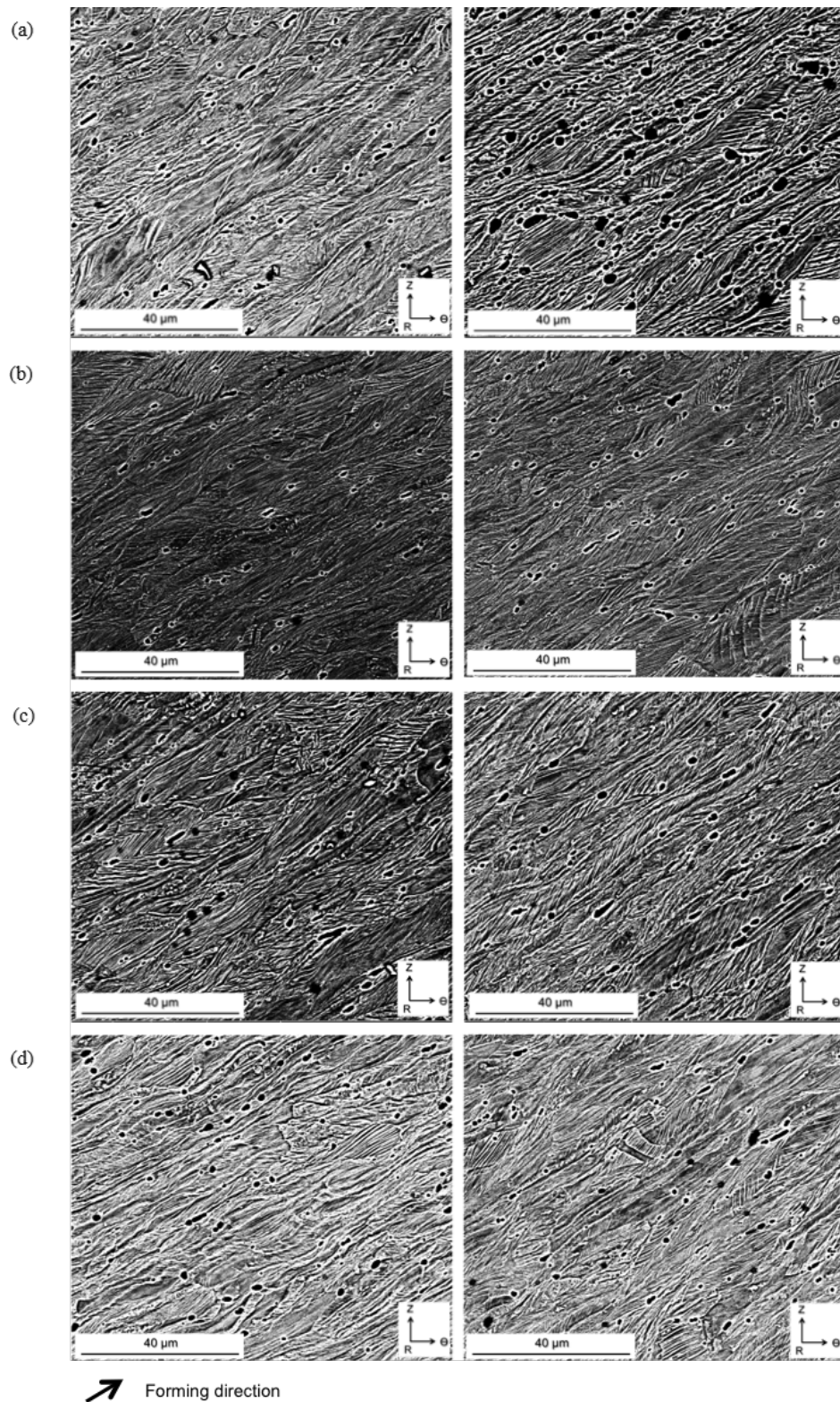


Figure 5.9: BS micrographs of the shear formed material – areas M3 (left) and M5 (right) for parts (a) P<sub>21</sub>, (b) P<sub>23</sub>, (c) P<sub>27</sub>, and (d) P<sub>29</sub>.



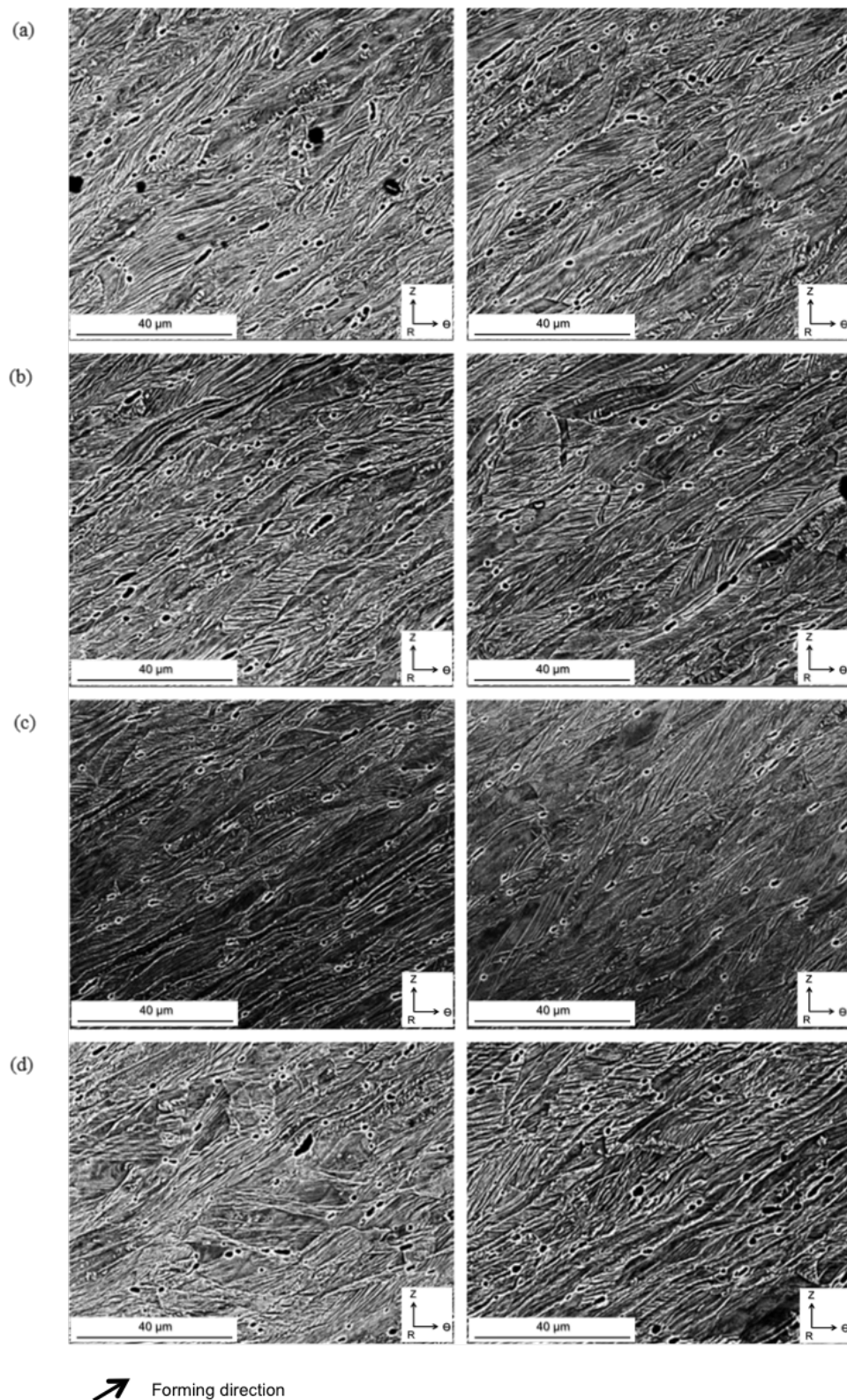


Figure 5.10: BS micrographs of the shear formed material – areas M3 (left) and M5 (right) for parts (a) P<sub>219</sub>, (b) P<sub>221</sub>, (c) P<sub>225</sub>, and (d) P<sub>227</sub>.



According to the pictures, it seemed that the mechanism of deformation was simple shear. Simple shear is defined as a specific mechanism of deformation, which is detected when one direction of the initial material which is free to rotate on both ends remains constant and everything else rotates relative to it. Figure 5.11-(a) illustrates this phenomenon with the transformation of a square to a rhombus along with the rotation of the ellipsoid axes from their original position, which is another characteristic of simple shear. This mechanism was identified on the BS images of Figures 5.9 and 5.10 where elongation of the grains and shear bands along the main ellipsoid axis can be seen. Although the actual stress-strain state in the material can be significantly triaxial and complex, the process model can be simplified assuming that at each contact between roller and material only elementary simple shear takes place. In this case, the intensity of this shear,  $\gamma$ , can be estimated as  $\alpha$  tangent. Figure 5.11-(b) is the plot of the shear as a function of the cone angle. The shear for the current geometry was about  $\gamma = 1.6$ .

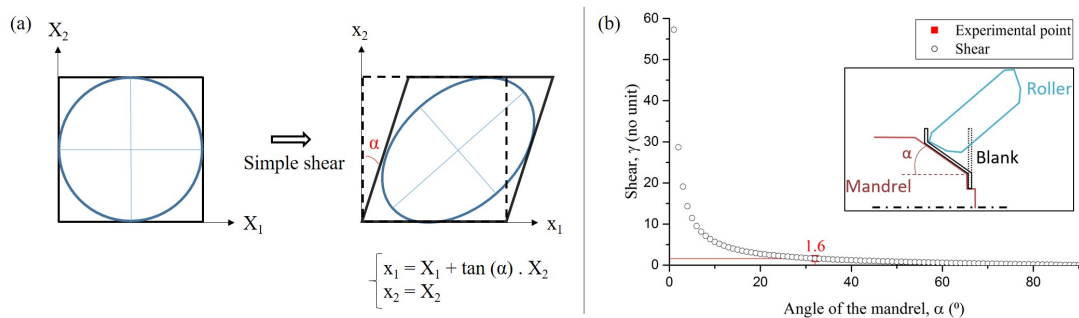


Figure 5.11: Simple shear: (a) illustration of the principle and (b) plot of the shear as a function of the cone angle.

An EBSD map was acquired for P<sub>27</sub> in the middle of the thickness of area M4 and an austenite to martensite transformation was observed. Figure 5.12 gives the PFs. According to the Kurdjumov-Sachs orientation relationship, the plane  $\{111\}_{\text{FCC}}$  is parallel to  $\{110\}_{\text{BCC}}$ . This could be seen in these specific PFs as the same elements were in the same areas, which was characteristic of shear transformation. This transformation of austenite to martensite was also proved by the part becoming magnetic. By comparing the PF  $\{111\}_{\text{FCC}}$  to the PFs presented by Barnett and Montheillet (2002), an equivalent strain of about 1.7 was identified. A few of the main torsion texture components, which are defined in Figure 5.13, were noticed on the PFs  $\{111\}$ . ODFs were calculated to look at this deformation in more detail. In

the case of simple shear deformation, the specific components B and  $\bar{B}$  are identified on ODFs displayed at  $\Phi = 55^\circ$  and  $\Phi_2 = 45^\circ$ . They are generally observed for these settings at  $\Phi_1 = 0^\circ, 120^\circ, 240^\circ$  and  $\Phi_1 = 60^\circ, 180^\circ, 300^\circ$  for B and  $\bar{B}$  respectively (Mohamed Zaky Ahmed, 2009). Figure 5.12 gives the ODFs of the FCC and BCC phases. In both cases, the components B and  $\bar{B}$  were identified whereas the components  $A_1^*$ ,  $A_2^*$  and C only appeared clearly for the FCC phase. According to these results, the mechanism of deformation was identified as simple shear.

Area M4 was studied in more detail by acquiring EBSD maps at both surfaces of the sample. The PFs and ODFs are given in Figure 5.14. On average the amount of martensite phase observed on the roller contact face was 60 % greater than the amount observed on the mandrel contact face. The PFs of both surfaces showed some shear deformation, which was more significant on the surface in contact with the roller. For the surface against the mandrel, on the ODF of the FCC phase none of the B or  $\bar{B}$  components were identified and only the B components were noted for the BCC phase. For the surface in contact with the roller, for both phases, the components B and  $\bar{B}$  were clearly observed. For the FCC phase, even some  $A_1^*$  and  $A_2^*$  components were recorded. Furthermore, by comparing Figures 5.12 and 5.14, the density of distribution for the FCC and BCC phases appeared to increase from the roller surface to the surface in contact with the mandrel.

For the eight parts studied, some low-force hardness tests were performed to investigate any hardness changes across the part. The results for area M1, considered as the as-received material, met the value given by the material certificate in Table 5.7. The outcomes showed a variation within the part of 5 HV1 in the shear formed areas, which suggested that the microstructure was reasonably homogeneous in this area, as was borne out in Figures 5.9 and 5.10. The highest hardness values were recorded at the transition of as-received and shear formed areas with 370 HV1. Furthermore, the values observed were generally higher on the roller side whereas the mandrel side and middle of the sample had similar lower values, which confirmed that the amount of martensite and so the deformation were more significant on the roller side.

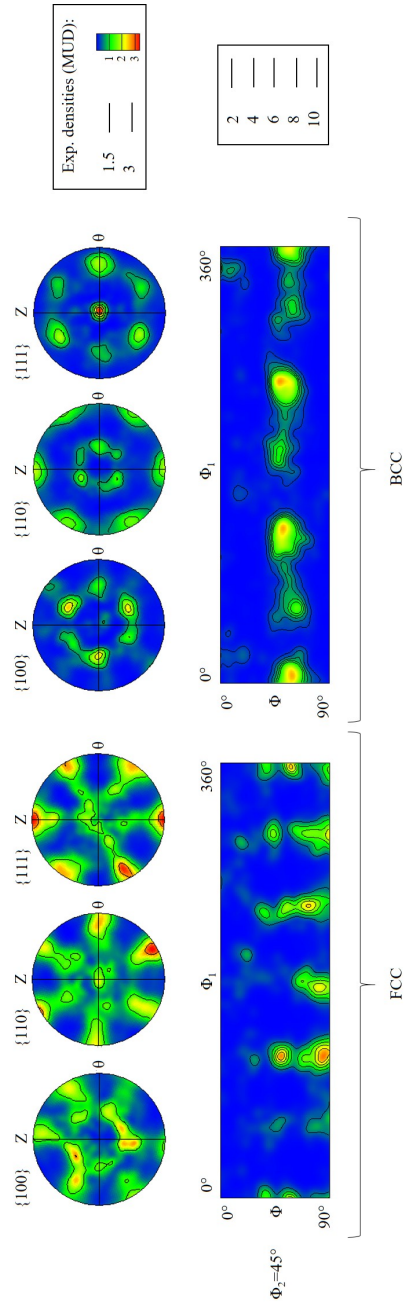


Figure 5.12: Texture representations for part P27 in the middle of the thickness of area M4 (top: PFs, bottom: ODFs).

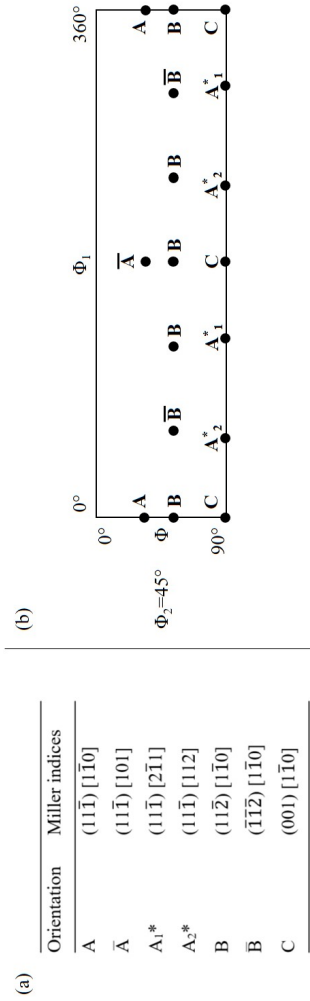


Figure 5.13: Main torsion texture components: (a) Miller indices and (b) Representation on ODFs – Adapted from Mohamed Zaky Ahmed (2009).

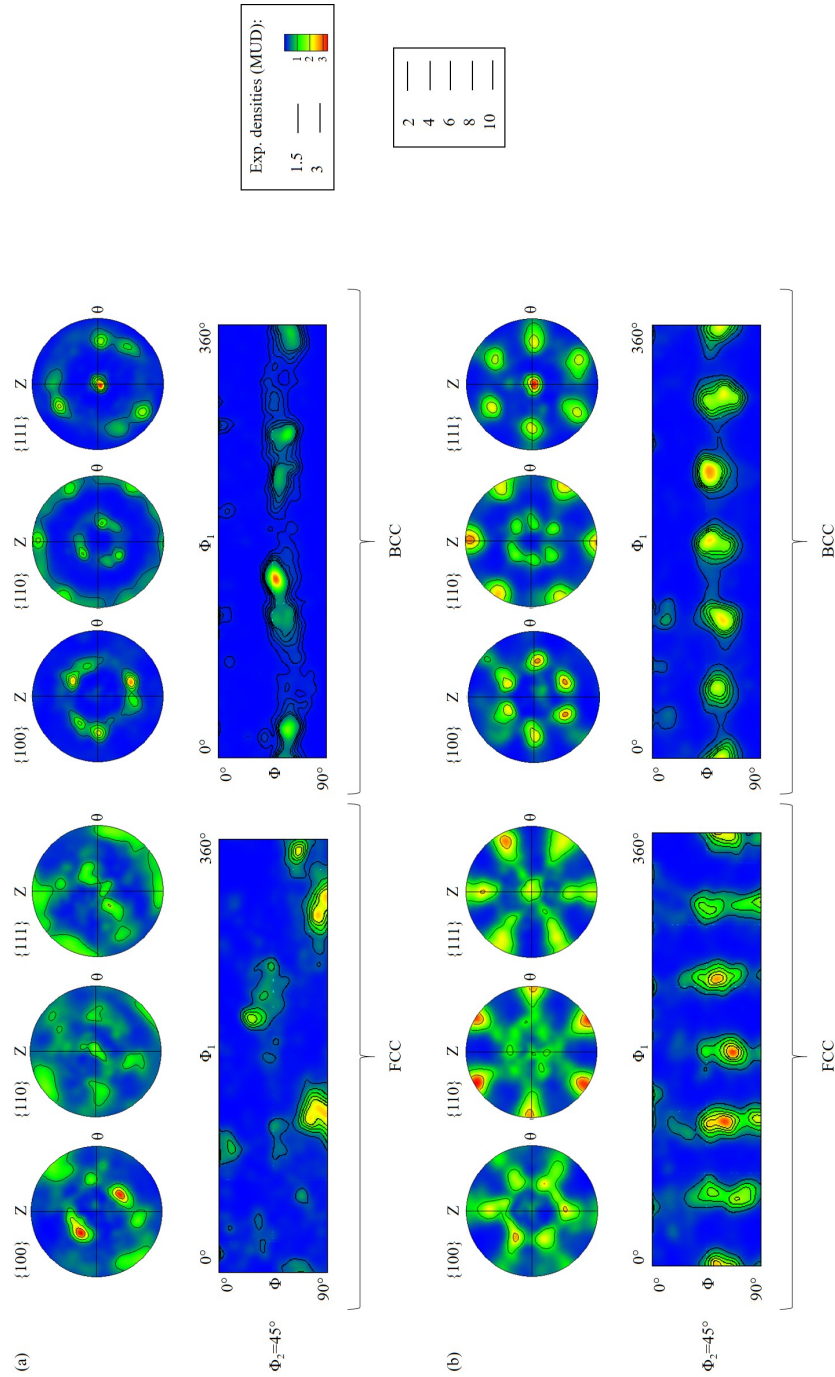


Figure 5.14: Texture representations for part P27 at the surfaces of area M4: (a) mandrel surface and (b) roller surface (top: PFs, bottom: ODFs).

A statistical analysis was performed on the hardness results in terms of average hardness value for this small factorial DoE. The prediction interval of the numerical predictive model obtained was as wide as the range of average value obtained therefore this model was discredited. However, it was noted that using painted on lubricant reduced the hardness of the part by 19.5 HV1 on average. Indeed, as efficient cooling helps the formation of martensite, which is much harder than the austenitic phase, lower hardness values were recorded when using painted on lubricant as no flooded coolants were utilised as recommended by the manufacturer.

## 5.4 Conclusions

The repeatability of the flow former was demonstrated to be good with variations of the cone angle and thickness of  $0.07^\circ$  and 0.06 mm respectively. According to the literature review, feeds and speeds are considered as KPVs, which was confirmed here. The feed rate was a significant factor for all the predictive numerical models generated. Using the established numerical predictive models, the optimisation of the outputs showed that a prioritisation of multiple features would be required as the optimised values were not always obtained with the same values of KPVs.

It was shown that accurate numerical predictive models link the geometry and the surface finish to the KPVs for this particular geometry and CNC program. When not using painted on lubricant the effect of the surface speed on the cone angle and final thickness were inverted and nullified respectively, which might have been due to the number of rollers utilised or the compelling effect of the lubricant. In all experiments completed to this point, the thickness across the part was inconsistent and greater than the expected value given by the sine rule. This was probably due to the choice of the gap between roller and mandrel or the textural state of the as-rolled material.

The surface roughness was overall considerably reduced by being shear formed, especially the outer roughness. As in the studies of Chen et al. (2001) and Kunert et al. (2005), decreasing the feed rate reduced the outer roughness. Conversely no effects of the spindle speed were recorded. This difference did not seem to originate from the difference of material, thickness or even the tool nose radius. The formula given by Runge (1993) was not material dependent and suggested that the impact of the spindle speed was the same for every set of parameters. Furthermore, in the study

of Chen et al. (2001) the thickness was taken into account and whatever its value, the same tendencies were observed. In the current study, the spindle speed was changing during the process to allow a constant surface speed which might have explained why the effect of the spindle speed on the outer surface finish was non-existent. The inner roughness was found to be independent of the feeds and speeds whereas the literature had shown a significant effect of the feeds in all cases. Furthermore, dimpled skin was noted on the inner surface of the part. This highlighted a lack of pressure between workpiece and mandrel, a phenomenon which according to the literature occurs when the gap between roller and mandrel is too large.

The initial material which presented relatively equiaxed grains evolved to a structure with elongated grains after being shear formed. During the forming operation, its hardness doubled to reach values around 370 HV1 mainly due to work hardening in which martensite transformation play a major part. High local deformation was observed in the form of shear bands along the  $\theta$  axis of the cylindrical coordinates and slightly tilted from the shear forming direction. Micrographs and hardness analysis showed a homogeneous microstructure along the shear formed length of the part. A transformation of austenite to martensite was observed. The primary mechanism of deformation was identified as simple shear thanks to experimental and theoretical shears and identification of the main torsion texture components on the PFs and ODFs for both FCC and BCC phases. Furthermore, an increased shear deformation was observed from the surface against the mandrel to the surface in contact with the roller. The neutral zone identified by Zhan et al. (2016) on 6 mm thick blanks of Al alloy was not observed even though the cone angle and feed rate employed were similar. It was unlikely to be due to the spindle speed and might have been down to the mechanical properties of the material.

The neutral zone identified by Zhan et al. (2016) on 6 mm thick blanks of Al-alloy was not observed even though the cone angle and feed rate employed were similar. The neutral zone might have not developed or the martensite transformation could have potentially masked it as relatively low strain was required for the shift from austenite to martensite to occur.

## Chapter 6

# Shear forming of Inconel 718

Chapter 6 presents the work undertaken on the shear forming of Inconel 718. In parallel with the present study, a Aerospace Technology Institute–Shear Forming project (ATI–SF) studied the roughness and geometrical outcomes as well as the microstructure of Inconel 718 parts using optical microscopy and hardness testing. The EngD project contributed to the ATI–SF mainly by enabling better understanding of the material behaviour through microstructure and texture analyses using SEM and EBSD techniques conducted by the author.

First, Chapter 6 describes the experimental work undertaken within the ATI–SF project that the author helped designed. The microstructure and texture of the as-received and as-formed materials are then detailed prior to and after heat treatment. Lastly, the results are discussed and compared with previous work and literature.

### 6.1 Experimental work

The ATI–SF experiments focused on  $20^\circ$ ,  $43^\circ$ , and  $53^\circ$  geometries. These cone angles were representative of the extreme and most common angles of typical conical parts used within gas turbine engines. Initial thicknesses of 6 mm and 12 mm were shear formed. The drawings of the final shear formed parts are given in Appendix E (pp. 198–204). For each geometry, the 6 mm thick blanks were shear formed following the same factorial DoE approach. The variables chosen were the spindle speed, feed rate, and roller nose radius. The first two KPVs varied from a constant 150 RPM to 450 RPM and 0.4 mm/rev to 0.6 mm/rev with increments of 150 RPM and 0.1 mm/rev.

The nose radius was either of 6 mm or 8 mm. Eighteen parts were therefore shear formed for each angle with a 6 mm initial thickness. Due to a limited number of 12 mm thick blanks, only two combinations of KPVs were tried for each angle – 150 RPM, 0.5 mm/rev with a nose radius of 6 mm then 8 mm.

## 6.2 As-received material

### 6.2.1 Before heat treatment

In this EngD project, the samples were prepared for observation as described in Appendix C (pp. 162–165). The parts were cut into five areas of interest, denoted M1–M5 as can be seen in Figure 4.1 (p. 53). The chemical composition and mechanical properties of the as-received sheets are given in Tables 6.1 and 6.2.

*Table 6.1: Inconel 718: Chemical composition of the different sheets.*

	Composition (weight, %)			Composition (weight, %)	
	6 mm thick	12 mm thick		6 mm thick	12 mm thick
Nickel	53.20	52.40	Manganese	0.24	0.23
Chromium	18.20	18.20	Silicon	0.09	0.04
Iron	Balance	18.60	Coper	0.05	0.05
Niobium + Tantalum	/	4.96	Carbon	0.34	0.32
Molybdenum	3.06	3.03	Phosphorus	<0.005	<0.005
Titanium	1.03	1.01	Sulfur	<0.002	<0.002
Aluminium	0.46	0.51	Boron	0.004	0.004
Cobalt	0.34	0.32			

For both thicknesses, the work undertaken in the ATI–SF study revealed that elongated grains were present in the rolling direction, which is typical of rolling structures. A mix of coarse and small elongated grains were observed in the rolling direction. This duplex banded structure was probably due to discontinuous dynamic and static recrystallisation at elevated temperatures (Perez and Konkova, 2015). A large amount of annealing twins was also observed. The microstructure morphology was similar in the different areas observed (Perez and Konkova, 2015).



Table 6.2: Inconel 718: Mechanical properties of the different sheets.

	Tensile test at room temperature		Tensile test at elevated temperature			Stress rupture temperature			Aged hardness	Grain size ( $\mu\text{m}$ )							
	$\sigma_u$ (MPa)	Elongation (%)	Temperature ( $^{\circ}\text{C}$ )	$\sigma_u$ (MPa)	$\sigma_u$ (MPa)	Elongation (%)	Temperature ( $^{\circ}\text{C}$ )	Stress (MPa)			Hours	Elongation (%)					
6 mm thick	889	410	49	1(A)	649	1162	1045	29	1(B)	649	724	450	57	1(B)	203 HV	1(A)	7.5
	1427	1200	21	1(B)	649	1151	1027	30	1(C)	649	724	189	56	1(C)		429 HV	1(B)
	1420	1151	22	1(C)													
12 mm thick	876	455	48	1(A)	649	1151	979	30	1(B)	649	724	182	35	1(B)	203 HV	1(A)	6.5
	1441	1220	21	1(B)	649	1124	931	33	1(C)	649	724	169	32	1(C)		418 HV	1(B)
	1420	1158	21	1(C)													

A) 941°C to 996°C  
 B) 941°C to 996°C; Step 1: 718°C, 8 h in air, furnace cool; Step 2: 621°C, 8 h in air, air cool total time: 18 h.  
 C) 941°C to 996°C; Step 1: 954°C, 1 h in argon, air cool; Step 2: 718°C, 8 h in air, furnace cool; Step 3: 621°C, 8 h in air, air cool total time: 18 h.

All aged test specimens were aged after final machining.

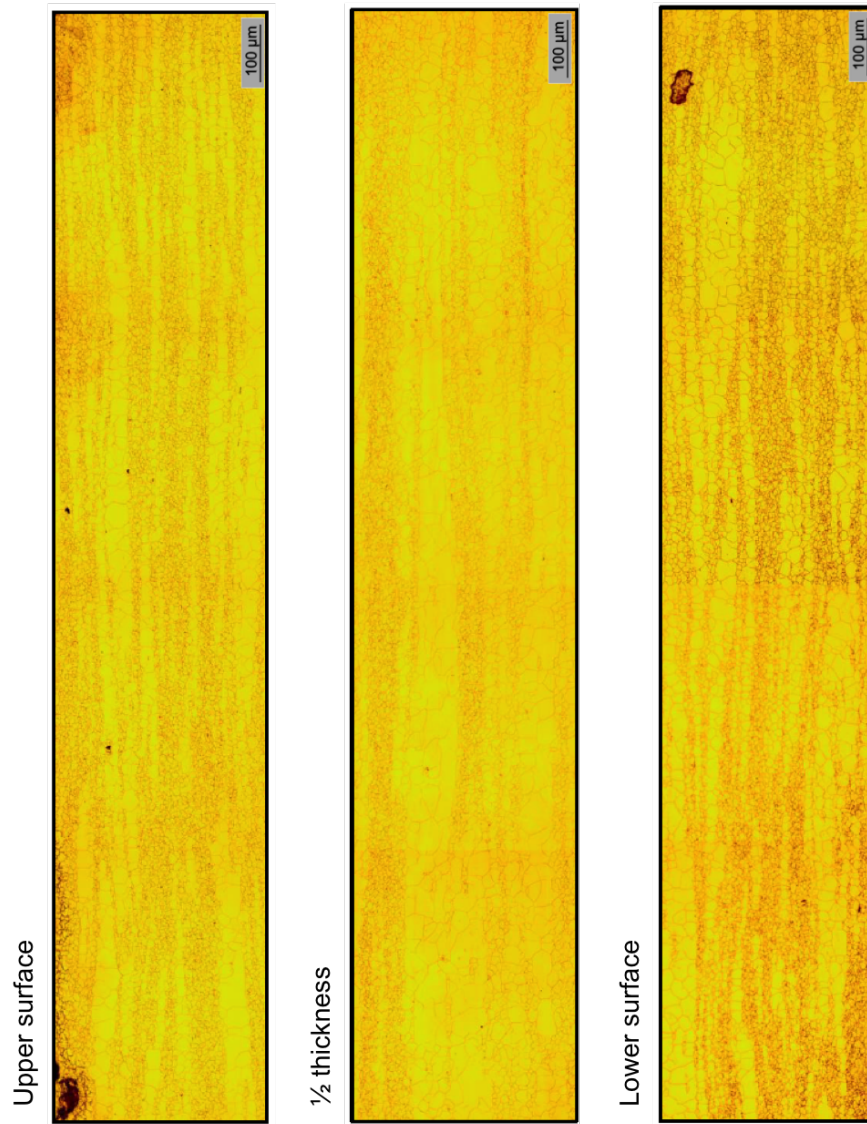


Figure 6.1: Optical micrographs of the 6 mm thick as-received material along the rolling direction (Perez and Konkova, 2015).

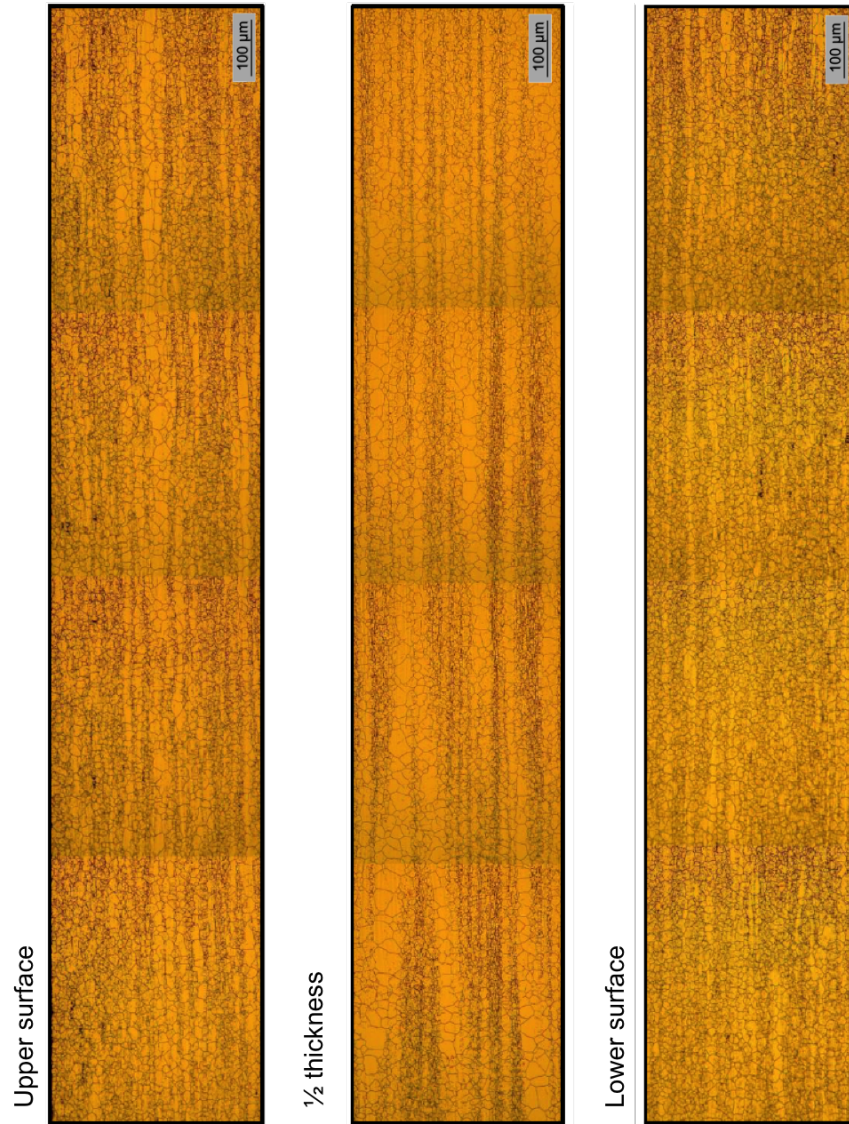


Figure 6.2: Optical micrographs of the 12 mm thick as-received material along the rolling direction (Perez and Konkova, 2015).

The average grain size was estimated to be about double the size given in the material certificates, i.e. larger grains were observed with 11.5–22.1  $\mu\text{m}$  and 9.0–18.7  $\mu\text{m}$  for the 6 mm and 12 mm thick sheets. These results were obtained by EBSD analysis considering the grain area instead of the grain diameter for enhanced accuracy as the grain aspect ratios were of 2.0 and 1.8 respectively.

Hardness measurements of 217–253 HV2 and 218–235 HV2 were recorded for the 6 mm and 12 mm thick sheets, which was about 10 % more than the values given in the material certificates. As shown in Figures 6.1 and 6.2, a higher level of deformation in the upper and lower thicknesses was noted with longer and thinner grains along the rolling direction in these areas.

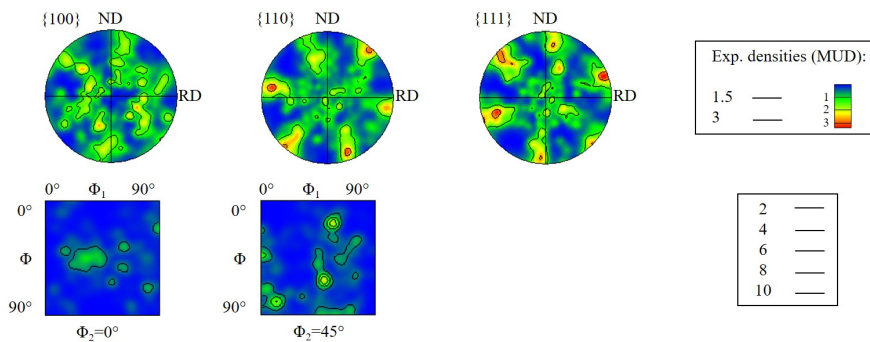


Figure 6.3: Texture of the 6 mm thick as-received material before heat treatment (top: PFs, bottom: ODFs).

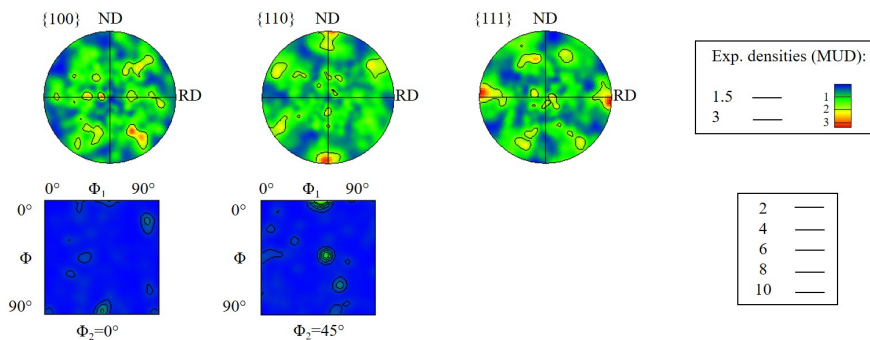


Figure 6.4: Texture of the 12 mm thick as-received material before heat treatment (top: PFs, bottom: ODFs).

The texture before heat treatment was illustrated by PFs and ODFs, as seen in Figures 6.3 and 6.4. The ODFs did not reveal any strong components for  $\Phi_2 = 0^\circ$  and



$\Phi_2 = 45^\circ$ . Hence the as-received material had a relatively weak rolling texture for both thicknesses, which was not surprising as hot rolling was performed followed by solution treating causing recrystallisation.

### 6.2.2 After heat treatment

After shear forming, the parts were heat treated. To meet the requirements of the material specification MSRR7116, the heat treatment performed was:

- Solution heat treating: 30 min  $\pm$  5 min at 980°C  $\pm$  10°C gas fan quench
- Double-step aging:
  - 8 h  $\pm$  15 min at 720°C  $\pm$  10°C vacuum cool at 50–60°C/h
  - 8 h  $\pm$  15 min at 620°C  $\pm$  10°C gas fan quench (Tuckwood, 2016a)

This heat treatment is common for Inconel 718 as presented in Chapter 3, Subsection 3.5 (pp. 46–48).

The grain size for the as-received material following heat treatment was estimated at 9.2–18.3  $\mu\text{m}$  and 12.9–18.8  $\mu\text{m}$  for the 6 mm and 12 mm thick sheets. These results were obtained by EBSD analysis considering the grain area instead of the grain diameter for enhanced accuracy as the grain aspect ratios were of 2.1 and 1.8 respectively. The grain size and aspect ratio before and after heat treatment were similar, but the duplex banded structure was not as pronounced after heat treatment as shown in Figure 6.5. Furthermore, the hardness almost doubled compared with the as-received material before heat treatment for both thicknesses (Konkova, 2015). The average volume fraction of the  $\delta$ -phase after heat treatment was of 0.19 %. These results were obtained using contrast image analysis from SEM pictures of each specimen at three different magnifications.

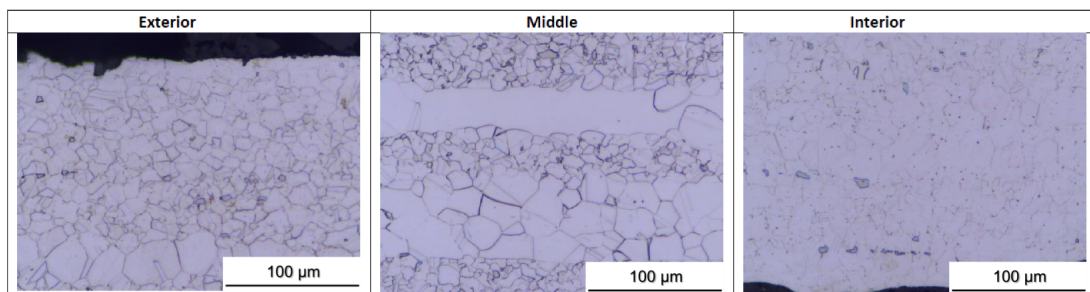


*Figure 6.5: Optical micrographs of the 6 mm thick as-received material after heat treatment along the rolling direction (Konkova, 2015).*

The texture after heat treatment was illustrated by PFs and ODFs, as shown in Figures 6.6 and 6.7. The texture components were weaker than before full heat treatment, which was expected. The ODFs did not reveal any strong components for  $\Phi_2 = 0^\circ$  and  $\Phi_2 = 45^\circ$ .

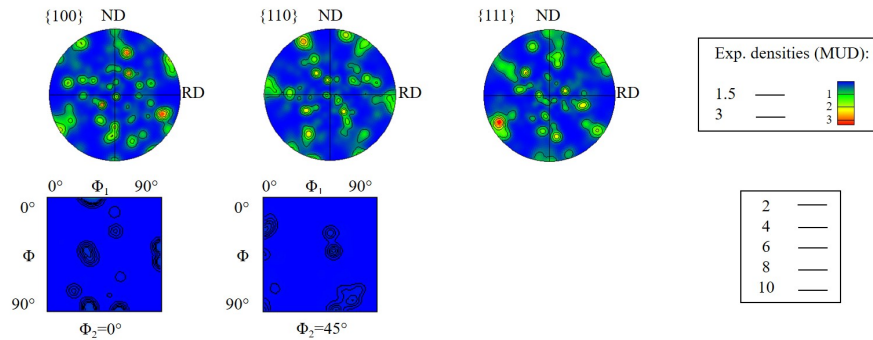


Figure 6.6: Texture of the 6 mm thick as-received material after heat treatment (top: PFs, bottom: ODFs).

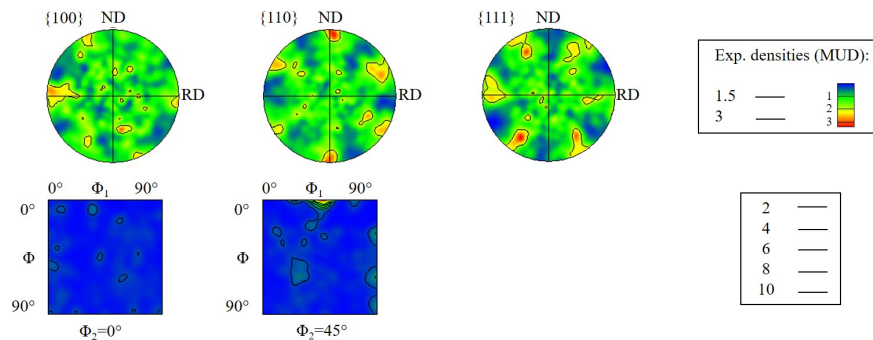


Figure 6.7: Texture of the 12 mm thick as-received material after heat treatment (top: PFs, bottom: ODFs).

## 6.3 Shear formed material

Across all shear formed parts the material flowed along the roller path, which was more apparent in the transition areas (M2 and M5). In these transition areas, the ATI-SF team clearly identified grain banding, which originated from the sheet material. This did not comply with the requirements of the material specification MSRR7116. Furthermore, microstructural inhomogeneities were noted across the different areas of a same part as well as across its thickness prior to and after heat

treatment. In the rolling direction, elongated grains were identified as well as small grains. The ATI–SF study concluded that the microstructure was probably driven by grain compression and that the intergranular shear bands were proof of shear mechanism (Perez and Konkova, 2015). The microstructure was classified as duplex with fine grains reaching 3.3  $\mu\text{m}$  and some coarse grains with a size of 65.8  $\mu\text{m}$ . A higher level of deformation at the surfaces in contact with the roller and mandrel was identified as finer grains were observed.

Hardness values in the shear formed areas M3 and M4 were similar and higher than in other zones. The lowest hardness value was observed in area M5. The results obtained in area M1 were comparable to the hardness observed on the as-received material. After heat treatment, smaller differences were observed but the same tendencies as before heat treatment remained.

### 6.3.1 Selection of parts

The work undertaken in the ATI–SF project revealed that the parts formed with a spindle speed of 150 RPM and a feed rate of 0.5 mm/rev had a better microstructure consistency. Although the impact of the feed rate, spindle speed, and roller nose radius was noted, not enough combination of KPVs were analysed to clearly determine their effects and interactions.

In this EngD project, to study further the microstructure after shear forming, eight Inconel 718 parts were selected as displayed in Table 6.3. This selection was based upon the mechanical tests undertaken in the ATI–SF project in order to link the results of these with the process parameters with minimal additional testing required from Rolls-Royce. The analysis of these eight parts helped establish the impact of the cone angle, initial thickness, and roller nose radius. As failure occurred on the 20° geometry while using the 8 mm nose radius, this part was not included in the study.

### 6.3.2 Before heat treatment

Figure 6.8 presents optical micrographs of part P<sub>Inco</sub>3 before heat treatment, on which the duplex microstructure is clearly identified. The grain size after shear forming was on average of 9.6  $\mu\text{m}$ , with a range of 4.5–13.4  $\mu\text{m}$ . Shear forming led to a reduction of the grain size compared with the as-received material. As described in

Chapter 4, Section 4.5 (pp. 61–62) a statistical analysis was undertaken. According to Equation 6.1, the average grain size was dependent on the cone angle and its square. The assessment and the statistical significance of the factors are given in Table 6.4. The smaller the cone angle was, the smaller the grain size became, which was explained by an increased deformation.

*Table 6.3: DoE employed for the microstructural analysis of the Inconel 718 shear formed parts.*

<b>Part identification*</b>	$\alpha$ (°)	$S_0$ (mm)	$\rho_R$ (mm)
P <sub>Inco</sub> 1	20	6	6
P <sub>Inco</sub> 2	20	12	6
P <sub>Inco</sub> 3	43	6	6
P <sub>Inco</sub> 4	43	12	6
P <sub>Inco</sub> 5	43	12	8
P <sub>Inco</sub> 6	53	6	6
P <sub>Inco</sub> 7	53	12	6
P <sub>Inco</sub> 8	53	12	8

\* P<sub>Inco</sub>: P for Part and Inco for set of experiments on Inconel 718

$$\text{Grain size before HT } (\mu\text{m}) = \sqrt{210.2 - 13.44 \text{ Cone angle} + 0.2318 \text{ Cone angle}^2} \quad (6.1)$$

The texture of areas M2–M5 was analysed using PFs and ODFs. As seen in Chapter 5 (p. 81), seven torsion texture components exist and were identified on the PFs and ODFs. The recorded intensity of these components was statistically studied, however, no significant impacts of the cone angle, initial thickness, and roller nose radius were demonstrated. An illustration of the texture obtained is given in Figure 6.9. The shear texture was generally more apparent in areas M4 and M5.



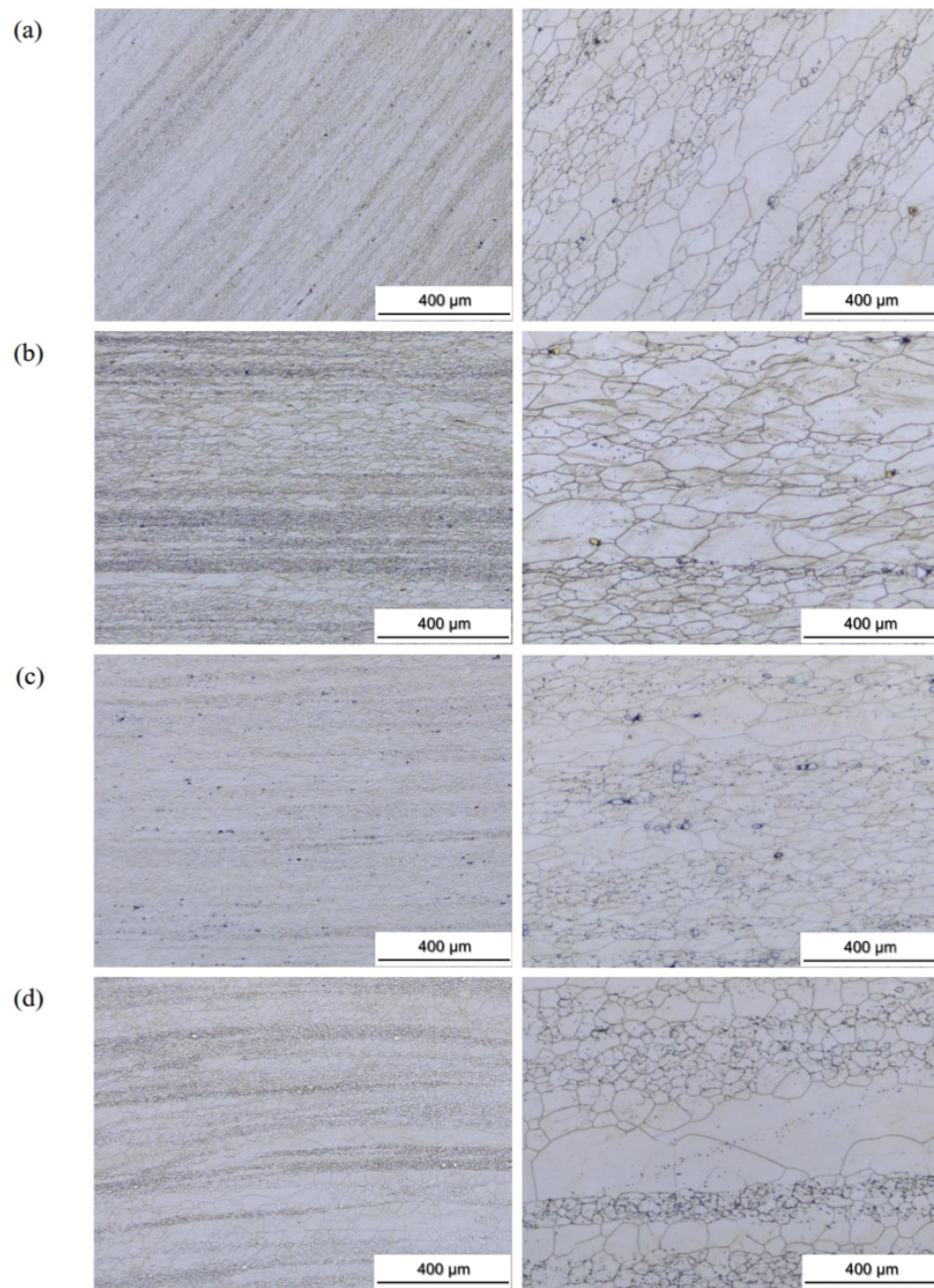


Figure 6.8: Optical micrographs of part  $P_{Inco3}$  before heat treatment in areas (a) M2, (b) M3, (c) M4, and (d) M5 (Konkova, 2015).

Table 6.4: Assessment of the predictive models and statistical significance of the factors and their interactions for the grain size and torsion component B.

Assessment of the predictive model	Grain size		Intensity of the torsion component B after heat treatment	
	prior to heat treatment	after heat treatment		
SSE	22159	49585	0.06	
$s_{\varepsilon}$	24.34	26.43	0.37	
$R_{adj}^2$ (%)	81.29	90.14	94.70	
F-value of the model	16.2	32.99	42.69	
Critical F-value	At 95 %	5.79	6.59	
	At 99 %	13.27	16.69	
Confidence interval at 95 % *	$\pm 36.12$	$\pm 39.22$	$\pm 0.63$	
Prediction interval at 95 % *	$\pm 72.24$	$\pm 78.45$	$\pm 1.22$	
Statistical significance of the factors	<i>Cone angle</i>	26.78	45.68	68.66
	<i>Cone angle</i> <sup>2</sup>	8.86	27.95	/
	<i>Thickness</i>	/	/	12.67
	<i>Cone angle.Thickness</i>	/	/	13.87
	At 95 %	6.61	6.61	7.71
	At 99 %	16.26	16.26	21.20

\* The values given are in micro-millimetres square for the grain size.

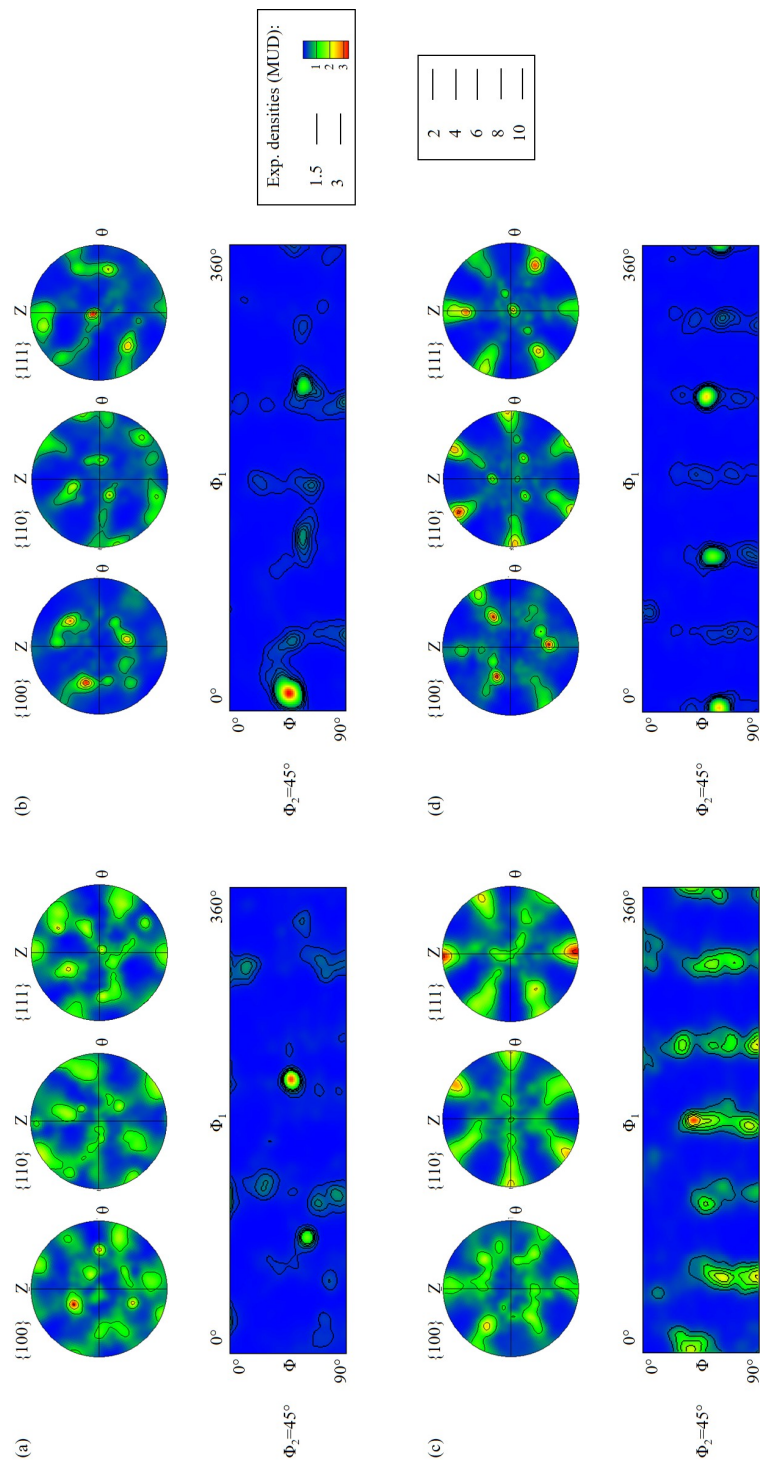


Figure 6.9: Texture of part  $P_{Inco3}$  before heat treatment in areas (a) M2, (b) M3, (c) M4, and (d) M5.

### 6.3.3 After heat treatment

The grain size after shear forming was on average of 10.9  $\mu\text{m}$ , with a range of 4.6–15.9  $\mu\text{m}$ . As shown in Figure 6.10, the duplex structure was still observed after heat treatment. The heat treatment led to a slight increase in grain size compared with the as-formed material. Statistical analysis was undertaken and according to Equation 6.2, the smaller the cone angle was, the smaller the grain size became as for the as-formed material. The assessment and the statistical significance of the factors are given in Table 6.4.

$$\text{Grain size after HT } (\mu\text{m}) = \sqrt{409.9 - 27.68 \text{ Cone angle} + 0.4469 \text{ Cone angle}^2} \quad (6.2)$$

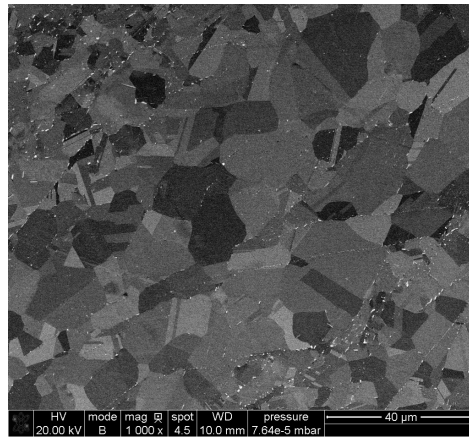


Figure 6.10: Backscattered micrograph of part  $P_{Inco3}$  after heat treatment in area M3.

Using contrast image analysis from SEM pictures of each specimen at three different magnifications, the amount of  $\delta$ -phase was recorded and analysed. Its average volume fraction was estimated at 0.49 % with values between 0.14 % and 1.25 %, however, no significant impacts of the cone angle, initial thickness, and roller nose radius were identified.

An illustration of the texture obtained is given in Figure 6.11. The shear texture was not as strong as before heat treatment, however, the texture of areas M2–M5 was still analysed using PFs and ODFs. As above, the intensity of the torsion components was statistically studied. According to Equation 6.3, the larger the cone angle was, the smaller the intensity of the torsion component B was, which was explained by a

reduction of the material deformation. It was found that for a cone angle of 23.5° or more, an increase of the initial thickness led to a reduction of the intensity of the component B when looking at the mid-thickness of the part. Below this value the tendency seemed inverted. The assessment and the statistical significance of the factors and their interaction are given in Table 6.4. No other links between process parameters and torsion components were found.

$$\begin{aligned} \text{Intensity component } B \text{ after } HT = & 3.90 + 0.0197 \text{ Cone angle} \\ & + 0.257 \text{ Initial thickness} - 0.01101 \text{ Cone angle} \cdot \text{Initial thickness} \end{aligned} \quad (6.3)$$

## 6.4 Conclusions

Although the microstructural assessment on the initial material revealed a non-conformity with the material specification MSRR7116 as a duplex microstructure was observed, the use of the material was considered suitable for shear forming applications within Rolls-Royce. As for the 304L stainless steel parts, after forming, the initial grains evolved to more elongated grains following the roller path. Moreover hardness increased. High local deformation was observed in the form of shear bands as previous, however, microstructural inhomogeneities were noted along the shear formed length. This could be explained by the lack of consistency observed in the initial sheets of Inconel 718.

Although the numerical predictive models of the grain size before and after heat treatment were poor (high sum of squares for error (*SSE*) and standard error of estimate ( $s_e$ )), the cone angle and its square were clearly identified as significant factors. The smaller the cone angle was, the more deformation was required leading to a smaller final grain size. This phenomenon correlated with the results of the work of Radović et al. (2012) on the shear forming of 3 mm thick Al-alloy.

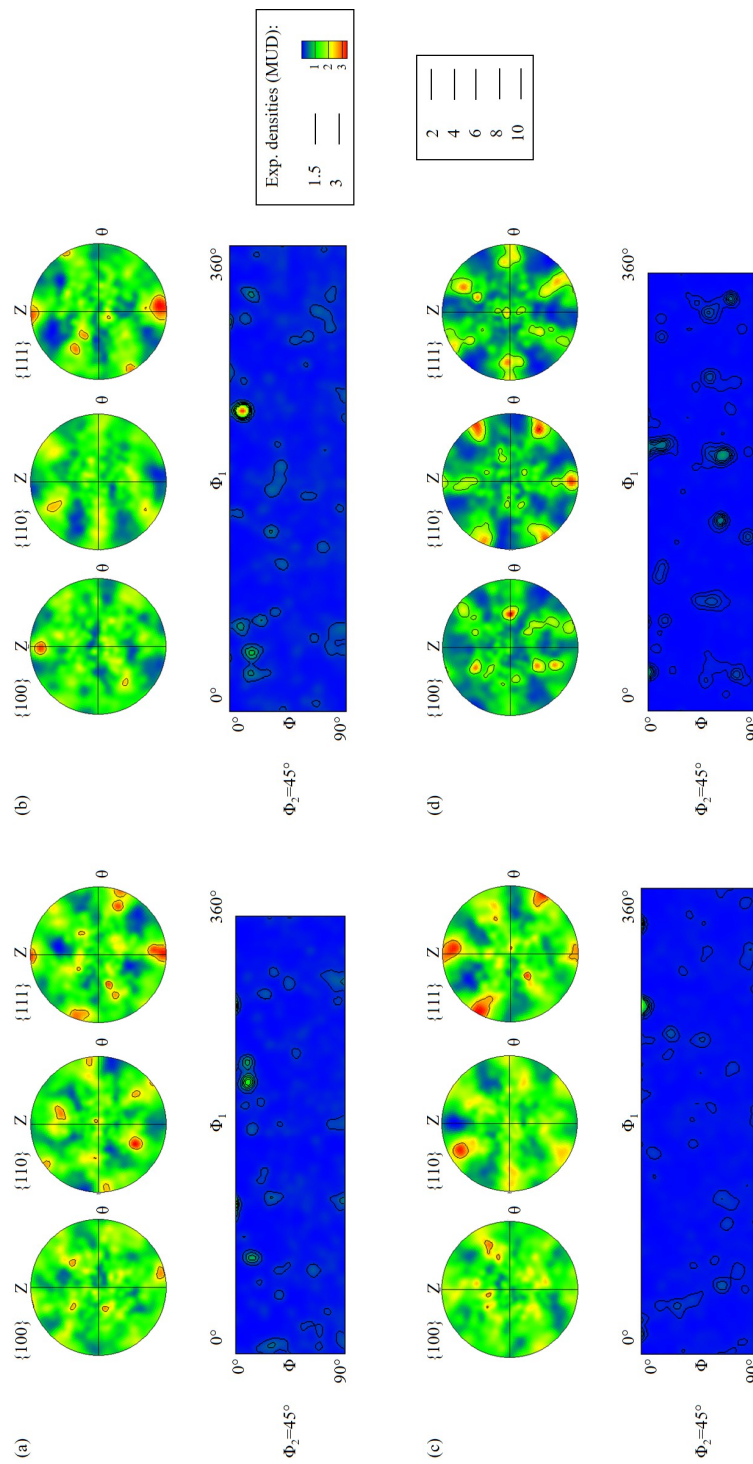


Figure 6.11: Texture of part  $P_{Inco3}$  after heat treatment in areas (a) M2, (b) M3, (c) M4, and (d) M5.



The texture analysis revealed as in Chapter 5 a simple shear deformation mechanism, the main torsion components being identified on the PFs and ODFs. Only the torsion component B was statistically linked to the cone angle, initial thickness, and their interaction. A larger cone angle led to a smaller intensity of B explained by a reduction of the material deformation. For cone angles larger than  $23.5^\circ$ , the intensity of B in the mid-thickness of the part decreased with an increased initial thickness. Interestingly, this phenomena was found to be inverted at angles under  $23.5^\circ$ . A potential explanation could be that the model established does not fit accurately such small angles where the deformation is significant. More runs at a cone angle of  $20^\circ$  or less could help reinforce this hypothesis.

Referring back to Chapter 3, the heat treatment operation after cold working is crucial for restoration processes to occur. In the current chapter it was clear that recrystallisation was promoted only after heat treatment. A slight grain growth was also noted, which was maybe limited by the original duplex microstructure. Not enough mechanical tests were performed in the ATI-SF project to link the final microstructure and texture to the mechanical properties. It is recommended that further mechanical testing is undertaken to have a better understanding of the shear forming process on the final mechanical properties of the part.

As described in Chapter 3, the control of the amount of  $\delta$ -precipitates was crucial as it could deteriorate the hardening of the material. Throughout the forming and heat treatment operations, less than 4% of  $\delta$ -precipitates was observed and so the heat treatment was considered adequate.

In this project, it was impossible to link the metallurgical outcomes to some of the KPVs considered as having significant impacts on the geometry and surface finish. In the future studying a potential link of such KPVs with the microstructural aspects would be of interest as at present this has not been studied and could help develop further the understanding of the shear forming process.

## Chapter 7

# Shear forming of thicker 304L stainless steel

Chapter 7 focuses on the forming of 304L stainless steel blanks with an initial thickness of 15 mm. The 43° geometry was selected to undertake this work as it corresponded to the most common angle of the Rolls-Royce's components targeted in the use of shear forming.

First, this chapter deals with the preparation required prior to forming. Secondly, the experiments undertaken are described. Then, statistical analyses of the surface roughness and geometrical outputs are introduced. The metallurgical work is presented in an additional section. Finally, a discussion around this stream of work is given.

### 7.1 Preparation prior to forming

The blanks and shear formed parts (Figures 7.1 and 7.2, pp. 103–104) were drawn in order to match the new starting thickness and geometry. The current 43° tooling was designed to enable the shear forming of initial thicknesses between 6 mm and 12 mm in order to meet the ATI-SF requirements. Consequently, to shear form thicker material with this tooling, a new mandrel insert and tailstock adaptor had to be designed and manufactured. The assembly drawing of the 43° geometry (Figure 7.3, p. 105) helps demonstrate the link between the mandrel (2), its insert (4), and the tailstock adaptor (7). The designs of the tooling, blanks, and shear formed parts are given in Appendix F (pp. 205–224). In the latter, the manufacture of the tooling is also detailed.



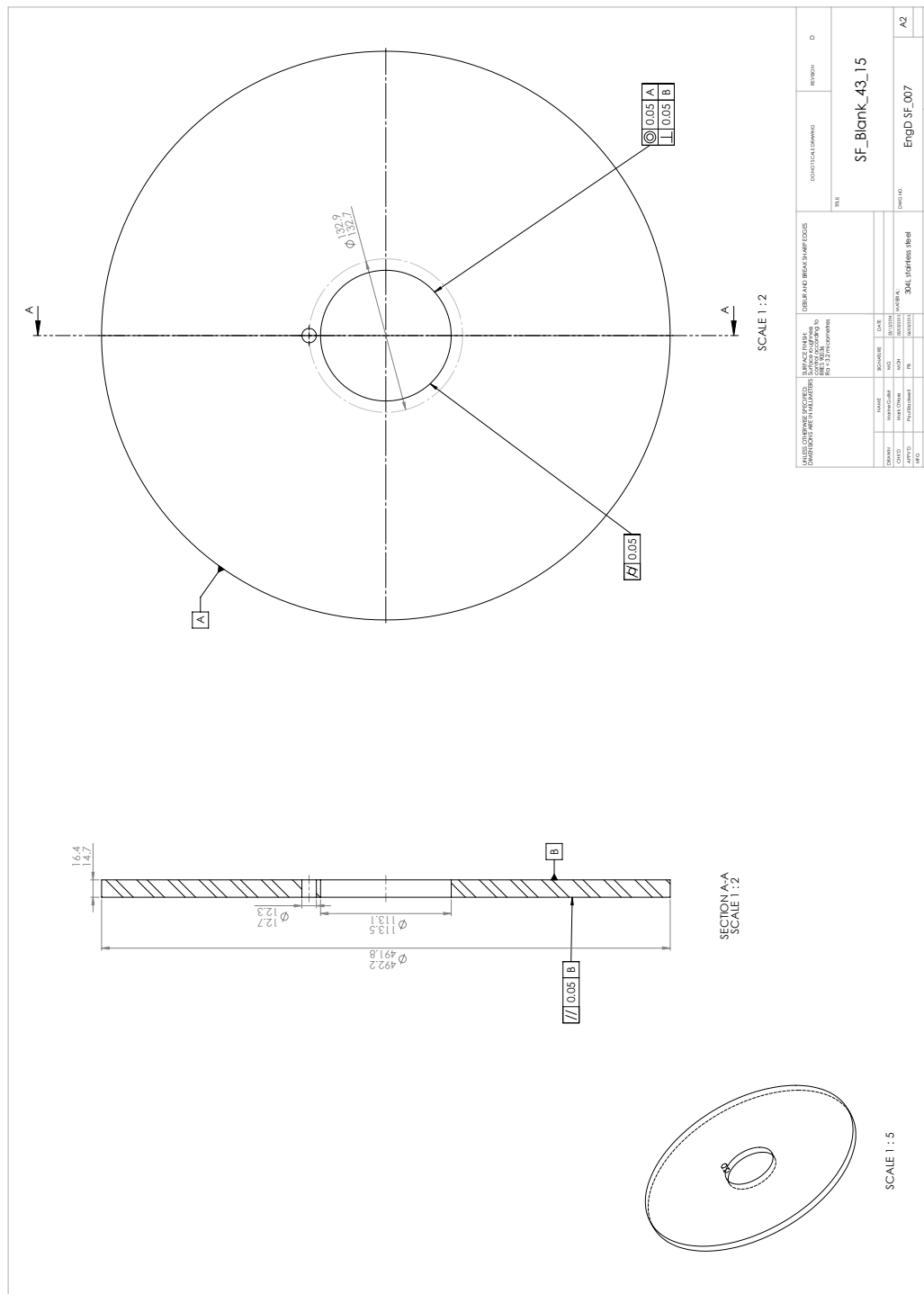


Figure 7.1: Drawing: Blank – 43°, 15 mm thick, EngD – EngD\_SF\_007, “SF\_Blank\_43\_15”.

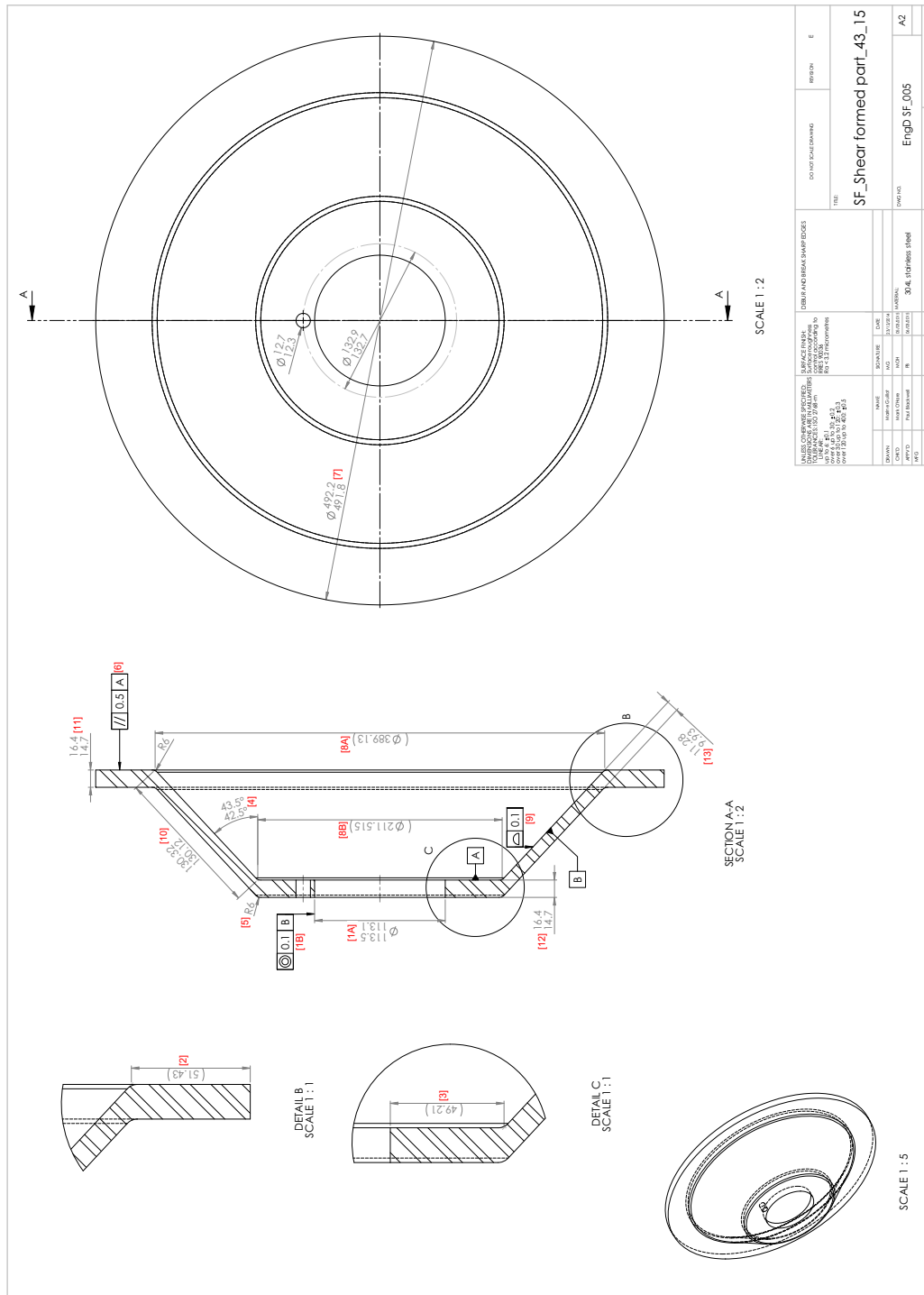


Figure 7.2: Drawing: Shear formed part – 43°, 15 mm thick, EngD – EngD SF\_005, “SF\_Shear formed part\_43\_15”.

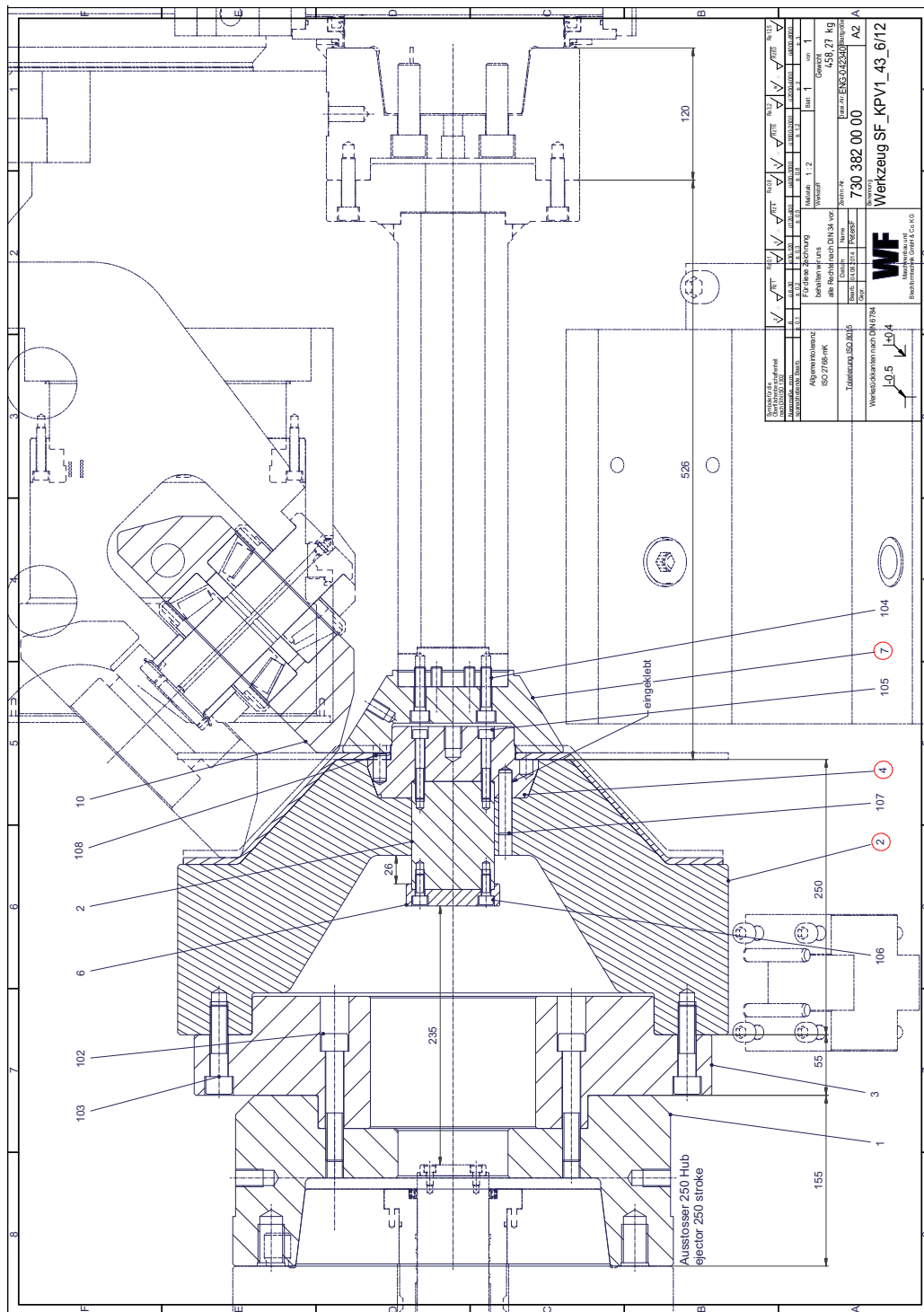


Figure 7.3: Assembly drawing – 43° geometry – 730 382 00 00, “Werkzeug SF\_KPV1\_43\_6/12” .

## 7.2 Experiments

### 7.2.1 Set-up

In the ATI–SF project, the set-up parts were usually completed with a feed rate ( $F$ ) of 0.5 mm/rev, a spindle speed ( $Sp$ ) of 150 RPM, and using a single roller with a 6 mm nose radius ( $\rho_R$ ). As a result, in this EngD project, for the set-up, the blanks were shear formed on the 43° geometry employing the 6 mm nose radius roller identified as SF60216003N and using these same process parameters.

The work completed in the ATI–SF project for the 43° geometry was used for guidance to estimate the compressive deformation previously defined in Equation 2.2 (Chapter 2, Subsection 2.4.1, p. 16) and the depth to add on the Z axis to form such a thickness. The added depth on the Z axis corresponds to how much further the roller has to travel towards the mandrel to reach the appropriate cone length. Subsection C.1.4.3 (pp. 158–160) provides more detail.

According to the report entitled TRP368\_KPV1 Trial outcomes (Tuckwood, 2016b), for Inconel 718 blanks with a starting thickness of 6 mm, the geometry was achieved by using a compressive deformation of 39.0 % and an added depth along the Z axis of 0.5 mm. In the ATI–SF project, it was found by experimental work that due to the nature of the material, the 304L stainless steel set-up parts had to be completed with a compressive deformation of 33.5 % and an added depth along the Z axis of 0.1 mm. For the thicker parts completed in the ATI–SF project on this same angle (KPV3), 304L stainless steel blanks with an initial thickness of 12 mm were shear formed with a compressive deformation of 40.5 % and an added depth along the Z axis of 2.5 mm.

An extrapolation of these results for the 15 mm thick 304L stainless steel blanks gave a compressive deformation and depth of 44.0 % and 3.55 mm respectively. During a dry run, such a deformation level was discovered to be impossible to achieve due to a collision between roller and tailstock adaptor. The first set-up part (S1) was then shear formed with a lower compressive deformation of 35.2 % to prove the formability of such a thickness. As this was a success, the outside diameter of the tailstock adaptor was machined down, allowing the second set-up part (S2) with a compressive deformation of 44.0 % to be formed. S1 and S2 were geometrically

checked using a CMM to understand the impact of the compressive deformation. If there is true shear forming, the final thickness should be exactly as defined in the sine rule. Using the measurements of the final thickness for parts S1 and S2, considering a cone angle of  $43^\circ$ , a relationship between compressive deformation and final thickness was established. This showed that the compressive deformation had to be set at 38.0 % for S3 in order to follow the sine rule. Table 7.1 is an extract of the geometrical measurements for these three set-up parts. Figure 7.2 (p. 104), a drawing of the 15 mm thick shear formed part, was labelled to help localise the elements of interest. The results presented in Table 7.1 showed that being closer to the sine rule also made other geometrical features better, such as the cone form, straightness of the shear formed length as well as the outer flange angle. According to these results, it was unnecessary to compress even as much as in the ATI-SF tests for the 12 mm thick 304L stainless steel blanks. For this reason, it was not essential to machine down the new tailstock adaptor. This was explained by the different aims of the EngD and ATI-SF projects. In the EngD project, the aim was to get close to true shear forming, i.e. close to the sine rule, whereas in the ATI-SF project the aim was to be within tolerance. S2 was completed with an added depth of 5.10 mm as the 3.55 mm extrapolated were not enough to obtain the shear formed length. Even if the compressive deformation employed was not optimum, it was concluded that this depth was still not long enough. Then four other set-up parts (S3 to S6) were completed with a 38.0 % compressive deformation and different depths in order to establish the ideal value. Table 7.2 gives the geometrical measurements of the relevant features for these parts. Using the results of the shear formed length, a trendline was created to fit the points. A polynomial equation of second order was found, from which the best depth to use was deduced, here 6.00 mm. However, the desired shear formed length of 130.22 mm could not be achieved with this distance. This was limited by the back face of the mandrel, as for the thick blanks shear formed in the ATI-SF trials.

Table 7.1: Set-up of parts S1–S3.

	Part identification		
	S1	S2	S3
1 Compressive deformation (%)	35.2	44.0	38.0
2 Initial thickness, $S_0$ [11] and [12] (mm)	15.24	15.20	15.25
3 Final thickness, $S$ [13] (mm)	10.70	9.74	10.46
4 Cone angle [4] (°)	43.17	42.67	43.23
5 Cone form [9] (mm)	0.45	0.24	0.11
6 Straightness (mm)	0.14	0.17	0.03
7 Outer flange angle (°)	0.99	0.71	0.11
8 Ideal final thickness, $S_1$ (mm)*	10.42	10.30	10.45

\* Row 8 = Row 2 x sin (Row 4)

[xx] Elements labelled on Figure 7.2 (p. 104)

Table 7.2: Set-up of parts S3–S6.

	Part identification			
	S3	S4	S5	S6
Depth (mm)	6.12	6.27	6.33	5.46
Cone form [9] (mm)	0.11	0.14	0.14	0.10
Final diameter [8A] (mm)	389.51	389.79	389.73	389.58
Shear formed length [10] (mm)	130.08	130.07	130.04	129.96
Outside diameter, $D_1$ [7] (mm)	493.86	494.65	494.51	494.12
Outer flange angle (°)	0.11	0.06	0.05	0.06

[xx] Elements labelled on Figure 7.2 (p. 104)

### 7.2.2 Choice of KPVs

For consistency of purpose, the selection of the KPVs had to be in the range of the ones used within the ATI–SF trials for KPV1. The CNC program is given in Sub-subsection C.1.4.3 (pp. 158–160). As mentioned in Chapter 6 (Section 6.1, p. 85),  $F$  and  $S_p$  were respectively set between 0.40 mm/rev and 0.60 mm/rev and

between 150 RPM and 450 RPM. The parts were shear formed using one roller only with a  $\rho_R$  of 6 mm or 8 mm. In KPV3, for the 43° geometry, due to the small amount of blanks available, only two values of  $F$  and  $Sp$  were employed, 0.50 mm/rev with 150 RPM and 0.60 mm/rev with 450 RPM. When forming the latter combination, a red circle appeared around the part at the point of contact with the roller, which was followed by failure as the roller became stuck to the part. Localised melting of the part was observed and hence temperatures around the melting point of Inconel 718 (1260–1336°C) were reached.  $Sp$  was judged too high. In consequence, lower values were employed in this project.

Table 7.3: KPVs employed for parts P1–P15b.

	Part identification	$F$ (mm/rev)	$Sp$ (RPM)	$\rho_R$ (mm)	
DoE	P1	0.60	240	6	Factorial DoE
	P2	0.40	120	6	Replicates
	P3	0.10	120	6	Additional parts
	P4	0.60	280	6	Failed parts
	P5	0.60	120	6	
	P6	0.10	280	6	
	P7	0.35	200	6	
	P8	0.60	200	6	
	P9	0.10	120	6	
	P10a	0.35	280	6	
	P10b	0.35	280	6	
	P11	0.35	120	6	
	P12	0.10	200	6	
	P13	0.60	120	6	
	P14	0.35	200	6	
	P00	0.35	185	6	
	P15a	0.10	280	8	
	P15b	0.10	280	8	

To select the range of  $F$  and  $Sp$ , six parts, denoted P1 to P6, were successfully shear formed using different values in order to see the impact on the roller loads, final

geometry, and surface finish of the final part. Table 7.3 lists the KPVs investigated in the order the parts were shear formed. Consequently, each of the factors  $F$  and  $Sp$  were chosen to be set at three levels; 0.10 mm/rev, 0.35 mm/rev, and 0.60 mm/rev, and 120 RPM, 200 RPM, and 280 RPM. The DoE was factorial in order to take into account the impact of each factor (linear and quadratic) as well as their interactions. To reinforce this experiment, the blanks were randomly formed. Furthermore, three of these previous combinations of  $F$  and  $Sp$ , randomly selected, were added to the DoE (parts P9, P11, and P14). Parts P1 to P6 were considered as part of the DoE with P1 and P2 being additional combinations of KPVs. Hence, the full DoE consisted of 14 parts ( $3^2 + 3 + 2 = 14$ ). P00 was a part run with constant spindle speed and P15a and P15b, parts unsuccessfully formed using a 8 mm nose radius roller. The drawings of the rollers are given in Figures 7.4 and 7.5.

### 7.2.3 Forming loads

Part P10b was successfully run with the same KPVs as P10a. Nevertheless, P15a and P15b both failed using the same KPVs. As the investigation of the potential reasons for these failures occurring was still ongoing, the experiments were stopped and no parts were successfully formed with  $\rho_R$  at 8 mm. This was also the reason why the blanks with a starting thickness of 20 mm were not shear formed.

The forming loads were recorded with SinuCom, a Siemens' software, using an interval of 0.04 s. Figure 7.6 (p. 113) shows an example of the roller radial and axial loads as a function of the time for part P1. The origin point (0,0) represented the first contact point roller/blank. Five stages seemed noticeable and could potentially be justified as follows:

- Start: During the first 5 s, the roller was pushing against the blank, but the blank had no points of contact with the conical face of the mandrel.
- Stationary state – axial load: At 5 s, the roller had moved along the Z axis by about half the initial thickness of the blank. The blank was now in contact with the roller and the conical face of the mandrel, which explained the increase in the loads. From that point, the same amount of material was locally pushed by the roller with no other interactions and so the axial load stabilised.



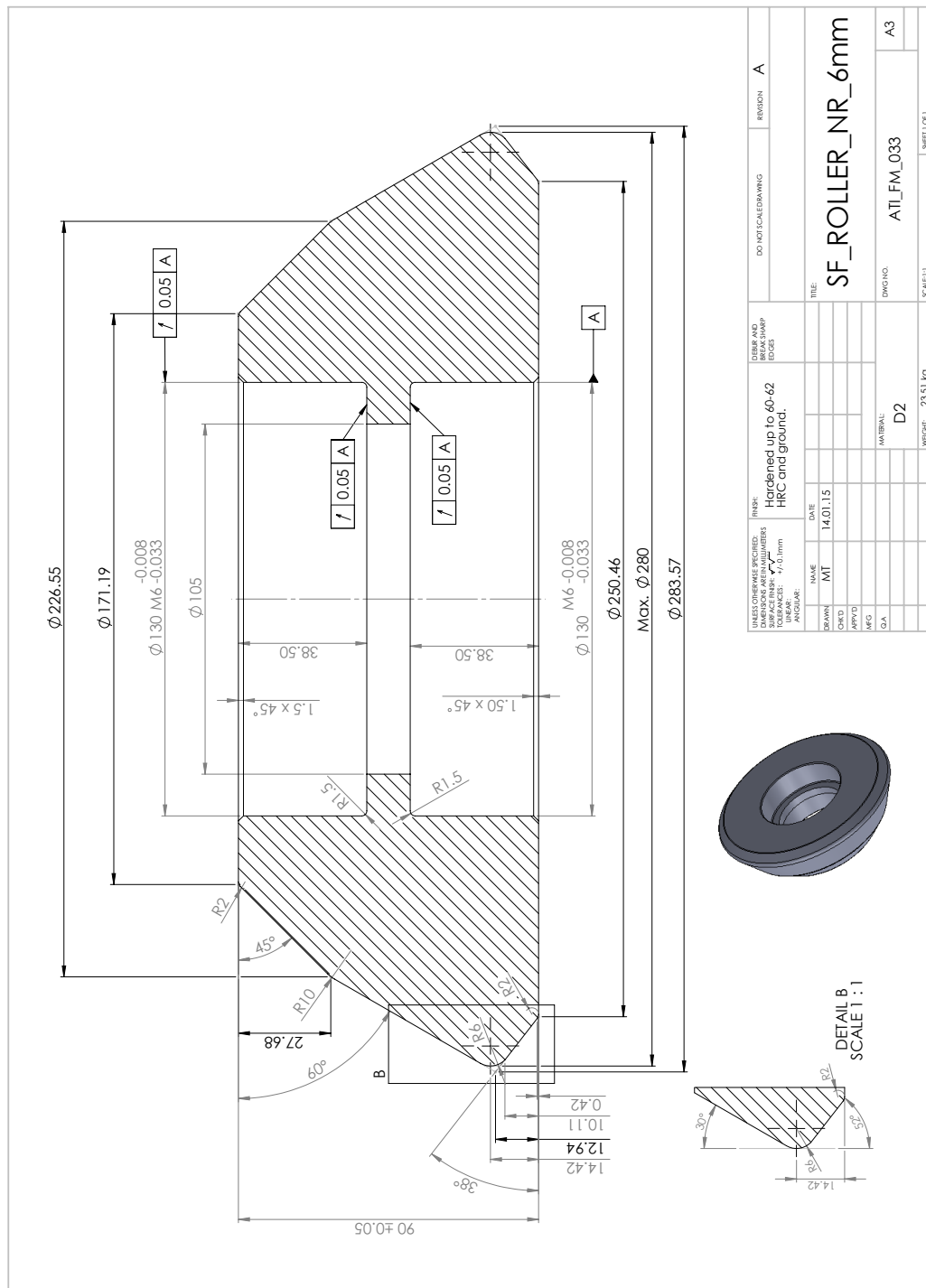


Figure 7.4: Drawing: 6 mm nose radius roller – ATI-SF – ATI FM 033, “SF\_ROLLER\_NR\_6mm”.

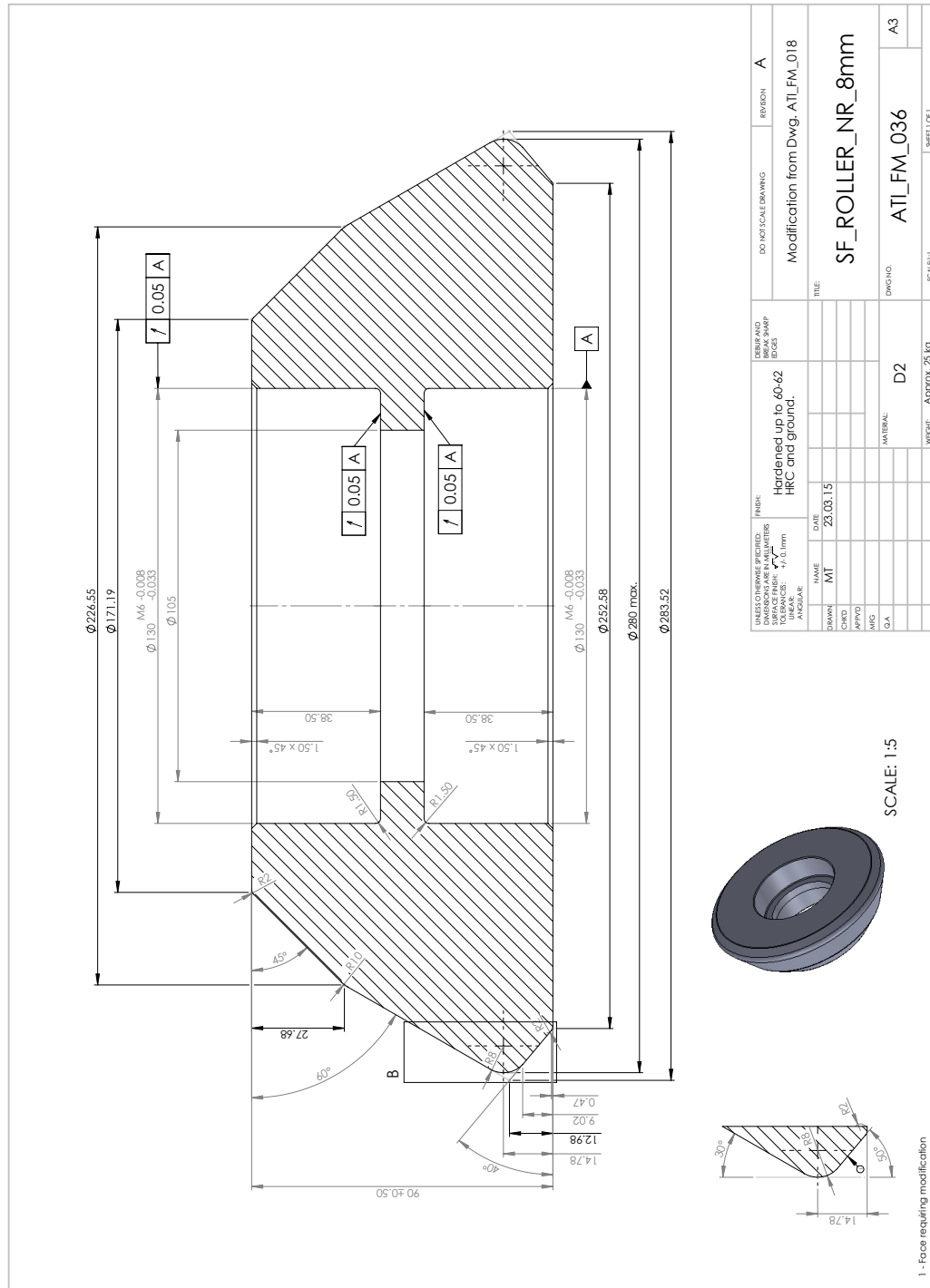


Figure 7.5: Drawing: 6 mm nose radius roller – ATI-SF – ATI FM 036, “SF\_ROLLER\_NR\_8mm”.

- Stationary state – radial load: The radial load took longer to reach a steady state. This was likely to be due to the springback; the part tended to stretch in the radial direction. Here, this load seemed to keep constant at 25 s, which matched about a quarter of the Z distance to form.
- End of forming: The 43° mandrel had a back face towards which the blank was pushed at the end of the forming operation. This should have been where an increase of the forces was observed. This rise happened approximately at 52.5 s. At this time, the position of the roller was at -76.3 on the Z axis, the material should have therefore been at 3.6 mm away from this back face. This was probably due to the external flange not being straight and slightly lying against the back face. A peak was observed for both loads at approximately 58 s, end of the forming operation.
- End: At 58 s, the roller started to retract. Both loads returned to 0 kN within 5 s.

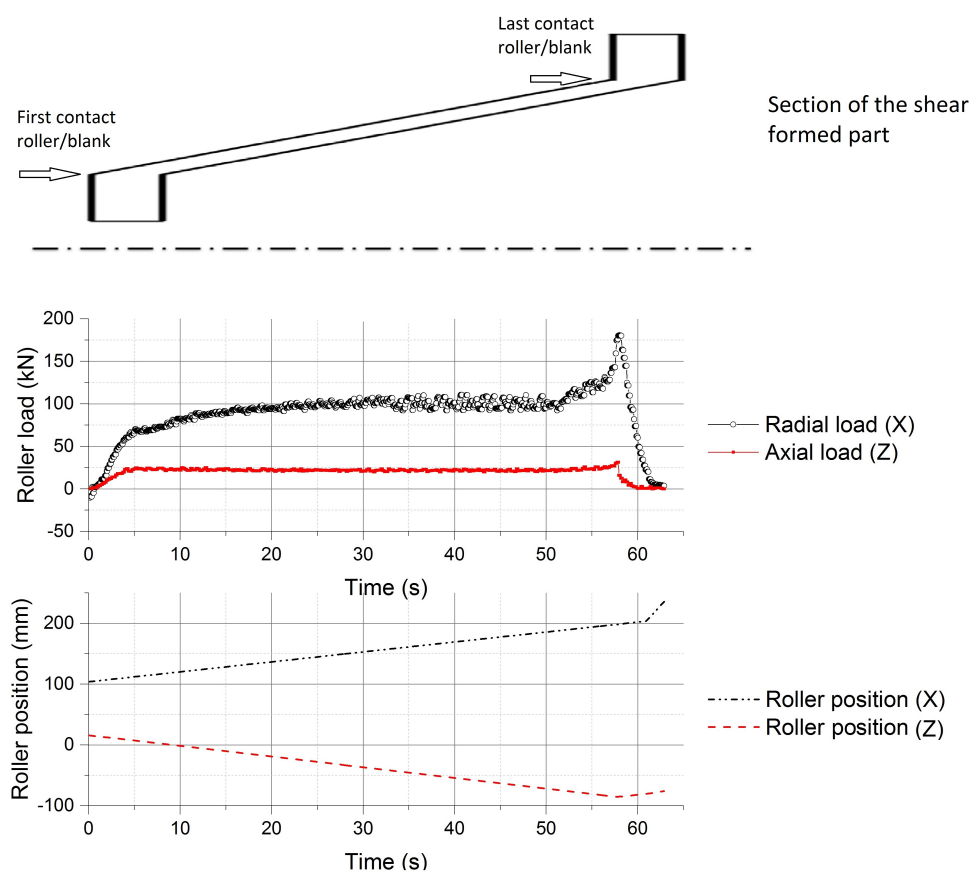


Figure 7.6: Plot of the roller radial and axial loads compared with the roller position – Example of part P1.

Both loads reached a stationary state as a constant gap between roller and mandrel was employed. Changing this value during the process would be likely to slightly change the pattern of the curves.

### 7.3 Geometrical and roughness analyses

The geometrical and roughness measurements were completed using the CMM and the portable surface roughness tester presented in Chapter 4. The measurement methods are described in Appendix C (pp. 175–59 and pp. 184–187). Table 7.4 gives the values of the geometrical features (Figure 7.2, p. 104) and roughness for parts P1–P14 excluding P10a due to failure.

According to Table 7.4, the coaxiality [1B], outer flange length [2], and outside diameter [7] were greater than the upper tolerances for all measurements whereas the shear formed length [10] was under size. The radius [5], parallelism [6], final diameter [8A], first diameter [8B], cone form [9], and straightness were sometimes out of tolerance but their average was within tolerance with the exception of the cone form. The remaining features were always within tolerance. The spread of the measured values was consistent for each feature considering the range of KPVs chosen. Although P15a and P15b led to failure, their final geometry and surface roughness were measured. The features within tolerance were the same and not many variations were observed when compared to P6, which formed successfully using the same KPVs.

Statistical analyses were performed on the final geometrical and roughness outputs of parts P1–P14 excluding P10a. The initial thickness at the outer [11] and inner [12] flanges as well as the internal diameter [1A] were not analysed statistically as they were independent of the shear forming operation. Furthermore, no impacts of the KPVs were registered for the coaxiality [1B] and outer flange angle. Predictive models were established for the other features and are given below. Their assessment and the statistical significance of the factors and/or their interactions as well as the optimised values are given in Table 7.5 (pp. 117–118). The quadratic effect of the factor  $F$  and its interaction with  $Sp$  were not significant enough to be considered in the models. For every output, with the exception of the parallelism [6],  $F$  had a significant impact.

Table 7.4: Geometrical and roughness measurements – Parts P1–P14 excluding P10a.

	Values observed			Standard deviation	Tolerances	
	Maximum	Minimum	Average		Upper	Lower
Internal diameter, $d$ [1A] (mm)	113.27	113.16	113.22	0.03	113.50	113.10
Coaxiality [1B] (mm)	0.41	0.12	0.28	0.08	0.10	0.00
Outer flange length [2] (mm)	54.63	52.01	52.98	0.84	51.73	51.13
Inner flange length [3] (mm)	49.43	48.99	49.21	0.14	49.51	48.91
Cone angle [4] (°)	43.31	43.07	43.19	0.09	43.50	42.50
Radius [5] (mm)	5.96	5.85	5.91	0.03	6.10	5.90
Parallelism [6] (mm)	0.61	0.22	0.37	0.12	0.50	0.00
Outer flange angle (°)	0.43	0.04	0.20	0.13	/	/
Outside diameter, $D_1$ [7] (mm)	498.97	493.73	495.66	1.77	492.20	491.80
Final diameter [8A] (mm)	389.80	389.30	389.55	0.16	389.63	388.63
First diameter [8B] (mm)	212.08	211.13	211.59	0.30	212.02	211.02
Cone form [9] (mm)	0.29	0.07	0.18	0.06	0.10	0.00
Shear formed length [10] (mm)	130.10	129.81	129.99	0.07	130.32	130.12
Outer flange thickness [11] (mm)	15.30	15.19	15.24	0.03	16.40	14.70
Inner flange thickness [12] (mm)	15.33	15.23	15.27	0.02	16.40	14.70
Final thickness, $S$ [13] (mm)	10.46	10.07	10.31	0.12	11.28	9.93
Straightness (mm)	0.15	0.02	0.07	0.04	0.10	0.00
Inner surface roughness, $R_i$ ( $\mu\text{m}$ )	2.18	1.42	1.84	0.20	3.20	0.00
Outer surface roughness, $R_o$ ( $\mu\text{m}$ )	1.28	0.48	0.85	0.22	3.20	0.00

$$\text{Outer flange length (mm)} = 54.411 - 3.855 F \quad (7.1)$$

$$\text{Inner flange length (mm)} = 49.4561 - 0.6649 F \quad (7.2)$$

$$\text{Cone angle (}^\circ\text{)} = 43.2357 + 0.2265 F - 0.000691 Sp \quad (7.3)$$

$$\text{Radius (mm)} = 5.9502 - 0.1161 F \quad (7.4)$$

$$\text{Parallelism (mm)} = 0.1792 + 0.001031 Sp \quad (7.5)$$

$$D_1 \text{ (mm)} = 498.683 - 8.150 F \quad (7.6)$$

$$\text{Final diameter (mm)} = 389.986 - 0.363 F - 0.001639 Sp \quad (7.7)$$

$$\text{First diameter (mm)} = 212.104 - 1.398 F \quad (7.8)$$

$$\text{Cone form (mm)} = 0.2607 - 0.2290 F \quad (7.9)$$

$$\begin{aligned} \text{Shear formed length (mm)} &= 129.545 + 0.1998 F + 0.00382 Sp \\ &\quad - 0.000009 Sp^2 \end{aligned} \quad (7.10)$$

$$S \text{ (mm)} = 10.1123 + 0.5390 F \quad (7.11)$$

$$\text{Straightness (mm)} = 0.1223 - 0.1412 F \quad (7.12)$$

$$R_i \text{ (}\mu\text{m)} = 2.0633 - 0.611 F \quad (7.13)$$

$$R_o \text{ (}\mu\text{m)} = 0.5554 + 0.796 F \quad (7.14)$$

The models for the outer flange length [2] and outside diameter [7], and for the cone form [9] and straightness had respectively confidence and prediction intervals wider than their related tolerance band. Consequently, these models should only be used to give a rough idea of the output value. The outer [2] and inner [3] flange lengths, radius [6], outside [7], first [8B] and final [8A] diameters, cone form, straightness, and inner surface roughness decreased when  $F$  increased. Conversely, the cone angle [4], shear formed length [10], final thickness [13], and outer surface roughness increased as  $F$  was raised. The cone angle, final diameter, and shear formed length also depended on  $Sp$ . The shear formed length was even dependent on  $Sp^2$ . Figure 7.7 gives the surface plots of these three models as well as the output values used to create the models.

A statistical analysis of the thickness measured at the top, middle, and bottom of the shear formed length was completed.  $F$  was the only factor to impact it as for the average final thickness value studied previously. It was noticed that the final thickness slightly increased towards the end of the shear forming operation. In Table 7.5 (p. 118) the target value for the final thickness was calculated with the sine rule considering the average cone angle ( $43.19^\circ$ ) and the initial thickness  $((15.24 + 15.27) / 2)$ .

A statistical analysis of the outer roughness along the shear formed length was also undertaken. At the top of the part, near the inner flange, no KPVs seemed to impact the roughness whereas in the second quarter the roughness depended on  $F$ ,  $Sp$ , and  $Sp^2$ . For the bottom half,  $F$  was the only factor to impact the outer roughness as for the average roughness value. It was decided not to introduce new models for the outer roughness as its values along the shear formed length were within tolerance and hence did not require adjustment. Even if the consistency along the shear formed parts was reasonable, a way to make it better would be to use a constant surface speed. The outer roughness of P00 fluctuated by  $0.06 \mu\text{m}$  only.

Table 7.5: Assessment of the predictive models for the final part geometry and statistical significance of the factors and/or their interactions.

	Outer flange length [2]	Inner flange length [3]	Cone angle [4]	Radius [5]	Parallelism [6]	Outside diameter [7]	Final diameter [8A]	First diameter [8B]	Cone form [9]
SSE	1.52	0.03	0.05	0.01	0.13	6.57	0.11	0.17	0.02
$s_e$	0.36	0.05	0.07	0.02	0.11	0.74	0.10	0.12	0.04
$R_{adj}^2$ (%)	83	87	43	51	25	84	62	85	61
F-value of the model	65.4	91.1	5.9	14.5	5.4	67.8	11.8	77.3	21.8
Critical F-value	At 95 %	4.7	4.0	4.7	4.7	4.7	4.0	4.7	4.7
	At 99 %	9.3	7.2	9.3	9.3	9.3	7.2	9.3	9.3
Confidence interval at 95 % *	$\pm 0.32$	$\pm 0.05$	$\pm 0.07$	$\pm 0.02$	$\pm 0.08$	$\pm 0.65$	$\pm 0.10$	$\pm 0.11$	$\pm 0.03$
Prediction interval at 95 % *	$\pm 0.84$	$\pm 0.12$	$\pm 0.16$	$\pm 0.05$	$\pm 0.24$	$\pm 1.74$	$\pm 0.24$	$\pm 0.28$	$\pm 0.09$
<b>Statistical significance of the factors and/or their interactions</b>									
F	65.4	91.0	6.4	14.5	/	67.8	7.3	77.3	21.8
Sp	/	/	6.0	/	5.4	/	15.0	/	/
F <sup>2</sup>	/	/	/	/	/	/	/	/	/
Sp <sup>2</sup>	/	/	/	/	/	/	/	/	/
F.Sp	/	/	/	/	/	/	/	/	/
At 95 %	4.7	4.7	4.8	4.7	4.7	4.7	4.8	4.7	4.7
At 99 %	9.3	9.3	9.6	9.3	9.3	9.3	9.6	9.3	9.3
Critical F-value									
Target value*	51.43	49.21	43.00	6.00	0.00	492.00	389.13	211.52	0.10
Best possible fit *	52.10	49.21	43.06	5.94	0.30	493.79	389.31	211.52	0.12
Optimised values	F	0.60 mm/rev	0.37 mm/rev	0.10 mm/rev	0.10 mm/rev	0.60 mm/rev	0.60 mm/rev	0.42 mm/rev	0.60 mm/rev
	Sp	/	/	/	120 RPM	/	280 RPM	/	/

\* The confidence and prediction intervals, the target value, and the best possible fit are in millimetres with the exception of feature [4] and the surface roughness measurements, which are in degree and micrometres respectively.

Table 7.5 Continued: Assessment of the predictive models for the final part geometry and statistical significance of the factors and/or their interactions.

	Shear formed length [10]	Final thickness [13]	Straightness	Inner surface roughness	Outer surface roughness
<i>SSE</i>	0.01	0.05	0.01	0.32	0.31
<i>s<sub>e</sub></i>	0.03	0.06	0.03	0.16	0.16
<b>Assessment of the predictive model</b>					
<i>R<sub>adj</sub><sup>2</sup></i> (%)	74	78	58	34	49
F-value of the model	13.1	42.8	16.4	7.7	13.6
Critical F-value	At 95 % At 99 %	4.7 9.3	4.7 9.3	4.7 9.3	4.7 9.3
Confidence interval at 95 % *	± 0.04	± 0.05	± 0.02	± 0.15	± 0.39
Prediction interval at 95 % *	± 0.08	± 0.14	± 0.06	± 0.14	± 0.38
<b>Statistical significance of the factors and/or their interactions</b>					
<i>F</i>	19.2	42.8	16.4	7.7	13.6
<i>Sp</i>	5.6	/	/	/	/
<i>F</i> <sup>2</sup>	/	/	/	/	/
<i>Sp</i> <sup>2</sup>	7.4	/	/	/	/
<i>F.Sp</i>	/	/	/	/	/
At 95 %	5.0	4.7	4.7	4.7	4.7
At 99 %	10.0	9.3	9.3	9.3	9.3
<b>Optimisation of the output value</b>					
Target value*	130.22	10.44	0.00	0.00	0.00
Best possible fit *	130.09	10.44	0.04	1.70	0.64
Optimised values	<i>F</i> 0.60 mm/rev <i>Sp</i> 220 RPM	0.60 mm/rev /	0.60 mm/rev /	0.60 mm/rev /	0.10 mm/rev /

\* The confidence and prediction intervals, the target value, and the best possible fit are in millimetres with the exception of feature [4] and the surface roughness measurements, which are in degree and micrometres respectively.



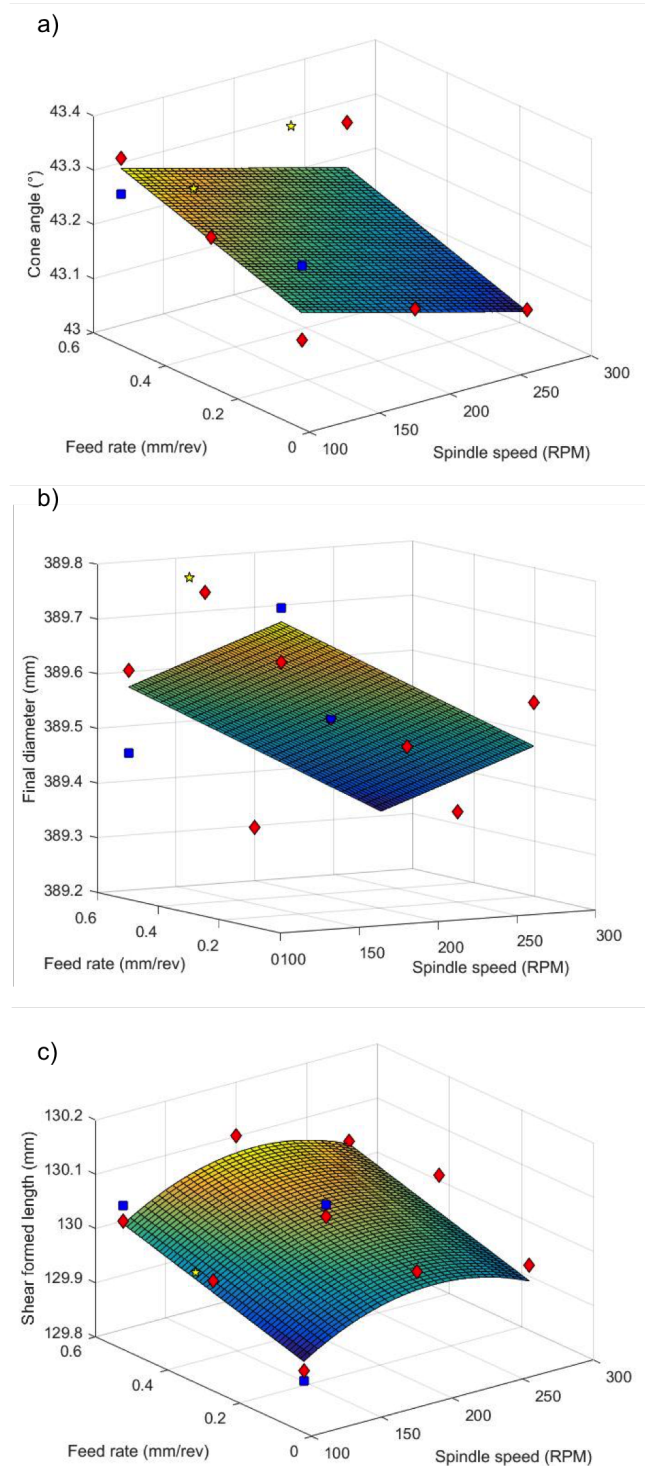


Figure 7.7: Surface plot of three predictive models: (a) the cone angle, (b) final diameter, and (c) shear formed length (Yellow stars: Additional parts — Blue squares: Repeats — Red diamonds: Factorial DoE).

When optimising all the models at a time by targeting the nominal values, the best set of parameters was 0.60 mm/rev and 280 RPM even if the outer flange length, radius, outside diameter, cone form, and shear formed length were still out of tolerance. P13 had the least features out of tolerance including the outer flange length, outside diameter, first diameter, and shear formed length. This showed that without statistical analysis, the best set of parameters would have been set at 0.60 mm/rev and 120 RPM. These are not the optimum parameters and would have been selected simply due to random error.

The three sets of repeat parts showed a maximum difference in the measurements of 0.20° and 0.73 mm for the angular and linear features respectively. In terms of roughness, a maximum of 0.29 µm and 0.16 µm were recorded for the outer and inner roughness. Due to failure at part P10a, the roller identified as SF60316004R was used. This latter did not seem to reduce the outer roughness as much as with the previous roller.

## 7.4 Metallurgical work

To enable better understanding of the material behaviour during the shear forming process, the microstructure and texture were observed. The samples were prepared for observation as described in Appendix C (pp. 162–165). SEM using EBSD techniques was utilised. The chemical composition and mechanical properties of the as-received sheet are given in Tables 7.6 and 7.7.

*Table 7.6: Chemical composition (% by mass) of the 15 mm thick 304L stainless steel as-received sheet.*

Material	Heat number	Chemical composition (%)							
		<i>C</i>	<i>Cr</i>	<i>Mn</i>	<i>N</i>	<i>Ni</i>	<i>P</i>	<i>S</i>	<i>Si</i>
304L	293958	0.018	18.09	1.900	0.0852	8.10	0.038	0.001	0.316

Table 7.7: Mechanical properties of the 15 mm thick 304L stainless steel as-received sheet.

Ultimate tensile strength	Yield strength at		Elongation after fracture	
	0.2 %	1 %	A50	A5
589 MPa	277 MPa	311 MPa	59 %	56 %

### 7.4.1 As-received material

The EBSD analysis revealed that the as-received material, represented by off-cuts, had approximately equiaxed grains with an average grain size of 18.7–23.0  $\mu\text{m}$  with 80 % of the grains being greater or equal to 15.7  $\mu\text{m}$ . The initial material was heterogeneous and its microstructure can be seen in Figure 7.8.

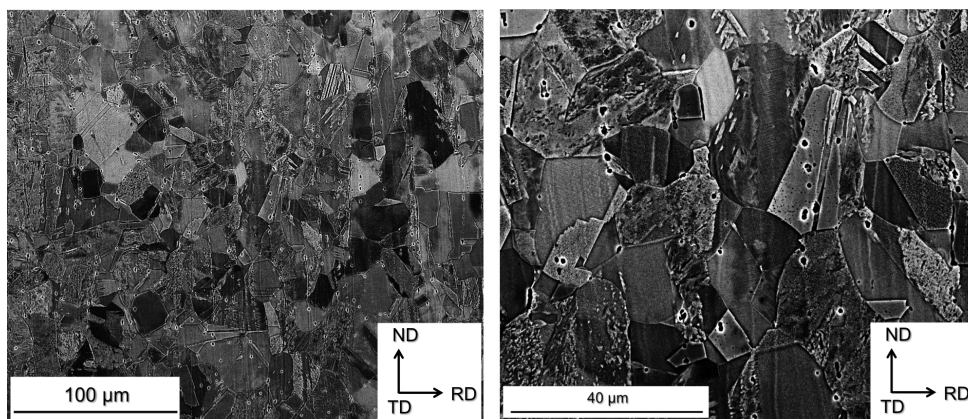


Figure 7.8: BS micrographs of the 15 mm thick as-received material.

According to Kumar et al. (2004), the PFs  $\{111\}_{\text{FCC}}$  and  $\{110\}_{\text{BCC}}$  of cold rolled 304 stainless steel should both have two elements at each side of the centre (right and left for the orientation shown in Figure 7.9) and a third one in the centre for the martensite. Here the latter was only slightly noticeable. Furthermore, the ODFs did not reveal any strong components for  $\Phi_2 = 0^\circ$  and  $\Phi_2 = 45^\circ$  and so as for the 304L stainless steel as-received material studied previously, a relatively weak rolling texture was observed.

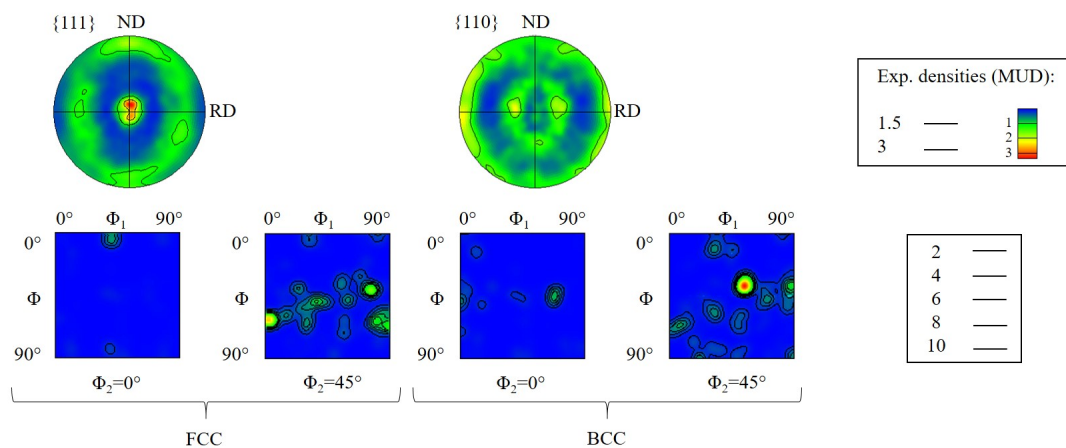


Figure 7.9: Texture of the 15 mm thick as-received material (top: PFs, bottom: ODFs).

### 7.4.2 Shear formed material

Due to the failures encountered with the 8 mm nose radius, only the impacts of the feed rate and spindle speed were observed through the selection of parts P3 to P6, which included the lowest and highest levels of process parameters employed in the full DoE. The shear formed areas, M2 to M5, presented elongated grains following the roller path and no microstructural differences were noted within the same part. As a result, only the micrographs obtained for these parts in area M3 are given in Figure 7.10. Shear bands were noted with primary orientations along the  $\theta$  axis of the cylindrical coordinates and slightly tilted from the shear forming direction. These aligned shear bands had a principal spacing around 1  $\mu\text{m}$ . To study further the microstructure, EBSD maps were acquired.

The grain size after shear forming was on average of 4.1  $\mu\text{m}$ , with a range of 2.9–4.3  $\mu\text{m}$  and an aspect ratio of 2. The texture was analysed using PFs and ODFs and can be seen in Figures 7.11 and 7.12. Increasing the feed rate and/or the spindle speed seemed to give a stronger texture.

Larger grains were observed on the mandrel side with an average of 4.7  $\mu\text{m}$  whereas smaller grains were noted on the roller side with an average of 3.4  $\mu\text{m}$ . As a change of texture was revealed in Chapter 5 across the thickness, it was considered crucial to investigate such a phenomenon for thicker parts. It appeared for all four parts that the texture was stronger on the roller and mandrel sides compared with the

mid-thickness as illustrated in Figure 7.13. No significant differences were noted between sides.

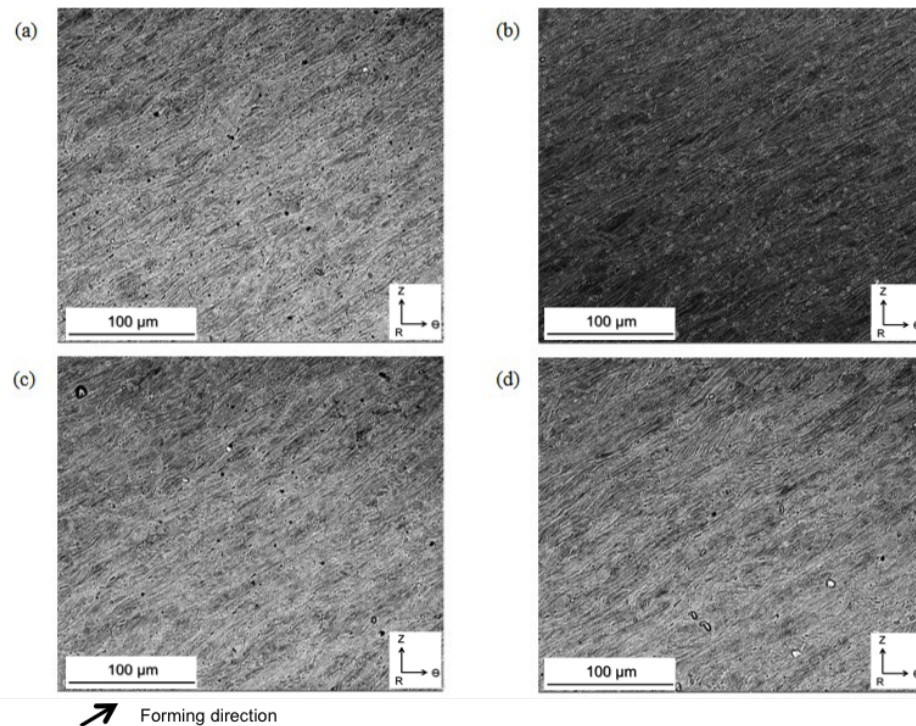


Figure 7.10: BS micrographs of the shear formed material in area M3 for parts (a) P3, (b) P4, (c) P5, and (d) P6.

## 7.5 Summary

Firstly, the set-up of the experiments was shown to have a significant impact on certain features of the final geometry. This could also have a role in the final microstructure and texture of the material as different compression deformations might be involved. Further research should be undertaken to identify clearly the impact of different compression deformations, i.e. gap between roller and mandrel. In the literature the gap between roller and mandrel was taken into consideration for geometrical and roughness outputs only but more work could be undertaken to look at the impact on the geometrical tolerance bands as well as the material microstructure and texture. In this set of experiments it appeared that a set-up enabling true shear forming allows narrower tolerance bands to be obtained in terms of geometrical features and a lower compression deformation of the material.

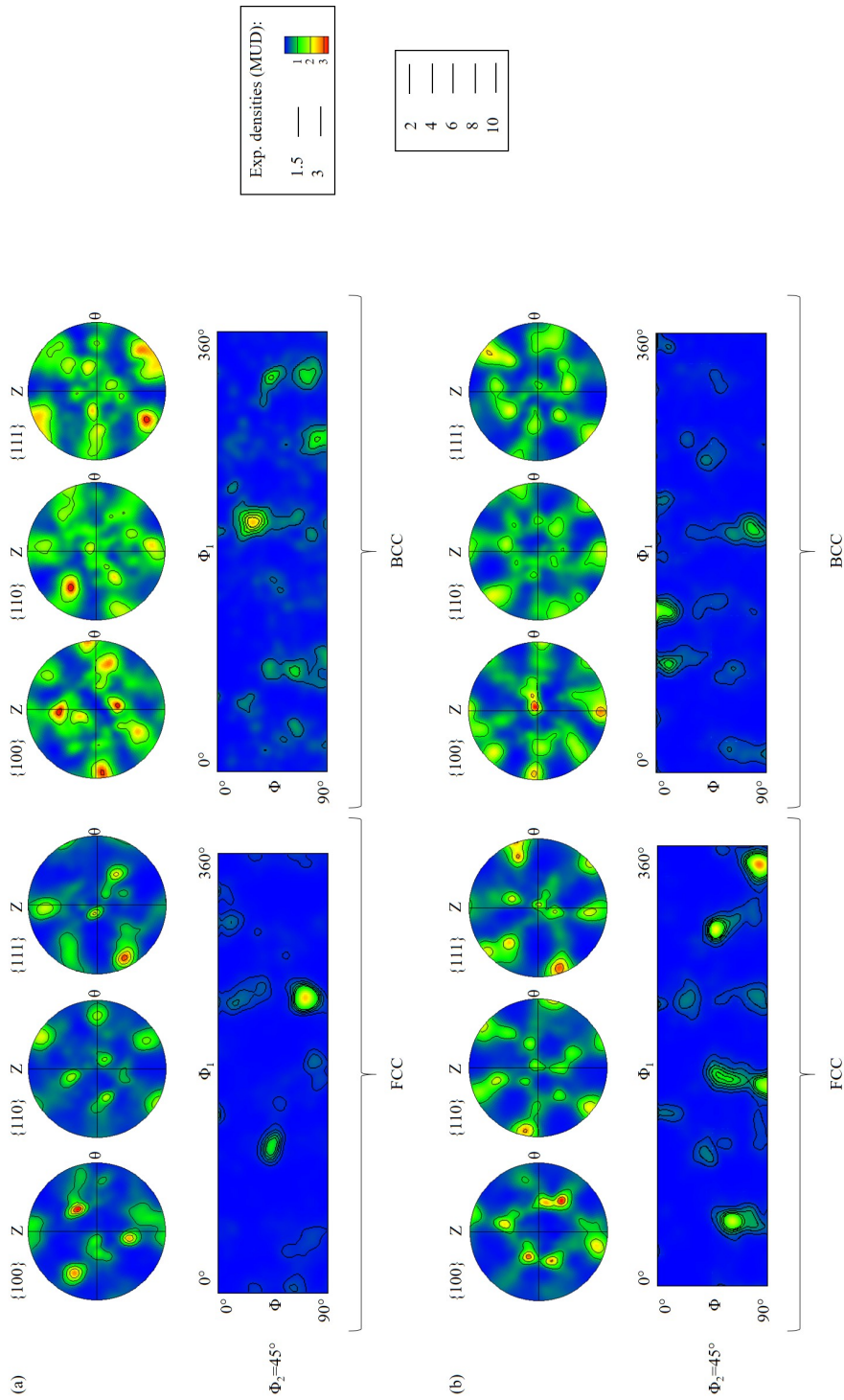


Figure 7.11: Texture of parts (a) P3 and (b) P4 in the middle of area M3.



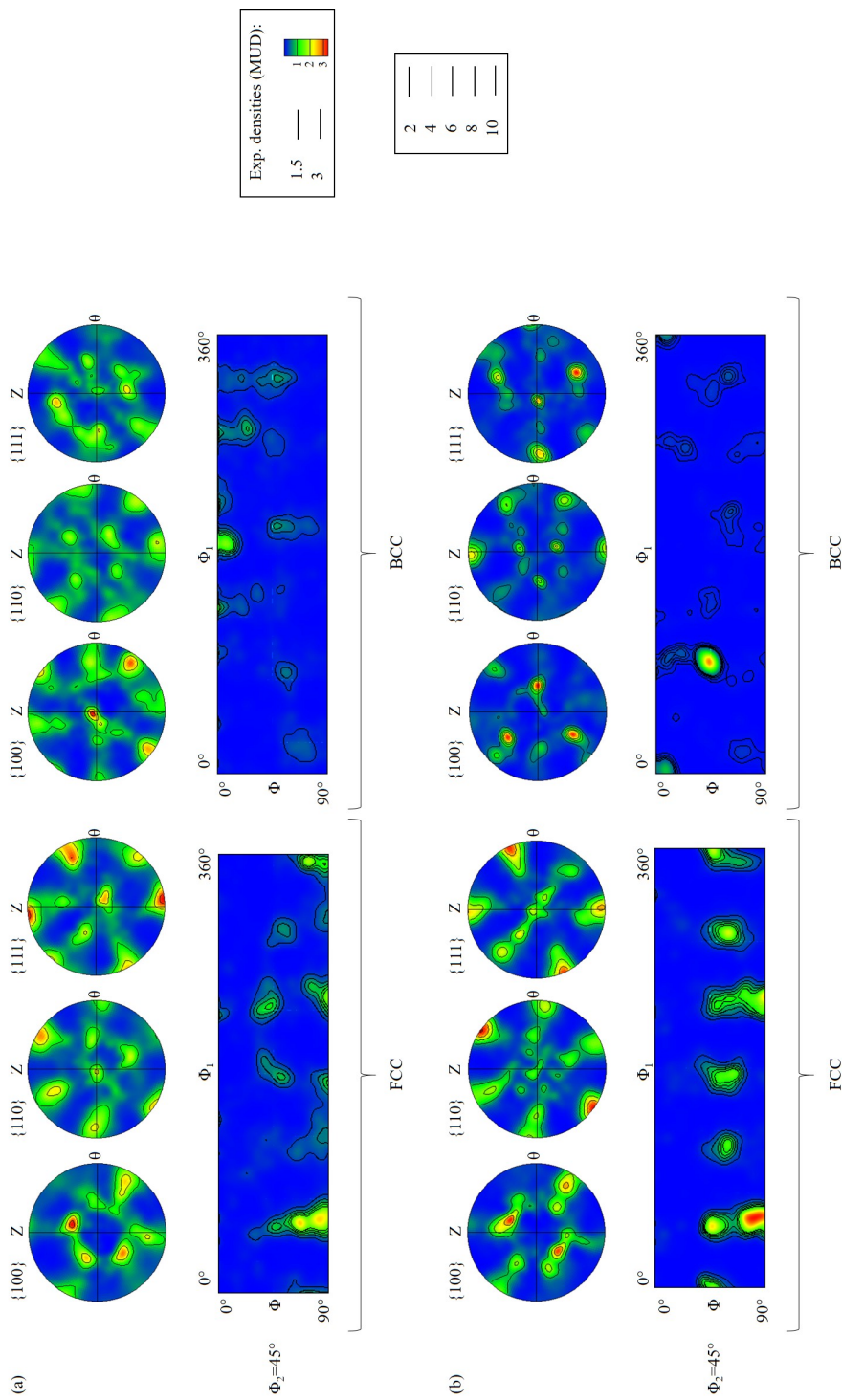


Figure 7.12: Texture of parts (a) P5 and (b) P6 in the middle of area M3.

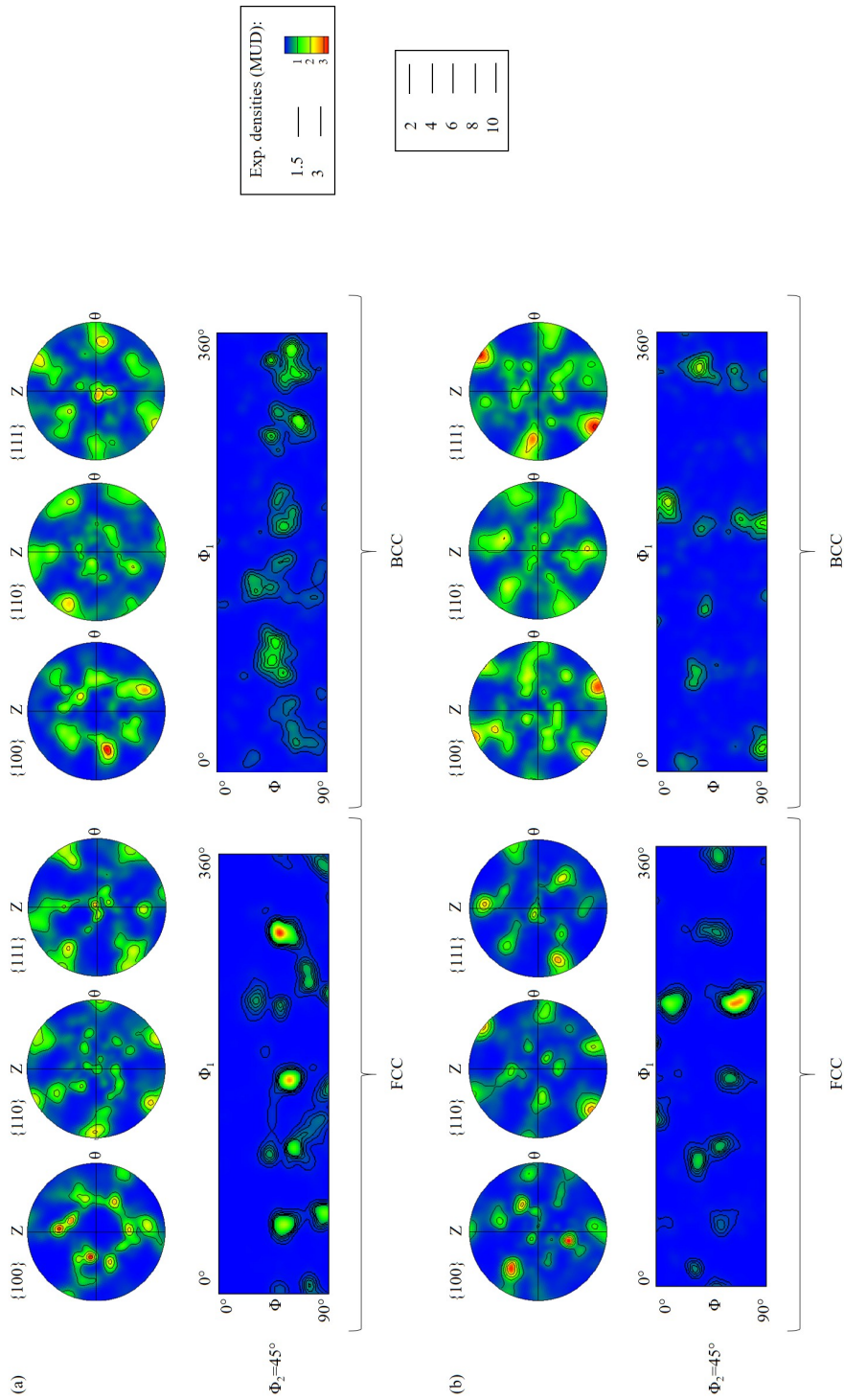


Figure 7.13: Texture of parts P3 on the (a) mandrel and (b) roller sides of area M3.



According to the literature, the tolerances of the cone angle and the circumferential wall thickness achieved for a similar size of part made of copper were also met here for a 15 mm thick part of 304L stainless steel. The average surface finish was not as good on the 304L stainless steel part but Runge (1993) did not mention which type of roller was utilised or what the initial starting roughness was.

In this chapter, the inner surface roughness was found to be independent of the spindle speed like in the works of Chen et al. (2001) and the previous experiments undertaken in this EngD project. It was the first time that the impact of the feed rate on the inner roughness was noted in this EngD project but unlike in the studies of Chen et al. (2001, 2005) and Kunert et al. (2005) on Al-alloys, increasing the feed rate led to a smoother inner finish. According to the literature, the outer roughness outcomes recorded here were typical of the shear forming process in terms of values (Bewlay and Furrer, 2006). So far in this EngD project, no impacts of the spindle speed were observed, which differed from the literature. A potential explanation was the use of a changing spindle speed, but a constant spindle speed was used in this last set of experiments therefore this hypothesis was not verified. Finally, when reducing the feed rate, a reduced outer roughness was observed such as in the previous experiments and in the works of Chen et al. (2001, 2005) and Kunert et al. (2005). The feed rate had a significant impact on most of the geometrical features as seen so far. As for the previous factorial DoE, an increase of the feed rate led to a rise of the cone angle and of the final thickness. Thanks to the numerical predictive models an optimisation of each feature was possible. This showed the importance of statistical analysis but also the need to establish which features are crucial for the final use of the part.

The as-received material had a heterogeneous microstructure with an average grain size about the same as for 6 mm thick sheets. The texture prior to forming was relatively weak. After the shear forming operation, elongated grains with shear bands were present along the roller path as in the previous experiments. The main torsion components characteristics of a simple shear deformation mechanism were once more observed in PFs and ODFs. A stronger texture was noted when the feed rate and spindle speed were increased but statistical analysis would be required to confirm this phenomenon as it can simply be random. For the 6 mm thick 304L stainless steel parts, a decrease of deformation across the thickness was observed, the surface in contact with the roller being the more deformed. Here for a thicker part, the texture was stronger on both sides of the thickness compared with its middle. Further studies

on thick material should be undertaken to analyse further such a texture as this may impact the final mechanical properties.

# Chapter 8

## Summary, conclusions, and future work

Chapter 8 is the last chapter of the thesis. It gives a summary of the research undertaken in this EngD project. Then, the findings are discussed and compared with the literature. Conclusions are drawn leading to recommendations for future work.

### 8.1 Summary and discussion

As mentioned in Subsection 1.3.2 of Chapter 1 (pp. 6–7), four research questions were raised from which three objectives were derived.

- O1 – Describe the state of the art for the shear forming of 304L stainless steel and Inconel 718
- O2 – Identify and study the effect of the key processing variables on the geometry and surface roughness of the component when applied to 304L stainless steel and Inconel 718 through experimental work using a systematic approach
- O3 – Study the microstructure and texture of 304L stainless steel and Inconel 718 post shear forming in order to identify the material deformation mechanism

To meet these objectives, this thesis has addressed the following areas of work:

- State of the art for the shear forming process applied to 304L stainless steel and Inconel 718

- Identification, impact and optimisation of the KPVs on the geometry, roughness, and texture of final shear formed components
- Microstructural considerations when shear forming applied to both materials

Triangulation technique and use of secondary data were adopted throughout the literature reviews presented in Chapters 2 and 3 in order to meet objective O1. Chapter 2 reported that although the metal spinning methods were first developed with the art of potting clay in ancient Egypt, their advancement essentially occurred during the past few decades with the growth of near-net-shape manufacturing. Achievable shear formed geometries range from parts with a cone angle of  $3^\circ$  to  $85^\circ$ . In the literature, the effects of KPVs on the geometry and roughness were studied on relatively soft and thin materials often within a narrow range of parameters. Furthermore, this literature survey showed the importance of detailing measurement methods to take into account measurement errors and allow comparison across several studies. As a result, Chapter 4 of this thesis detailed the measurement methods and the calibrations and procedures employed are described in Appendix B. The range of errors was established and the interpretation of the results was drawn accordingly.

Chapter 3 revealed that both Inconel 718 and 304L stainless steel are widely used across diverse sectors. As a result, their chemical composition, microstructure, and mechanical properties are well-known. Two publications dealt with microstructural considerations when shear forming for Al and Al-Mg alloys – alloys which have a common crystal structure with the materials studied. Conversely, no publications linking Inconel 718 and 304L stainless steel to the shear forming process were found showing a clear gap of knowledge that this EngD project intended to fill throughout Chapters 5 to 7.

Chapter 5 presented the first shear forming work undertaken at the AFRC on the industrial scale flow former. Capability and repeatability of the process were studied on the  $31.5^\circ$  geometry. According to the geometrical outcomes, control over this process was achievable against geometry. Nevertheless, the feed rate and spindle speed were identified as KPVs. The main contribution to knowledge was given in Chapter 5, where the primary mechanism of deformation was identified as simple shear. According to the literature, it was so far only considered as close to pure bending for large cone angles whereas pure shear seemed more appropriate for smaller cone angles. Furthermore, a factorial DoE approach allowed the establishment of accurate numerical predictive model for the geometry and roughness

of the final part. The tendencies observed were the same as those observed in the literature with the exception of the spindle speed. In the experiments of Chapter 5, the spindle speed was changing during the process to allow a constant surface speed, which might explain why the results differ.

Chapter 6 focused on the influence on microstructure when shear forming Inconel 718. As for Chapter 5, elongated grains following the roller path were observed as well as an increased hardness. Shear bands, characteristics of high local deformation, were noted. The grain size was dependent on the cone angle. A smaller grain size was observed for smaller angles due to an increased deformation, which correlated with the findings of Chapter 3. The statistical analysis of the texture revealed a significant link between the torsion component B and the cone angle, initial thickness, and their interaction. Furthermore, for angles larger than  $23.5^\circ$  the intensity of B at mid-thickness was decreased when using a thicker blank. Such a phenomenon could be crucial for the final mechanical properties of the part. Recrystallisation was promoted only after heat treatment and the amount of  $\delta$ -phase was kept under 4 %. The two-step aging heat treatment was thus considered as adequate.

Finally, Chapter 7 showed that the experimental methodology can have a significant impact on the final geometry of the part. Tighter tolerance bands were met by being closer to true shear forming. Overall the feed rate always had a significant impact on the geometrical features. When optimising the process by the means of the numerical predictive models, the ranking of geometrical features was found essential as more than one set of parameters was suitable. Throughout this EngD project, the inner roughness was found to be independent of the spindle speed. The impact of the feed rate was only noted in the set of experiments presented in Chapter 7. No effects of the spindle speed on the outer roughness was recorded, which differed from the literature. Conversely, the impact of the feed rate was consistent. Using a lower feed rate always resulted in a reduction in the outer roughness. The microstructure of thicker components correlated with the outcomes of the previous experiments. Although in Chapter 5 an increased deformation was registered from the surface in contact with the mandrel to the one in contact with the roller, for thicker materials a neutral zone such as in the literature was observed in the middle of the thickness. As the area of each deformation zone is particular to the amount of plastic deformation seen, for thinner thicknesses the deformation zones on both sides of the thickness could be overlapping.

## 8.2 Contributions to knowledge

1- The feeds and speeds were identified as main KPVs as they had a significant impact across the different thicknesses and geometries, which was established by a systematic approach. The predictive numerical models showed that the feed rate impacted almost all the geometrical features. Furthermore, decreasing the feed rate reduced the outer surface roughness, which was found independent of the spindle speed.

*The numerical predictive models showed how essential it is to consider which geometrical features matter on any given parts when using shear forming. This influences the set-up and process optimisation as well as the design for manufacture. Shear forming was demonstrated to be a capable and repeatable process. Control over this process was proven and so shear forming could be considered as a production process.*

2- The shear forming of thick material with thicknesses up to 15 mm was shown to be possible. Considering the upper capabilities of the flow former in terms of forces and the geometric control demonstrated, the shear forming of even thicker material is believed to be achievable. The design and manufacturing envelope for shear forming could therefore be opened up and an increase of the potential applications to conical aerospace structures could be easily noted.

*When shear forming thicker material, a reduced texture in the middle section of the thickness compared to the outer surfaces (neutral zone) was noted, which was not observed with thinner materials in this project. If a larger design and manufacturing envelope was to be considered, such phenomenon should be taken into account.*

3- The grain size was found dependent on the cone angle. Furthermore, the primary mechanism of deformation of the shear forming process was identified as simple shear, which constituted the main contribution to knowledge. The statistical analysis of the texture of the Inconel 718 parts after a two-step aging treatment revealed a significant link between the torsion component B and the cone angle, initial thickness, and their interaction. The yield strength after shear forming compared with the current forged components was generally 10 % greater in the case of Inconel 718.

*The improvement of the mechanical properties is believed to originate principally from the refined grain size observed after shear forming. Elongated grains following*

*the roller path were observed as well as shear bands, and an increased hardness. As mentioned in Chapter 2, understanding the material behaviour will help develop further the shear forming process by the means of process modelling and so will allow a reduction of the cost in terms of mechanical testing.*

### **8.3 Limitations and future work**

Even though the research questions identified at the beginning of this EngD project were answered, some note should be made of the limitations of this study and the possible improvements that could be made. Thanks to the description of the measurement methods employed in this project, the comparison of further studies with the present work should be eased.

The main drawback of this work was the inability to link the final microstructure and texture to the mechanical properties of the final component due to a lack of data. It is recommended that Rolls-Royce undertake additional mechanical tests to establish such a link in order to confirm that thicker shear formed components are still capable of meeting design intent. Such a work could reduce the requirements in terms of mechanical testing and so reduce the costs involved with shear forming research projects.

Secondly, knowing the material behaviour will help develop better simulation of the shear forming process. However, understanding the forces involved remains essential. Investigations of the software used to monitor tool loading, feeds and speeds, and roller positions are crucial to establish the relevance of the data given in this thesis. If a software issue were to be proven, further studies on the impact of forces should be considered. To fully understand the shear forming process, different materials could be produced and similar analysis could be carried out.

According to Section 8.1, the tendencies observed for the inner and outer roughness were not always consistent within this project and in the literature. In Chapter 7, it was shown that the roller itself can induce major differences in the outcomes. Further studies are recommended to get a deeper understanding of the elements impacting the final roughness and to elaborate a better control over them.

# **Appendix A**

## **Paper A**

This appendix contains Paper A, which mainly studied the impact of the processing variables on the geometry of 304L stainless steel shear formed components. This paper was presented at the 13<sup>th</sup> International Cold Forming Congress in September 2015 and Chapter 5 of this thesis is partially based on it.



## Characterisation and development of the incremental shear forming process for advanced structures

Marine Guillot, Andrzej Rosochowski  
(DMEM, University of Strathclyde)  
Paul Blackwell  
(AFRC, University of Strathclyde)  
Elizabeth Moore, Steven Halliday  
(Rolls-Royce plc)

### ABSTRACT

Shear forming is an incremental forming process that transforms a starting pre-form in 2D plate condition, into 3D structures of typically conical geometry. Roller(s) shear the pre-form onto a conical mandrel, resulting in a reduction of the starting wall thickness. The benefits of the process can be described in terms of improved material utilisation, enhanced product characteristics, good surface finish, consistent geometric control and reduced production costs. The process has potential application to a wide range of conical geometries used within advanced aerospace structures, which are currently manufactured from bulk forgings, with high associated machining costs.

The paper explores the effect of key processing parameters on the formability of 304L stainless steel material, shear formed using an industrial flow forming/shear forming/spinning machine. A Design of Experiments (DoE) approach was used to study the relationship of feed rate, spindle speed and coolant/lubricant systems to the component geometry, surface finish, microstructure and hardness. Regression equations that link the process parameters to the geometry and surface finish were obtained by statistical analysis. Scanning Electron Microscopy (SEM) and hardness testing was used to characterise the shear formed material and enable an improved understanding of the material behaviour throughout the shear forming process.

### 1. INTRODUCTION

Shear forming, also known as flow forming, shear spinning, shear turning, power spinning or spin forging, is an incremental cold forming process. It is used to obtain rotationally symmetrical hollow shapes that can be conical, concave, convex or a combination of these. A pre-form is clamped against the mandrel by a tailstock and the mandrel is driven to a rate of rotation that is known as spindle speed. One or more rollers are used to form the part by following a programed path with a controlled feed rate. The material flows only in the direction parallel to the rotational axis, see Figure 1. In most cases of shear forming only a single pass is necessary.

The sine law (1) defines the final wall thickness  $S_1$ , for an ideal conical part, as a function of the cone angle  $\alpha$  (also called the angle of shear) and the initial wall thickness  $S_0$ :

$$S_1 = S_0 \cdot \sin \alpha \quad (1)$$

The gap between the mandrel and the roller(s) controls the wall thickness reduction, which is set to be in accordance with the sine law. A minimum angle of shear that is possible is suggested to be between 10 and 18° and is known to be dependent on the material used, however, smaller angles as low as 3 to 4° can be achieved using multiple passes (Runge, 1993). Common materials employed for shear forming are copper, steel, nickel and aluminium, although a wider range of other materials have also been shear formed (Runge, 1993).

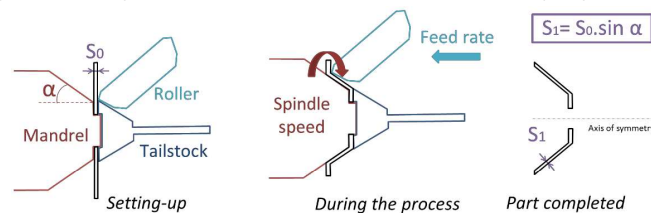


Figure 1: Shear forming principle

## 2. EXPERIMENTAL SETUP

Trials were completed within the Advanced Forming Research Centre (AFRC), Renfrew, UK, using a WF Maschinenbau und Blechformtechnik GmbH 3-roller-flow forming and spinning machine of the type STR 600 3/6. In this study, 6mm thick 304L stainless steel pre-forms were used with an outer diameter of 430mm. The initial hardness of the material was 88HRB. The pre-forms were shear formed onto a mandrel with a cone angle of 31.50° using a single roller with a 3mm nose radius.

### 2.1. Process parameters

The shear forming parameters are multiple. In this study, process parameters associated with the material type, initial thickness, roller nose radius, number of rollers, mandrel cone angle and roller path were held constant. Three of the process parameters were selected as factors: feed rate, surface speed and coolant/lubricant. The surface speed, also called cutting speed, was held constant during the process; its value directly impacts the spindle speed which is automatically calculated by the flow forming machine using the following relationship:

$$\text{Spindle speed (RPM)} = \text{Surface speed (m/min)} / (\pi * \text{Diameter (m)}) \quad (2)$$

The spindle speed decreases during the process as the diameter increases. The oil-based coolant used was Houghton Hocut 795B with a maximum flow rate of 400 L/min. For the parts where coolant flow was set to 0, a lubricant was brushed onto the preform prior to forming; this was a protective/lubricating coating called Driform 61A, which is a dispersion of inorganic and polymeric solid lubricants, within a solution of organic resin in isopropanol.

### 2.2. Experimental design

For this study, a full three-level factorial DoE was carried out using the three variable parameters as experimental factors: F, S and C, see Table 1. This 3<sup>3</sup> design generated 27 runs. An additional two-level factor L was included in the experiment, however, this did not increase the number of runs as L was only used when C was at Level 3. Using statistical analysis, this DoE allows the prediction of the main effects of each factor as well as their interactions (except the interaction CL). It is then possible to generate second order equations linking these factors to the outputs (Grove & Davis, 1992).

**Table 1:** Variation of the process parameters

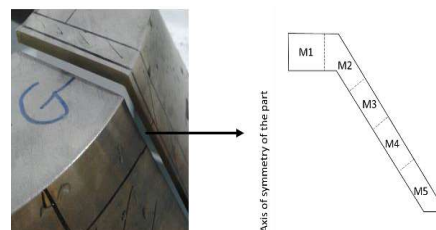
Process parameters	Notation	Levels		
		Level 1	Level 2	Level 3
Feed rate (mm/rev)	F	1.0	0.8	0.6
Surface speed (m/min)	S	480	400	300
Coolant (L/min)	C	400	200	0
Lubricant	L	0 (=No)		1 (=Yes)

### 2.3. Outputs

The first output analysed for this study was the *component geometry*, represented by the first diameter shear formed (i.e. where first contact is made by roller), the angle of shear and the average shear formed thickness. It was measured by using a 3D scanner (ATOS GOM with a MV 320 volume). A rotating table was used to partially automate this operation as well as a fixture frame into which the part was located in order to increase the accuracy of the measurements. All measurements were completed using the software ATOS GOM Inspection Professional III Rev.02. Maximum errors (machine and operator) of 0.06% and 0.01% were observed respectively for the angle of shear and for the length of the other measurements.

The *surface finish* was measured using an optical 3D micro coordinate system, the Alicona InfiniteFocus, with objective x20. Measurements achieved vertical and lateral resolutions of up to 50nm and 881nm respectively. In order to meet the ISO 4288 standard, the evaluation length was set to exceed 4mm with a sampling length,  $L_c$ , chosen at 0.8mm. In order to meet the ISO 4287 standard, the arithmetical mean deviation of the profile ( $R_a$ ) is given by averaging five calculated profiles which represents a width of 5 pixels. Replicas of the part were used for measurement due to the geometry and size of the parts. The maximum error (machine and operator) observed for the measurement for the same replica and between part/replica (machine and operator) were 10.16% and 10.94% respectively.

The *metallurgical work* was completed on a selection of parts from the factorial DoE. Eight parts were assessed for the three factors at level 1 and 3. A cross section slice was taken from each part using Electrical Discharge Machining (EDM) which was then sectioned into five specific areas of interest, see Figure 2. The samples were analysed using Scanning Electron Microscopy (SEM), type FEI Quanta 250 FEG. Hardness tests were performed using a micro-hardness tester, type Zwick-Roell Indentec ZH $\mu$ , at 1 kg force, lens x20. The measurements were made in accordance with the ISO 6507-1 standard. The level of confidence in the results was 95%.

**Figure 2:** Preparation of a shear formed part for metallurgical work

### 3. RESULTS AND DISCUSSION

The experimental results for geometry and surface finish were studied by statistical analysis using an analysis of variance and F-tests. The assessment of a model depends on the sum of squares for error (SSE), the standard error of estimate ( $s_e$ ), the adjusted coefficient of determination ( $R^2_{adj}$ ) and the F-value of the model (Keller, 2001). Table 2 summarises these elements for all equations generated by statistical analysis in this section. The statistical significance of the factors and/or their interactions have been verified by comparing their F-value to the critical F-value, in this study at 95% and 99%, see Table 3.

**Table 2:** Assessments of the predicted models

	SSE	$s_e$	$R^2_{adj}$	F-value of the model
Equation 3	0.31	0.12	92.43	106.84
Equation 4	0.12	0.08	91.24	55.18
Equation 5	0.01	0.02	81.05	36.29
Equation 6	0.22	0.10	90.25	81.21

**Table 3:** Statistical significance of the factors and/or their interactions for each model

	F-value					Critical F-value	
	S	F	L	SL	FL	at 95%	at 99%
Equation 3	102.95	209.74	7.83			4.28	7.88
Equation 4	8.49	10.16	206.91	6.34	48.84	4.32	8.02
Equation 5		39.19	74.02			4.26	7.82
Equation 6*		112.45	22.55		5.43	4.28	7.88

\* The model was refitted due to an outlier. It implies only a change of the coefficients with significant factors kept the same, which is why the F-values given are those calculated before refitting the model.

#### 3.1. Geometry

The effect of the process parameters on the first diameter shear formed is given by the following equation:

$$\text{First diameter shear formed (mm)} = 249.264 - 0.003 S + 1.973 F - 0.132 L \quad (3)$$

The 95% confidence interval of this prediction is  $\pm 0.10\text{mm}$ ; the factor C has no impact. Increasing F and/or decreasing S leads to an increase in the first diameter shear formed. If the lubricant is used, a smaller first diameter is obtained for the same set of parameters (S, F). These results are illustrated by Figure 3. According to Figure 3, in order to obtain the target value of the first diameter, the optimum parameters are:  $S=480\text{ m/min}$ ,  $F=0.6\text{ mm/rev}$ ,  $C=0\text{ L/min}$  and lubricant ( $L=1$ ). Using a low feed rate at the first contact point is required to obtain the appropriate diameter.

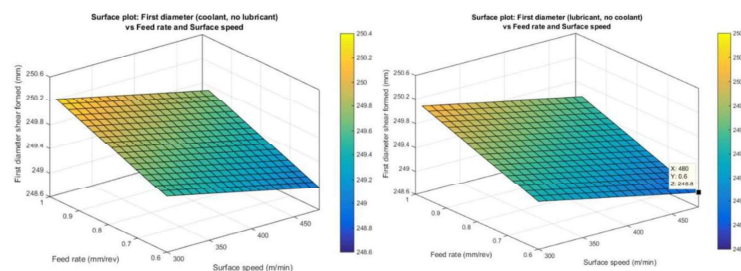


**Figure 3:** Effect of process parameters on the first diameter shear formed

The effect of the process parameters on the angle of shear is given by:

$$\text{Angle of shear (}^\circ\text{)} = 31.919 + 0.001 S - 0.359 F - 0.201 L - 0.001 SL + 1.320 FL \quad (4)$$

The angular accuracy at the 95% confidence interval of this prediction is  $\pm 0.08^\circ$ . The aim is to optimise the angle of shear to be as close as possible to the cone angle ( $31.50^\circ$ ). The optimum parameters are:  $S=300$  m/min,  $F=1$  mm/rev and no lubricant ( $L=0$ ), which results in a  $31.90^\circ$  angle. These parameters are opposite to that required for the first diameter shear formed. Figure 4 shows the different behaviours that the angle of shear follows, where for coolant and no lubricant, the angle of shear rises for an increase in  $S$  and/or a decrease in  $F$ . However, for lubricant and no coolant, the angle of shear is insensitive to  $S$  and increases with increasing  $F$ .

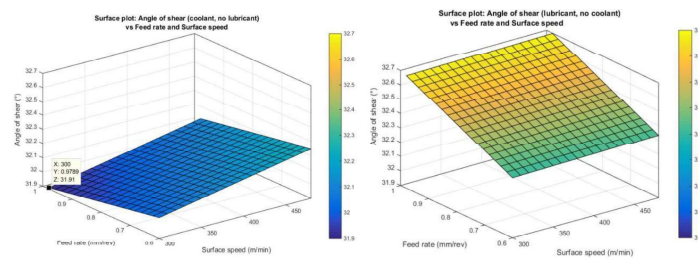


Figure 4: Effect of process parameters on the angle of shear

The average thickness of the part can be predicted as a function of the process variables as given by Equation 5. The results are illustrated by Figure 5.

$$\text{Average thickness (mm)} = 3.203 + 0.144 F - 0.069 L \quad (5)$$

The 95% confidence interval of this prediction is  $\pm 0.01$ mm and the factors  $S$  and  $C$  have no impact. Increasing  $F$  leads to an improvement in the accuracy of the average thickness of the part. A difference in the average thickness of around  $0.07$  mm is dependent on the presence of lubricant. Ideally, the average thickness meets the sine law (1). In this case, for an exact  $31.50^\circ$  angle, the final thickness given is  $3.135$ mm. The works of Kunert et al. did not conclude that the feed rate impacts the average wall thickness. This might be explained by the predominance of other significant parameters not considered as variables in this study.

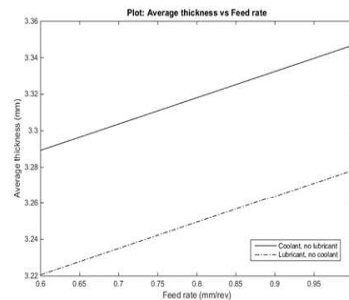


Figure 5: Effect of process parameters on the average thickness

### 3.2. Surface finish

The average Ra value of the part can be predicted as a function of F and L:

$$\text{Average Ra value } (\mu\text{m}) = 0.012 + 1.508 F - 0.143 L + 0.469 FL \quad (6)$$

The 95% confidence interval of prediction for this model is  $\pm 0.08\mu\text{m}$ . Whatever the value of F, the average Ra value is lower when shear forming with coolant and no lubricant. The minimum values occur when the minimum feed rate is used. According to (Chen et al., 2001), (Runge, 1993) and (Kunert et al., 2005) a lower feed ratio (feed rate over spindle speed) leads to a better surface finish. In this study, a lower feed rate leads to a better surface finish and the spindle speed had no measurable impact. This difference to the literature does not seem to originate from the difference of material, thickness or even the tool nose radius. The formula given by (Runge, 1993) suggests that the impact of the spindle speed is the same for every set of parameters. Furthermore, in (Chen et al., 2001) the thickness is taken into account and whatever its value, the same tendencies are observed. In the current study, the spindle speed was changing during the process to allow a constant surface speed which may explain why the impact of the spindle speed on the surface finish is inexistent. All the values recorded in both cases meet the specification for this part:  $Ra < 3.2\mu\text{m}$ .

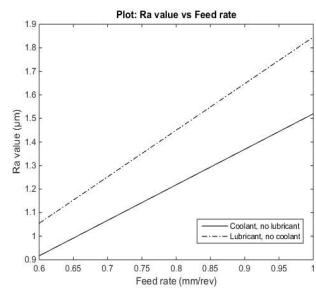


Figure 6: Effect of process parameters on the average Ra value

### 3.3. Metallurgy

Figure 7 shows the typical microstructures observed in areas M1 and M5 of the same part, see Figure 2. The microstructure of the plate pre-form has an average grain size of  $20\mu\text{m}$  (ASTM 8-9), M1. After shear forming, the deformed grains are elongated in the shear forming direction,

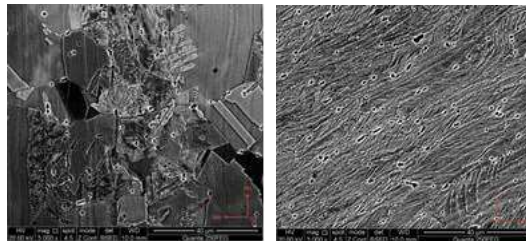


Figure 7: Microstructures before (M1, left) and after (M5, right) shear forming, 304L stainless steel

M5. They have aligned shear bands with a principal spacing on the order of  $1\mu\text{m}$ . The hardness in this area is 368HV1 compared to the hardness of 186HV1 prior to shear forming.

#### 4. CONCLUSION

The geometrical dimensions are mainly controlled by the tool path and the mandrel/roller clearance. However, in this study, it is clear that the surface speed, feed rate and use of lubricant have a measurable impact on the geometry and surface finish of the parts. Not underestimating the impact of such process parameters is crucial. Equations have been derived to characterise the relationships between the inputs and outputs as well as the interactions between the different input parameters. These allow a prediction of the system response. The feed rate has a dominant effect as shown by Equation 3 to Equation 6; this makes it the main process parameter to understand and control.

Shear forming has a clear effect on the microstructure and hardness. Further detailed assessments such as Electron Back-Scatter Diffraction (EBSD) analysis are planned to better characterise the effect of the process on microstructure.

#### ACKNOWLEDGEMENT

Special thanks to the company Rolls-Royce for its financial support and to the Advanced Research Forming Centre (AFRC) for its co-operation. A particular mention to Stephen Ross, who provided valuable guidance during the shear forming trials.

**REFERENCES**

Chen, M. D. Hsu, R. Q. Fuh, K. H., 2001, Forecast of shear spinning force and surface roughness of spun cones by employing regression analysis, *International Journal of Machine Tools and Manufacture*, vol. 41, no. 12, pp. 1721-1734

Grove, D.M. and Davis, T.P., 1992, *Engineering Quality & Experimental Design*, New York: Longman Scientific & Technical

Keller, G., 2001, *Applied Statistics with Microsoft Excel*, USA: Duxbury, Thomson Learning

Kunert, J., Ewers, R., Kleiner, M., Henkenjohann, N. and Auer, C., 2005, Optimisation of the shear forming process by means of multivariate statistical methods, Technische Universität Dortmund, Dortmund

Runge, M., 1993, *Spinning and Flow forming*, Landsberg/Lech: Leifield GmbH, Werkzeugmaschinenbau/Verlag Moderne Industrie AG



# **Appendix B**

## **Paper B**

This appendix contains Paper B, which principally studied the final microstructure of the components in order to establish the deformation mechanism involved when shear forming. This paper was presented at the 12<sup>th</sup> International Conference on Technology of Plasticity in September 2017 and Chapter 5 of this thesis is partially based on it.



Available online at [www.sciencedirect.com](http://www.sciencedirect.com)

ScienceDirect

Procedia Engineering 00 (2017) 000–000

Procedia  
Engineering

[www.elsevier.com/locate/procedia](http://www.elsevier.com/locate/procedia)

International Conference on the Technology of Plasticity, ICTP 2017, 17-22 September 2017,  
Cambridge, United Kingdom

## Shear forming of 304L stainless steel – microstructural aspects

M. Guillot<sup>a,\*</sup>, T. McCormack<sup>b</sup>, M. Tuffs<sup>b</sup>, A. Rosochowski<sup>a</sup>, S. Halliday<sup>b</sup>,  
P. Blackwell<sup>a</sup>

<sup>a</sup>University of Strathclyde, 75 Montrose Street, Glasgow G1 1XJ, United-Kingdom

<sup>b</sup>Rolls-Royce, PO Box 31, Derby DE24 8BJ, United-Kingdom

### Abstract

Shear forming is an incremental cold forming process. It transforms 2D plates into 3D structures commonly consisting of conical geometry. Roller(s) push the blank onto a cone-shaped mandrel, resulting in a decrease of the initial thickness. The shear forming process has diverse advantages, such as improved material utilisation, enhanced product characteristics, good surface finish, consistent geometric control and reduced production costs. Shear forming has potential applications in a wide range of conical geometries used within advanced aerospace structures, which are currently manufactured from bulk forgings with high associated machining costs.

Research findings related to shear forming have been published over the past two decades, however, important remaining questions have still to be answered, with this paper addressing one such gap associated with the material deformation mechanism. Several studies have demonstrated the impact of key process variables on the final geometry and surface roughness, such as the feeds, roller nose radius and mandrel/roller offset. Although the material outputs are essential, as they link directly with the mechanical properties of the final components, the microstructure and texture of the material after shear forming have rarely been studied. Achieving a greater understanding in this area could reduce the reliance upon mechanical testing to validate the process and ease the exploitation route of the technology into advanced aerospace applications.

Firstly, this paper presents the principle of shear forming and its related terminology. Then, a brief overview of the shear forming process including its history and origin is given. The areas of focus are a selection of the main variables encountered within this process which could impact the final properties. The generation of local stresses due to deviations from the sine law, the angle variations, and forces required during the forming operation are also considered. This is explored in the context of forming 304L stainless steel plates.

\* Corresponding author.

E-mail address: [marine.guillot@strath.ac.uk](mailto:marine.guillot@strath.ac.uk)

1877-7058 © 2017 The Authors. Published by Elsevier Ltd.

Peer-review under responsibility of the scientific committee of the International Conference on the Technology of Plasticity.

This paper is written based upon experiments which observed a 52% thickness reduction using one roller. Scanning Electron Microscopy (SEM), Electron BackScatter Diffraction (EBSD) and hardness testing were utilised to characterise the shear formed material. The initial heterogeneous microstructure with relatively equiaxed grains evolved into a microstructure with elongated grains along with shear bands. A texture analysis revealed a simple shear mechanism of deformation, and theoretical and experimental shears were found to match.

Identifying the mechanism of deformation was the first step to a better understanding of the effect imparted by the shear forming process on the material. Further studies will look at the impact of the key process variables on both the microstructure and texture as well as heat treatment optimisation.

© 2017 The Authors. Published by Elsevier Ltd.

Peer-review under responsibility of the scientific committee of the International Conference on the Technology of Plasticity.

*Keywords:* incremental forming; shear forming; stainless steel; simple shear.

## 1. Introduction

Shear forming is also known as flow forming, shear spinning, shear turning, power spinning, or spin forging. It is an incremental cold forming process which manufactures rotationally symmetrical conical, concave, or convex hollow profiled engineering components. Minimal waste and a dimensional accuracy similar to that of machined components are obtained using today's CNC flow formers. Shear forming should not be mistaken for conventional spinning, as the latter combines tension and compression of the material without intentional thickness reduction of the starting blank. Conversely, shear forming involves only compression forces and reduces the initial material thickness [1]. Although spinning methods were born with the art of potting clay in ancient Egypt [2], the first papers mentioning shear forming were published 60 years ago and its expansion has mainly occurred over the past two decades.

Fig. 1 describes shear forming's three operational steps: 1. a flat circular blank is clamped against a mandrel by a tailstock; 2. the mandrel is rotated; 3. one or more rollers then force the blank to incrementally take the shape of the mandrel by following a programmed path using a controlled feed rate. Generally, only a single pass is required to produce the final shape but multiple passes can be undertaken to enhance dimensional control.

The final thickness of the part,  $S_1$ , is determined from the sine law (Equation 1), where  $\alpha$  is the angle of the mandrel and  $S_0$  the initial blank thickness. The key impact of the sine law is that a small angle  $\alpha$  will produce a smaller thickness  $S_1$ , requiring larger levels of deformation. As such, the minimum angle of the mandrel possible to shear form is in the range 10 to 18°, dependent on the material being formed; smaller angles as low as 3 to 4°, however, can be achieved using multiple passes [1]. Deviations from the sine law are sometimes observed and lead to failure or defects in the part, which are due to induced stress, a phenomenon directly noticeable on the flange of the workpiece. Material build-up is one of the main causes of deviation and can be prevented by using more rollers and/or multiple passes [3].

$$S_1 = S_0 \cdot \sin(\alpha) \quad (1)$$

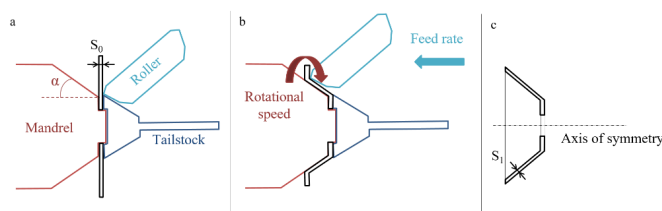


Fig. 1. Shear forming principle: (a) Set-up; (b) In operation; (c) Part completed.

During shear forming, axial, radial, and tangential forces are generated between the blank and the roller, out of which the tangential force is usually found to be the smallest. Multiple researchers have attempted to calculate the latter by considering shear deformation or a combination of shear deformation and bending strain. In 2001, Chen et

al. [4] linked these forces to the process variables and in 2003, Kim et al. [5] obtained convergence of experimental and theoretical tangential forces by considering a pure shear model. Understanding the forces required to shear form a blank is essential to define the limitations of such a process and this involves understanding the material behavior as well as the effect of process parameters. Although Zhan et al. [6] and Radović et al. [7] studied the microstructure and texture of shear formed components made of Al and Al-Mg alloys, the material deformation mechanism was not identified. Common materials currently industrially shear formed are steel, copper, aluminum, and nickel, plus a much wider range of materials have been successfully shear formed in laboratory trials [1]. Potential future applications include a wide spectrum of conical structures used in gas turbine engines, aerospace structures and military equipment.

## 2. Experimental set-up

The material used in this study was a 6 mm thick 304L stainless steel sheet that had been hot rolled, solution annealed, and pickled in accordance with the standard EN 10088-2. Its chemical composition and mechanical properties are given by Tables 1 and 2 respectively. Prior to shear forming, the blanks were water jet cut with an external diameter of 430 mm and an internal diameter of 150 mm.

Table 1. Chemical composition (% by mass) of the as-received sheet.

C	Cr	Mn	N	Ni	P	S	Si
0.018	18.050	1.773	0.067	8.035	0.031	0.002	0.449

Table 2. Mechanical properties of the as-received sheet.

Ultimate tensile strength	Yield strength at		Elongation after fracture		Vickers hardness
	0.2%	1%	A50	A5	
635 N/mm <sup>2</sup>	348 N/mm <sup>2</sup>	391 N/mm <sup>2</sup>	52 %	53 %	186 HV1

Shear forming experiments were carried out at the Advanced Forming Research Centre (AFRC) – University of Strathclyde, using a WF Maschinenbau 3-roller-flow forming and spinning machine of the type STR 600 3/6 pictured in Fig. 2 (a). One 3 mm nose radius roller was utilised to shear form the blanks onto a mandrel with a 31.5° angle, which according to the sine law corresponds to a thickness reduction of 52%. The resultant geometrical transformation is shown by Fig. 2 (b). During the process, the surface speed and feed rate were held constant at 480 m/min and 1.0 mm/rev respectively. An oil-based coolant, Houghton Hocut 795B, was employed at a flow rate of 400 L/min.

Five specific areas of interest taken from a cross-sectional slice of the final parts, identified by Fig. 2 (c), were then analysed using Scanning Electron Microscopy (SEM) and Electron BackScattered Diffraction (EBSD), with a microscope type FEI Quanta 250 FEG. Hardness tests were performed using a micro-hardness tester of type Zwick-Roell Indentec ZHμ, at 1 kg force. The measurements were made in accordance with the ISO 6507-1 standard. The level of confidence in the results was of 95%. The values taken into account for this study are an average of the three indents across the thickness of the sample.

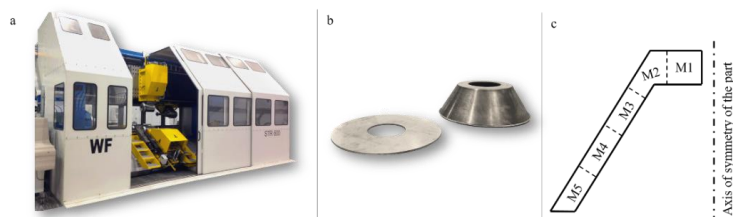


Fig. 2. (a) Flow former; (b) Blank and shear formed part; (c) Areas of metallurgical interest.

Micrographs were taken in BackScatter (BS) mode. The coordinate systems adopted for reporting the microstructural data of area M1 were the rolling direction (RD), transverse direction (TD) and normal direction (ND) whereas the cylindrical coordinates (R,  $\theta$ , Z) were used for the remaining areas. The texture was analysed by EBSD with a step size of 1.0 and 0.3  $\mu\text{m}$  for the as-received and shear formed areas respectively. Pole Figures (PFs) and Orientation Distribution Functions (ODFs) were displayed using the settings given by Tables 3 and 4.

Table 3. Settings employed to generate the PFs.

Half width	Cluster size	Coordinate system	Projection type	Projection hemisphere	Planes	Colours	Contour lines
10°	5°	R, $\theta$ , Z	Stereographic	Upper	{100}, {110}, {111}	Max. intensity at 6	Step width of 1.5 Max. at 6

Table 4. Settings employed to generate the ODFs.

Half width	Cluster size	Coordinate system	Colours	Contour lines	Sample symmetry	Method	Resolution	Calculation
Gaussian, 5°	5°	R, $\theta$ , Z	Rainbow	At 2, 4, 6, 8, and 10	Triclinic	Gaussian estimation	128x32x32	Based on full map

### 3. Results and discussion

Fig. 3 shows the micrographs of the part in the different areas of interest. From EBSD analysis it was estimated that the as-received material, represented by area M1, had approximately equiaxed grains with an average grain size of 11.3  $\mu\text{m}$  (ASTM 9.5-10) with 70% of the grains being under or equal to 10.0  $\mu\text{m}$ . The initial material was heterogeneous and had a relatively weak rolling texture.

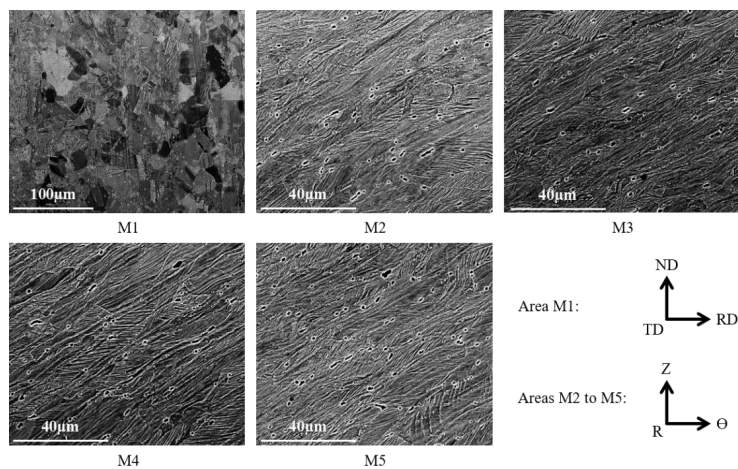


Fig. 3. Micrographs along the shear formed part.

The shear formed areas, M2 to M5, presented elongated grains and only slight microstructural differences were noticed. Shear bands representative of high local deformation during plastic deformation were observed. They presented primary orientations along the  $\theta$  axis of the cylindrical coordinates and slightly tilted from the shear forming direction. These aligned shear bands were ascertained with a principal spacing around 1  $\mu\text{m}$ . Simple shear, a specific

mechanism of deformation, is detected when one direction of the initial material which is free to rotate on both ends remains constant and everything else rotates relative to it. Fig. 4 (a) illustrates this phenomenon with the transformation of a square to a rhombus along with the rotation of the ellipsoid axes from their original position, which is another characteristic of simple shear. This mechanism was identified on the BS images of Fig. 3 (areas M2 to M5) where elongation of the grains and shear bands along the main ellipsoid axis are shown. Although the actual stress-strain state in the material can be significantly triaxial and complex, the model of the process can be simplified assuming that at each contact between the roller and material only elementary simple shear takes place. In this case, the intensity of this shear,  $\gamma$ , can be estimated as  $\alpha$  tangent. Fig. 4 (b) is the plot of the shear as a function of the angle of the mandrel. The shear for the current geometry was about  $\gamma=1.6$ .

An EBSD map was acquired in the middle of the thickness of area M4 and an austenite to martensite transformation was observed. The PFs are given by Fig. 5. According to the Kurdjumov-Sachs orientation relationship, the plane  $\{111\}_{fcc}$  is parallel to  $\{110\}_{bcc}$ . This can be seen in these specific PFs as they show the same elements in identical areas, which is characteristic of shear transformation. This transformation of austenite to martensite was also proved by the part becoming magnetic. By comparing the PF  $\{111\}_{fcc}$  with the PFs presented by Barnett et al. [8], an equivalent strain of about 1.7 was identified. Few of the main torsion texture components, which are defined in Fig. 6, were noticed on the PFs  $\{111\}$ .

To look at this deformation in more detail, ODFs were calculated. In the case of simple shear deformation, the specific components B and  $\bar{B}$  are identified on ODFs displayed at  $\Phi=55^\circ$  and  $\Phi_2=45^\circ$ . They are generally observed for these settings at  $\Phi_1=0, 120, 240^\circ$  and  $\Phi_1=60, 180, 300^\circ$  for B and  $\bar{B}$  respectively [9]. The ODFs of both fcc and bcc phases are given by Fig. 5. In both cases, the components B and  $\bar{B}$  were identified whereas the components  $A_1^*$ ,  $A_2^*$  and C only appeared clearly for the fcc phase. According to these results, the mechanism of deformation was simple shear.

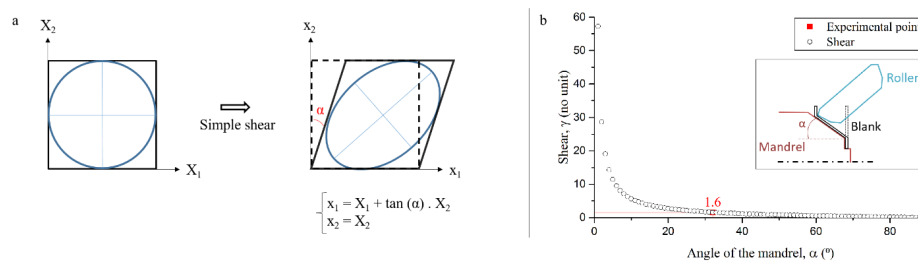


Fig. 4. Simple shear: (a) Illustration of the principle; (b) Plot of the shear as a function of the angle of the mandrel.

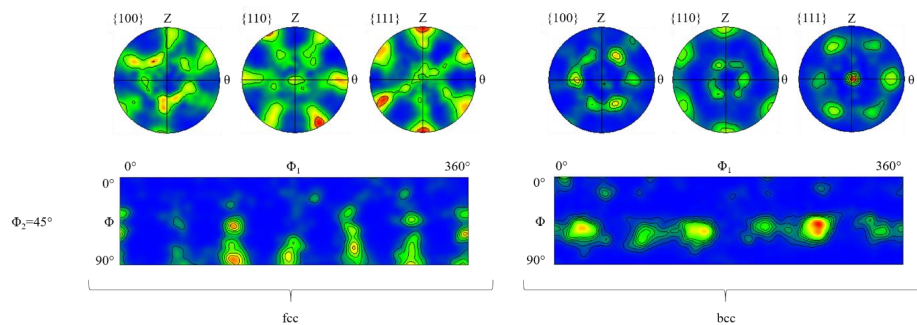


Fig. 5. Texture representations for the middle of the thickness of area M4 (top: PFs; bottom: ODFs).

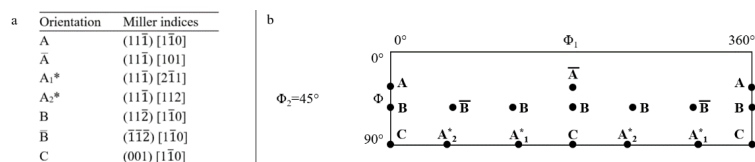


Fig. 6. Main torsion texture components: (a) Miller indices; (b) Representation on ODFs.

Some low-force hardness tests were performed to see if the hardness changed across the part. The results for area M1, considered as the as-received material, met the data given by the material certificate in Table 2. The outcomes showed a variation within the part of 5HV1 in the shear formed areas, which suggests that the microstructure is reasonably homogeneous in this area, as is borne out in Fig. 3. The highest hardness values were recorded at the transition of as-received and shear formed areas with 370HV1.

#### 4. Conclusions

The initial material with relatively equiaxed grains evolved to a structure with elongated grains after being shear formed. Its hardness doubled during the process to reach values around 370HV1. High local deformation was observed in the form of shear bands along the  $\theta$  axis of the cylindrical coordinates and slightly tilted from the shear forming direction. Micrographs and hardness analysis showed a homogeneous microstructure along the shear formed length of the part. A transformation of austenite to martensite was observed, which was proved in practice by the part becoming magnetic. The main mechanism of deformation was identified as simple shear thanks to experimental and theoretical shears and identification of the main torsion texture components on the PFs and ODFs for both fcc and bcc phases of the material.

Shear forming has a clear effect on the microstructure, hardness and texture of the material. The effect of process parameters on the resulting material characteristics of the formed component is of great relevance to this technology and further studies should explore this area. Also planned are detailed assessments across the thickness of shear formed parts to establish the existence of any gradient. These are important considerations which should be included at the early design stage of any engineering component shaped by shear forming.

#### Acknowledgements

Special thanks to Rolls-Royce and the Engineering and Physical Sciences Research Council (EPSRC) for their financial support. A particular mention to the University of Strathclyde, especially the AFRC, whose co-operation and technical assistance were greatly appreciated.

#### References

- [1] M. Runge, Spinning and flow forming, Leifeld GmbH, Ahlen, 1993.
- [2] C.C. Wong, T.A. Dean, J. Lin, A review of spinning, shear forming and flow forming processes, *Int. J. Mach. Tools Manuf.* 43 (2003) 1419-1435.
- [3] O. Music, J.M. Allwood, K. Kawai, A review of the mechanics of metal spinning, *J. Mater. Process. Technol.* 210 (2010) 3-23.
- [4] M.D. Chen, R.Q. Hsu, K.H. Fuh, Forecast of shear spinning force and surface roughness of spun cones by employing regression analysis, *Int. J. Mach. Tools Manuf.* 41 (2001) 1721-1734.
- [5] C. Kim, S.Y. Jung, J.C. Choi, A lower upper-bound solution for shear spinning of cones, *Int. J. Mech. Sci.* 45 (2003) 1893-1911.
- [6] M. Zhan, X. Wang, H. Long, Mechanism of grain refinement of aluminium alloy in shear spinning under different deviation ratios, *Mater. Des.* 108 (2016) 207-216.
- [7] L. Radović, M. Nikačević, B. Jordović, Deformation behaviour and microstructure evolution of AlMg6Mn alloy during shear spinning, *Trans. Nonferrous Met. Soc. China* 22 (2012) 991-1000.
- [8] M.R. Barnett, F. Montheillet, The generation of new high-angle boundaries in aluminium during hot torsion, *Acta Materialia* 50 (2002) 2285-2296.
- [9] M.M.Z. Ahmed, The development of thick section welds and ultra-fine grain aluminium using friction stir welding and processing, University of Sheffield, 2009.

# Appendix C

## Equipment

Appendix C gives more detail on the equipment presented in Chapter 4. Its technical data are provided as well as the related calibration routes, standards and/or specifications, and procedures. Their understanding was essential to ensure accurate comparisons with future work. When appropriate, the methodology employed is also explained in more detail.

First, the technical data, shear forming configuration, CNC program, data outputs, and calibration and procedures of the flow former are described. Secondly, the machines used for the metallurgical analysis are detailed, which includes the material preparation, the microstructure and texture observations and analyses, and the hardness study. Secondly, the concept of surface texture is discussed and the factors affecting surface texture are discussed. The measurement of the surface roughness with non-contact and contact methods is highlighted. Then, the section dedicated to the geometrical analysis presents the contact and non-contact instruments. The measurement methods involved in their use are described.

### C.1 The flow former

#### C.1.1 Introduction

As previously mentioned, the machine which shear formed the parts was a 3-Roller-Flow Forming and Spinning Machine. According to WF Maschinenbau und



Blechformtechnik GmbH (c. 2014), the German manufacturer of the flow former, “The machine is designed for flow-forming of tubes and rotationally symmetric hollow bodies with constant or varying wall thicknesses. The machine design allows economic production of parts with bottom in forward [i.e. cup shaped] and tubes in reverse flow-forming.”. This industrial scale machine is approximately 9.3 m long, 4.2 m high, and 4.8 m wide. It is used for cylindrical flow forming, spinning, shear forming or a combination of these processes. The delivery of the flow former to the AFRC occurred at the end of October 2013 and is illustrated in Figure C.1. The final commissioning was completed on the 9<sup>th</sup> of December 2013, with the first part shear formed the following week.



*Figure C.1: Delivery and installation of the flow former at the AFRC.*

### C.1.2 Shear forming configuration explained

When set up for shear forming, the physical configuration of the flow former remains the same. Figures C.2 and C.3 (pp. 153–154) show the arrangement of the flow former with the tooling geometry employed for the site acceptance trials as well as the roller geometry. The main elements of the shear forming tooling are listed below:

- The mandrel insert (4) was tethered to the mandrel (2) by the cylinder (5). The blank was located on the mandrel insert, whose final geometry was defined by the profile of the mandrel. These two elements were not one unique part for two

reasons. Firstly, the design of the mandrel insert depended on the internal diameter and thickness of the blank. Since it was conceivable that multiple parts, with varying internal diameters and/or wall thicknesses, might have been required to be formed on a single mandrel, it was advantageous that the mandrel consisted of two elements which could be fully removed from each other. This would help reduce costs in terms of tooling and also manufacturing time since it would be more efficient to change only the mandrel insert rather than the full mandrel. Secondly, it was not uncommon for the shear formed part to become stuck on the mandrel post forming due to the heat and work generated throughout the shear forming process. In this case, an ejector (area C8-D8 in Figure C.2) pushed the mandrel insert slightly out from the mandrel, which indirectly forced the part clear of the mandrel.

- The tailstock adaptor (7) and tailstock (8) were bolted together. They clamped the blank into position. Like the mandrel insert, the tailstock adaptor was removable to reduce costs and manufacturing time. Its design was dependent on the design of the mandrel insert as shown in Figure C.2.
- The roller (0) and its housing are apparent in Figure C.2 in the upper middle section of the machine assembly drawing. The roller deformed the material onto the mandrel during the shear forming operation.

### C.1.3 Technical data

The technical capabilities of the flow former are given in Table C.1. There were three rollers available with the set-up of this machine, which were positioned at 120° apart. For cylindrical flow forming, all three rollers were forming whereas in shear forming only one or two rollers were typically utilised. For ease of tool changing, it was usually one (or two) of the bottom rollers that was used for shear forming, as can be seen in Figure C.4-(a).

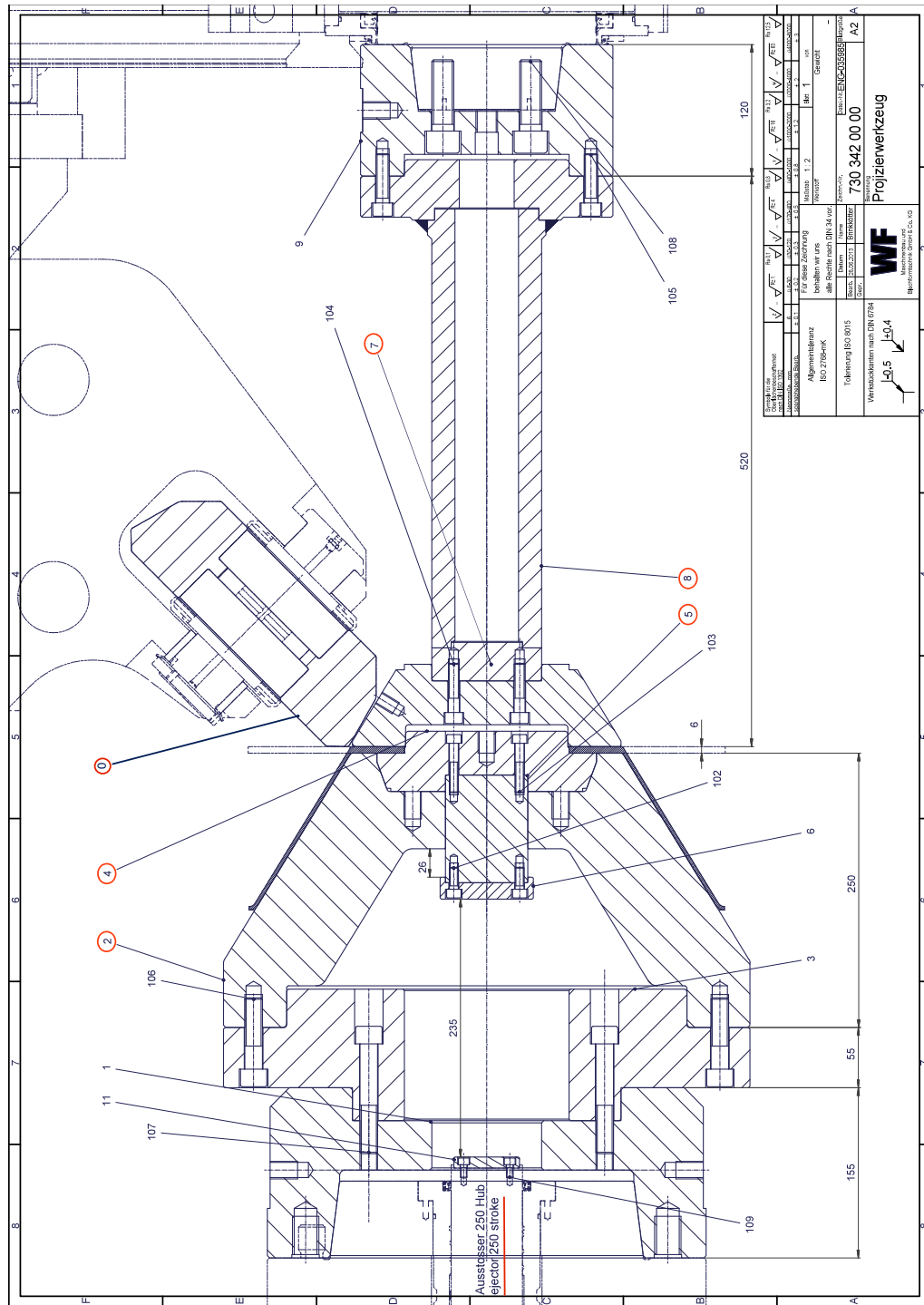


Figure C.2: Assembly drawing of the 31.5° geometry – 730 342 00 00 “Projizierwerkzeug”.



*Table C.1: Flow former capabilities: Feed, spindle speed, coolant, and geometry (WF Maschinenbau und Blechformtechnik GmbH, 2013).*

<b>Feed capabilities</b>	
Movement of the flow forming support	Length direction: max. each 2,600 mm Radial direction: each 315 mm
Feed force of the 3 flow forming supports	Length direction: max. each 500 kN Radial direction: each 350 kN
Working speed of the 3 flow forming supports	Length direction: max. 2 m/min Radial direction: max. each 5 m/min
Fast speed of the 3 flow forming supports	Length direction: max. 10 m/min Radial direction: max. 1 m/min
<b>Spindle speed capabilities</b>	
Revolution number of main spindle	120–700 RPM
Main spindle: Gear 1	120–240 RPM
Main spindle: Gear 2	240–400 RPM
Main spindle: Gear 3	400–700 RPM
<b>Coolant capabilities</b>	
Flow rate of coolant pump	Approx. 400 L/min
Type of coolant	Houghton Hocut 795B (oil-based)
<b>Geometry capabilities</b>	
Workpiece diameter	60–600 mm
Material thickness	Suggested max. 12–15 mm

#### C.1.4 CNC program

The flow former used CNC code to individually program each of the main axes, i.e. the X and Z directions of the roller(s) (Figure C.4-(b)), as well as the direction and speed of the main spindle. The CNC code was divided into two sections – the set-up and working files.

### C.1.4.1 Set-up file

The set-up file was composed of the following elements:

- A subsection for each of the three rollers which included their positions, dimensions, and offsets
- A subsection “Tooling/Spindle/Tailstock Settings” which specified the dimensions of these elements as well as the material thickness, machine gear, and starting spindle speed,  $Sp$
- A subsection for the “W Axis/Tailstock Settings” which gave the positions of the tailstock and tailstock adaptor, and the clamping force to be exerted by the tailstock during forming. The “W axis” subsection also contained an option to include a fix-stop function into the program. This function acted to slow down the approach of the tailstock as it neared the clamping point of the part in order to reduce the risk of tooling/part collisions. The W axis was defined by the centreline of the tailstock.
- A subsection “Stripper Settings” which was only used for cylindrical flow forming
- A subsection “Centre Cylinder Setting for Load/UnloadPart” which defined the position of the Q axis, where the axis centreline was defined by the centreline of the mandrel insert
- A subsection “Roller Holder Settings” which defined the offsets and angles of the roller housings
- A subsection “Program Settings” included the offsets between rollers, and whether or not these offsets were applied. This subsection also allowed for the ejector, stripper, W and Q axes to be enabled or disabled.

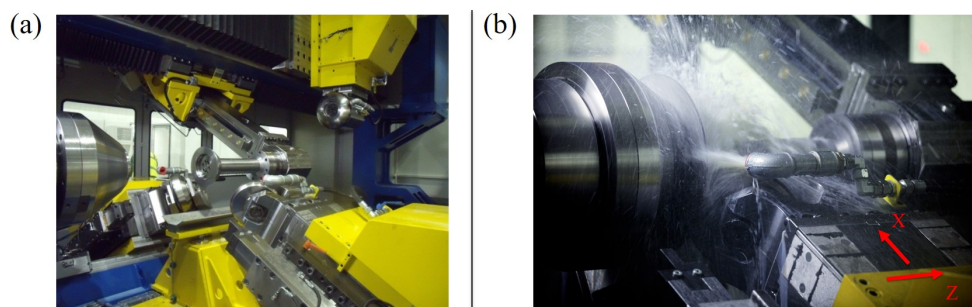


Figure C.4: (a) Shear forming set-up and (b) Shear forming operation.

### C.1.4.2 Working file – Chapter 5

The working file was where the main programming was stored and defined the tool path, feed rate, and spindle speed. The CNC program used for the trials presented in Chapter 5 was written by WF according to the AFRC's requirements. Its working file is given in Figure C.5.

```

; - Start of Working Channel 1 / Support 1-
;
;=====
N010 G18 G55 G90 G94 Diamof
N020 G55 G01 X2=123.25 X3=123.25 F1000
N025 G55 G01 Z2=5.90 Z3=5.90 F1000
N030 G95
N110 LIMS=700
N120 G96 S400 M03 M10
N130 G01 X2=123.25 Z2= 5.9 X3=123.25 Z3= 5.9 F=1.0
N140 G01 X2=129.984 Z2=-5.0 X3=129.984 Z3=-5.0
.....
N150 G01 X2=206.434 Z2=-130.0 X3=206.434 Z3=-130.0
N155 G97
N160 G94 G01 X2=223.85 Z2=-130.0 X3=223.85 Z3=-130.0 F1000 M05 M11
;=====
;
; - End of Working Channel 1 / Support 1-

```

Figure C.5: CNC program: Working file used during the commissioning.

The main elements of this working file were:

- The feed rate: “G94”, lines N010 and N160, involved a linear feed rate ( $F_m$ ). It was set at 1000 mm/min when approaching and retracting the rollers as indicated at lines N020, N025, and N160 by “F1000”. “G95”, line N030, involved a revolutionary feed rate ( $F$ ). During the forming operation,  $F$  was set at 1.0 mm/rev as seen at line N130 with “F=1.0”.
- The spindle speed and surface speed: As expressed at line N110, the spindle speed ( $Sp$ ) was limited at 700 RPM, which was the machine capability. As explained in Chapter 2, Subsection 2.4.1 (p. 17), either  $Sp$  or  $Su$  is kept constant when shear forming. “G96 S400”, line N120, provided a constant surface speed ( $Su$ ) of 400 m/min. A constant  $Sp$  could be obtained by using “G97”. “M03”, line N120, showed that the mandrel was rotating clockwise.

- The tool path: The two bottom rollers of the flow former were carrying out the forming. Their set of coordinates were (X2, Z2) and (X3, Z3). As the zero of the work offset was at the front face of the mandrel for the Z axis, the first Z coordinates represented the thickness of the blank, which was measured at 5.9 mm as indicated at lines N025 and N130.

The first X coordinates were “X2 = 123.25” and “X3 = 123.25”, lines N020 and N130. They were calculated as shown below considering the points A (Xa, Za = 0), B (Xb, Zb = 5.9), and C (Xc, Zc = 5.9) given in Figure C.6.

$$X_c = \underbrace{\frac{247.7}{2}}_{X_a} - 5.9 \times \tan(31.5^\circ) + \frac{2.57}{\cos(31.5^\circ)} = 123.25$$

Xb

247.7 mm and 2.57 mm were the mandrel first diameter and the gap between roller and mandrel chosen by WF according to their knowledge of the shear forming process.

“X2 = 129.984 Z2 = -5.0 X3 = 129.984 Z3 = -5.0” was the second set of coordinates. The angle followed by the tool path was set at 31.7° as demonstrated below.

$$\tan^{-1}\left(\frac{129.984 - 123.25}{5.9 + 5}\right) = 31.7^\circ$$

“X2 = 206.434 Z2 = -130.0 X3 = 206.434 Z3 = -130.0” was the next set of coordinates. The angle was reduced from 31.7° to 29.36°.

$$\tan^{-1}\left(\frac{206.434 - 129.984}{5.9 + 130}\right) = 29.36^\circ$$

This change was justified by WF as a way to better control the springback, which corresponds to an inclination of the tool path as presented in Chapter 2, Subsection 2.4.1 (p. 16).

“X2 = 223.85 Z2 = -130.0 X3 = 223.85 Z3 = -130.0” was the last set of coordinates used for the extraction of the rollers.

### C.1.4.3 Working file – Chapter 7

The shear forming program was written using the ATI-SF program for the 43° geometry as a guide. Figure C.7 gives the new working file for a part with an initial thickness of 15.32 mm to be run with *F* and *Sp* at 0.5 mm/rev and 150 RPM. The meaning of the codes for the feed rate and spindle speed was provided in in the



previous sub-subsection and thus only the tool path is discussed here.

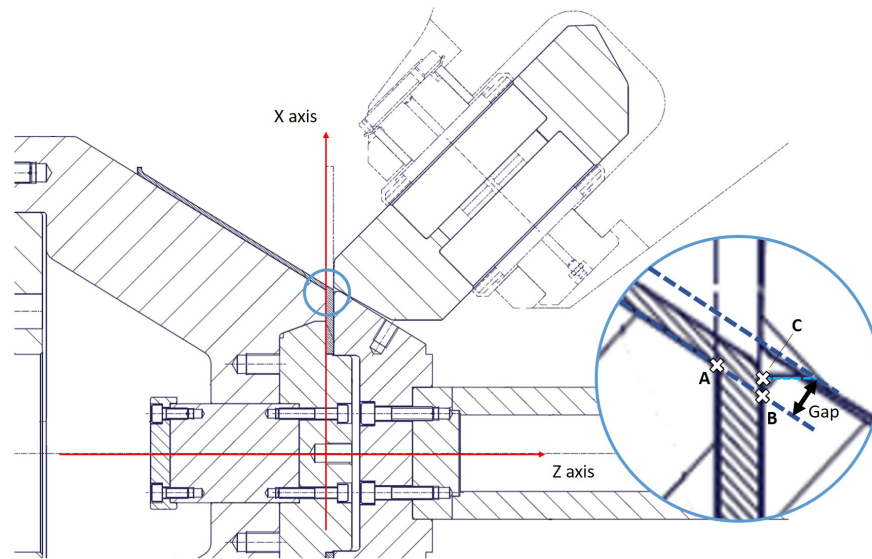


Figure C.6: CNC program: Illustration first set of X coordinates.

```

; - Start of Working Channel 1 / Support 1-
;
;=====
N010 G18 G55 G90 G94 Diamof
N020 G55 G01 X3=104.465 F250
N030 G55 G01 Z3=15.32 F250
N040 G95
N050 LIMS=600
N060 G97 S150 M03 M10
N070 G01 X3=104.465 Z3= 15.32 F=0.5 ; Start point
N080 G01 X3=198.868 Z3=-85.915 ; End point of cone
N090 G01 X3=198.868+5 Z3=-85.915+5 ; Roller slightly retracted
N100 G94 G01 X3=245.0 Z3=-75.0 F1000 M05 M11 ; Roller fully retracted
;=====
;
; - End of Working Channel 1 / Support 1-
;
;=====

```

Figure C.7: Working file of the CNC program – 43° geometry, 15.32 mm thick blank.

Only one roller was forming, roller 3, which was located at the bottom of the flow former and closest to the machine door. Its coordinates were (X3,Z3). As the zero of

the work offset was at the front face of the mandrel for the Z axis, the first Z coordinate represented the 15.32 mm thickness of the blank, “Z3 = 15.32” at lines N030 and N070. The first X coordinate, “X3 = 104.465” was given in lines N020 and N070. This value was calculated by using the first diameter of the mandrel, here 211.515 mm, and the 9.503 mm gap between rollers and mandrel, which gave the 38.0 % of compressive deformation determined above.

$$X3 = \frac{211.515}{2} - 15.32 \times \tan(43^\circ) + \frac{9.503}{\cos(43^\circ)} = 104.465$$

“X3 = 198.868 Z3 = -85.915”, line N080, was the set of coordinates for the end point of the cone. In this case, the tool path was a straight line. Indeed, changing the angle of the tool path at the beginning of the process to compensate for springback as suggested by WF (see previous sub-subsection) was considered irrelevant by the ATI-SF team. The same method as in the ATI-SF project was followed here. This set of coordinates was calculated considering the last diameter of the mandrel, 389.131 mm, and the 6 mm depth obtained previously.

$$Z3 = -\frac{\frac{389.131-211.515}{2}}{\tan(43^\circ)} + 15.32 - 6.00 = -85.915$$

$$X3 = 104.465 - (-85.915 - 15.32) \times \tan(43^\circ) = 198.868$$

At line N090, “X3 = 198.868 + 5 Z3 = -85.915 + 5” was the third set of coordinates. This was for the roller to move slightly away from the part after forming. The last set of coordinates represented the full extraction of the rollers: “X3 = 245.00 Z3 = -75.00” at line N100.

### C.1.5 Data recording

A key element of this flow former was the ability to record data during the forming process. Recording data was a crucial element of trials as it enabled the following analyses to be conducted:

- Ensure that the recorded values were the same as the input values.
- Reconstruct and check the accuracy of the tool path given by the CNC program.
- Ensure that all KPVs remained within the predetermined limits during the forming operation.
- Link inputs and outputs together.

The machine itself could record up to two parameters at any given time, however, using SinuCom, a Siemens' software, it was possible to document multiple parameters at a time. Training on this software took place in June 2014 at the AFRC. Even though SinuCom was external to the machine controller, the number of parameters that could be registered depended on the memory capacity of the controller. Consequently, if cycle times were short then more parameters could be recorded. It was also possible to change the sampling frequency of the software to register multiple parameters for a longer period of time. For shear forming, the most common parameters documented were:

- Actual positions of each roller on the X and Z axes, shown in Figure C.4-(b)
- Loads of each roller on the X and Z axes
- Spindle speed,  $Sp$

The coolant rate was controlled by valves which were installed inside the flow former and were manually adjustable. At the time of writing, it was not possible to record the coolant rate with either the machine controller or the external software SinuCom. For the coolant rate to be controlled, the installation of a flow meter would be required. As a result, only an approximate value of the coolant rate was known. This was estimated by the extent to which the valves were opened in the machine.

### C.1.6 Calibration and procedures

The calibration of the flow former, when set up for shear forming, included the calibration of the following components:

- Spindle
- Roller(s)
- Tailstock
- Mandrel

For all these elements, the calibration was completed using a dial test indicator to verify the true running of each component. A second verification of the spindle was carried out using a stroboscope on the main spindle at three different values of  $Sp$  (100 RPM, 300 RPM, and 500 RPM). The AFRC's calibration procedure (Ward, 2015) stated that the components listed below should be calibrated after each of the following events:

- Tool change

- Part damage
- Tooling damage
- Tooling collision

In the event of tooling damage or collision, the totality of the tooling may be required to be calibrated depending on the severity and area of the damage. A full calibration record had been maintained since June 2015.

In July 2015, a standard operating procedure was written for the flow former. This provided guidance on the procedure to:

- Set the X and Z offsets.
- Ensure the right CNC program had been loaded onto the machine console.
- Ensure the dimensions of the tailstock, mandrel, spindle, and roller(s) were correct.

A check-list constituted the safe system of protocol and was required to be filled in after a set-up and/or when a different CNC program was loaded onto the machine console. It summarized all the checks that must be completed before any forming operations could take place. For shear forming, five categories were identified for verification, which were CNC program, roller dimensions, mandrel dimensions, tailstock dimensions, and program settings. Furthermore, each month a company specialising in industrial fluids, Houghton, analysed the coolant within the flow former to assess the concentration of the fluid and to check for any contaminations.

## **C.2 Metallurgical analysis**

### **C.2.1 Metallurgical sample preparation**

As explained in Chapter 4, a good metallurgical sample preparation was essential to observe both microstructure and material texture. The first step was the cutting of the samples. In this project, this was completed either with a Buehler abrasive cutter AbrasiMatic™300 or with a Buehler linear precision saw IsoMet™5000 (Figure C.8 – Cutting). This same equipment was used to cut the as-received material.

Secondly, each sample was mounted with a Buehler automatic hot mounting press SimpliMet®3000 (Figure C.8 – Mounting) using a conductive resin, here

PhenoCure. This operation eased the handle of samples during the grinding and mechanical polishing step.

Then, a Buehler grinder-polisher EcoMet<sup>®</sup>300 Pro was employed for the grinding operation using SiC papers with different grit sizes, number of SiC particles per square inch. The mechanical polishing, opposed to the chemical polishing which requires the use of electrodes, involves the use of different cloths and liquid suspensions. The grinding/polishing methods used in this EngD project for Inconel 718 and 304L stainless steel are respectively given in Tables C.2 and C.3. Between each step, the specimen and equipment were cleaned with water to avoid any contaminations. Lastly, a Buehler vibratory polisher VibroMet<sup>®</sup>2 was used to get a high quality polished surface (Figure C.8 – Grinding and polishing). This operation is highly recommended to achieve good results when looking at the material texture. This step was completed using MasterMet Colloidal silica 0.02  $\mu\text{m}$  and MasterPrep 0.05  $\mu\text{m}$  Alumina suspension for Inconel 718 and 304L stainless steel respectively.



*Figure C.8: Metallurgical preparation – Equipment.*

Etching was sometimes necessary to reveal the microstructure. This corrosion of the polished surface uses chemical solutions called etchants. Etchants generally attack the grain boundaries, but a few can also attack other elements such as precipitates and carbides. Conventional etching can be undertaken either using a cotton wool drenched in the specific etchant and applied onto the specimen surface, or the specimen can be dipped in a beaker full of etchant. Depending on the material and its history, this operation lasts from a few seconds to a few minutes.

Table C.2: Grinding and mechanical polishing method applied to Inconel 718 – adapted from Vander Voort (2007).

Surface	Abrasive/Size	Load lb. (N)	Speed (RPM)	Rotation	Time (min)
CarbiMet waterproof paper	P240-grit SiC water cooled	6 (27)	260	Comp*	5
CarbiMet waterproof paper	P400-grit SiC water cooled	6 (27)	260	Comp	3
CarbiMet waterproof paper	P800-grit SiC water cooled	6 (27)	260	Comp	3
CarbiMet waterproof paper	P1200-grit Sic water cooled	6 (27)	260	Comp	3
UltraPol 9 µm	9 µm MetaDi Polycrystalline diamond suspension	6 (25)	150	Contra**	4
Trident 3 µm	3 µm MetaDi Polycrystalline diamond suspension	6 (22)	150	Contra	5
TexMet 1 µm	1 µm MetaDi Polycrystalline diamond suspension	6 (20)	150	Contra	6
MicroCloth 0.05 µm	MasterMet Colloidal silica 0.02 (90% MasterMet 2 + 10% water)	6 (20)	150	Contra	12

\*Comp = Complementary (platen and specimen holder both rotate in the same direction)

\*\*Contra = Platen and specimen holder rotate in opposite directions

Electrolytic etching is another etching method widely employed. The specimen is immersed in the etching solution, electrolyte, and connected to the anode (positive pole) of a direct current source. Then, the cathode (negative pole) is put in contact with the surface of the specimen, and the metal of the anode starts to dissolve. Normally the cathode is platinum or some other passive metal while the specimen is the anode. The duration of this operation depends on the material, the concentration of the electrolyte, and the voltage selected. To avoid the formation of spots, i.e. area etched much more and appearing darker than the rest of the specimen, the cathode is moved on average every 15 s. In this EngD project, for both materials, this method was performed to reveal the grains by attacking the grain boundaries. The electrolyte was a solution of

oxalic acid ( $H_2C_2O_4$ ) and a hydrochloric acid (HCl) solution for 304L stainless steel and Inconel 718 respectively.

*Table C.3: Grinding and mechanical polishing method applied to 304L stainless steel – adapted from Vander Voort (2007).*

Surface	Abrasive/Size	Load lb. (N)	Speed (RPM)	Rotation	Time (min)
CarbiMet waterproof paper	P240-grit SiC water cooled	6 (27)	250	Comp*	5
CarbiMet waterproof paper	P400-grit SiC water cooled	6 (27)	250	Comp	3
CarbiMet waterproof paper	P800-grit SiC water cooled	6 (27)	250	Comp	3
CarbiMet waterproof paper	P1200-grit Sic water cooled	6 (27)	250	Comp	3
UltraPol 9 $\mu$ m	9 $\mu$ m MetaDi Polycrystalline diamond suspension	6 (27)	140	Comp	5
Trident 3 $\mu$ m	3 $\mu$ m MetaDi Polycrystalline diamond suspension	6 (27)	140	Comp	5
MicroCloth 0.05 $\mu$ m	MasterPrep 0.05 $\mu$ m Alumina suspension	6 (27)	120	Contra**	2.5

\*Comp = Complementary (platen and specimen holder both rotate in the same direction)

\*\*Contra = Platen and specimen holder rotate in opposite directions

## C.2.2 Hardness analysis

### C.2.2.1 Specifications and standards

The hardness measurements were performed at the AFRC using the micro-hardness tester Zwick-Roell Indentec ZH $\mu$ -AFHD shown in Figure C.9-(a). Rolls-Royce's engineering specification JES161 specifies that "Hardness testing methods, verification of the equipment and interpretation of the results shall comply with the requirements of MSRR9969." (Rolls-Royce plc, 2013) Rolls-Royce's material specification MSRR9969 states that "Hardness testing, machine calibration

and control procedures shall be in accordance with one of the relevant international standards detailed below, except where this document overrides.” (Rolls-Royce plc, 2012); for Vickers hardness test, ISO standard 6507 and ASTM E384. Therefore, the measurements were carried out following the ISO standard 6507-1 as described in Chapter 4, Subsection 4.2.2 (pp. 53–54).

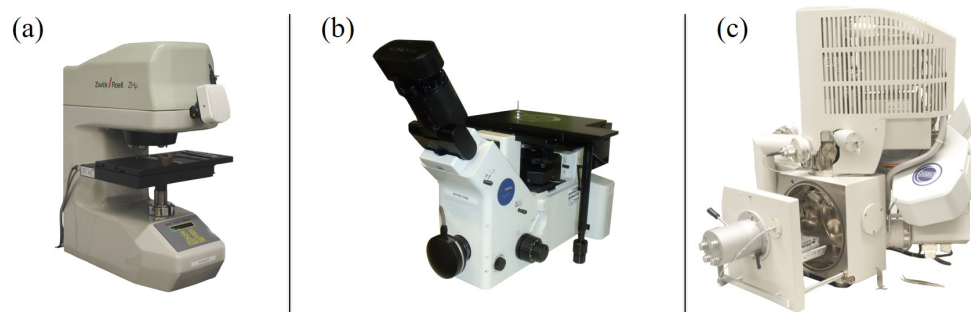


*Figure C.9: Material science equipment: (a) Micro-hardness tester – Zwick-Roell Indentec ZH $\mu$ -AFHD, (b) Optical microscope – Olympus GX51, and (c) SEM – FEI/Oxford Instruments Quanta 250 FEG.*

### C.2.2.2 Calibration, repeatability, and accuracy

The Indentec ZH $\mu$ -AFHD was calibrated annually by the manufacturer Indentec in accordance with the ISO standard 6507-2 (British Standard Institution, 2006b) and ASTM E384 (ASTM International, 2011). Its indenters were calibrated once. It is generally recommended to calibrate them every two years when in an industrial environment. Furthermore, monthly intermediate checks were completed and a record was maintained. Periodic checks by the user were required by Rolls-Royce plc (2012). Within the AFRC, these checks were not mandatory as the machine had no emergency stops, and so were not carried out for this machine. Until March 2015, the annual calibration was undertaken for three different loads for the Vickers indenter (1 kgf, 0.3 kgf, and 0.2 kgf), and the optical measuring system was checked for the 50x lens only. The British Standard Institution (2006b) states that “Each test force used within the working range of the testing machine shall be measured.” This quality issue was raised and fixed during the next annual calibration. In this EngD project, some of the hardness tests were carried out before that whereas the 20x lens had not been verified. As the machine was tested and found to be acceptable prior to service and calibration, the results were considered as acceptable.



A type 1 gauge study is typically employed “to evaluate the capability of a measurement process. This study evaluates the combined effects of bias and repeatability based on multiple measurements from a single part. A type 1 gauge study should be done prior to conducting other gauge repeatability and reproducibility studies, which determines how much of the observed process variation is due to measurement system variation. Bias examines the difference between the observed average measurement and a reference or master value. It tells how accurate the gauge is when compared to a reference value.” (Minitab Inc., 2013) The repeatability of the measurements was consequently established by performing a type 1 gauge study. The Vickers hardness of a calibration block was checked 20 times. The indents were automatically measured by the Indentec ZH $\mu$ -AFHD. The reference value and tolerances used were as specified on the calibration block. According to the British Standard Institution (2012), the variability of the repeatability obtained classified the measurement system as unacceptable. A second type 1 gauge study was completed by measuring the indents manually. The results are given in Table C.4. The variability of the repeatability was drastically reduced but still too high to consider the measurement system as acceptable. As no other improvements could be implemented, this equipment was used in this study. The six standard deviations of the mean ( $6\sigma$ ) was about 16.46 HV1. The true value thus lay within  $\pm 8.23$  HV1 of the measured value with a confidence interval of 99.7 %.

Table C.4: Type 1 gauge studies of Indentec ZH $\mu$ -AFHD.

	%Variability (repeatability)	%Variability (repeatability and bias)	$6\sigma$	True value lies within	Bias
Automatic measurement	81.32	133.65	28.04	$\pm 14.02$ HV1	-1.35
Manual measurement	47.73	49.90	16.46	$\pm 8.23$ HV1	+0.15

The Indentec ZH $\mu$ -AFHD’s accuracy was regularly measured using the calibration block, and had always been within the 95 % confidence interval required. Consequently, even if the range of hardness values varied through this EngD project, overall, the Indentec ZH $\mu$ -AFHD was considered as accurate enough for this study. Considering these results, the measurements were given with an uncertainty band of  $\pm 9$  HV1.

### C.2.3 Microstructure observation

#### C.2.3.1 GX51, an inverted optical microscope

Optical microscopes, also called light microscopes, use the visible light. The objective lens collect the reflection of the light emanating from the sample and create a real image (image located in the plane of convergence) of the specimen. Their second lens or group of lenses, called eyepiece, magnify this image and an enlarged virtual image (opposed to real image) of the sample is obtained. Micrographs are acquired using a charge-coupled device camera and can be directly seen on the computer screen. Optical microscopes are either upright compound or inverted, looking at the specimen respectively from above and below. In this study, the inverted optical microscope Olympus GX51 presented in Figure C.9-(b) was utilised.

#### C.2.3.2 FEI/Oxford Instruments Quanta 250 FEG, a scanning electron microscope

An alternative to the optical microscope is the use of an SEM, which provides higher resolution, magnification, and better adaptability (Goodhew et al., 2004, Exner and Weinbruch, 2004). Figure C.9-(c) shows the FEI/Oxford Instruments Quanta 250 FEG which was employed in this study.

An SEM scans the sample placed in its high or low vacuum chamber with a focused electron beam and produces the corresponding topographic image. The sample is penetrated by primary electrons. This interaction between electrons and atoms of the sample generates different signals, such as X-rays, photons, and emitted electrons, which allows the identification of the sample composition and topography. The new electrons, called emitted electrons, have different energies. The SEM detectors, either secondary electron (SE) or BS, collect these electrons. The SE detector amasses the secondary electrons, electrons with an energy less than 50 electron volts and coming from a layer of the surface in the order of a few nanometres. For a better image contrast, the BS detector is generally utilised as it catches the back-scattered electrons, which have an energy between 50 electron volts and the initial energy, also called primary energy.

**C.2.3.3 Electron backscatter diffraction**

In this project, the material texture, phase identification, and grain size were observed with the SEM using EBSD techniques. EBSD utilises a beam of electrons which is projected against the specimen surface. The diffracted backscattered electrons go through a phosphor screen creating the Kikuchi diffraction patterns. The latter are collected by a charge-coupled device camera. Tilting the specimen to 70° helps maximise the number of backscattered electrons collected. The EBSD techniques emerged in the past 10–15 years (Randle, 2009) and many publications detail their principle, such as the works of Dingley and Randle (1992) and Schwartz et al. (2009), which will not be repeated here. According to Mingard et al. (2007), “the maximum step size used must be < 20 % of the actual mean grain size for an error of about 10 %, or < 12 % for a 5 % error”. Mingard et al. (2007) also stated that indexing rates greater than 50 % are suitable when using noise reduction to ‘infill’ non-indexed points. Considering this statement, the step size used for the EBSD map acquisition was satisfactory.

**C.3 Surface roughness analysis****C.3.1 Definitions**

The main technical terms employed in the study of the surface texture are defined in Table C.5. “The surface texture is what is left after the overall form of the surface has been removed. [...] Once the form has been removed the surface texture is composed of three components [...] known as primary profile, waviness, and roughness.” (Leach, 2014) Figure C.10 illustrates the difference between these components. The roughness profile refers to irregularities under 500 µm that can be influenced by factors such as high frequency tool vibrations, tool surface, and lubricant quality and filtration. Surface roughness is a quality control check as it impacts mechanical properties and part functionality, such as friction ability, fluid dynamics, coating adherence, corrosion resistance, and wear and tear (Le Roux, 2012). The surface roughness was therefore of crucial interest in this study.

Table C.5: Definitions of technical terms related to the surface texture – adapted from British Standard Institution (2000), British Standard Institution (1997b), and Leach (2014).

Term	Notation	Definition
Arithmetical mean deviation of the profile	$Ra$	“Arithmetical mean of the absolute ordinate values $Z(x)$ within a sampling length”
Evaluation length	$ln$	“Length in the direction of the X-axis used for assessing the profile under evaluation”
Mean width of the profile elements	$RSm$	“Mean value of the profile widths $X_s$ within a sampling length”
Ordinate value	$Z(x)$	“Height of the assessed profile at any position x”
Primary profile	/	“Total profile after application of the short wavelength filter, $\lambda_s$ ”
Profile element	/	“Profile peak and the adjacent profile valley”
Profile element width	$X_s$	“Length of the X-axis segment intersecting with the profile element”
Profile filter $\lambda_s$	$\lambda_s$	“Filter that defines where the intersection occurs between the roughness and shorter wavelength components present in a surface”
Profile filter $\lambda_c$	$\lambda_c$	“Filter that defines where the intersection occurs between the roughness and waviness components”
Profile filter $\lambda_f$	$\lambda_f$	“Filter that defines where the intersection occurs between the waviness and longer wavelength components present in a surface”
Real surface	/	“Surface limiting the body and separating it from the surrounding medium”
Roughness profile	/	“Profile derived from the primary profile by suppressing the longwave component using the profile filter $\lambda_c$ ; this profile is intentionally modified”
Root-mean-square deviation of the profile	$Rq$	“Root-mean-square value of the ordinate values $Z(x)$ within a sampling length”
Sampling length	$lr$	“Length in the direction of the X-axis used for identifying the irregularities characterizing the profile under evaluation”
Surface profile	/	“Profile that results from the intersection of the real surface by a specified plane”
Waviness profile	/	“Profile derived by subsequent application of the profile filter $\lambda_f$ and the profile filter $\lambda_c$ to the primary profile, suppressing the longwave component using the profile filter $\lambda_f$ , and suppressing the shortwave component using the profile filter $\lambda_c$ ; this profile is intentionally modified”

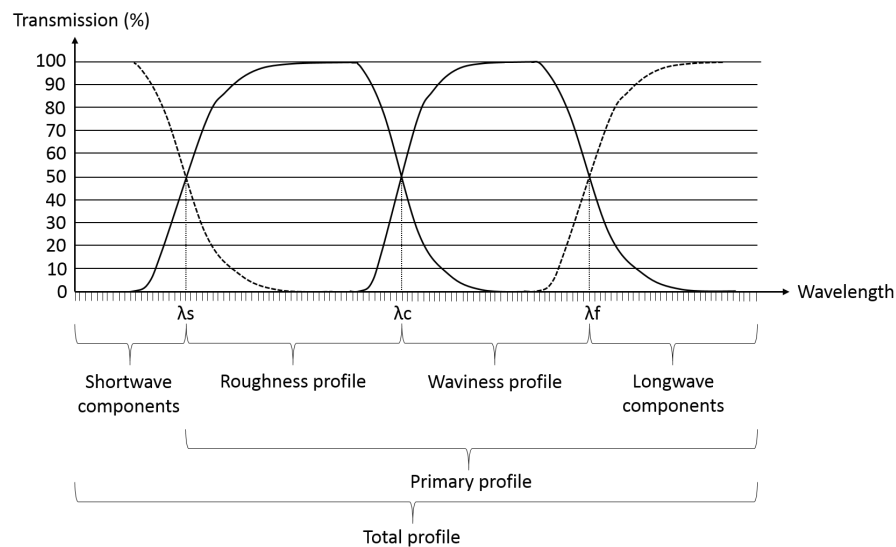


Figure C.10: Transmission characteristics of the filters for the different surface texture profiles – adapted from British Standard Institution (2000).

### C.3.2 InfiniteFocus, a non-contact method

The Alicona InfiniteFocus G4 presented in Figure C.11-(a) “is an optical 3D micro coordinate system for form and roughness measurement. Measurements achieve a vertical resolution of up to 10 nm. This system also operates on large measurement areas and volumes. Its results are traceable and ensure repeatable accuracy. Users benefit from these features, those of a coordinate measurement system and those of a surface measurement instrument.” (Alicona, c. 2014) As previously mentioned in Chapter 4, due to the size of the shear formed parts, replicas of the surface were taken in order to use the InfiniteFocus as shown in Figure C.11-(b). The resin was applied to the parts after cleaning and removal of grease as specified in Rolls-Royce’s engineering specification JES137 (Rolls-Royce plc, 2000). Before shear forming, for consistency of purpose, an arrow was drawn on the blank always at the same position to help identify the area to measure.

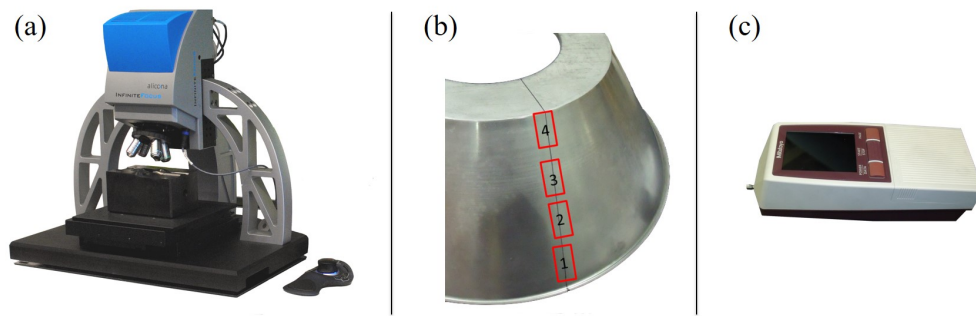


Figure C.11: Roughness measuring equipment: (a) Optical 3D micro-coordinate system for form and roughness measurement – Alicona InfiniteFocus G4, (b) Surface roughness measurements along the shear formed length, and (c) Portable surface roughness tester – Mitutoyo Surftest SJ-210.

### C.3.2.1 Measurement method, specifications, and standards

To determine the adequate machine parameters, a first measurement was taken perpendicular to the lay<sup>1</sup> to meet the Rolls-Royce’s aerospace engineering specification RRES90036 (Rolls-Royce plc, 2009). It was found that:

- The arithmetical mean deviation of the profile ( $Ra$ ) was in the order of  $1\ \mu\text{m}$ .
- The root-mean-square deviation of the profile ( $Rq$ ) was in the order of  $5\ \mu\text{m}$ .

According to the InfiniteFocus’ documentation, such a result matched the use of the 20x objective. The working distance is the distance from the lens of the objective to the topmost position of the specimen when focused, here 13 mm. The resolution limits for this objective are given in Table C.6. The vertical and lateral resolutions of a 3D measurement are respectively the smallest height step that can be measured and the smallest distance of a double-height-step that can be reconstructed without changing the amplitude. When studying the roughness, the appropriate lateral resolution was directly indicated by the InfiniteFocus, which was a default value depending on the selected objective, here  $293\ \mu\text{m}$ . In contrast, the vertical resolution was given by the operator and had to be approximately a third of  $Rq$  to get accurate results (Zaworka, 2011). After each measurement, the ideal vertical resolution (identified from the  $Rq$  obtained for the specific measurement) was calculated and compared with the input value. If the absolute difference between the two values was greater than 100 nm, a new measurement was undertaken with the appropriate vertical resolution.

<sup>1</sup>Lay: “The predominant direction of machining tool or grinding marks producing the surface texture.” (Rolls-Royce plc, 2009)

Table C.6: Resolution limits for the 20x objective of InfiniteFocus (Zaworka, 2011).

Vertical resolution	Lateral resolution
Lowest: 2.73 $\mu\text{m}$	Lowest: 8.80 $\mu\text{m}$
Highest: 50 nm	Highest: 881 nm

The values of the evaluation length ( $l_n$ ) and sampling length ( $l_r$ ) had to meet the ISO standard 4288 (British Standard Institution, 1997c). If the profile was random, these values were adjusted automatically by the software. However, if the profile was periodic, they had to be implemented manually. The shear formed parts had a periodic profile due to the roller nose radius. According to the ISO standard 4288, if nothing is specified on the drawing, the mean width of the profile elements ( $RS_m$ ) has to be determined. By using the table given in this standard, knowing the  $RS_m$  value allowed the identification of the appropriate  $l_n$  and  $l_r$ , here 1.25 mm and 0.25 mm respectively. However, Rolls-Royce plc (2000) states that “The sampling length used shall be 0.8 mm unless otherwise specified on the component definition.”, which matched a  $l_n$  of 4 mm according to the ISO standard 4288. It was chosen to follow Rolls-Royce’s engineering specification JES137, and so  $l_n$  and  $l_r$  were respectively set to exceed 4 mm and at 0.8 mm. When using the  $l_n$  and  $l_r$  provided by the ISO standard 4288,  $R_a$  was generally up to three times greater than when using the settings given in Rolls-Royce’s engineering specification JES137. As a result, a part considered within tolerance in this study might have been out of tolerance using the European standard. At the time of writing, Rolls-Royce required  $R_a$  to be less than 3.2  $\mu\text{m}$  for shear formed components.

### C.3.2.2 Calibration, repeatability, and accuracy

The InfiniteFocus was serviced and calibrated annually for form and roughness, and for all objective lenses. No specific standards were followed. This annual calibration looked at the following elements:

- Mechanical, optical, and electrical (software) elements
- Optical and illumination alignment
- Parallelism

- Squareness
- Straightness
- Lateral and vertical accuracies

Furthermore, every month, the form and roughness were checked, each with a specific artefact using respectively the full range of objectives and the 50x objective. A full record was maintained.

The repeatability of the measurements and their reliability when using a replica instead of the part were assessed by performing two type 1 gauge studies. A small area of a shear formed part was cut in order to fit under the InfiniteFocus. Then, its replica was taken. The first study involved measuring  $Ra$  of the replica 26 times whereas the second study looked at  $Ra$  of the corresponding part. Each time the full set-up was redone to include the operator error when judging where the middle of the replica/part sits. Furthermore, there were no reference values for  $Ra$  for either the replica or part, so the input values were the average of the 26 measurements, which thus lead to a bias of 0. Table C.7 gives the results. A variability of the repeatability of 4.16 % and 3.99 % was respectively identified for the measurement of the replica and the part. According to British Standard Institution (2012), these values allowed the measurement system to be considered acceptable for both replica and part. The six standard deviations of the mean ( $6\sigma$ ) were about  $0.13\ \mu\text{m}$ . Therefore, the true values lay within  $\pm 0.07\ \mu\text{m}$  of the measured values with a confidence interval of 99.7 %. As the difference of the average values obtained in both studies was about  $0.03\ \mu\text{m}$ , using replicas instead of the part was reliable.

Table C.7: Type 1 gauge studies of InfiniteFocus for both replica and part.

	Reference value	% Variability (repeatability)	$6\sigma$	True value lies within
Replica	1.34	4.16	0.13	$\pm 0.07\ \mu\text{m}$
Part	1.31	3.99	0.13	$\pm 0.07\ \mu\text{m}$

The accuracy of an instrument is the difference between the value measured and the real value of the piece. It slightly fluctuates for each piece. The InfiniteFocus' accuracy was regularly measured using a calibration block and had been within the parameters defined by the manufacturer. Furthermore, the



repeatability results were acceptable. Even if the range of  $Ra$  varied through this EngD project, overall, the InfiniteFocus was considered as accurate enough for this study. Considering these results,  $Ra$  was given with two significant digits and an uncertainty band of  $\pm 0.1 \mu\text{m}$  was judged appropriate.

### C.3.3 Surftest SJ-210, a contact method

#### C.3.3.1 Measurement method, specifications, and standards

The Surftest SJ-210 shown in Figure C.11-(c) “consists of a stylus that physically contacts the surface being measured and a transducer to convert its vertical movement into an electrical signal.” (Leach, 2014). “A Mitutoyo portable surface roughness tester able to operate independently of mains power and make measurements on almost any parts of a workpiece of practically any sizes. [...] An alarm warns when the stylus should be checked for wear. This equipment complies with the applicable international standards concerning definition and calculation of the values of surface roughness parameters. In addition to calculation results, sectional calculation results and assessed profiles, bearing curves, and amplitude distribution curves can be displayed.” (Mitutoyo, c. 2012)

The technical data of the Surftest SJ-210 is given in Table C.8. The ideal stylus tip radius ( $r_{tip}$ ) depends on  $lr$ . In this study, as explained in Sub-subsection C.3.2.1 (p. 173),  $lr$  was set at 0.8 mm. According to Table 1 of the ISO standard 3274, such a sampling length matched the use of a maximum  $r_{tip}$  of  $2 \mu\text{m}$  or “For surfaces with  $Ra > 0.5 \mu\text{m}$  or  $Rz > 3 \mu\text{m}$ ,  $r_{tip}=5 \mu\text{m}$  can usually be used without significant differences in the measurement result.” (British Standard Institution, 1997b) As the conditions of the previous quote were met, the use of a  $r_{tip}$  of  $5 \mu\text{m}$  was accepted, which was the radius chosen in this study. The static measuring force is “the force exerted by the stylus tip when in its mean position as it rests on the surface” (British Standard Institution, 1997b). It is stated that its nominal value is 0.75 mN. In this study, this force was set at 4 mN.

Table C.8: Technical data of Surftest SJ-210 (Mitutoyo, c. 2012).

Reference number	Measuring range	Measuring speed	Drive unit	Digital filters
178-561-02E	17.5 mm	0.25, 0.5, 0.75 mm/s 1 mm/s (returning)	Standard type	Gaussian 2CR75 PC75
Detector range	Measuring force	Stylus tip radius	Detector conical taper angle	
360 $\mu\text{m}$ (-200 to 160 $\mu\text{m}$ )	4 mN	5 $\mu\text{m}$	90°	

As mentioned in Subsection C.3.1 (p. 169), filters allow the distinction between primary profile, waviness, and roughness. Different types exist. A Gaussian filter was selected as required by Rolls-Royce plc (2009). Furthermore, as previously stated,  $l_n$  and  $l_r$  were respectively set to exceed 4 mm and at 0.8 mm.

### C.3.3.2 Calibration, repeatability, and accuracy

The Surftest SJ-210 was not serviced or calibrated. Only the calibration block supplied with the instrument was verified annually. Monthly checks were not in place due to the low frequency of use. Prior to utilisation, operators should calibrate the Surftest SJ-210 by using the roughness measurement calibration block at least five times. Operators were advised to have a reference part specific to the batch and to measure it before each series of measurements. A record should be kept. According to the ISO standard 5436-1 (referred in the ISO standard 3274, which is called by Rolls-Royce's aerospace engineering specification RRES90036), "The calibration of the existing wide range of instruments in all modes of operation calls for more than one type of measurement standard." (British Standard Institution, 2001) Table C.9 gives the five types of artefact given in this standard. The only calibration block utilised in this study was of type D. The artefacts of types A and B were specific to stylus instruments but were not available at the AFRC. To detect any potential problems, the recommendations given by Leach (2014) were followed: "When checking the condition of the stylus, the user is advised to maintain historical records of the instrument reading for a chosen surface texture parameter (usually  $R_a$ ) against the value for the calibration artefact quoted on its calibration certificate. [...] If there is a 10 % difference in the value obtained compared with the historical data, the user

should be alerted to the fact that there may be a potential problem with the stylus which should be examined for signs of wear or damage.” An historical record was created for the SurfTest SJ-210 in December 2015. It included the date,  $Ra$ , and the percentage of difference compared with the previous record for the artefact of type D used during calibration.

*Table C.9: Calibration artefacts for surface roughness measurement (British Standard Institution, 2001).*

Type: Name	Use
Type A: Depth measurement standard	“These measurement standards are for calibrating the vertical profile component of stylus instruments.”
Type B: Tip condition measurement standard	“These measurement standards are primarily for calibrating the condition of the stylus tip.”
Type C: Spacing measurement standard	“These measurement standards are used primarily for calibrating vertical profile components. They may also be used for calibrating horizontal profile components if the spacing of the grooves is held within limits acceptable for this purpose. The purpose of the series of measurement standards is to enable the transmission characteristics to be checked for a number of spacings and amplitudes.”
Type D: Roughness measurement standard	“These measurement standards are for overall calibration of instruments.”
Type E: Profile coordinate measurement standard	“These measurement standards are intended for calibrating the profile co-ordinate system of the instrument.”

Rolls-Royce plc (2009) states that: “The capability of the surface roughness measurement for a particular feature shall be determined by Gauge Repeatability and Reproducibility (Gauge R&R) studies. Note that the repeatability of the surface roughness measurement on a single part will depend on the repeatability of the part fixture and the short range (local) variation in surface roughness on the part. If local variation exists in the surface roughness the surface roughness can be assessed using the max rule ISO 4288: 1996 to improve the repeatability of the measurement.” The full Gauge R&R study completed on shear formed parts in November 2014 with the SurfTest SJ-210 failed. It was likely to be due to the fact that variations of the surface

roughness were observed along the shear formed length and the area to measure was not clearly specified on each part. Rolls-Royce is going to publish a new standard for the measurement of the surface roughness, in which a Gauge R&R study will no longer be required. Consequently, instead of a full Gauge R&R study, a type 1 gauge study was completed on the same part as previously. Doing so allowed the comparison of results across two measurement instruments – the InfiniteFocus and the SurfTest SJ-210. The results are given in Table C.10. Each time the full set-up was redone to include the operator error when judging where the middle of the part sits. The results were analysed in the same way as previously. A variability of the repeatability of 13.34 % was obtained, so it could be said that “the measurement system may be acceptable depending on the importance of the application, cost of the gauge, cost of repairs, etc.” (British Standard Institution, 2012) The six standard deviations of the mean ( $6\sigma$ ) was about 0.42  $\mu\text{m}$ . Consequently, the true value lay within  $\pm 0.21 \mu\text{m}$  of the measured value with a confidence interval of 99.7 %. The conclusions were:

- For the same reasons as in Sub-subsection C.3.2.2, SurfTest SJ-210 was considered as accurate enough for this study.
- The InfiniteFocus was more consistent than the SurfTest SJ-210 even if both were considered as acceptable for this study.
- In 2015, due to time constraints, it was decided to use the SurfTest SJ-210. When interpreting the final results, it was important to take into account that the difference of the means between both instruments was about 0.18  $\mu\text{m}$ .

*Table C.10: Type 1 gauge study of SurfTest SJ-210.*

	<b>Reference value</b>	<b>%Variability (repeatability)</b>	<b><math>6\sigma</math></b>	<b>True value lies within</b>
Part	1.13	13.34	0.43	$\pm 0.21 \mu\text{m}$

## C.4 Geometrical analysis

### C.4.1 ATOS III Triple Scan, a non-contact method

The GOM ATOS III Triple Scan seen in Figure C.12-(a) was a non-contact instrument available at the AFRC, which was utilised for geometrical analyses. According to GOM Optical Measuring Techniques (c. 2014), “The ATOS series of industrial optical 3D scanners provide accurate scans with detailed resolution at high speeds. ATOS delivers 3D measurement data and analysis for industrial components such as sheet metal parts, tools and dies, turbine blades, prototypes, injection moulded parts, castings, and more. Instead of measuring single points or with a laser, ATOS captures an object’s full surface geometry precisely in a dense point cloud or polygon mesh.”

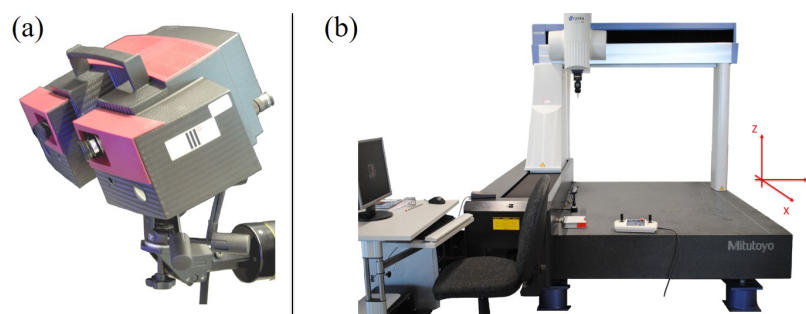


Figure C.12: Geometry measuring equipment: (a) 3D scanner – GOM ATOS III Triple Scan and (b) Coordinate Measurement Machine – Mitutoyo Crysta-Apex C 121210.

All the shear formed parts completed within this project without an outer flange were measured geometrically using the ATOS III Triple Scan. For that, the appropriate sensor and lenses were determined by the geometry and volume of the part to scan. In this study, the measurement volume selected was MV 320. Table C.11 gives its technical data.

Table C.11: Technical data of MV 320 for ATOS III Triple Scan (GOM mbH, 2011).

Volume name	Measuring point distance	Measuring volume (LxWxH) in mm	Recommended reference points
MV 320	95.46 $\mu\text{m}$	320x240x240	1.5 mm $\varnothing$
Measuring distance	Camera angle	Focal length camera lenses	Focal length projector lens
490 mm	28°	24 mm	30 mm

#### C.4.1.1 Measurement method

Once the scanning operation was completed, the features of interest were collected using the software ATOS Professional V7.5. A sketch of a shear formed part without an outer flange is given in Figure C.13.

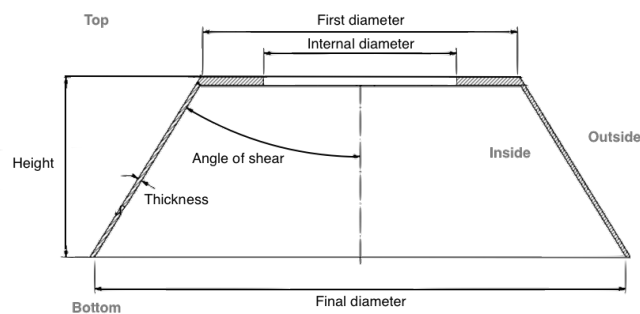


Figure C.13: Sketch of a shear formed part without an outer flange.

Six sections of the shear formed part were created, all positioned at 60° apart from each other (Figure C.14-(a)). This allowed the geometrical features to be measured a few times and their average value to be calculated. The only exception was for the internal diameter. For this feature, a first plane (plane 1) was built on the outside top surface of the part. Then, a parallel plane was created at a distance of half the initial thickness. The internal diameter was measured by inserting a circle in this last plane as illustrated in Figure C.14-(b).

For each of the six sections, the tool calliper measured the height. This was the distance between the lowest point in the perpendicular direction to plane 1 and plane 1 itself (Figure C.14-(c)).

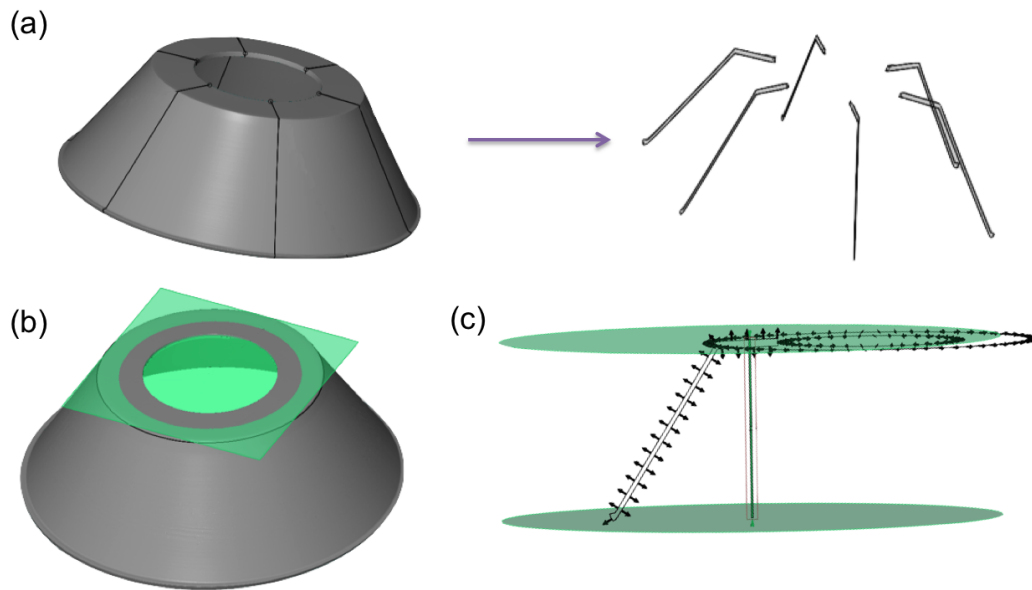


Figure C.14: Measurements with ATOS III Triple Scan: (a) Part sections, (b) Internal diameter, and (c) Height.

To measure the first diameter, on each section, on the outside top of the part, two fitted lines and their intersection point were constructed (Figure C.15-(a)). The distances between the intersection points of two opposite sections were measured, which were the measurements of the first diameter. The fitted lines were built close to the extremities of the first diameter as the shear formed section was not always straight. Therefore, fitting the lines on the whole shear formed length introduced errors, and could lead to a value of the first diameter smaller than the mandrel itself.

The measurement of the final diameter was similar. On each section, two fitted lines and their intersection point were created on the bottom of the part. The distances between the intersection points of two opposite sections were measured to obtain the measurements of the final diameter (Figure C.15-(b)). The fitted lines were constructed close to the extremities of the final diameter as the part was not completely shear formed and a “lip” was left. Consequently, fitting the lines on the whole shear formed length introduced errors, and could lead to an incorrect value of the final diameter.

For each section, a fitted line was created in the middle of the shear formed length (Figure C.16-(a)). The cone angle was the angle between this line and a perpendicular line to plane 1.

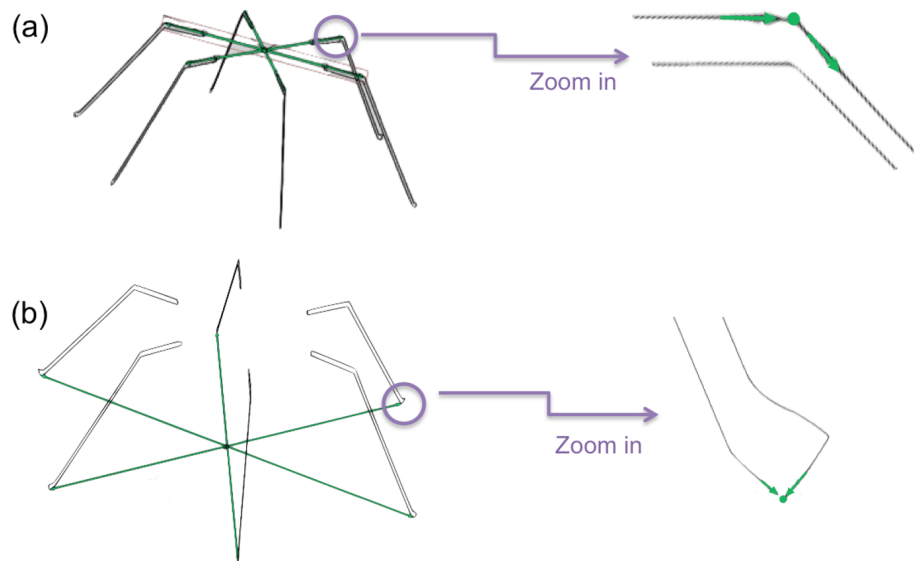


Figure C.15: Measurements with ATOS III Triple Scan: (a) first diameter and (b) final diameter.

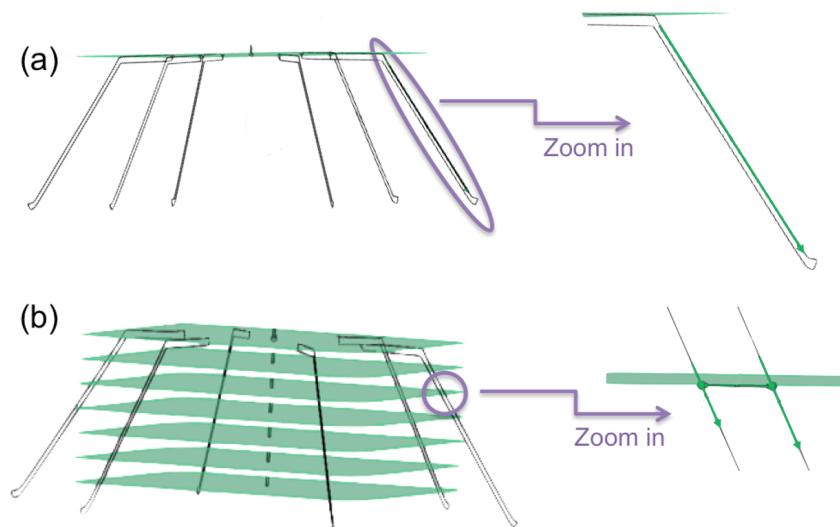


Figure C.16: Measurements with ATOS III Triple Scan: (a) cone angle and (b) average thickness.

To be able to measure the average thickness, six planes parallel to plane 1 were created at 20 mm apart from each other (Figure C.16-(b)). Then, on each section and for each height of the six planes, two fitted lines were constructed on the inside and outside of the part. For each section, the intersection points between each fitted line and the corresponding plane were added. The distance between two points of the same



section at the same height gave the pseudo thickness. The average thickness was the average of the 36 pseudo thicknesses multiplied by the cosine of the cone angle.

#### C.4.1.2 Calibration, repeatability, and accuracy

The ATOS III Triple Scan was not serviced or calibrated annually. However, the ball plate was calibrated every year according to the German standard VDI 2618 and monthly checks were undertaken using this ball plate for each volume. Furthermore, the calibration plates were calibrated every five years. Each time the volume was changed, these were used for calibration. A full record of the calibration was maintained.

Due to time constraints, a type 1 gauge study was not performed using the ATOS III Triple Scan. Each part was measured three times. Each time the full set-up was redone. According to Table C.12, the results for the three scans were close with a maximum variation of  $0.2^\circ$  and 0.05 mm respectively for the cone angle and linear measurements.

*Table C.12: Three measurements of a same part with ATOS III Triple Scan.*

	<b>Internal diameter (mm)</b>	<b>Cone angle (<math>^\circ</math>)</b>	<b>Height (mm)</b>	<b>First diameter (mm)</b>	<b>Final diameter (mm)</b>	<b>Average thickness (mm)</b>
1	149.66	31.99	142.87	249.30	422.31	3.24
2	149.65	31.99	142.88	249.29	422.30	3.25
3	149.65	31.97	142.89	249.32	422.35	3.25

#### C.4.2 Crysta-Apex C 121210, a contact method

The contact instrument, the Mitutoyo Crysta-Apex C 121210 shown in Figure C.12-(b), was a Coordinate Measurement Machine (CMM) installed within the AFRC. According to Mitutoyo (c. 2015a), the Mitutoyo Crysta-Apex C “is designed and constructed using all Mitutoyo’s experience in CNC CMM technology, this machine is built using lightweight materials and an innovative moving-bridge type machine structure, providing high motion stability, high accuracy, and affordability. The temperature correction function (16–26°C) can yield accurate measurements

even on the shop floor.” The technical data for Crysta-Apex C 121210 are given in Table C.13.

*Table C.13: Technical data of Crysta-Apex C 121210 (Mitutoyo, c. 2015b).*

Measuring range	Workpiece	Accuracy ISO 10360-2
X axis: 1,205 mm	Max. height: 1,200 mm Max. table loading: 2,000 kgf	Maximum Permissible Error of length measurement: $MPE_E = (2.5+0.4L/100) \mu\text{m}$ where $Lm$ is the measuring length in mm
Y axis: 1,205 mm		
Z axis: 1,005 mm		
Resolution	Measuring speed	
0.1 $\mu\text{m}$	1–5 mm/s	

#### C.4.2.1 Measurement method

To aid the understanding of this subsection, one of the 15 mm thick shear formed parts of this EngD project is taken as example. The annotated drawing is given in Figure C.17. The measurements were established in a different way depending on the features. Table C.14 (pp. 186–187) explains how the labelled features of the example drawing were measured.

#### C.4.2.2 Calibration, repeatability, and accuracy

The Crysta-Apex C 121210 was serviced and calibrated annually according to the ISO standards 10360-2 (British Standard Institution, 2010a) and 10360-5 (British Standard Institution, 2010b). The probes were checked on a daily basis using the calibration sphere, which was calibrated every year. Furthermore, before each batch of parts, a reference part was measured and its measurements were compared with previous results. If no reference parts were available, a gauge block was used instead. A full record of the calibration was maintained.

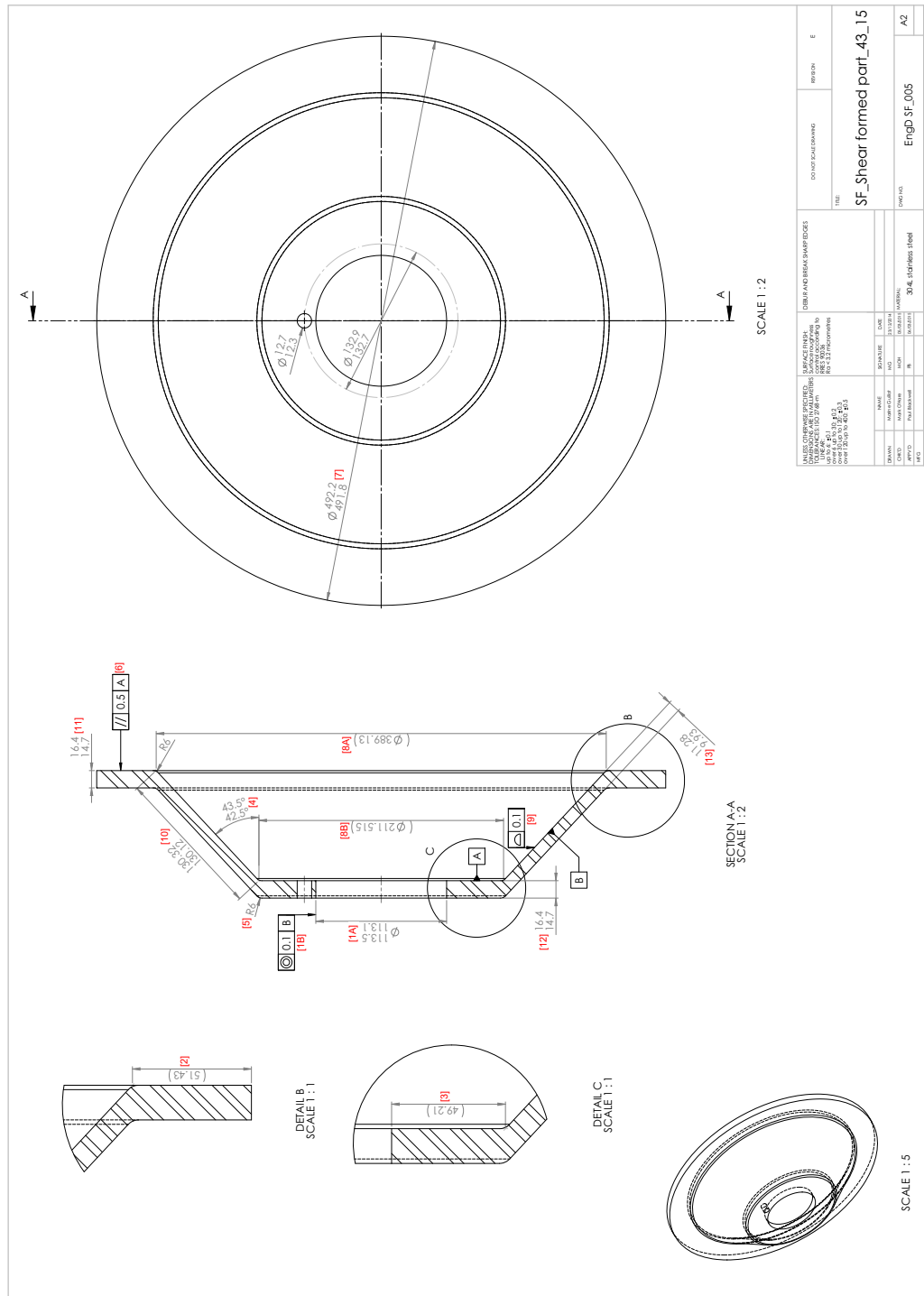


Figure C.17: Shear formed part – 43°, 15 mm thick, EngD SF\_005, “SF\_Shear formed part\_43\_15”.

Table C.14: Measurement strategy using Crysta-Apex C 121210.

Identification feature	Number of points	Geometric element	Notes
[1A]	21	Cylinder	3 circles of 7 points
[1B]	42	Coaxiality	Coaxiality between the cylinder [1A] and the cone 21 points cylinder [1A] + 21 points cone
[2]	2	Distance	Distance between the point on the outside edge of the flange and the intersection point between the line on the flange and the line on the cone
[3]	2	Distance	Measurements taken on the inside of the cone for the left, right, front, and back sections of the part Distance between the point on the inside edge of the flange and the intersection point between the line on the flange and the line on the cone
[4]	26	Angle	Measurements taken on the inside of the cone for the left, right, front, and back sections of the part Angle between the line on the cone and the cone axis (datum B) Measurements taken on the inside of the cone for the left, right, front, and back sections of the part 21 points cone [1B] + 5 points line
[5]	5	Circle	Partial arc results may not be accurate Measurements taken on the inside of the cone for the left, right, front, and back sections of the part Planes are the best fits and will not show the angle of the flange.
[6]	42	Planes	21 points for each of the two planes The flange angles have also been output for information. They are calculated between the flange line and the datum A plane.
[7]	9	Circle	Will be affected by the angle of the flange
[8A] and [8B]	8	Circle	Circles are constructed from the intersection points, which are calculated from the intersection of the line on the one and the line on the flange.
[9]	45	Cone	5 points on each of the 16 lines (8 for the one, 8 for the flange) Tolerance on form only, not position

Table C.14 Continued: Measurement strategy using Crysta-Apex C 121210.

Identification feature	Number of points	Geometric element	Notes
[10]	2	Distance	Distance between the intersection of the outer flange and the cone and the intersection of the cone and the inner flange. Measurements taken on the outside of the cone for the left, right, front, and back sections of the part
[11]	2	Distance	Distance in the Z direction between the points measured on the top and bottom of flange
[12]	2	Distance	Measurements taken on the outside of the cone for the left, right, front, and back sections of the part
[13]	2	Distance	Distance in the Z direction between the points measured on the top and bottom of flange Measurements taken on the outside of the cone for the left, right, front, and back sections of the part Distance in the X direction between the points taken on the inside and outside of the cone Measurements taken on both sides of the cone, at the top, middle, and bottom of the part for the left, right, front, and back sections of the part

A first type 1 gauge study was performed to compare the results given by both equipment (the ATOS III Triple Scan and the Crysta-Apex C 121210) for a shear formed part without an outer flange. The shear formed part measured three times by the ATOS III Triple Scan was used for that. This part was measured 35 times by the Crysta-Apex C 121210. The first five times were considered as warm-up and the 30 next ones as actual measurements. To allow a direct comparison of the results between these devices, the method of measurement followed was the same as explained in Sub-subsection C.4.1.1 (p. 180). Table C.15 gives the results when considering the average of the results obtained with the ATOS III Triple Scan as reference value. The variability of the repeatability was less than 1.00 % for all features with the exception of the first diameter (12.80 %). This value supported the conclusion that “the measurement system may be acceptable depending on the importance of the application, cost of the gauge, cost of repairs, etc.” (British Standard Institution, 2012) In this study, the measurement system was considered as acceptable.

*Table C.15: Type 1 gauge study of Crysta-Apex C 121210 for a part without outer flange.*

	<b>%Variability (repeatability)</b>	<b>%Variability (repeatability and bias)</b>	<b>6<math>\sigma</math></b>	<b>True value lies within</b>	<b>Bias</b>
Internal diameter (mm)	0.98	-3.36	0.004	$\pm 0.002$	-0.052
Cone angle ( $^{\circ}$ )	0.12	0.14	0.001	<i>pm</i> 0.000	-0.007
Height (mm)	0.63	-0.12	0.006	$\pm 0.003$	-0.640
First diameter (mm)	0.70	-0.41	0.007	$\pm 0.003$	-0.270
Final diameter (mm)	12.80	14.5	0.128	$\pm 0.064$	-0.012
Average thickness (mm)	0.33	0.36	0.002	$\pm 0.001$	-0.007

For all features, the biases were negative, meaning that the measurements taken with the Crysta-Apex C 21210 were on average below the ones obtained with the ATOS III Triple Scan. The absolute levels of the biases were quite low – under 0.1 mm and  $0.1^{\circ}$  with the exception of the height and first diameter whose bias were less than 0.7 mm and 0.3 mm respectively. As mentioned in Sub-subsection C.4.1.1 (p. 180), these two features were difficult to measure due to the “lip” shape and the shear formed

length not always being straight. This explained why the bias was greater for both elements. Overall similar results were obtained using both the Crysta-Apex C 121210 and the ATOS III Triple Scan. Therefore, without performing a type 1 gauge study on the ATOS III Triple Scan, it was relevant to say that this equipment could be considered as acceptable for this study. When interpreting the final results obtained using the two different instruments, the bias will have to be taken into account.

The second type 1 gauge study was performed to understand the repeatability of the measurements for a shear formed part with an outer flange. As for the first study, the shear formed part was measured 35 times. The method of measurement was as stated in the previous sub-subsection. The results are given in Table C.16 (p. 190). As no reference values existed for this part, the input values were the average of the 30 measurements, which thus lead to a bias of 0. The results gave variabilities of the repeatability up to 5.68 %. According to the British Standard Institution (2012), this value allowed the measurement system to be acceptable.

In this EngD project, overall, the biggest length to be measured for the shear formed parts was of 492 mm. According to the data given in Table C.13 (p. 184), the accuracy of the Crysta-Apex C 121210 for the shear formed part measurements was always less than 4.5  $\mu\text{m}$ . As the measurements between the ATOS III Triple Scan and the Crysta-Apex C 121210 were similar, the ATOS III Triple Scan was considered as accurate enough for this study.

## **C.5 Design of Experiments and statistical analysis**

An experiment is “An operation carried out under controlled conditions to discover an unknown effect or establish a hypothesis or to illustrate a known law. In an engineering environment, an experiment is a series of trials which produce quantifiable outcomes.” (Antony, 2014)

Table C.16: Type 1 gauge study of Crysta-Apex C 121210 for a part with outer flange.

	% Variability (repeatability)	$6\sigma$	True value lies within
Internal diameter (mm)	0.52	0.002	$\pm 0.001$
Coaxiality (mm)	4.97	0.005	$\pm 0.002$
Outer flange length (mm)	0.21	0.001	$\pm 0.001$
Inner flange length (mm)	0.19	0.001	$\pm 0.001$
Cone angle ( $^{\circ}$ )	0.09	0.001	$\pm 0.000$
Radius (mm)	5.68	0.011	$\pm 0.006$
Parallelism of the outer flange - top plane (mm)	0.48	0.002	$\pm 0.001$
Outer flange angle ( $^{\circ}$ )	0.10	0.001	$\pm 0.001$
Outside diameter (mm)	0.72	0.003	$\pm 0.001$
389 diameter (mm)	0.00	0.000	$\pm 0.000$
211 diameter (mm)	0.29	0.003	$\pm 0.001$
Form of cone (mm)	0.00	0.000	$\pm 0.000$
Formed length (mm)	0.68	0.001	$\pm 0.001$
Outer flange thickness (mm)	0.09	0.002	$\pm 0.001$
Inner flange thickness (mm)	0.09	0.002	$\pm 0.001$
Shear formed thickness bottom (mm)	0.14	0.002	$\pm 0.001$
Shear formed thickness middle (mm)	0.13	0.002	$\pm 0.001$
Shear formed thickness top (mm)	0.13	0.002	$\pm 0.001$
Straightness (mm)	0.43	0.000	$\pm 0.000$

### C.5.1 Experimental approaches and terminology

DoE is “a scientific approach that allows the experimenter to understand a process and to determine how the input process variables or design parameters influence the output or response (or quality characteristic). DoE is a powerful technique used for discovering a set of variables or parameters which are most important to a process or system and then determine at what levels these variables or parameters should be kept to optimize the performance of the process/system.” (Antony, 2014) Antony (2014) and Rosochowski (2013) defined the main terms associated with a DoE as follows:



- Interaction: The effect of one factor on the response is influenced by the level of another factor.
- Level: A set value of a parameter used in an experiment.
- Process/design parameter (or factor): An input to the process which can be manipulated during the experiment.
- Randomisation: The running of experiments in random order. Generally, this technique is employed when the process is not stable or if the stability of the process is unknown. This represents an attempt to neutralize the effect of all kinds of systematic extraneous variation.
- Replication: The repeating of a few (or all) of the runs in a randomized fashion. This allows the estimation of the experimental error and a better evaluation of the effect of factors and their interactions.
- Response/quality characteristic: The output of a process.
- Run (or trial): A single combination of parameter settings.
- Significance: The determination of whether a process or design parameter (or factor) actually has any real effects on the process response.

### C.5.2 Statistical analysis

Statistical analysis is “a combination of statistical methods and statistical thinking. The general function of a statistical analysis is to harvest experimental data for knowledge acquisition.” (Rosoehowski, 2013) This is used to distinguish between significant and insignificant effects in an experiment. The latter is arising from random variation. Keller (2001) explained that the assessment of a model depends on:

- The sum of squares for error ( $SSE$ ): This is a measure of variation or deviation from the mean, which considers the sum of squares from the factors and from random chance or error.
- The standard error of estimate ( $s_e$ ), also called standard error of the regression: This is a measure of the model fit. This is expressed in the units of the response variable and “represents the standard distance data values fall from the regression line, or the standard deviation of the residuals.” (Minitab Inc., 2013)
- The adjusted coefficient of determination ( $R_{adj}^2$ ): “Percentage of response variable variation that is explained by its relationship with one or more predictor variables, adjusted for the number of predictors in the model. This

adjustment is important because the coefficient of determination ( $R^2$ ) for any models will always increase when a new term is added. A model with more terms may appear to have a better fit simply because it has more terms. However, some increases in  $R^2$  may be due to chance alone.  $R_{adj}^2$  is a useful tool for comparing the explanatory power of models with different numbers of predictors.  $R_{adj}^2$  will increase only if the new term improves the model more than would be expected by chance. It will decrease when a predictor improves the model less than expected by chance.” (Minitab Inc., 2013)

- The F-value: F-test is a purely numerical method for identifying which effects can be treated as real. The factors and model are said to be statistically significant if their F-value exceeds a specified threshold, called critical value. Here, the critical values at 95 % were used.

A perfect model will have  $SSE$  and  $s_\varepsilon$  that tend to 0,  $R_{adj}^2$  that tends to 1 and a F-value that tends to infinity. Two elements can help determine if the model is accurate and useful, these are:

- The confidence interval at 95 %: “Represents a range that the mean response is likely to fall within given specified settings of the predictors.” (Minitab Inc., 2013)
- The prediction interval at 95 %: “Represents a range that a single new observation is likely to fall within given specified settings of the predictors. The prediction interval is always wider than the corresponding confidence interval because of the added uncertainty involved in predicting a single response versus the mean response.” (Minitab Inc., 2013)

In some cases, these intervals might be larger than the tolerance band and therefore the model could not be used accurately. Furthermore, before performing any statistical analyses, the output values were plotted using a boxplot. This tool summarizes graphically the distribution of a sample and shows its shape, central tendency, and variability. With this tool, outliers which are observations that are beyond the upper or lower whisker are identified. Figure C.18 gives an example. Identifying outliers was necessary as this could have changed the predictive model. When an outlier was observed, a first predictive model was established and used to calculate the predicted response for the specific run which presented an outlier. Then, the measured value was replaced by the calculated one in order to produce a new and more accurate predictive model.

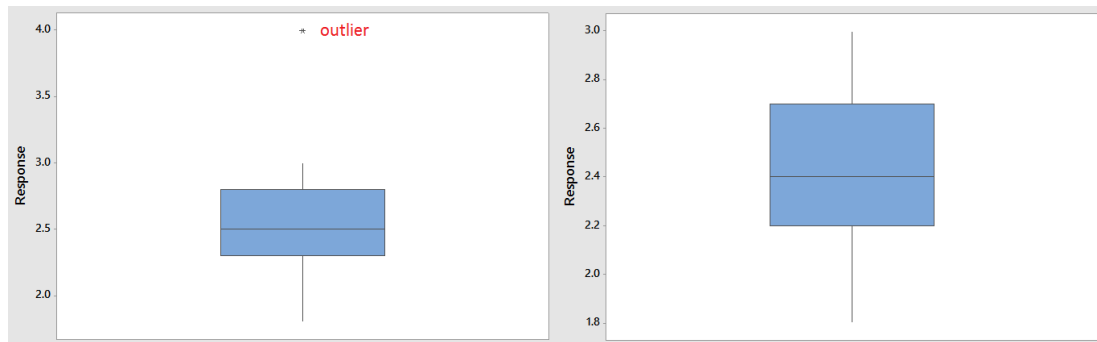


Figure C.18: Boxplot of a sample with (left) and without (right) outlier.

Residuals plots, additional analytic tools offered by Minitab software, were also employed. They are “used to examine the accuracy of model fit in regression and ANOVA. Examining residual plots helps determine if the ordinary least squares assumptions are being met. If these assumptions are satisfied, then ordinary least squares regression will produce unbiased coefficient estimates with the minimum variance.” (Minitab Inc., 2013) In this study, four different plots were generated to determine the validity of the predictive models.

- Normal probability plot of residuals: “The points in this plot should generally form a straight line if the residuals are normally distributed. If the points on the plot depart from a straight line, the normality assumption may be invalid.” (Minitab Inc., 2013)
- Residuals versus fitted values: “This plot should show a random pattern of residuals on both sides of 0. If a point lies far from the majority of points, it may be an outlier. There should not be any recognizable patterns in the residual plot. For instance, if the spread of residual values tend to increase as the fitted values increase, then this may violate the constant variance assumption.” (Minitab Inc., 2013)
- Histogram of the residuals: “An exploratory tool to show general characteristics of the residuals including typical values, spread, and shape. A long tail on one side may indicate a skewed distribution. If one or two bars are far from the others, those points may be outliers.” (Minitab Inc., 2013)
- Residuals versus order of data: “This is a plot of all residuals in the order that the data was collected and can be used to find non-random error, especially of time-related effects. This plot helps check the assumption that the residuals are uncorrelated with each other.” (Minitab Inc., 2013)

Figure C.19 is an example of the plots that can be generated.

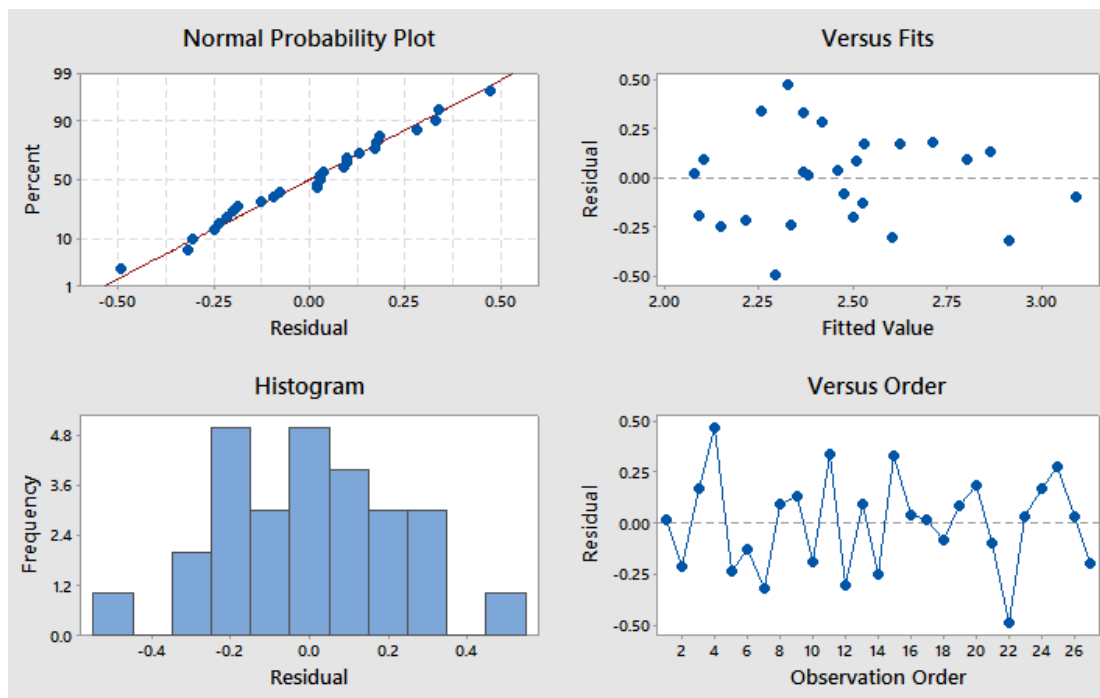


Figure C.19: Four types of residual plots used in this study.

# **Appendix D**

## **Data sheet**

As previously stated in Chapter 5, all the information about each part was reported in a specific data sheet. Appendix D is a blank version of it.

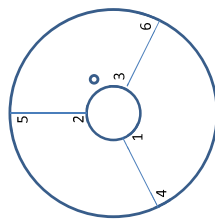
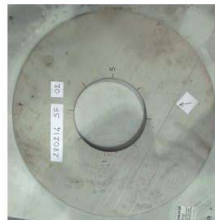
**Data sheet – Shear Forming**

Date: / / 201  
 Project: EngD Shear Forming (Thicker Material)  
 Name of part:  
 CNC Program:

Person running machine:

Initial disc details:

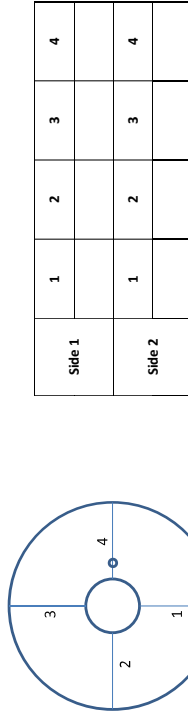
Date:  
 Material: 304L stainless steel  
 Material reference AFRC: RC  
 Initial internal disc diameter: mm  
 Measurement of the thickness (in mm):



1	2	3	4	5	6

⇒ Average thickness: mm

Measurement of the surface roughness according to Roils-Royce specification RRES 90036 via the portable surface roughness tester "Mitutoyo - Surftest SJ-210" (Ra in µm):



⇒ Average surface roughness: µm

Pictures of the preform on both sides Y/N:

Comments on the disc (scratches, surface default...):

Sheet number:

Position in sheet (cross right number):

7	6	3	2
8	5	4	1

Process details:

Comments on the machine before shear forming (grease, tools cleaned...):

Main parameters:

Nb of roller(s) used	Feed rate (rev/min)	Spindle speed (rpm)	Rotation	Coolant rate (L/min)	Grease/Lubricant type

Comments on the process (did not spin true, part warm, problems during process...):

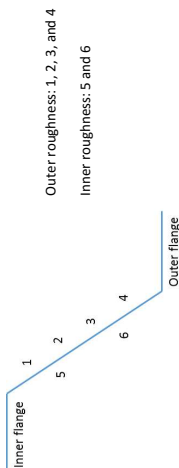
Comments on the machine after shear forming (problems with tooling, damages...):

Other comments:  
 .....  
 .....

Surface roughness final part:

Date:

Measurement of the surface roughness according to Roll-Royce specification RRES 900036 via the portable surface roughness tester "Mitutoyo - Surftest SJ-210"



<b>First slice</b>	1	2	3	4	5	6
<b>Second slice (+ 120°)</b>	1	2	3	4	5	6
<b>Third slice (+ 240°)</b>	1	2	3	4	5	6

Ra measurement in µm

- ⇒ Average surface roughness:
- Inner: µm
- Outer: µm

Other comments:  
 .....  
 .....

Other comments:  
 .....  
 .....

Type of data machine recorded:  
 .....  
 .....

Name of data machine:

Camera during process Y/N:

Final part details:

Comments on the final conical part (surface finish, defaults...):  
 .....  
 .....

SOM after shear forming Y/N:

CMM after shear forming Y/N:

Surface roughness after shear forming Y/N:

Part to be cut after shear forming for metallurgical analysis Y/N:

ATOS III Triple Scan - final part:

Date:

Name folder:

Lenses used:

Photogrammetry used:

Number of dots used for outside:

Deviation between the 2 scans:

Other comments:  
 .....  
 .....

CMM - final part:  
 .....  
 .....

Date:

Name programme used:

Name folder:

## **Appendix E**

### **Geometries completed in the ATI–SF**

This appendix contains the drawings of the final shear formed parts completed in the ATI–SF. The work presented in Chapter 6 is based on these geometries. Figures E.1, E.2, and E.3 are the drawings of the parts shear formed with a 6 mm thick blank onto the 20°, 43°, and 53° geometries. Figures E.4, E.5, and E.6 are the drawings of the parts shear formed with a 12 mm thick blank onto the 20°, 43°, and 53° geometries.



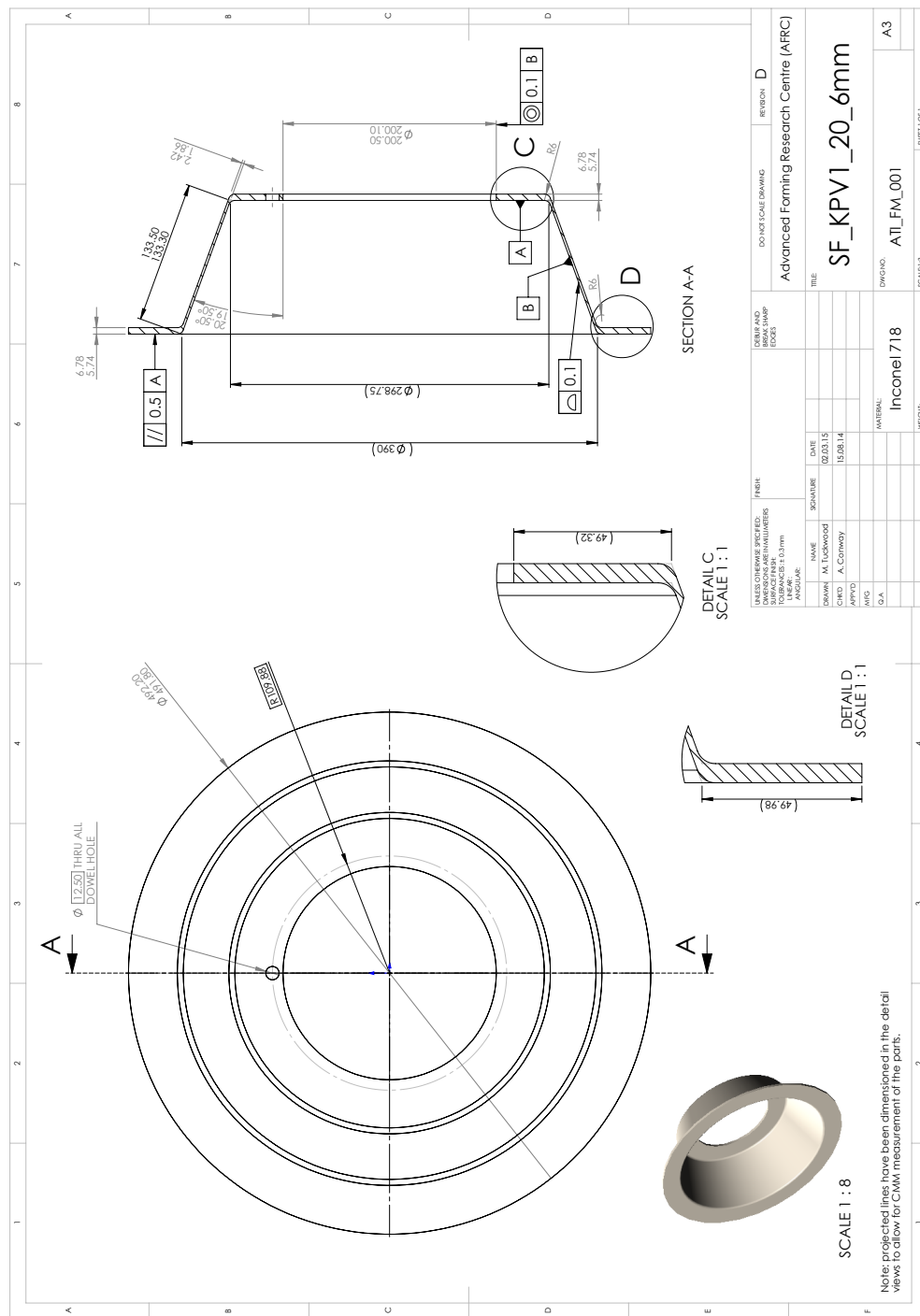


Figure E.1: Drawing: Shear formed part – 20°, 6 mm thick, ATI-SF – ATL FM 001, “SF\_KPV1\_20\_6mm”.



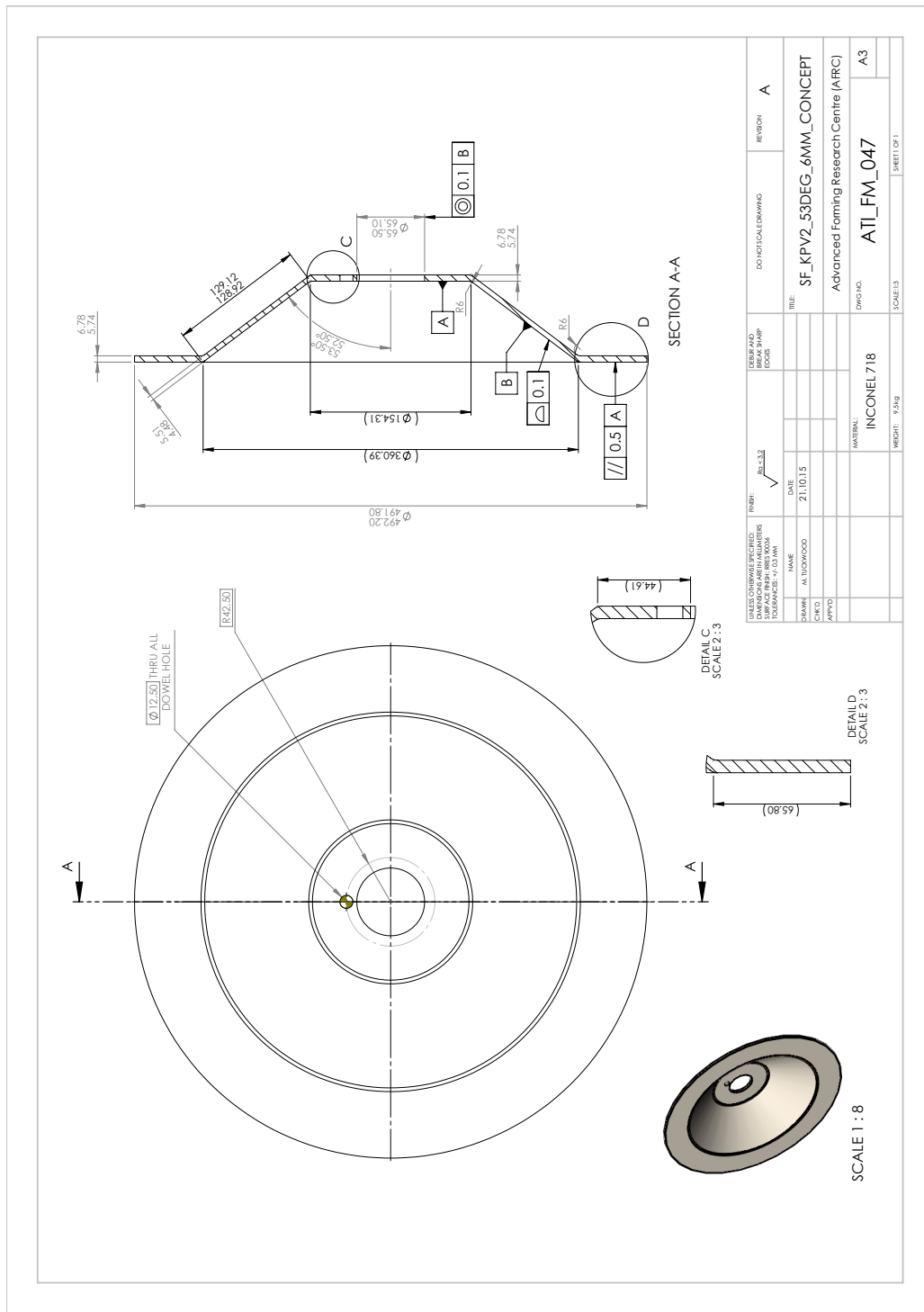


Figure E.3: Drawing: Shear formed part – 53°, 6 mm thick, ATI-SF – ATI FM 047, “SF\_KPV2\_53DEG\_6mm\_CONCEPT”.

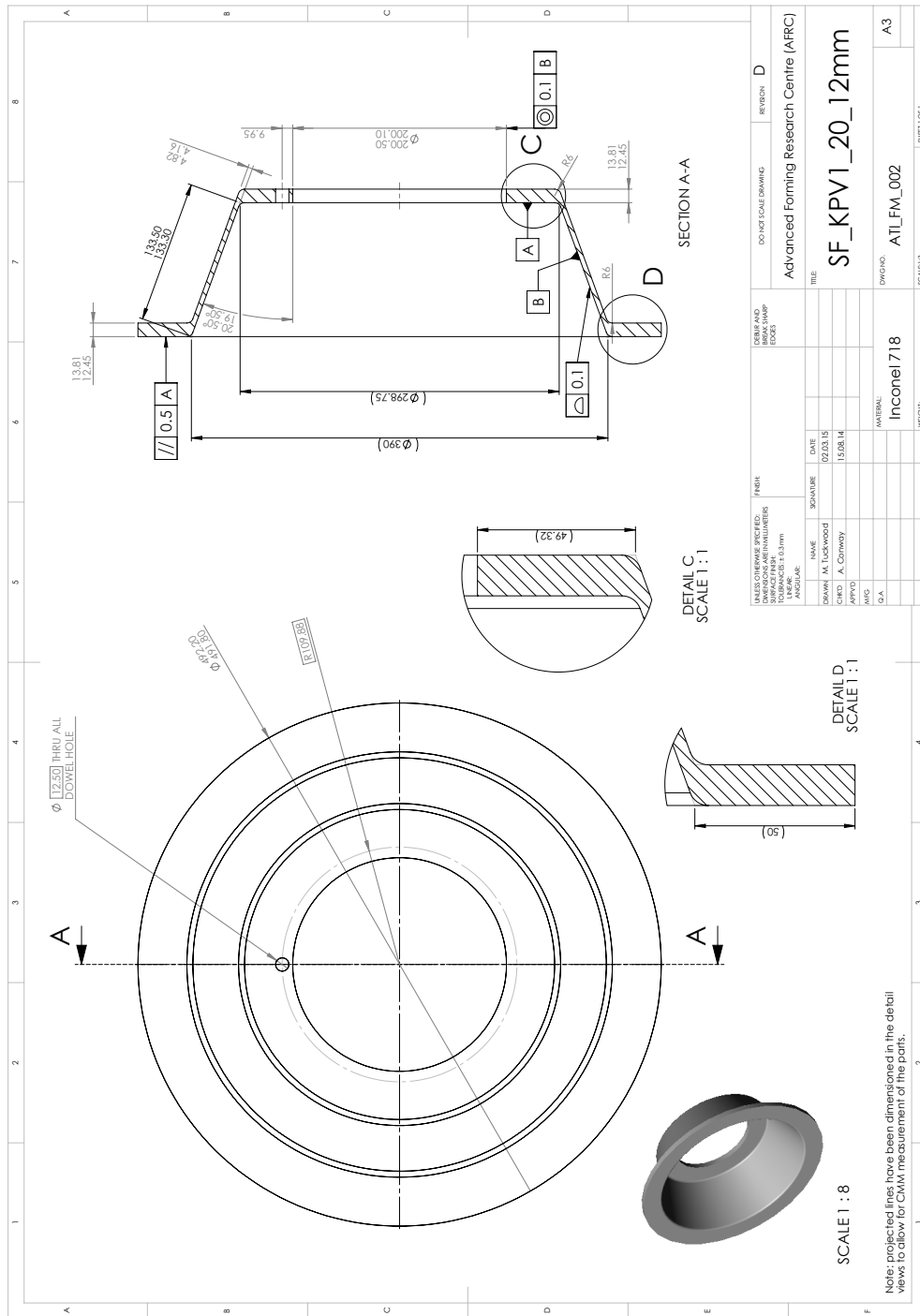


Figure E.4: Drawing: Shear formed part – 20°, 12 mm thick, ATI-SF – ATI FM 002, “SF\_KPVI\_20\_12mm” .

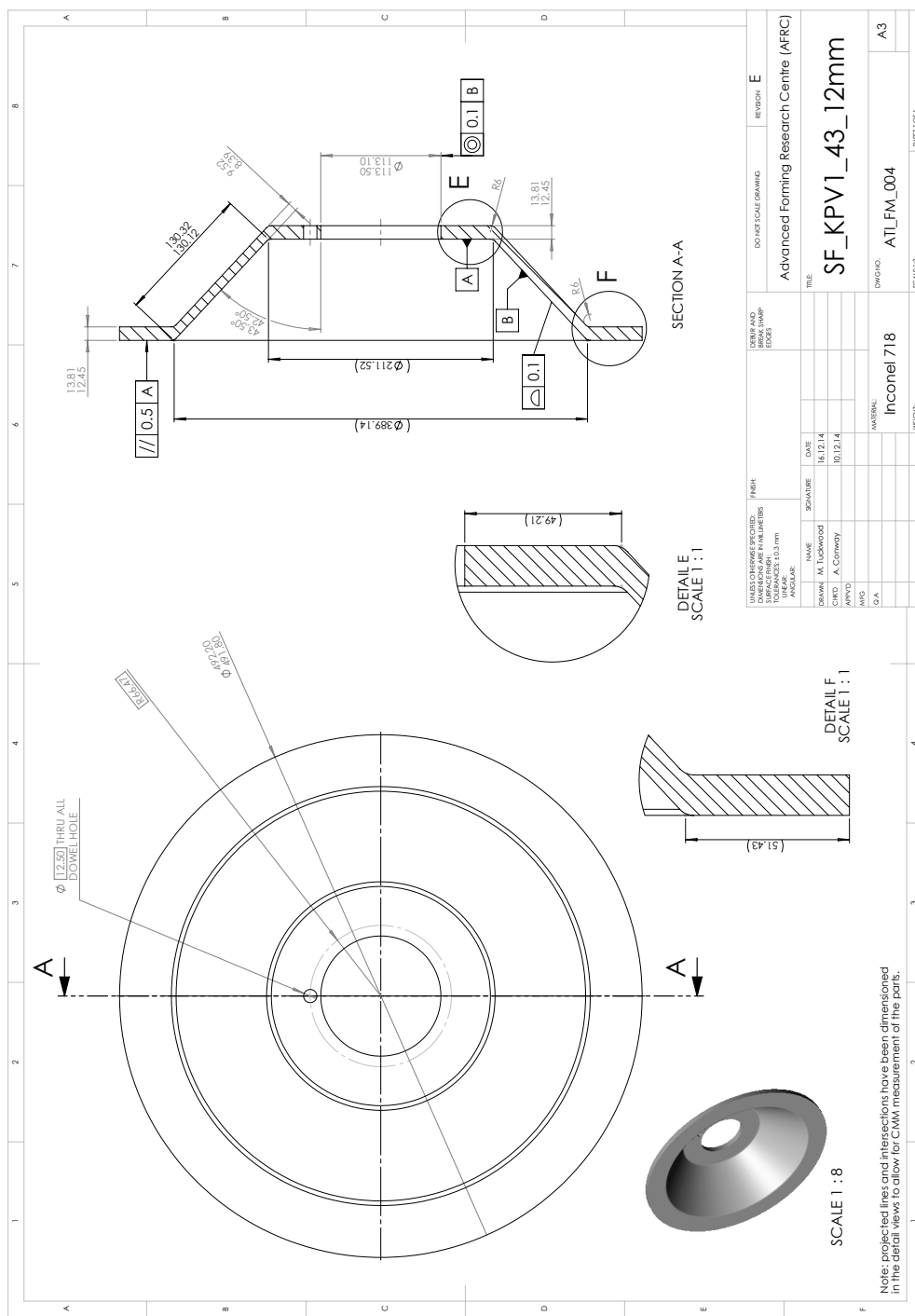


Figure E.5: Drawing: Shear formed part – 43°, 12 mm thick, ATI-SF – ATI FM 004, “SF\_KPVI\_43\_12mm”.

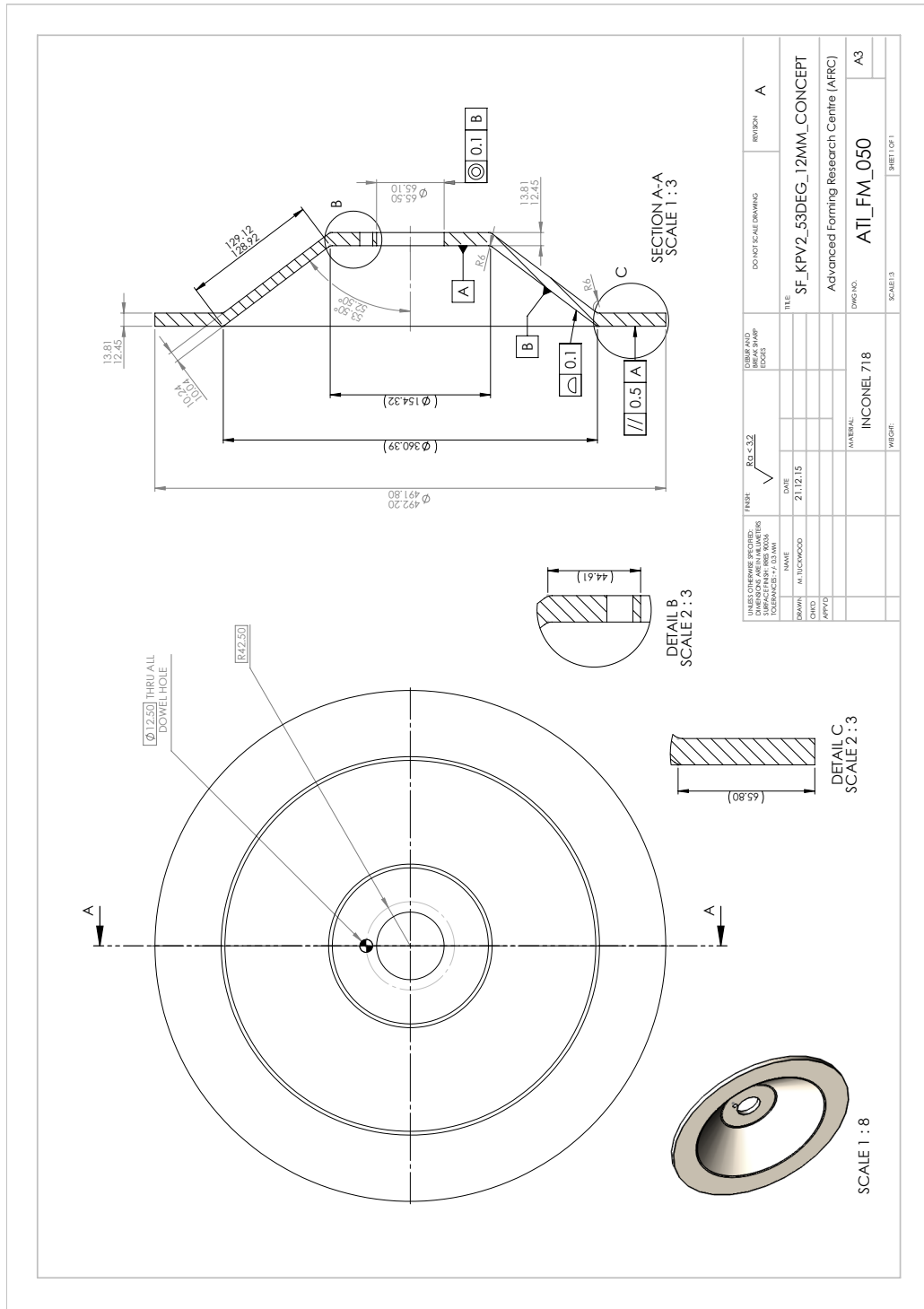


Figure E.6: Drawing: Shear formed part – 53°, 12 mm thick, ATI-SF – ATI FM 050, “SF\_KPV2\_53DEG\_12mm\_CONCEPT”.

# Appendix F

## New designs

As mentioned in Chapter 7, Appendix F details the design of the shear formed parts with greater thicknesses ( $> 6$  mm). Secondly, the design of the blanks required to achieve such geometries is described. Finally, the design and manufacture of the new mandrel insert and tailstock adaptor are explained.

Note that initially, the shear forming of blanks with an initial thickness of 15 mm and 20 mm was considered. Due to failures of the bearings and rollers during the experiments on the 15 mm thick blanks and as their investigation was still ongoing, none of the 20 mm thick blanks were formed. Nevertheless, the design of these 20 mm thick blanks and their corresponding shear formed parts are presented in this appendix as the tooling designs were dependent on them.

### F.1 Shear formed parts: new design

As presented in Chapter 6, the ATI-SF team worked on the  $43^\circ$  tooling with thicknesses of up to 12 mm as illustrated in Figure F.1 (p. 207). For comparison purposes, the drawings for the new thicknesses were defined in the same way as they were previously specified in the ATI-SF project. Figures F.2 and F.3 (pp. 208–209) are the new shear formed part drawings.

For the same reasons as previously stated, the first attempt to shear form such thicknesses was undertaken using 304L stainless steel. The material sheets complied with the ISO standard 18286 in terms of thickness tolerances. For both drawings

EngD SF\_005 and EngD SF\_006, when not specified otherwise, the linear and angular tolerances were set at medium range in accordance with the BS standard 22768-1 (British Standard Institution, 1993). In consequence, tolerances depended on the range in which the specific dimension was located. For example, a length under 6 mm had tighter tolerances than a length of 200 mm. This was the main difference with the drawings of the ATI-SF project. This change did not impact the critical features, which had the same tolerances as for the ATI-SF drawings.

The surface roughness was analysed by following Rolls-Royce's aerospace engineering specification RRES 90036 (Rolls-Royce plc, 2009). According to this specification,  $Ra$  had to be less than 3.2  $\mu\text{m}$ . Although the limit value and specification to follow were not specified on the ATI-SF drawings, they were as stated above.

## F.2 Blanks: new design

The blanks were designed in accordance with the requirements from the new shear formed parts and in the same way as in the ATI-SF project, as previously specified in Section F.1. Figure F.4 (p. 210) is the ATI-SF drawing for a 12 mm thick blank and Figures F.5 and F.6 (pp. 211–212) are the new designs.

All dimensions on these drawings had specified tolerances so nothing else was added. For the new drawings, the datum B of Figure F.4 was moved to the outside diameter so the geometrical tolerance of concentricity on the inside diameter did not refer to itself.

As mentioned earlier, the surface roughness analysis complied with Rolls-Royce's aerospace engineering specification RRES 90036. The manufacturer followed the ISO standard 18286 for the surface finish of its sheets. This standard states that the type of process was 1D, meaning "free of scale" according to the BS standard 10028-7 (British Standard Institution, 2008).  $Ra$  was chosen to be less than 3.2  $\mu\text{m}$  (N8), the same as for the shear formed parts. Although the limit value and specification to follow were not specified on the ATI-SF drawings, they were as specified above.



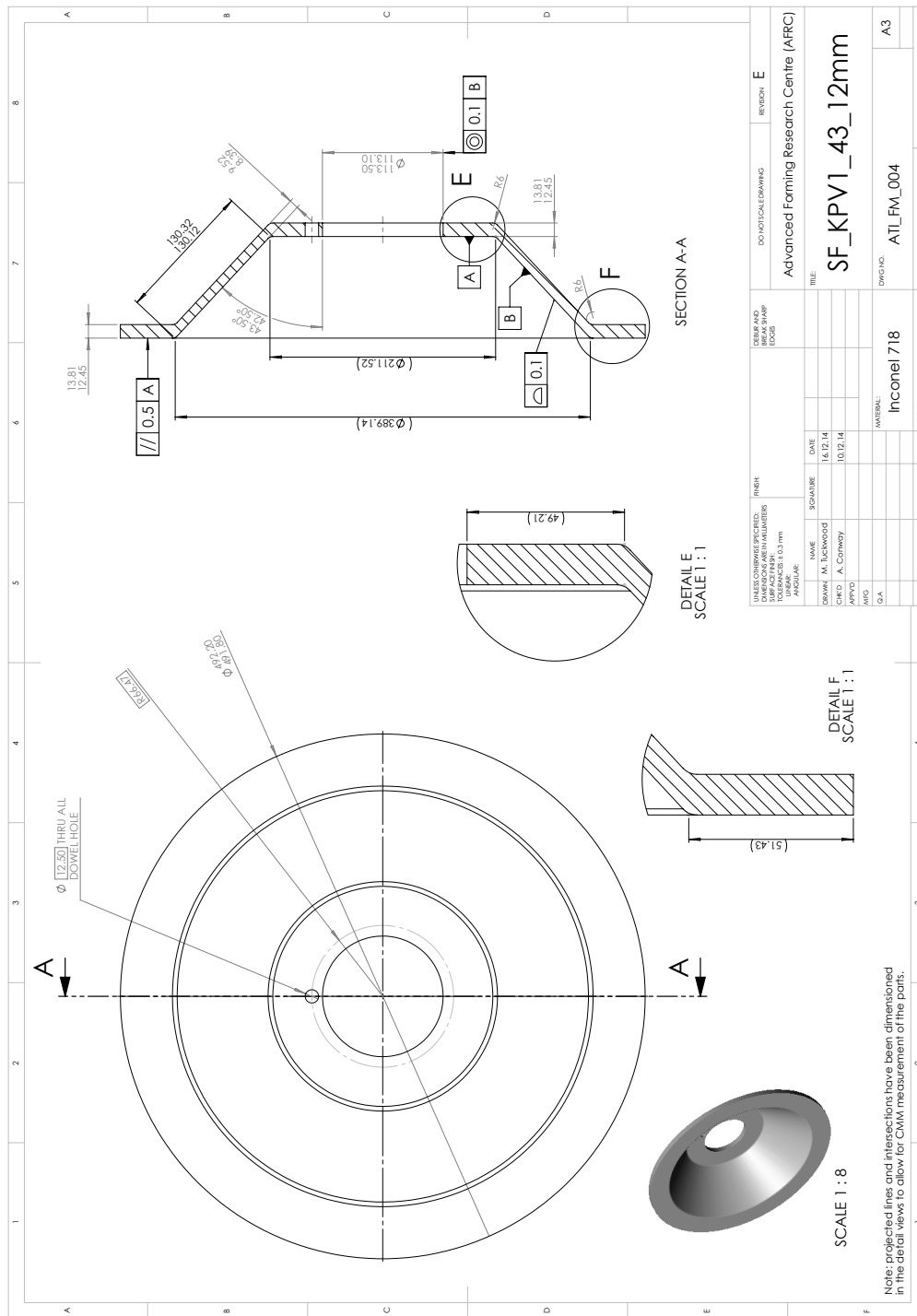


Figure F.1: Drawing: Shear formed part – 43°, 12 mm thick, ATI-SF – ATI FM 004, “SF\_KPVI\_43\_12mm”.

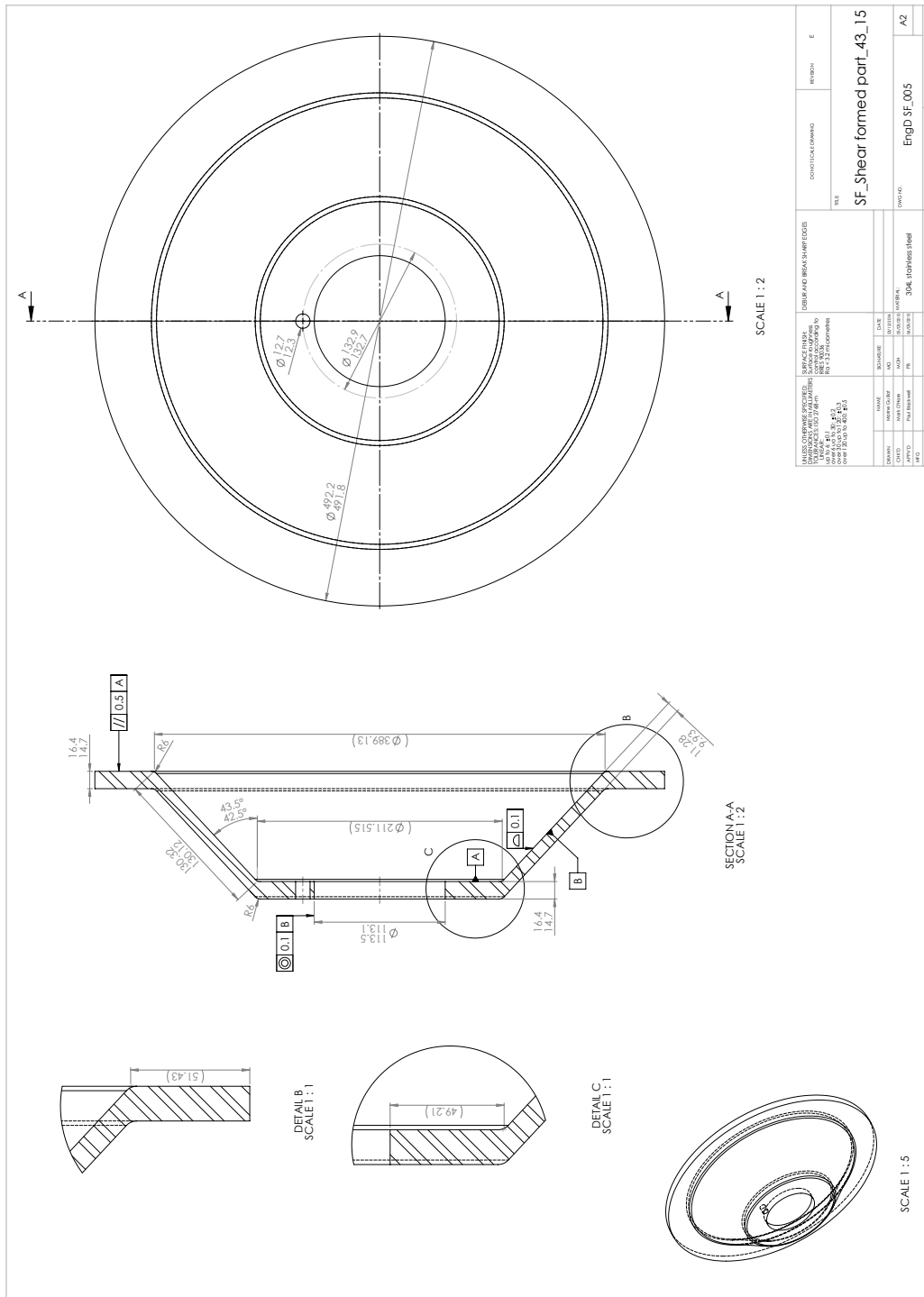


Figure F.2: Drawing: Shear formed part – 43°, 15 mm thick, EngD – EngD SF\_005, “SF\_Shear formed part\_43\_15”.

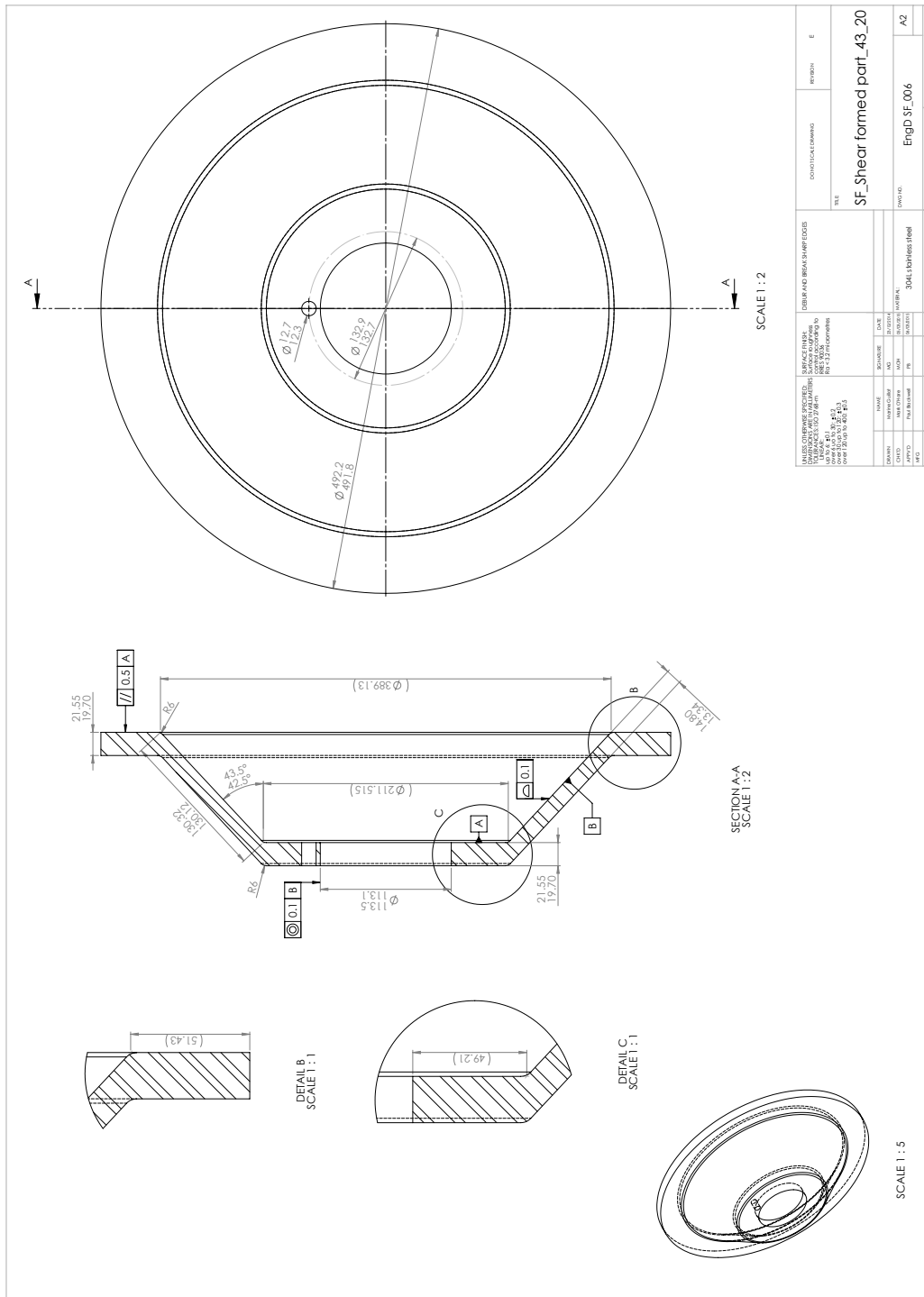


Figure F.3: Drawing: Shear formed part – 43°, 20 mm thick, EngD – EngD SF\_006, “SF Shear formed part\_43\_20”.

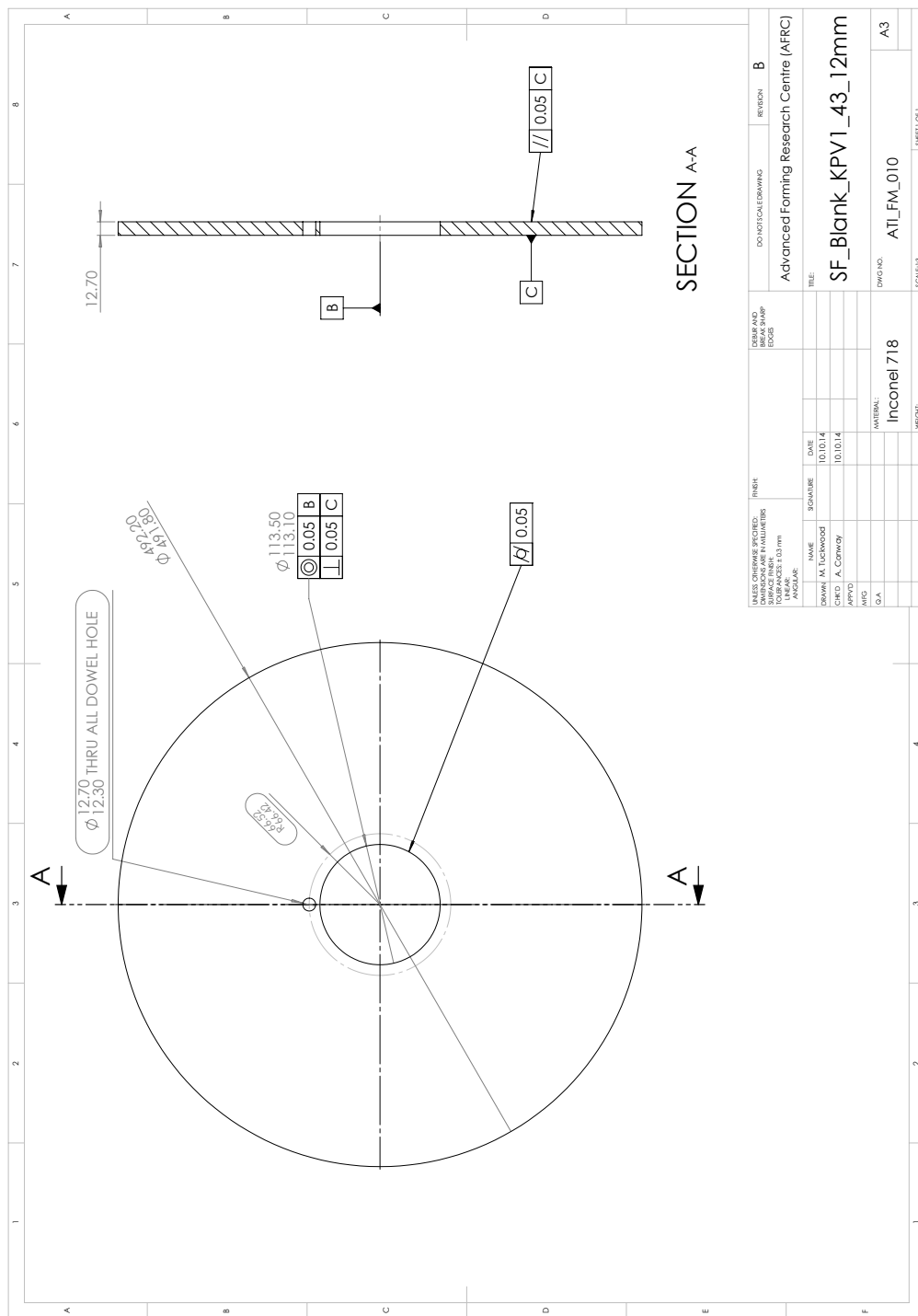


Figure F.4: Drawing: Blank – 43°, 12 mm thick, ATI-SF – ATI FM 010, “SF\_Blank\_KPV1\_43\_12mm”.

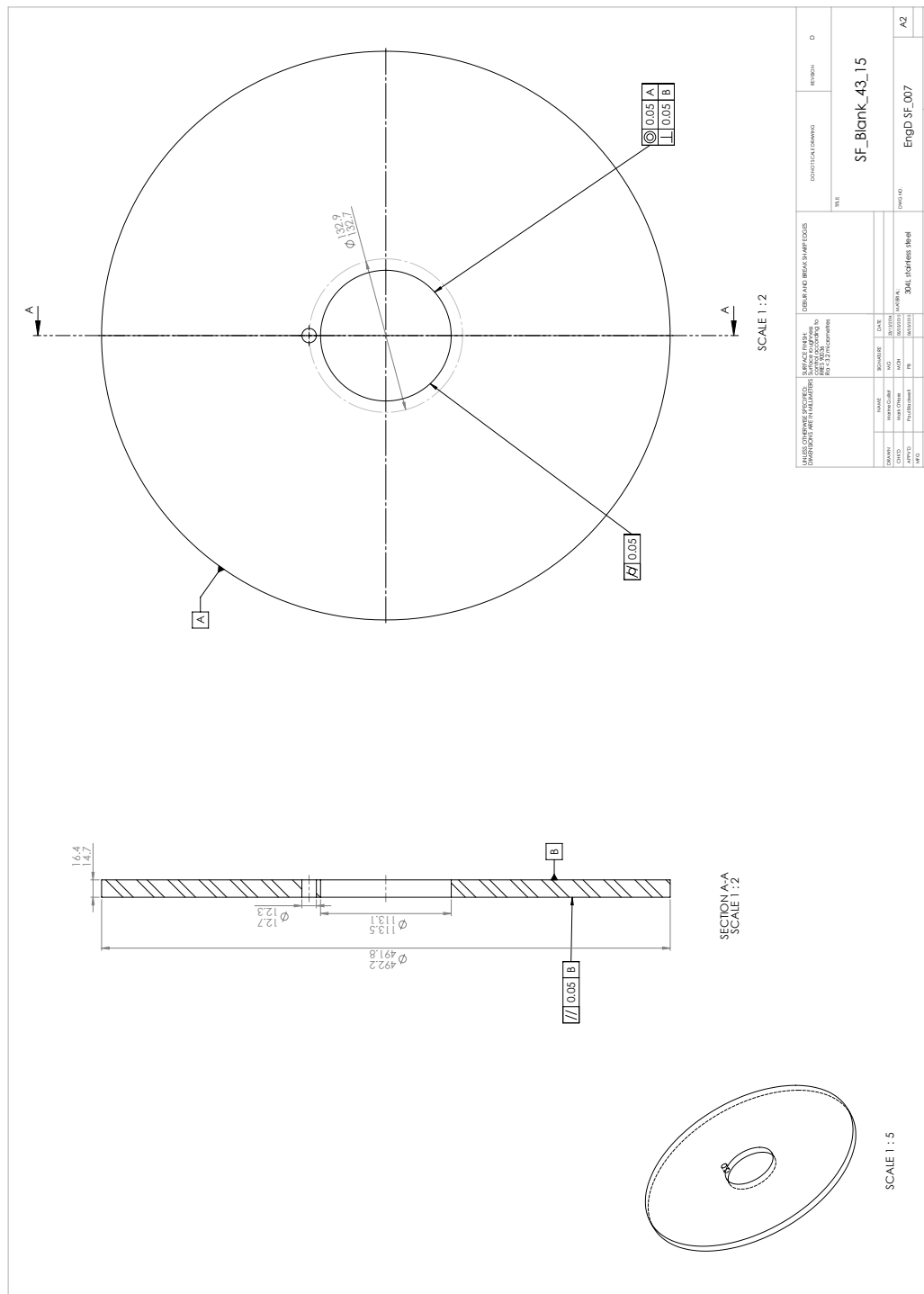


Figure F.5: Drawing: Blank – 43°, 15 mm thick, EngD – EngD SF\_007, “SF\_Blank\_43\_15”.



## F.3 Tooling: design and manufacture

### F.3.1 Mandrel insert: new design

The new mandrel insert was essentially designed by using the drawings of the current 43° and 31.5° mandrel inserts. The features discussed below were labelled in red on these drawings in order to make the reading of this subsection easier:

- Current 43° mandrel insert: features denoted  $M_{43}X^1$  (Figure F.7, p. 214)
- 31.5° mandrel insert: features denoted  $MX^2$  (Figure F.8, p. 215)
- New 43° mandrel insert: features denoted  $M_NX^3$  (Figure F.9, p. 216)

#### F.3.1.1 Locating the blank

In the ATI-SF project, the mandrel insert had two pin holes to locate the blanks. They had a different depth, one for each thickness. Here only one pin hole was utilised for both thicknesses and two different lengths of pins were employed accordingly. Consequently, feature  $M_N13$  was the only threaded pin hole for the new mandrel insert.

#### F.3.1.2 Sitting the blank

To enable the mandrel insert to support thicker blanks, features  $M_N1$  and  $M_N2$  had to be modified. Furthermore, with the previous designs of the mandrel inserts, the blank was not perfectly lying against the face of the mandrel insert. The edges at the intersections between features  $M_{43}3$  and  $M_{43}4$ , and features  $M3$  and  $M4$ , circled in red in Figure F.10, were not perfect right angles. Consequently, for the new mandrel insert, an undercut was added on this specific edge to prevent this phenomenon as shown in the Detail view C of Figure F.9 (p. 216).

---

<sup>1</sup>M for mandrel insert, 43 for the angle of the geometry, and X for the number of the specific feature

<sup>2</sup>M for mandrel insert and X for the number of the specific feature

<sup>3</sup>M for mandrel insert, N for new, and X for the number of the specific feature

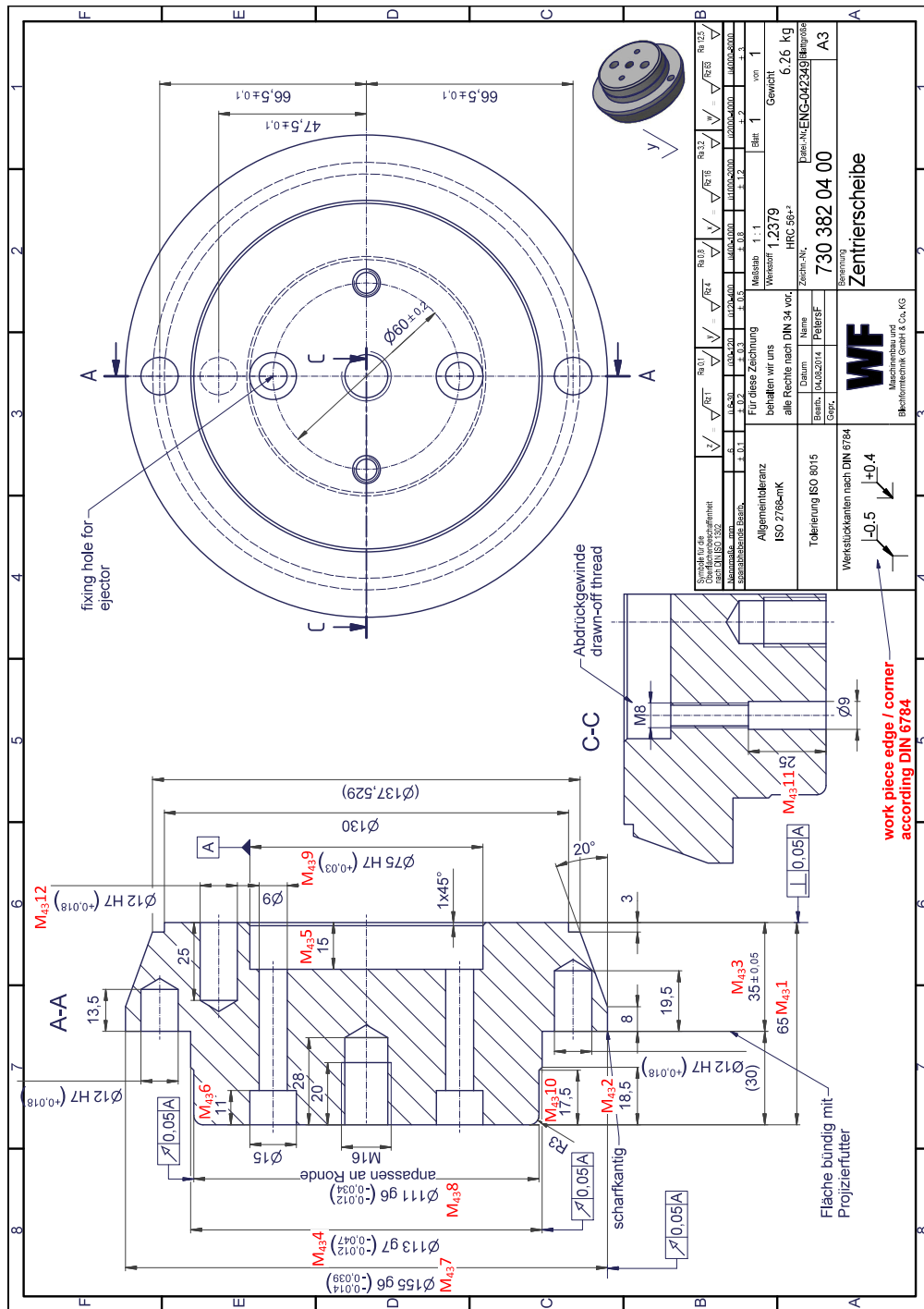


Figure F.7: Drawing: Mandrel insert – 43°, for blanks up to 12 mm thick, ATI-SF – 730 382 04 00, “Zentrierscheibe”.



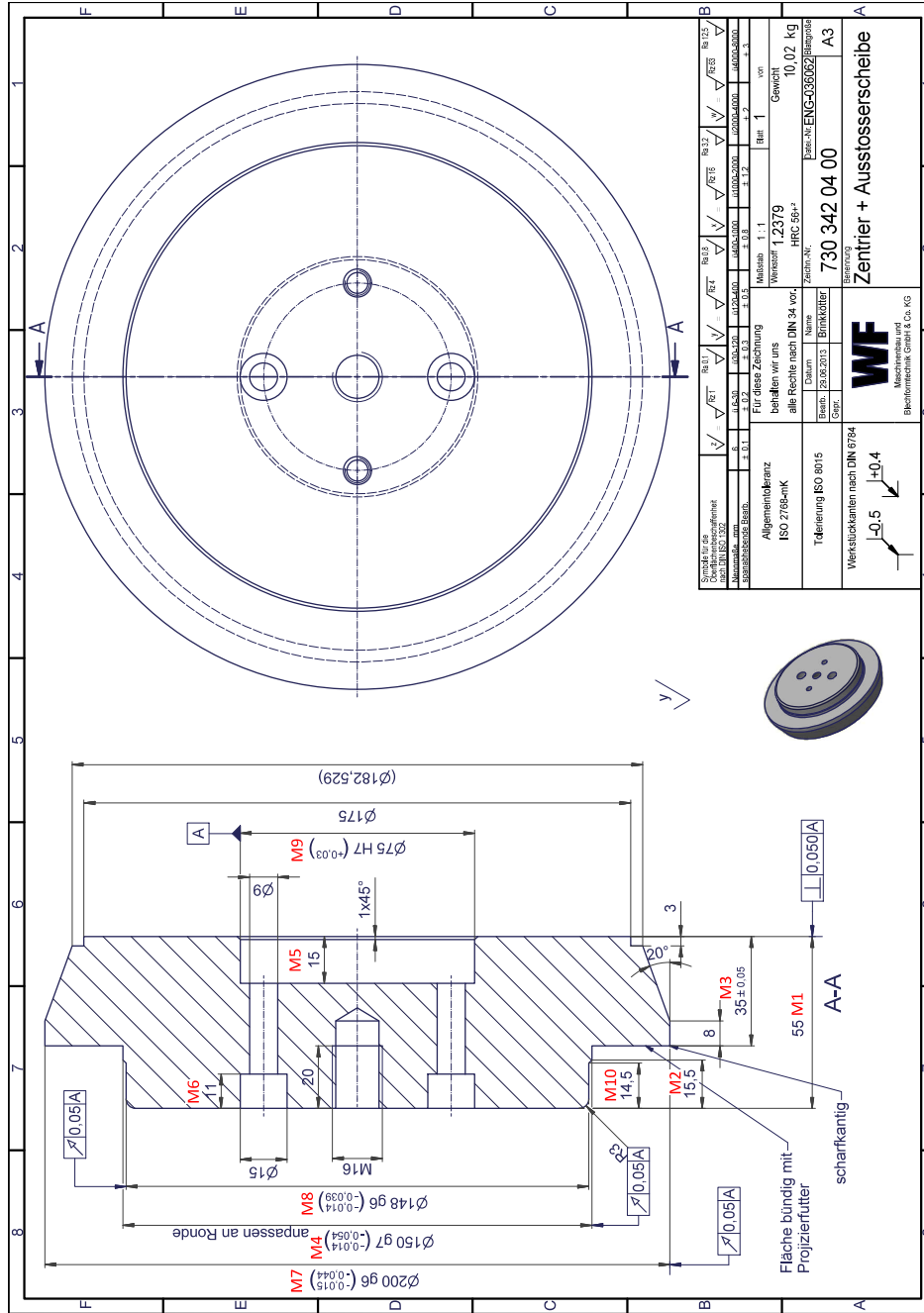


Figure F.8: Drawing: Mandrel insert – 31.5°, for blanks up to 6 mm thick – 730 342 04 00, “Zentrier + Ausstosserscheibe”<sup>4</sup>.

<sup>4</sup> The 150 mm diameter was machined down during the site acceptance trials in order to fit the blanks. A mistake was made on the concept design for those. (see Chapter ??, p. ??)

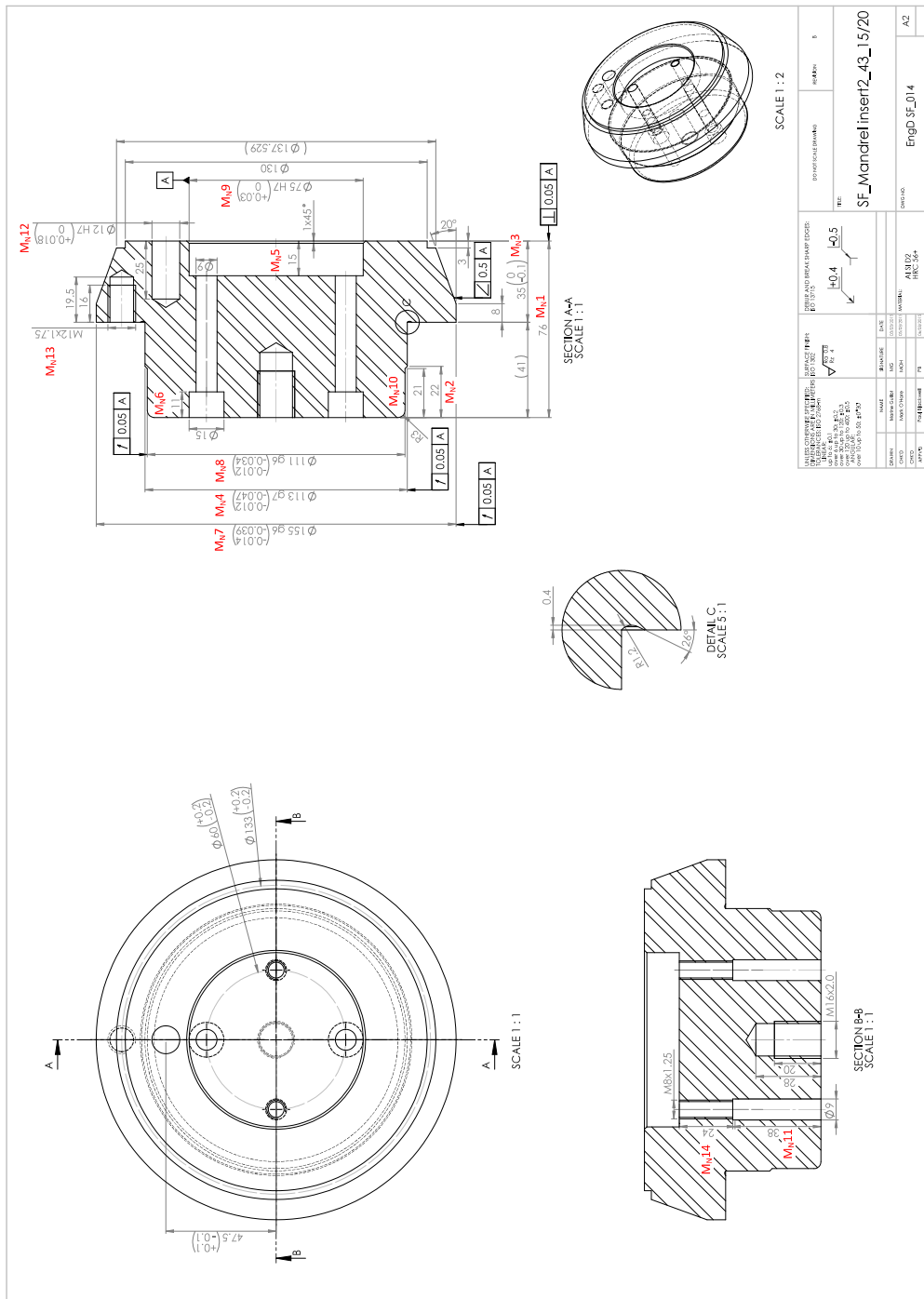


Figure F.9: Drawing: Mandrel insert – 43°, for blanks up to 20 mm thick, EngD – EngD SF\_014, “SF\_Mandrel insert2\_43\_15/20”.

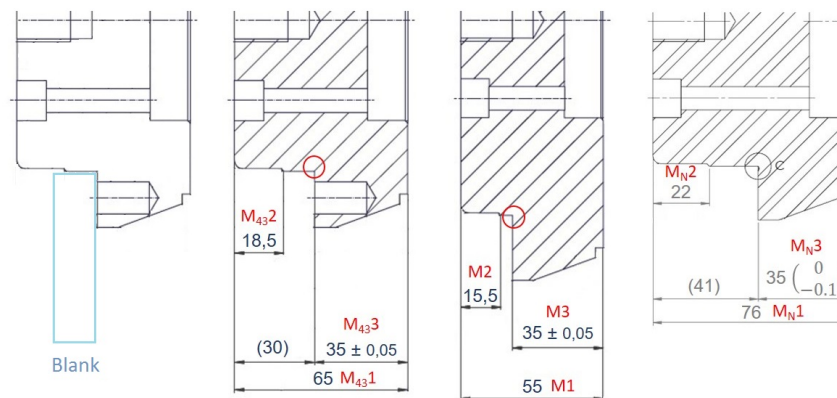


Figure F.10: Zoom in – Features 1 to 3: Current 43° (730 382 04 00), 31.5° (730 342 04 00), and new 43° (EngD SF\_014) mandrel inserts (from left to right).

### F.3.1.3 Tolerances, datum features, and surface finish

Even though some of the specified tolerances for the current 43° and 31.5° mandrel inserts were tight and in some cases would not be necessary, they were kept identical to the ones specified in WF drawings with the exception of feature  $M_{N3}$ . Indeed, by looking at the drawings of the mandrel and mandrel insert for the 43° geometry (Figure F.7, p. 214 and Figure F.11, p. 218), the mandrel insert appeared to be unlikely to fit exactly inside the mandrel due to the 35 mm wide tolerances used on both elements. In the worst case but still within tolerance, the mandrel could be at 34.95 mm and feature  $M_{N3}$  at 35.05 mm. The mandrel insert would then stick out by 0.1 mm. That was why this feature was measured using the CMM for both parts and it appeared that:

- For the mandrel, this width was 34.99 mm, so within tolerance.
- Feature  $M_{43.3}$  was at 35.08 mm, so out of tolerance.

Therefore, using the current tooling, the mandrel insert stuck out of the mandrel by approximately 0.09 mm. To prevent this issue with the new mandrel insert, the tolerances of feature  $M_{43.3}$  were changed to 35 mm ( ${}^0_{-0.1}$ ).

The datum features and geometrical tolerances were kept identical to the current drawing of the mandrel insert as can be seen in Figure F.11. Only an angularity feature was added to the current drawing to help have better control over the taper. The non-specified linear and angular tolerances, and surface finish were as formerly defined by WF.



### F.3.2 Tailstock adaptor: new design

The drawing of the new tailstock adaptor was essentially created by using the drawings of the current 31.5° and 43° tailstock adaptors. The features discussed below were labelled in red on these drawings in order to ease the reading:

- Current 43° tailstock adaptor: features denoted  $T_{43}X^5$  (Figure F.14, p. 221)
- 31.5° tailstock adaptor: features denoted  $TX^6$  (Figure F.15, p. 222)
- New 43° tailstock adaptor: features denoted  $T_NX^7$  (Figure F.16, p. 223)

#### F.3.2.1 Clamping the blank into position

At the start of the shear forming process, the tailstock adaptor came to clamp the blank, so the tailstock adaptor (7) had to fit into the mandrel insert (4) as shown in the 43° assembly drawing in Figure F.13. Features  $T_{43}1$  and  $T_{43}8$  fulfilled this purpose along with features  $T_{43}2$  and  $T_{43}9$ , which were modified accordingly as seen in Figure F.12.

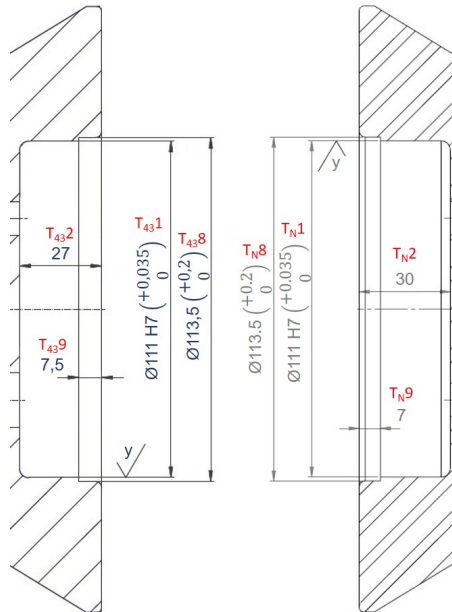


Figure F.12: Zoom in – Features 1, 2, and 9: Current 43° (730 382 07 00) and new 43° (EngD SF\_010) tailstock adaptors (from left to right).

<sup>5</sup>T for tailstock adaptor, 43 for the angle of the geometry, and X for the number of the specific feature

<sup>6</sup>T for tailstock adaptor and X for the number of the specific feature

<sup>7</sup>T for tailstock adaptor, N for new, and X for the number of the specific feature

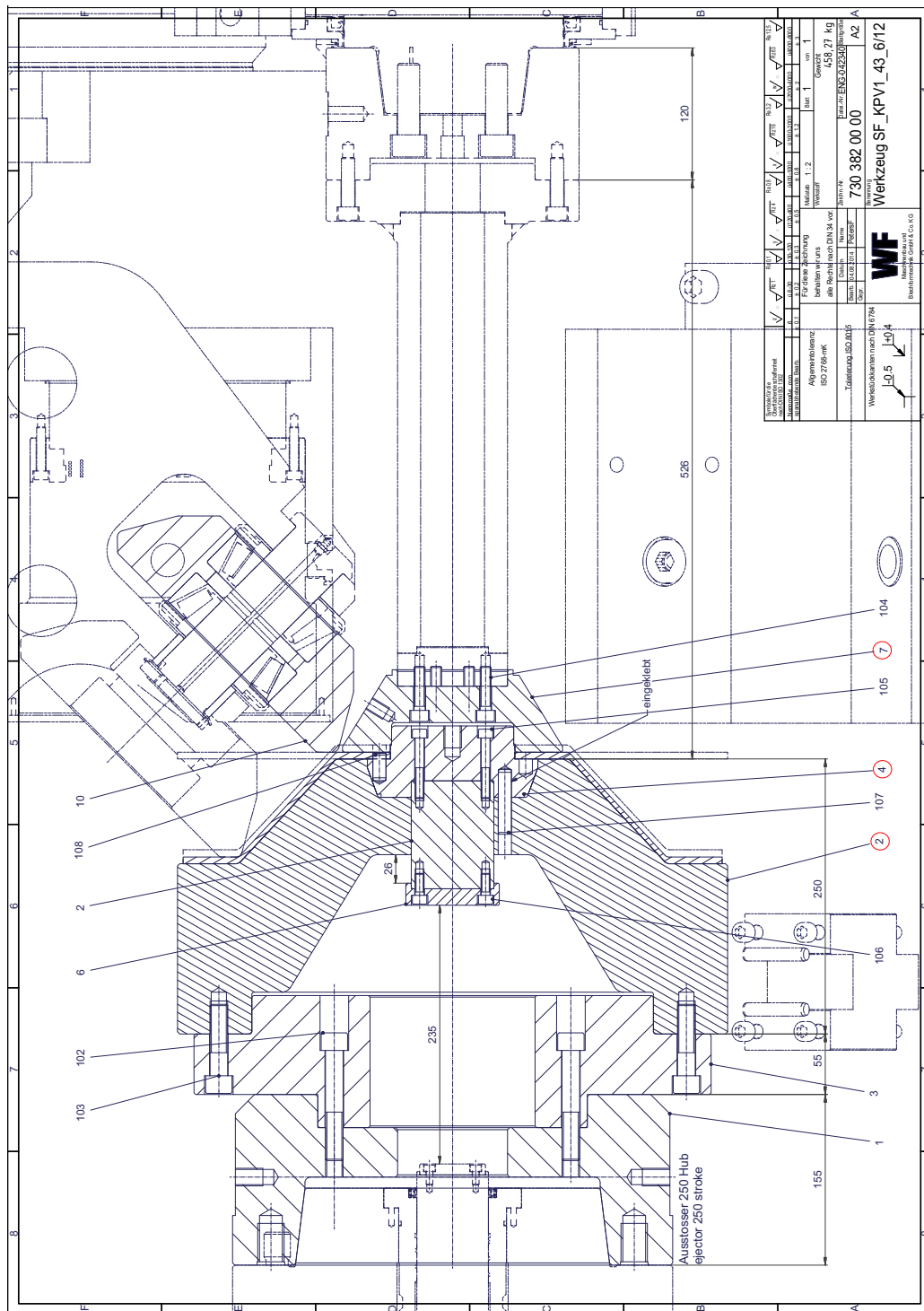


Figure F.13: Assembly drawing – 43° geometry – 730 382 00 00, “Werkzeug SF\_KPVI\_43\_6/12”.

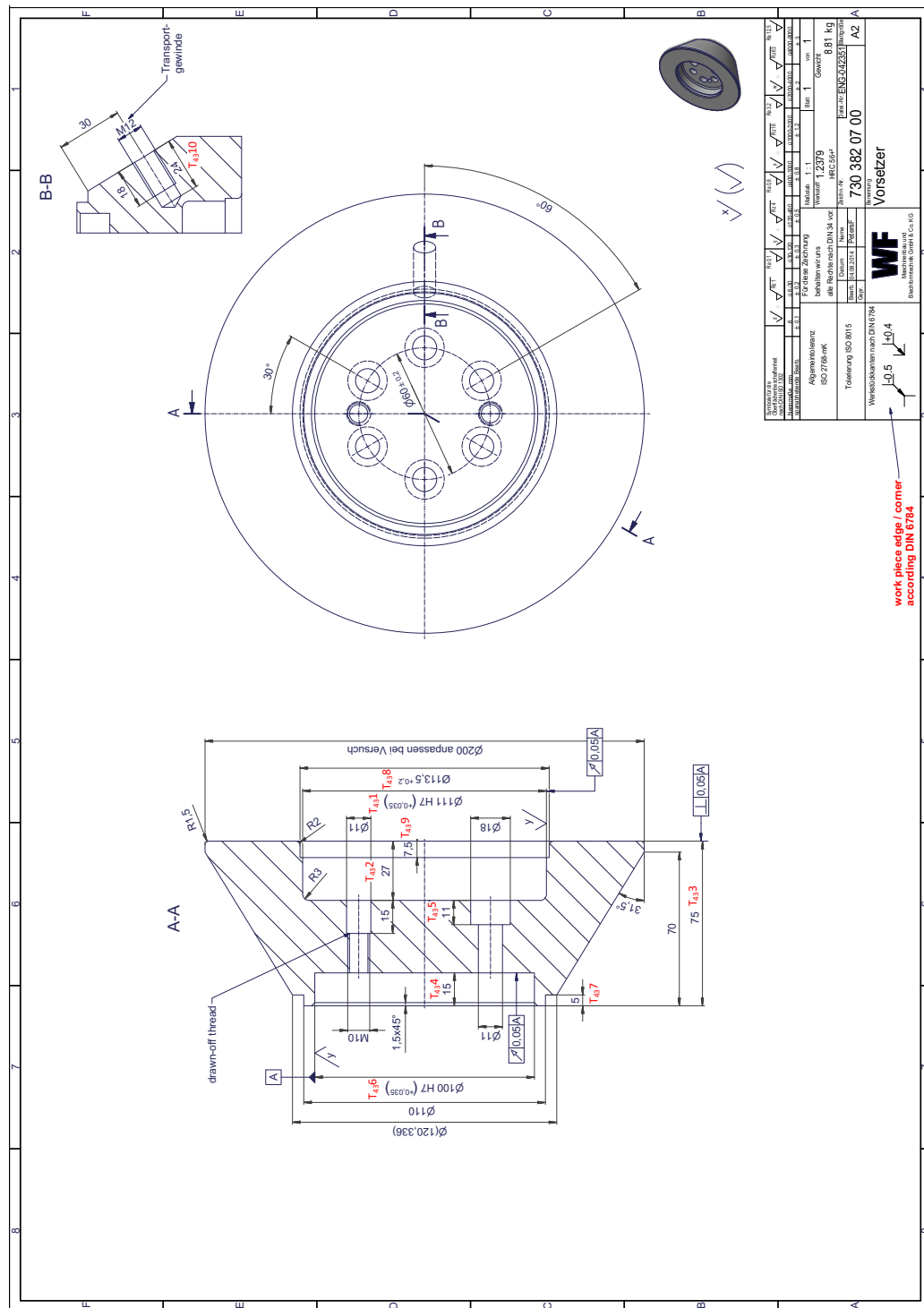


Figure F.14: Drawing: Tailstock adaptor – 43°, for blanks up to 12 mm thick, ATI-SF – 730 382 07 00, “Vorseizer”.





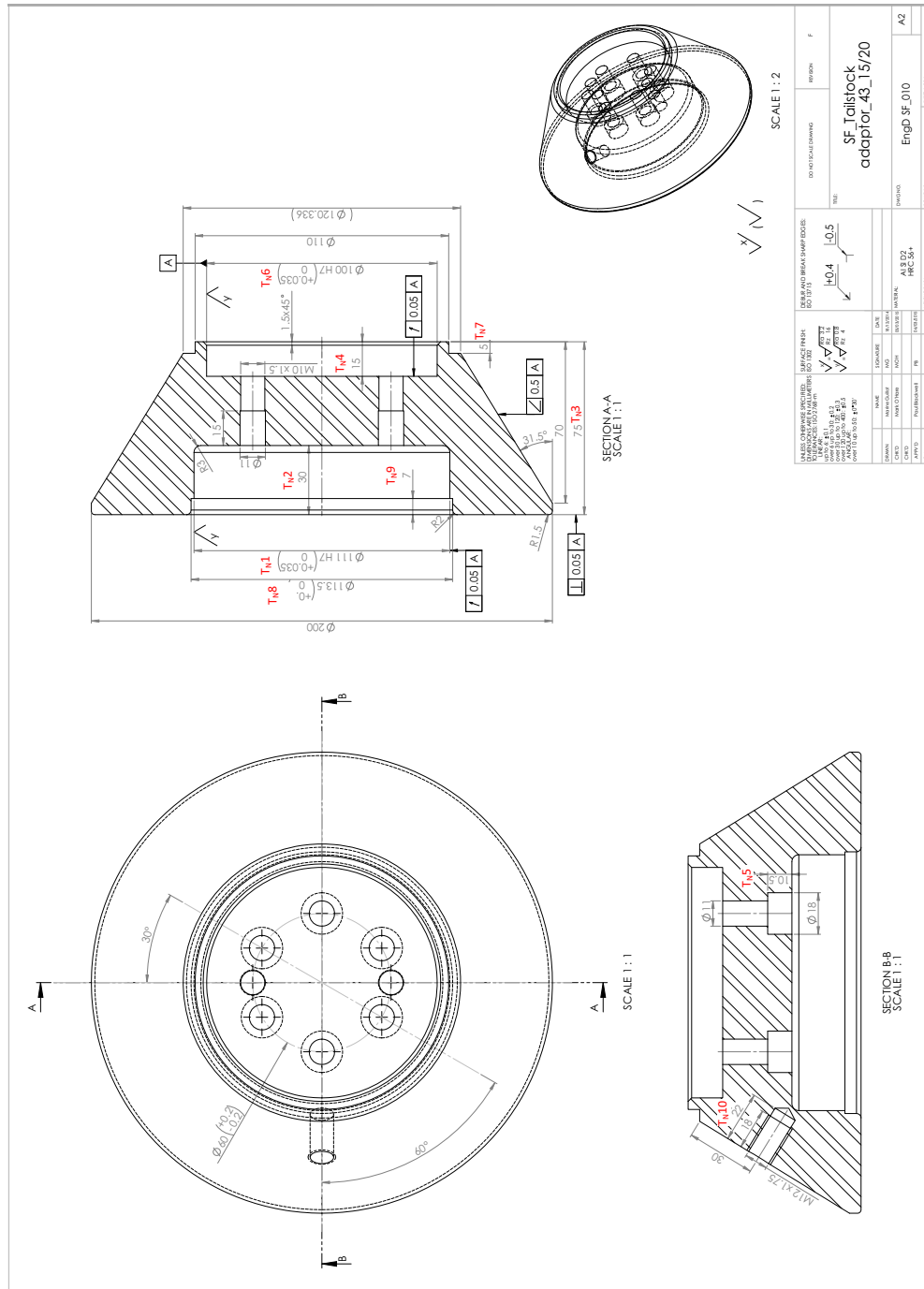


Figure F.16: Drawing: Tailstock adaptor – 43°, for blanks up to 20 mm thick, EngD SF\_010, “SF\_Tailstock adaptor\_43\_15/20”.

**F.3.2.2 Tolerances, datum features, and surface finish**

The datum features and geometrical tolerances were kept identical to the current drawing of the tailstock adaptor (Figure F.14, p. 221). Only an angularity feature was added to the current drawing to help have better control over the cone shape. The non-specified linear and angular tolerances, and surface finish were as formerly defined by WF.

**F.3.3 New tooling: manufacture and inspection**

Both the mandrel insert and tailstock adaptor were machined at the AFRC and hardened and triple tempered by Vacua-Therm Sales. After final machining, both elements of tooling were dimensionally inspected using a CMM and their surface finish was measured using a portable surface roughness tester. Both the new mandrel insert and tailstock adaptor were not always exactly within tolerance in terms of geometry and surface finish. However, this did not impact the critical features. The geometry and surface finish for the current 43° elements were not always within tolerance either. As a result, the new elements were considered acceptable after ensuring their fit with the other parts of the tooling. In the future, the AFRC will be more experienced in terms of tooling manufacture. The new CNC equipment recently received will help achieve tighter tolerances. No simulations of the interactions between tooling and part were undertaken as the new tooling elements were very similar to the current ones. In the future, if the tooling had to be drastically modified, simulation would have to be considered.

## References

- V. Acharya, S. Ramesh, and G.V.S. Murthy. *Characterization of Intermetallic Precipitates in Ni-Base Alloys by Non-destructive Techniques*. InTech, 2015. ISBN 978-953-51-2212-8.
- N. Alberti, L. Cannizzaro, E. Lo Valvo, and F. Micari. Analysis of metal spinning processes by the adina code. *Computers & Structures*, 32(3-4):517–525, 1989. doi: 10.1016/0045-7949(89)90343-X.
- Alicona. InfiniteFocus for form and roughness measurement. [Online] Available from: <http://www.aliconaco.uk/home/products/infinitefocus-standard.html> [Accessed: 30th March 2014], c. 2014.
- M. Amitava, P.K. De, D.K. Bhattacharya, P.K. Srivastava, and D.C. Jiles. Ferromagnetic properties of deformation-induced martensite transformation in AISI 304 stainless steel. *Metallurgical and Materials Transactions A*, 35(2):599–605, 2004. doi: 10.1007/s11661-004-0371-6.
- J. Antony. *Design of Experiments for Engineers and Scientists*. Elsevier Science & Technology Books, 2003. ISBN 0 75064 709 4.
- J. Antony. *Design of Experiments (DoE) for Process Optimisation*. University of Strathclyde, 2014.
- ASTM International. *ASTM E384-11 Standard Test Method for Knoop and Vickers Hardness of Materials*. ASTM International, West Conshohocken, 2011. doi: 10.1520/E0384-11E01.
- ASTM International. *ASTM A240/A240M-16a Standard Specification for Chromium and Chromium-Nickel Stainless Steel Plate, Sheet, and Strip for Pressure Vessels and for General Applications*. ASTM International, West Conshohocken, 2016a. doi: 10.1520/A0240\_A0240M-16A.
- ASTM International. *ASTM B637-16 Standard Specification for Precipitation-Hardening and Cold Worked Nickel Alloy Bars, Forgings, and Forging Stock for Moderate or High Temperature Service*. ASTM International, West Conshohocken, 2016b. doi: 10.1520/B0637-16.

- B. Avitzur and C.T. Yang. Analysis of power spinning of cones. *Journal of Engineering for Industry*, 82(3):231–244, 1960.
- S. Azadian, L.-Y. Wei, and R. Warren. Delta phase precipitation in Inconel 718. *Materials Characterization*, 53(1):7–16, 2004. doi: 10.1016/j.matchar.2004.07.004.
- I. Baker. Recovery, recrystallization and grain growth in ordered alloys. *Intermetallics*, 8(9):1183–1196, 2000. doi: 10.1016/S0966-9795(00)00031-5.
- O. Bapokutty, Z. Sajun, and J. Syarif. Stress relaxation behavior of heat treated Inconel 718. *Journal of Applied Sciences*, 12(9):870–875, 2012. doi: 10.3923/jas.2012.870.875.
- M.R. Barnett and F. Montheillet. The generation of new high-angle boundaries in aluminium during hot torsion. *Acta Materialia*, 50(9):2285–2296, 2002. doi: 10.1016/S1359-6454(02)00048-4.
- A. Bastos, S. Zaefferer, D. Raabe, and C. Schuh. Characterization of the microstructure and texture of nanostructured electrodeposited NiCo using electron backscatter diffraction (EBSD). *Acta Materialia*, 54(9):2451–2462, 2006. doi: 10.1016/j.actamat.2006.01.033.
- B.P. Bewlay and D.U. Furrer. Spinning. In *ASM Handbook Volume 14 B – Metalworking: Sheet Forming*. ASM International, 2006. ISBN 978-0-87170-710-9.
- J. Biehler, H. Hoche, and M. Oechsner. Corrosion properties of polished and shot-peened austenitic stainless steel 304L and 316L with and without plasma nitriding. *Surface and Coatings Technology*, 313:40–46, 2017. doi: 10.1016/j.surfcoat.2017.01.050.
- M. Blair. Cast stainless steels. In *ASM Handbook Volume 1 – Properties and Selection: Irons, Steels, and High Performance Alloys*. ASM International, 1990. ISBN 978-0-87170-377-4.
- British Standard Institution. *BS EN 22768-1:1993 General Tolerances – Part 1: Tolerances for linear and angular dimensions without individual tolerance indications*. British Standard Institution, 1993. ISBN 0 580 22604 2.

- British Standard Institution. *BS ISO 13565-1:1998 Geometrical Product Specifications (GPS) – Surface texture – Profile method: Surfaces having stratified functional properties – Part 1: Filtering and general measurement conditions*. British Standard Institution, 1997a. ISBN 0 580 27533 7.
- British Standard Institution. *BS EN ISO 3274:1998 Geometrical Product Specification (GPS) – Surface texture – Profile method: Nominal characteristics of contact (stylus) instruments*. British Standard Institution, 1997b. ISBN 0 580 27531 0.
- British Standard Institution. *BS EN ISO 4288:1998 Geometrical product specification (GPS) – Surface texture – Profile method: Rules and procedures for the assessment of surface texture*. British Standard Institution, 1997c. ISBN 0 580 27033 5.
- British Standard Institution. *BS EN ISO 4287:1998 +A1:2009 Geometrical Product Specification (GPS) – Surface texture – Profile method: Terms, definitions and surface texture parameters*. British Standard Institution, 2000. ISBN 978 0 580 59149 5.
- British Standard Institution. *BS EN ISO 5436-1:2001 Geometrical product specification (GPS) – Surface texture – Profile method: Measurement standards – Part 1: Material measures*. British Standard Institution, 2001. ISBN 0 580 38404 7.
- British Standard Institution. *BS EN ISO 6507-1:2005 Metallic materials – Vickers hardness tests – Part 1: Test method*. British Standard Institution, 2006a. ISBN 0 580 47674 X.
- British Standard Institution. *BS EN ISO 6507-2:2005 Metallic materials – Vickers hardness tests – Part 2: Verification and calibration of testing machines*. British Standard Institution, 2006b. ISBN 0 580 47588 3.
- British Standard Institution. *BS EN 10028-7:2007 Flat products made of steels for pressure purposes – Part 7: Stainless steels*. British Standard Institution, 2008. ISBN 978 0 580 55381 3.
- British Standard Institution. *BS EN 10360-2:2009 Geometrical Product Specifications (GPS) – Acceptance and reverification tests for coordinate measuring machines (CMM) – Part 2: CMMs used for measuring linear dimensions*. British Standard Institution, 2010a. ISBN 978 0 580 57009 4.

- British Standard Institution. *BS EN 10360-5:2010 Geometrical Product Specifications (GPS) – Acceptance and reverification tests for coordinate measuring machines (CMM) – Part 5: CMMs using single and multiple stylus contacting probing systems*. British Standard Institution, 2010b. ISBN 978 0 580 57466 5.
- British Standard Institution. *PD ISO/TR 12888:2011 Selected illustrations of gauge repeatability and reproducibility studies*. British Standard Institution, 2012. ISBN 978 0 580 65175 5.
- E. Cakmak, S.C. Vogel, and H. Choo. Effect of martensitic phase transformation on the hardening behavior and texture evolution in a 304L stainless steel under compression at liquid nitrogen temperature. *Materials Science and Engineering: A*, 589:235–241, 2014. doi: 10.1016/j.msea.2013.09.093.
- G. Camus. *Traitements thermomécaniques de l’alliage NC19FeNb (Inconel 718) pour différentes applications sur turbomachines industrielles et aéronautiques*. PhD thesis, National Polytechnic Institute of Toulouse, 1986.
- L.A. Chapman. Application of high temperature DSC technique to nickel-based superalloys. *Journal of Materials Science*, 39(24):7229–7236, 2004. doi: 10.1023/B:JMSE.0000048736.86794.12.
- M.D. Chen, R.Q. Hsu, and K.H. Fuh. Forecast of shear spinning force and surface roughness of spun cones by employing regression analysis. *International Journal of Machine Tools and Manufacture*, 41(12):1721–1734, 2001. doi: 10.1016/S0890-6955(01)00039-6.
- M.D. Chen, R.Q. Hsu, and K.H. Fuh. Effects of over-roll thickness on cone surface roughness in shear spinning. *Journal of Materials Processing Technology*, 159(1): 1–8, 2005. doi: 10.1016/j.jmatprotec.2003.07.017.
- A. Das, S. Sivaprasad, M. Ghosh, P.C. Chakraborti, and S. Tarafder. Morphologies and characteristics of deformation induced martensite during tensile deformation of 304LN stainless steel. *Materials Science and Engineering: A*, 486(1):283–286, 2008. doi: 10.1016/j.msea.2007.09.005.
- J. R. Davis et al. *ASM specialty handbook: Heat-resistant materials*. ASM International, 1997.

- M. Dehmas, J. Lacaze, A. Niang, and B. Viguier. TEM study of high-temperature precipitation of delta phase in Inconel 718 alloy. *Advances in Materials Science and Engineering*, 2011, 2011. doi: 10.1155/2011/940634.
- D. Delagnes and P. Lours. Les aciers pour applications aéronautiques (AAA). Lecture from École des Mines d'Albi-Carmaux, 2011.
- J. Deleume. *Facteurs métallurgiques et mécaniques contrôlant l'amorçage de défauts de corrosion sous contrainte dans l'alliage 718 en milieu primaire des réacteurs à eau sous pression*. PhD thesis, Institut National Polytechnique de Toulouse, 2007.
- Y. Desvallées, M. Bouzidi, F. Bois, and N. Beaudé. Delta phase in Inconel 718: Mechanical properties and forging process requirements. *Superalloys*, 718(706): 281–291, 1994. doi: 10.7449/1994/Superalloys\_1994\_281\_291.
- A. Devaux, L. Nazé, R. Molins, A. Pineau, A. Organista, J.Y. Guédou, J.F. Uginet, and P. Héritier. Gamma double prime precipitation kinetic in Alloy 718. *Materials Science and Engineering: A*, 486(1):117–122, 2008. doi: 10.1016/j.msea.2007.08.046.
- D.J. Dingley and V. Randle. Microtexture determination by electron back-scatter diffraction. *Journal of Materials Science*, 27(17):4545–4566, 1992. doi: 10.1007/BF01165988.
- M. J. Donachie and S. J. Donachie. *Superalloys – A Technical Guide*. ASM International, Second edition, 2002. ISBN 0 87170 749 7.
- G. Duquesnoy. *Procédé de fabrication par fluotournage à chaud d'une pièce en un matériau non malléable à température ambiante et outillage correspondant*. Aérospatiale Société Nationale Industrielle, 1992. Patent No. EP0490756 (B1).
- H.L. Eiselstein and D.J. Tillack. The invention and definition of alloy 625. *Superalloys*, 718(625):1–14, 1991. doi: 10.7449/1991/Superalloys\_1991\_1\_14.
- O. Engler and V. Randle. *Introduction to texture analysis: macrostructure, microstructure and orientation mapping*. CRC Press, Second edition, 2009. ISBN 978 1 420 06365 3.

- H.E. Exner and S. Weinbruch. Scanning electron microscopy. In *ASM Handbook Volume 9 – Metallography and Microstructures*. ASM International, 2004. ISBN 978-0-87170-706-2.
- D.P. Field. Textured structures. In *ASM Handbook Volume 9 – Metallography and Microstructures*. ASM International, 2004. ISBN 978-0-87170-706-2.
- GOM mbH. *ATOS Professional V7.5 Manual*. Braunschweig, 2011.
- GOM Optical Measuring Techniques. ATOS – Industrial 3D Scanning Technology. [Online] Available from: <http://www.gom.com/metrology-systems/3d-scanner.html> [Accessed: 30th March 2014], c. 2014.
- P.J. Goodhew, J. Humphreys, and R. Beanland. Light and electron microscopy. In *ASM Handbook Volume 9 – Metallography and Microstructures*. ASM International, 2004. ISBN 978-0-87170-706-2.
- D.M. Grove and T.P. Davis. *Engineering Quality & Experimental Design*. Longman, 1992. ISBN 978 0 582 06687 8.
- E. Hagan and J. Jeswiet. A review of conventional and modern single-point sheet metal forming methods. *Proceedings of the Institution of Mechanical Engineers, Part B: Journal of Engineering Manufacture*, 217(2):213–225, 2003. doi: 10.1243/095440503321148858.
- M. Hayama, T. Murota, and H. Kudo. Deformation modes and wrinkling of flange on shear spinning. *Bulletin of JSME*, 9(34):423–433, 1966.
- J.P.T. Higgins and S. Green, editors. *Cochrane Handbook for Systematic Reviews of Interventions (Version 5.1.0)*. The Cochrane Collaboration, 2011. Available from: [www.handbook.cochrane.org](http://www.handbook.cochrane.org).
- Y. Huang and T. G. Langdon. The evolution of delta-phase in a superplastic Inconel 718 alloy. *Journal of Materials Science*, 42(2):421–427, 2007. doi: 10.1007/s10853-006-0483-z.
- R.E. Hummel. Iron and steel. In *Understanding materials science: history, properties, applications*, pages 141–154. Springer Science & Business Media, Second edition, 2004. ISBN 0-387-20939-5.



- F.J. Humphreys. A unified theory of recovery, recrystallization and grain growth, based on the stability and growth of cellular microstructures – I. The basic model. *Acta Materialia*, 45(10):4231–4240, 1997. doi: 10.1016/S1359-6454(97)00070-0.
- V. Kain, K. Chandra, K.N. Adhe, and P.K. De. Effect of cold work on low-temperature sensitization behaviour of austenitic stainless steels. *Journal of Nuclear Materials*, 334(2):115–132, 2004. doi: 10.1016/j.jnucmat.2004.05.008.
- S. Kalpakcioglu. A study of shear-spinnability of metals. *Journal of Engineering for Industry*, 83(4):478–483, 1961.
- Serope Kalpakjian. *Manufacturing processes for engineering materials*. Pearson Education India, 1984.
- K. Kawai and M. Hayama. Roller pass programming in conventional spinning by nc spinning machine. *Advanced Technology of Plasticity*, 2:711–718, 1987.
- K. Kawai, L.-N. Yang, and H. Kudo. A flexible shear spinning of axi-symmetrical shells with a general-purpose mandrel. *Journal of Materials Processing Technology*, 192:13–17, 2007. doi: 10.1016/j.jmatprotec.2007.04.008.
- G. Keller. *Applied Statistics with Microsoft Excel*. Cengage Learning, Inc, 2001. ISBN 978 0 534 37112 8.
- C. Kim, S.Y. Jung, and J.C. Choi. A lower upper-bound solution for shear spinning of cones. *International Journal of Mechanical Sciences*, 45(11):1893–1911, 2003. doi: 10.1016/j.ijmecsci.2003.11.002.
- J.H. Kim, J.H. Park, and C. Kim. A study on the mechanics of shear spinning of cones. *Journal of Mechanical Science and Technology*, 20(6):806–818, 2006. doi: 10.1007/BF02915944.
- F. Klocke and T. Wehrmeister. Laser-assisted metal spinning of advanced materials. In *Proceedings of the 4th LANE*, pages 1183–1192, 2004.
- T. Konkova. ATI Fast-Make Shear forming: Microstructure and hardness analysis of shear formed material (Inconel 718). Technical Report AFRC-415, Advanced Forming Research Centre, Inchinnan, 2015.

- C. Kubilay. *Flow forming of aeroengine materials*. PhD thesis, University of Manchester, 2014.
- B.R. Kumar, A.K. Singh, S. Das, and D.K. Bhattacharya. Cold rolling texture in AISI 304 stainless steel. *Materials Science and Engineering: A*, 364(1):132–139, 2004. doi: 10.1016/j.msea.2003.08.012.
- J. Kunert, R. Ewers, M. Kleiner, N. Henkenjohann, and C. Auer. Optimisation of the shear forming process by means of multivariate statistical methods. Technical report, Universität Dortmund, SFB 475 Komplexitätsreduktion in Multivariaten Datenstrukturen, 2005. doi: 10.17877/DE290R-14498.
- C.-M. Kuo, Y.-T. Yang, H.-Y. Bor, C.-N. Wei, and C.-C. Tai. Aging effects on the microstructure and creep behavior of Inconel 718 superalloy. *Materials Science and Engineering: A*, 510:289–294, 2009. doi: 10.1016/j.msea.2008.04.097.
- S. Le Roux. *La mesure des états de surface*. École des Mines d’Albi-Carmaux, 2012.
- R.K. Leach. *The Measurement of Surface Texture using Stylus Instruments*. National Physical Laboratory, 2014.
- R.B. Li, M. Yao, W.C. Liu, and X.C. He. Isolation and determination for  $\delta$ ,  $\gamma'$  and  $\gamma''$ -phases in Inconel 718 alloy. *Scripta Materialia*, 46(9):635–638, 2002. doi: 10.1016/S1359-6462(02)00041-6.
- J.H. Liu, H. Yang, and Y.Q. Li. A study of the stress and strain distributions of first-pass conventional spinning under different roller-traces. *Journal of Materials Processing Technology*, 129(1):326–329, 2002. doi: 10.1016/S0924-0136(02)00682-9.
- W.C. Liu, F.R. Xiao, M. Yao, Z.L. Chen, Z.Q. Jiang, and S.G. Wang. The influence of cold rolling on the precipitation of delta phase in Inconel 718 alloy. *Scripta Materialia*, 37(1):53–57, 1997. doi: 10.1016/S1359-6462(97)00062-6.
- D.T. Llewellyn. Work hardening effects in austenitic stainless steels. *Materials Science and Technology*, 13(5):389–400, 1997. doi: 10.1179/026708397790302214.
- P. Lours. *Procédé de mise en oeuvre et propriétés des métaux et alliages – Les superalliages*. Lecture from École des Mines d’Albi-Carmaux, 2011.

- F. Ma, H. Yang, and M. Zhan. Plastic deformation behaviors and their application in power spinning process of conical parts with transverse inner rib. *Journal of Materials Processing Technology*, 210(1):180–189, 2010. doi: 10.1016/j.jmatprotec.2009.07.006.
- P. Marshall. *Austenitic stainless steels: Microstructure and mechanical properties*. Springer Science & Business Media, 1984. ISBN 0-85334-277-6.
- M.F. McGuire. Austenitic stainless steels. In *Stainless steels for design engineers*, pages 69–78. ASM International, 2008. ISBN 978-0-87170-717-8.
- S.C. Medeiros, Y.V.R.K. Prasad, W.G. Frazier, and R. Srinivasan. Microstructural modeling of metadynamic recrystallization in hot working of IN 718 superalloy. *Materials Science and Engineering: A*, 293(1):198–207, 2000. doi: 10.1016/S0921-5093(00)01053-4.
- M. Milad, N. Zreiba, F. Elhalouani, and C. Baradai. The effect of cold work on structure and properties of AISI 304 stainless steel. *Journal of Materials Processing Technology*, 203(1):80–85, 2008. doi: 10.1016/j.jmatprotec.2007.09.080.
- K.P. Mingard, B. Roebuck, E.G. Bennett, M. Thomas, B.P. Wynne, and E.J. Palmiere. Grain size measurement by ebsd in complex hot deformed metal alloy microstructures. *Journal of Microscopy*, 227(3):298–308, 2007. doi: 10.1111/j.1365-2818.2007.01814.x.
- Minitab Inc. *Minitab 17.1.0 Statistical Software*. [Computer software]. State College, 2013. [www.minitab.com](http://www.minitab.com).
- E. J. Mittemeijer. Recovery, recrystallization and grain growth. In *Fundamentals of Materials Science*, pages 463–496. Springer, 2010. ISBN 978 3 642 10500 5.
- Mitutoyo. Surftest SJ-210 Portable Surface Roughness Tester. [Online] Available from: <http://www.mitutoyo.co.uk/form-measurement/surface-roughness/178-561-02e> [Accessed: 28th October 2015], c. 2012.
- Mitutoyo. Crysta-Apex C Coordinate Measuring Machine. [Online] Available from: <http://www.mitutoyo.co.uk/191-c2030> [Accessed: 14th January 2015], c. 2015a.
- Mitutoyo. Crysta-Apex C. [Online] Available from: <https://www.mitutoyo.co.uk/media/pdf/CMM/Crysta-ApexC.pdf> [Accessed: 14th January 2015], c. 2015b.

- MJC Engineering & Technology. MJC F1200.2300-4. [Online] Available from: <http://mjcengineering.com/machines/flow-forming-machines/mjc-f1200-2300-4/> [Accessed: 3rd May 2017], c. 2017a.
- MJC Engineering & Technology. MJC SPC-270.150. [Online] Available from: <http://mjcengineering.com/machines/custom-spinning-machines/mjc-spc-270-150/> [Accessed: 3rd May 2017], c. 2017b.
- M. Mohamed Zaky Ahmed. *The Development of Thick Section Welds and Ultra-Fine Grain Aluminium Using Friction Stir Welding and Processing*. PhD thesis, University of Sheffield, 2009.
- M.S. Mohebbi and A. Akbarzadeh. Experimental study and fem analysis of redundant strains in flow forming of tubes. *Journal of Materials Processing Technology*, 210(2):389–395, 2010. doi: 10.1016/j.jmatprotec.2009.09.028.
- K.-I. Mori and T. Nonaka. Simplified three-dimensional finite element simulation of shear spinning process based on axisymmetric modeling. *Journal of Manufacturing Processes*, 7(1):51–56, 2005. doi: 10.1016/S1526-6125(05)70081-5.
- P.E. Mosser, G. Leconte, J. Leray, A. Lasalmonie, and Y. Honnorat. Metallurgical aspects of forge modelling in alloy 718. *Superalloys*, pages 179–188, 1989.
- O. Music, J.M. Allwood, and K. Kawai. A review of the mechanics of metal spinning. *Journal of Materials Processing Technology*, 210(1):3–23, 2010. doi: 10.1016/j.jmatprotec.2009.08.021.
- Y.-S. Na, J.-T. Yeom, N.-K. Park, and J.-Y. Lee. Simulation of microstructures for Alloy 718 blade forging using 3D FEM simulator. *Journal of Materials Processing Technology*, 141(3):337–342, 2003. doi: 10.1016/S0924-0136(03)00285-1.
- A. Norton. Condition of Supply Approval Package for Shear Formed T1000 Front Panel Manufactured in Inconel 718 (MSRR7116) to Drawing number NQF004412. Technical Report Issue 7, Rolls-Royce plc, Derby, 2015.
- Outokumpu Stainless AB. *Handbook of Stainless Steel*. Outokumpu Oyj, 2013.
- Oxford Instruments. *Channel 5*. Bucks, February 2010.

- L. Peguet, B. Malki, and B. Baroux. Influence of cold working on the pitting corrosion resistance of stainless steels. *Corrosion Science*, 49(4):1933–1948, 2007. doi: 10.1016/j.corsci.2006.08.021.
- M. Perez and T. Konkova. ATI Fast-Make Shear forming: Microstructure and hardness analysis of as-received material (Inconel 718). Technical Report AFRC-TRP259, Advanced Forming Research Centre, Inchinnan, 2015.
- E. Quigley and J. Monaghan. Enhanced finite element models of metal spinning. *Journal of Materials Processing Technology*, 121(1):43–49, 2002. doi: 10.1016/S0924-0136(01)01138-4.
- D. Raabe. Recovery and recrystallization: Phenomena, physics, models, simulation. In *Physical Metallurgy (Fifth Edition)*, pages 2291–2397. Elsevier, 2014. ISBN 978-0-444-53770-6.
- L.M. Radović, M. Nikačević, and B. Jordović. Deformation behaviour and microstructure evolution of AlMg6Mn alloy during shear spinning. *Transactions of Nonferrous Metals Society of China*, 22(5):991–1000, 2012. doi: 10.1016/S1003-6326(11)61275-2.
- C.M.F. Rae and R.C. Reed. The precipitation of topologically close-packed phases in rhenium-containing superalloys. *Acta Materialia*, 49(19):4113–4125, 2001. doi: 10.1016/S1359-6454(01)00265-8.
- V. Randle. Electron backscatter diffraction: Strategies for reliable data acquisition and processing. *Materials Characterization*, 60(9):913–922, 2009. doi: 10.1016/j.matchar.2009.05.011.
- R.C. Reed. *The Superalloys: Fundamentals and Applications*. Cambridge University Press, 2008. ISBN 978 0 521 07011 9.
- A. Rollett, F.J. Humphreys, G.S. Rohrer, and M. Hatherly. *Recrystallization and related annealing phenomena*. Elsevier, 2004. ISBN 978-0-08-044164-1.
- Rolls-Royce plc. JES 137 Issue 9 – Engineering Specification: Surface Texture Control, April 2000.

- Rolls-Royce plc. MSRR7116 Issue 9 – Material Specification: Ni-19Cr-18Fe-5Nb-3Mo-0.9Ti-0.5Al Alloy Vacuum or electroflux Remelted Plate, Sheet and Strip, December 2006.
- Rolls-Royce plc. RRES 90036 – Aerospace Engineering Specification: Surface Texture Control, July 2009.
- Rolls-Royce plc. MSRR9969 Issue 13 – Material Specification: Procedural requirements for the hardness testing of metals, August 2012.
- Rolls-Royce plc. JES 161 Issue 8 – Engineering Specification: Hardness Testing Requirements, July 2013.
- A. Rosochowski. *Quality techniques in manufacturing*. University of Strathclyde, 2013.
- M.J. Roy and D.M. Maijer. Analysis and modelling of a rotary forming process for cast aluminum alloy a356. *Journal of Materials Processing Technology*, 226:188–204, 2015. doi: 10.1016/j.jmatprotec.2015.06.036.
- M. Runge. *Spinning and Flow forming*. Werkzeugmaschinenbau/Verlag Moderne Industrie AG, 1993.
- M. Saunders, P. Lewis, and A. Thornhill. *Research Methods for Business Students*. Pearson Education, Sixth edition, 2012. ISBN 978 0 273 75080 2.
- A.J. Schwartz, M. Kumar, B.L. Adams, and D.P. Field. *Electron backscatter diffraction in materials science*, volume 2. Springer, 2009. ISBN 978 0 387 88136 2.
- R Slater. A review of analytical and experimental investigations of the spin-forging of sheet metal cones. *Rotary Metalworking Processes*, pages 33–60, 1979.
- R.E. Smallman and R.J. Bishop. Mechanical behaviour of materials. In *Modern physical metallurgy and materials engineering*, pages 197–258. Butterworth-Heinemann, 1999. ISBN 978-0-7506-4564-5.
- T. Sourmail. *Simultaneous precipitation reactions in creep-resistant austenitic stainless steels*. PhD thesis, University of Cambridge, 2002.

- Special Metals. Inconel alloy 718. [Online] Available from: <http://specialmetals.com/documents/Inconel%20alloy%20718.pdf> [Accessed: 14th November 2016], c. 2015.
- N.S. Stoloff. Wrought and P/M superalloys. In *ASM Handbook Volume 1 – Properties and Selection: Irons, Steels, and High Performance Alloys*. ASM International, 1990. ISBN 978-0-87170-377-4.
- D. Sweeney and D. Atkinson. Design Rules & Aids (DRA) 62 Appendix 5 – Near Net Shape Manufacturing – Design Guide Flowforming. Technical Report Issue 1, Rolls-Royce plc, Derby, 2012.
- N.T. Switzner, E.T. Sawyer, W.A. Everhart, and R.L. Hanlin. Predicting microstructure and strength for aisi 304l stainless steel forgings. *Materials Science and Engineering: A*, 745:474–483, 2019.
- S.S.M. Tavares, D. Gunderov, V. Stolyarov, and J.M. Neto. Phase transformation induced by severe plastic deformation in the AISI 304L stainless steel. *Materials Science and Engineering: A*, 358(1):32–36, 2003. doi: 10.1016/S0921-5093(03)00263-6.
- S. Tin and T.M. Pollock. Phase instabilities and carbon additions in single-crystal nickel-base superalloys. *Materials Science and Engineering: A*, 348(1):111–121, 2003. doi: 10.1016/S0921-5093(02)00637-8.
- M. Tuckwood. Samulet II project 10.5 ATI Fast-Make: Shear forming metallurgical understanding – KPV1 residual stress assessment. Technical Report AFRC-367, Advanced Forming Research Centre, Inchinnan, 2016a.
- M. Tuckwood. Samulet II project 10.5 ATI Fast-Make: Shear forming capability – KPV1 trial outcomes. Technical Report AFRC-368, Advanced Forming Research Centre, Inchinnan, 2016b.
- G. F. Vander Voort. *BUEHLER SUM-MET The Science Behind Materials Preparation*. Buehler, 2007. ISBN 0 9752898 0 2.
- G.F. Vander Voort, G.M. Lucas, and E.P. Manilova. Metallography and microstructures of stainless steels and maraging steels. In *ASM Handbook Volume 9 – Metallography and Microstructures*. ASM International, 2004. ISBN 978-0-87170-706-2.

- G. Ward. WF STR 600-3/6 Flow Forming Equipment: Calibration Procedure. Technical report, Advanced Forming Research Centre, Inchinnan, 2015.
- S.D. Washkot and G. Aggen. Wrought stainless steels. In *ASM Handbook Volume 1 – Properties and Selection: Irons, Steels, and High Performance Alloys*. ASM International, 1990. ISBN 978-0-87170-377-4.
- WF Maschinenbau und Blechformtechnik GmbH. "Instruction manual: Installation, Introduction, Machine part," in *3-Roller-Flow forming and Spinning Machine, STR 600, 10/14058*. Sendenhorst, 2013.
- WF Maschinenbau und Blechformtechnik GmbH. Drawn- and flow-formed parts. [Online] Available from: [http://www.wf-maschinenbau.com/englisch/machines\\_drawn\\_flow-formed\\_parts.php](http://www.wf-maschinenbau.com/englisch/machines_drawn_flow-formed_parts.php) [Accessed: 17th March 2014], c. 2014.
- C.C. Wong, T.A. Dean, and J. Lin. A review of spinning, shear forming and flow forming processes. *International Journal of Machine Tools and Manufacture*, 43 (14):1419–1435, 2003. doi: 10.1016/S0890-6955(03)00172-X.
- Z. Wu, H. Bei, F. Otto, G.M. Pharr, and E.P. George. Recovery, recrystallization, grain growth and phase stability of a family of FCC-structured multi-component equiatomic solid solution alloys. *Intermetallics*, 46:131–140, 2014. doi: 10.1016/j.intermet.2013.10.024.
- J. Yang, Q. Zheng, M. Ji, X. Sun, and Z. Hu. Effects of different C contents on the microstructure, tensile properties and stress-rupture properties of IN792 alloy. *Materials Science and Engineering: A*, 528(3):1534–1539, 2011. doi: 10.1016/j.msea.2010.11.003.
- C. Zaworka. *Optical roughness measurement Basic – Version 5.3*. Kent, 2011.
- M. Zhan, H. Yang, J.H. Zhang, Y.L. Xu, and F. Ma. 3D FEM analysis of influence of roller feed rate on forming force and quality of cone spinning. *Journal of Materials Processing Technology*, 187:486–491, 2007. doi: 10.1016/j.jmatprotec.2006.11.114.
- M. Zhan, X. Wang, and H. Long. Mechanism of grain refinement of aluminium alloy in shear spinning under different deviation ratios. *Materials & Design*, 108:207–216, 2016. doi: 10.1016/j.matdes.2016.06.095.



- 
- L.X. Zhou and T.N. Baker. Effects on dynamic and metadynamic recrystallization on microstructures of wrought IN-718 due to hot deformation. *Materials Science and Engineering: A*, 196(1):89–95, 1995. doi: 10.1016/0921-5093(94)09717-8.